ABSTRACT

Title of Thesis: SLIDING MESH COMPUTATIONAL FLUID DYNAMICS SIMULATION OF A WIDE AND NARROW GAP INLINE ROTOR-STATOR MIXER

Degree Candidate: Karl Rustom Kevala

Degree and year: Master of Science, 2001

Thesis directed by: Professor Richard V. Calabrese
Department of Chemical Engineering

The FLUENT™ Computational Fluid Dynamics code was used to simulate the flow of water within an inline rotor-stator mixer. Two devices were simulated. Both had identical dimensions, except for the width of the shear gap: 4 mm for the 'wide gap' model and 0.5 mm for the 'standard gap' model. A two-dimensional approximation was used in conjunction with a RANS turbulence model and sliding mesh technique.

Simulated turbulence intensities and mass flow rates are more evenly distributed in the standard gap model. Further, turbulence and mean shear levels within the gap are minimal and probably not important for the production of dispersions. The most intense turbulence is near the

downstream stator slot wall, and it is due to fluid impingement. For the standard gap model, this region is more focused and of higher intensity. It is concluded that a narrow gap clearance is needed to produce high intensity stagnation flows on the stator teeth.

Simulation results are also compared with previously reported measurements acquired via Laser Doppler Anemometry. With respect to mean velocity, qualitative agreement is good. Quantitatively, neither the mean velocities nor turbulence values are well predicted. This discrepancy is believed to be due in large part to leakage flow over the top of the rotor and stator teeth and to the three-dimensional nature of the flow.

Future simulations should be carried out in three dimensions using more sophisticated turbulence models. Additionally, algorithms should be developed to decrease computation time by exploiting the periodic nature of rotor-stator flows.

SLIDING MESH SIMULATION OF A WIDE AND NARROW GAP INLINE ROTOR-STATOR MIXER

by

Karl Rustom Kevala

Thesis submitted to the Faculty of the Graduate School of the
University of Maryland, College Park in partial fulfillment
of the requirements for the degree of
Master of Science
2001

Advisory Committee:

Professor Richard V. Calabrese, Chair
Professor Raymond A. Adomaitis
Professor James W. Gentry

ACKNOWLEDGEMENTS

Thanks are due to many people who helped make it possible to write this thesis. First, I would like to express great appreciation and thanks to my wife, Jill, who has been very supportive of my switch in career path from chemist to chemical engineer, and who also assisted me in editing and correcting the final version of this manuscript.

Thanks to several people at the University of Maryland. Professor Richard Calabrese instructed me in the fundamentals of fluid mechanics, both in the classroom and informally as my advisor. Thanks also for his patience when I needed to leave the University for some time for a chemistry position before returning to finish this thesis and continue work here on very interesting engineering problems.

Thank you to Dr. Ved Mishra, who was very helpful to me at the beginning of this work by teaching me how to use meshing software, and also for providing the experimental data used for validation of the computational work here.

Thanks also to Dr. Randall Robinson, who helped make this work possible by setting up a cluster of high-end PC workstations for parallel computation of the simulations that form this work.

Special thanks go to Mr. Mark Meili and Dr. Thomas Niederkorn of The Procter and Gamble Company. They made possible more than two months of time on a high-end Silicon Graphics workstation at the Procter and Gamble Technology Center in Cincinnati Ohio, and also arranged financial support for travel and living expenses while I worked there.

Many thanks to Fluent Inc. which made available, at no cost, their computational fluid dynamics code. Fluent Inc. also provided training. Thank you to Dr. Lanre Oshniowa, of Fluent Inc., who gave a significant amount of his time to provide guidance and suggestions in modeling rotor-stator mixers with FLUENT™.

A big thank you is also in order to all the members of The High Shear Mixing Research Consortium at The University of Maryland for providing the financial support necessary for this work.

TABLE OF CONTENTS

LIST OF TABLES

LIST OF FIGURES

Chapter 1 Introduction

Analysis of results obtained from time dependent, turbulent, computational fluid dynamics (CFD) simulations of two different configurations of an inline rotor-stator mixer of the IKA type are reported. Simulations were performed with the FLUENT™ code in conjunction with a sliding mesh technique and two-dimensional approximation. This work also contains a brief comparison of simulation results with fixed frame and angle correlated Laser Doppler Anemometry (LDA) data for mean velocities and turbulent kinetic energies.

1.1 Background: Rotor-Stator Mixers in the Process Industry

Rotor-stator mixers are high-intensity, high-shear mixing devices that are widely used in the consumer products industry to make lotions, toothpastes, and crèmes. They are also used in many other industries for wet grinding, pigment suspension, food processing, and other formulations where dispersion, shearing, breakup, emulsification, or very fast mixing is required.

A rotor-stator mixer may be of the inline or continuous variety in which an input mixture is continuously fed in and an output stream is continuously siphoned off at the same rate. In this case, the device is simply a continuous stirred reactor. In some applications, the output from an inline device is recycled back into the rotor-

stator until it has reached a desired state (i.e. level of emulsification). Alternatively, a rotor-stator may be used as the mixing head for a batch type processing system.

A typical rotor-stator device used in the chemical processing industry is cylindrical in shape and consists of concentric rows of teeth separated by a very narrow circular gap region (~ 0.5 mm width). Alternating rows of teeth either rotate at high speed (rotor teeth) or are stationary (stator teeth). Fluid mixtures passing through the rotor-stator are accelerated tangentially while in the rotor region, pass into the gap where a very high shear may be experienced, and then impinge onto the stator teeth. In the rotor-stators used in industrial applications there are often many sets of rotor and stator teeth rows in which case the acceleration, shear, and impingement cycle is repeated several times as an element of fluid passes through the device. Figure 1-1 is a photograph of the simple (single row of rotor and stator teeth) inline rotor-stator device which is the focus of this study. A two-dimensional diagram of a radial cross section is shown in Fig. 1-2, and an axisymmetric cross section is shown in Fig. 1-3.

Turbulence, very high shear in the gap region, and impingement on the stator teeth are believed to be the reasons that rotor-stator mixers are so efficient as emulsification devices. These forces may also result in an enhanced rate of mixing (over a traditional turbine style mixer) which may be useful for speeding and/or increasing the selectivity of very fast reactions. Consider for example the sequence of reactions.

$$A + B \rightarrow R \qquad (1.2\text{-}1a)$$

$$B + R \rightarrow S \qquad (1.2\text{-}1b)$$

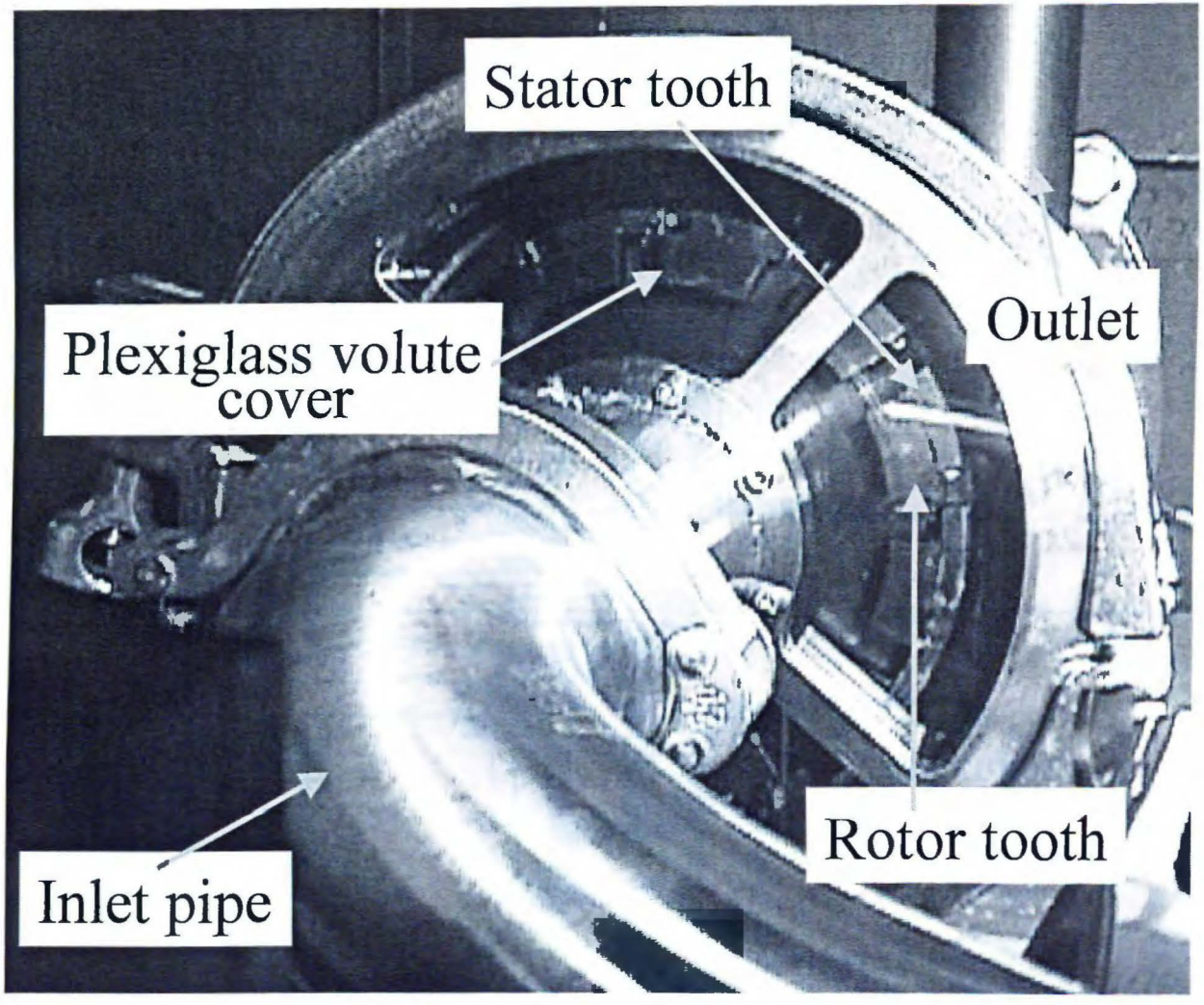

Figure 1-1. Photograph (front view) of the IKA type inline rotor-stator mixer.

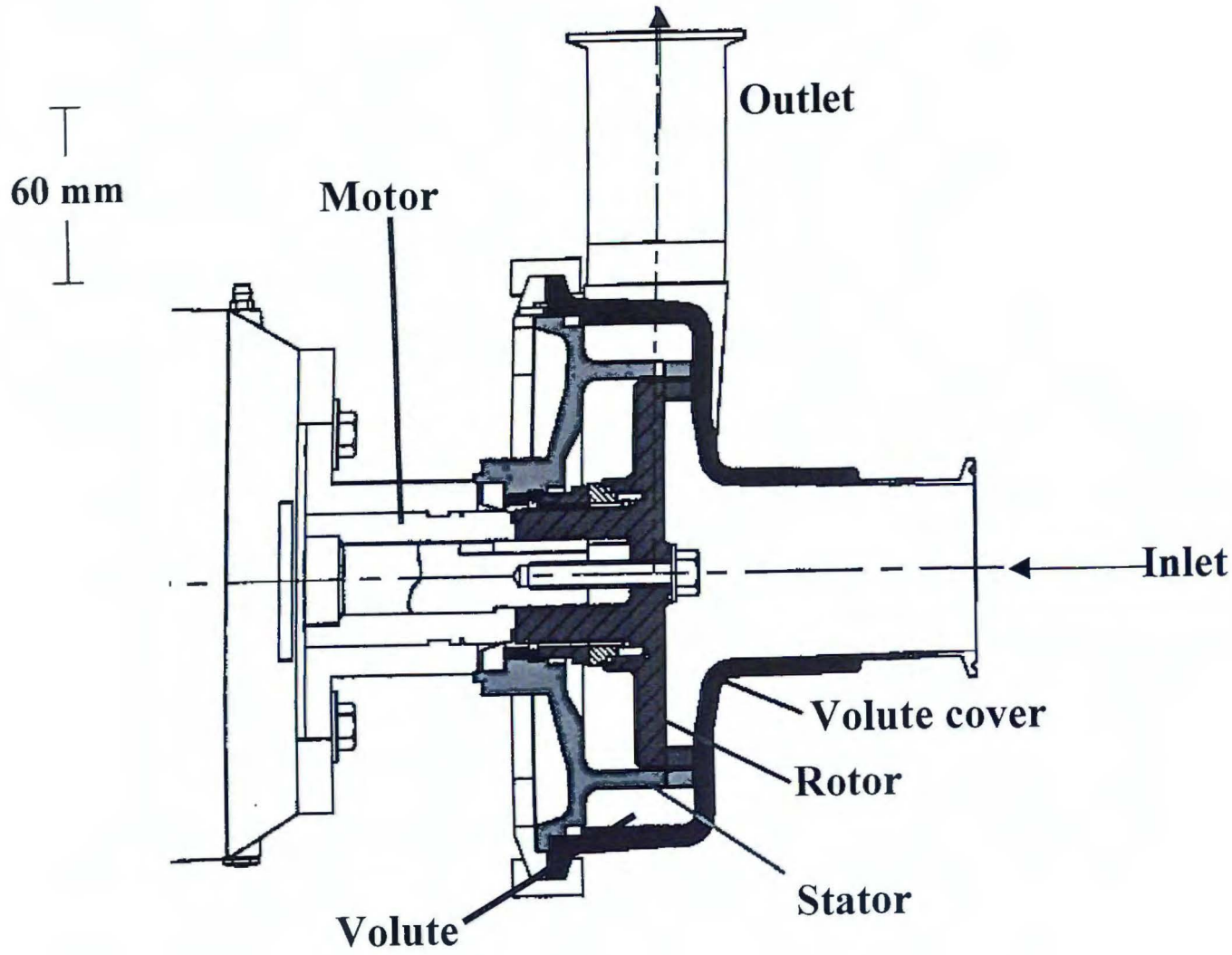

Figure 1-2. Radial cross section schematic of the IKA type inline rotor-stator mixer.

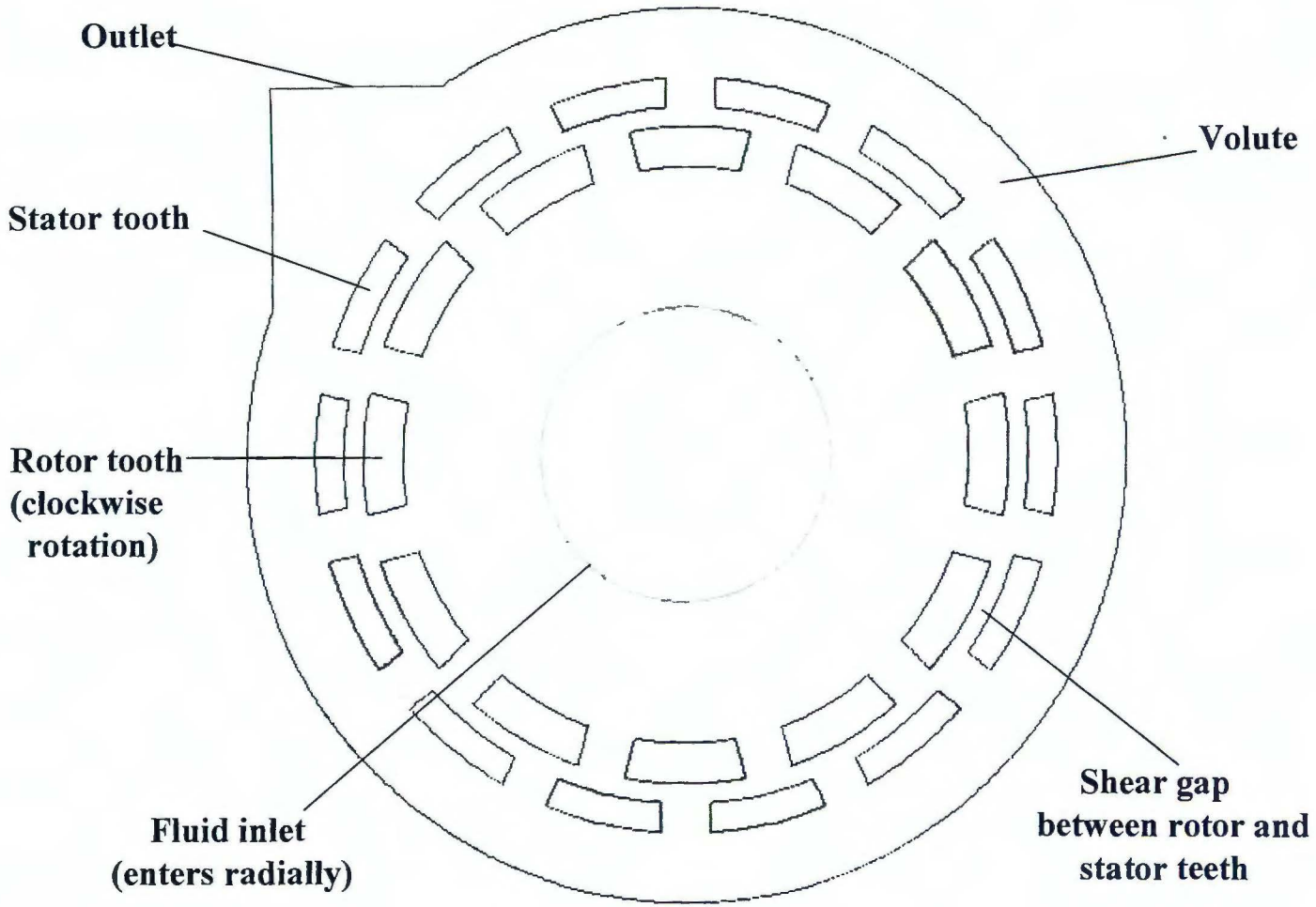

Figure 1-3. Axisymmetric cross section schematic of the IKA rotor-stator mixer simulated here.

where reactions 1.2-1a and b are controlled by rate constants k_1 and k_2 respectively, and the desired product is R. If k_1 is so large that the rate of Eq. 1.2-1a is determined only by the rate at which A and B are brought together, and $k_1 >> k_2$, then, even if mixing is 'slow', as long as B is a limiting reagent the overall selectivity will be good. However, if $k_1 \sim k_2$ then the nature of the flow and mixing in the reactor becomes very important (Carpenter, 1986). A high rate of micromixing may then be required to achieve good selectivity. Rotor-stator mixers are capable of creating very intense localized turbulence and therefore very intense and localized micromixing. Since the turbulence in rotor-stator mixers is localized, the power input required by them to achieve a high rate of micromixing is much less than what would be required to achieve the same rate in traditional stirred tanks. This makes rotor-stators potentially very useful for processes involving fast competing reactions. Reaction systems similar to Eq. 1.2-1 have been studied experimentally in both batch and continuous rotor-stator mixers (Bourne and Garcia-Rosas, 1986), and they have been found to be capable of imparting a high degree of selectivity for industrially applicable reactions.

To the author's knowledge, other than the work by Bourne, there is very little information available in the open literature on rotor-stator devices as used in the process industry.

1.2 Motivation Purpose and Scope

There is a considerable body of knowledge available to the practicing engineer who needs to design or scale up a stirred tank for use in a specific process. The state-of-the-art in stirred vessels has derived from numerous experimental studies designed

to understand either the bulk phenomenological characteristics, like power consumption and large scale fluid motion, or the fundamental nature of the flows occurring in them by using techniques like Laser Doppler Anemometry (LDA) (Stoots, 1989) to allow instantaneous measurement of a fluid's velocity at a given point by use of the Doppler effect. More recently, since the 1970's, Computational Fluid Dynamics (CFD), which is the use of computers to solve the discretized partial differential equations (PDE) which govern the flow of a fluid, have been used to provide insight into stirred tanks. For an incompressible fluid these PDEs are collectively known as the Navier-Stokes (N-S) and continuity equations (a set of four equations in three dimensions). CFD has been used to simulate both laminar and turbulent flows in stirred vessels and has shown promise in allowing for more rational design decisions for stirred vessels in the chemical industry.

Although rotor-stator devices are widely used throughout many industries, there is very little information available about the fundamental physics of flows occurring in them. As is the case with stirred tanks, it is desirable to be able to predict, through simulation, the effect that operating conditions such as rotational velocity, fluid viscosity and rheology, inlet mass flow rate, and rotor-stator geometry will have on the physical properties of rotor-stator flow fields and the mixing, shearing, breakup, reaction, and other processes occurring in them. If CFD can be used for the accurate simulation of rotor-stator mixers, it may allow for engineers to use it as a relatively inexpensive tool, saving time and expensive trial and error experimentation in at least the initial stages of process design and / or scale up. With the phenomenal increase in

computing power over the last few years, it is now reasonable to attempt accurate CFD simulations of rotor-stator mixers.

The purpose of this thesis is to present results for the isothermal, time dependent, turbulent simulations of water in a simplified inline rotor-stator device, custom made by IKA Works Inc. The simulations utilize a sliding mesh technique with the commercially available finite volume computational fluid dynamics code FLUENT™ version 5. A two-dimensional approximation is made. For turbulent flow, it is in general impossible or very difficult to directly solve the Equations of motion. Rather, the ensemble average of the equations is taken to yield the well known Reynolds Averaged Navier-Stokes Equations (RANS). The RANS equations lack closure due to the presence of the covariances of each of the fluctuating flow variables. In order to solve the RANS equations, the covariances are modeled. Of the several turbulence models available, the one chosen for this study is among the simplest and is called the Standard k-epsilon (Std k-ε) model. Here k stands for the kinetic energy of the fluid per unit mass of fluid contained in the turbulent fluctuations (also abbreviated as TKE) and ε is its rate of dissipation per unit mass (Mohammadi, 1997). The k-ε model was chosen because it is computationally one of the least expensive models, and it has been widely used for CFD in stirred tanks. Moreover, a study by Sturesson and Rasmuson (1995) found that the k-ε model gave similar results for the mean velocity field in a stirred tank compared to the much more sophisticated Reynolds Stress Model (RSM). In the RSM model, transport of each of the Reynolds stresses is modeled directly by a PDE rather than lumping them together in a turbulent

kinetic energy parameter. More details on how the k-ε turbulence model is used for closure of the RANS equations can be found in chapter 3, along with other details of the numerical procedures.

The simulations presented here are a continuation of work done by Epee-Bounya (1998) where a device similar to the one presently under consideration was simulated also using a two-dimensional approximation and the std k-ε turbulence model. Epee-Bounya's work laid a solid foundation for the simulation of rotor-stator mixers by showing that simulations could be done with a reasonable amount of computer resources and time and also that the results appeared, at least on a qualitative level, to be physically realistic. However, his simulations left several questions unanswered, in part due to the fact that the geometry he used for simulation was slightly different from the true device geometry and also because there exists no experimental data at the operating conditions of his simulations with which to make a comparison. Moreover, his simulations used a 1st order discretization scheme and the results obtained may be tainted by excessive numerical diffusion. Finally, his work was performed for only one set of operating conditions and one geometric configuration and therefore provide no insight into how flow characteristics may vary as a function of rotor speed, inlet flow rate, or shear gap width. The present thesis expands on previous work and attempts to:

1. Provide indications of how fine the computational mesh needs to be for simulations of this type by carrying out calculations on a 'medium' and 'fine' grid.

2. Investigate the sensitivity of the simulated flow to the type of outlet boundary condition.
3. Critically analyze the simulation time necessary to reach a steady periodic solution.
4. Provide a more thorough analysis of simulated flow characteristics.
5. Provide insight into the effect that the shear gap width may have on rotor-stator flow fields by simulating two devices: A 'wide gap' model with a gap width of 4 mm and a 'standard gap' model with a gap width of 0.5 mm.
6. Validate (or negate) assumptions used in the modeling approximations by running simulations at operating conditions (inlet mass flow rate and rotor speed) for which there is experimental LDA data of the velocity and turbulence fields available and performing a limited qualitative comparison of the results.

Although the scope of this thesis does not involve a detailed quantitative comparison between simulated and experimental results, later work is planned for a more in-depth comparison. The work here should provide direction for future three-dimensional simulations planned for the device used for this study, and also for simulation of more complex rotor-stators with fluids exhibiting more complex rheological behavior.

1.3 Device Overview

Dimensions of the physical rotor-stator mixers that are simulated are listed in Table 1-1. Dimensions of the two-dimensional axisymmetric domain used for simulation is shown in Fig. 1-4. Note that Table 1-1 includes a tooth 'depth' which

refers to the third dimension ignored in the simulations. Also note the difference in the rotor inner diameter between the actual physical device and the simulation domain (118 mm vs. 124.5 mm). This is due to an error during the mesh generation process. The resulting different rotor tooth lengths (8.25 mm simulation, 11 mm physical) is not expected to strongly affect the solution in or beyond the shear gap because the error is in the placement of the radially inner edge of the rotor tooth, not the edge near the shear gap. Further, as will be discussed later, three-dimensional effects may actually be more important.

Table 1-1. Physical Dimensions of the IKA Rotor-Stator Devices in mm

	Wide Gap Device		Standard Gap Device	
	Rotor	Stator	Rotor	Stator
Inner diameter	111	142	118	142
Outer diameter	134	154	141	154
Tooth length	11.5	6	11.5	6
Tooth width	24 (21.4°)	22 (17.6°)	26 (21.9°)	22 (17.6°)
Tooth depth	10	12	10	12
Slot width	10 (8.56°)	10 (8.08°)	10 (8.14°)	10 (8.08°)
Number of teeth	12	14	12	14
Volute outer Diameter	182.5		182.5	
Gap width	4		0.5	

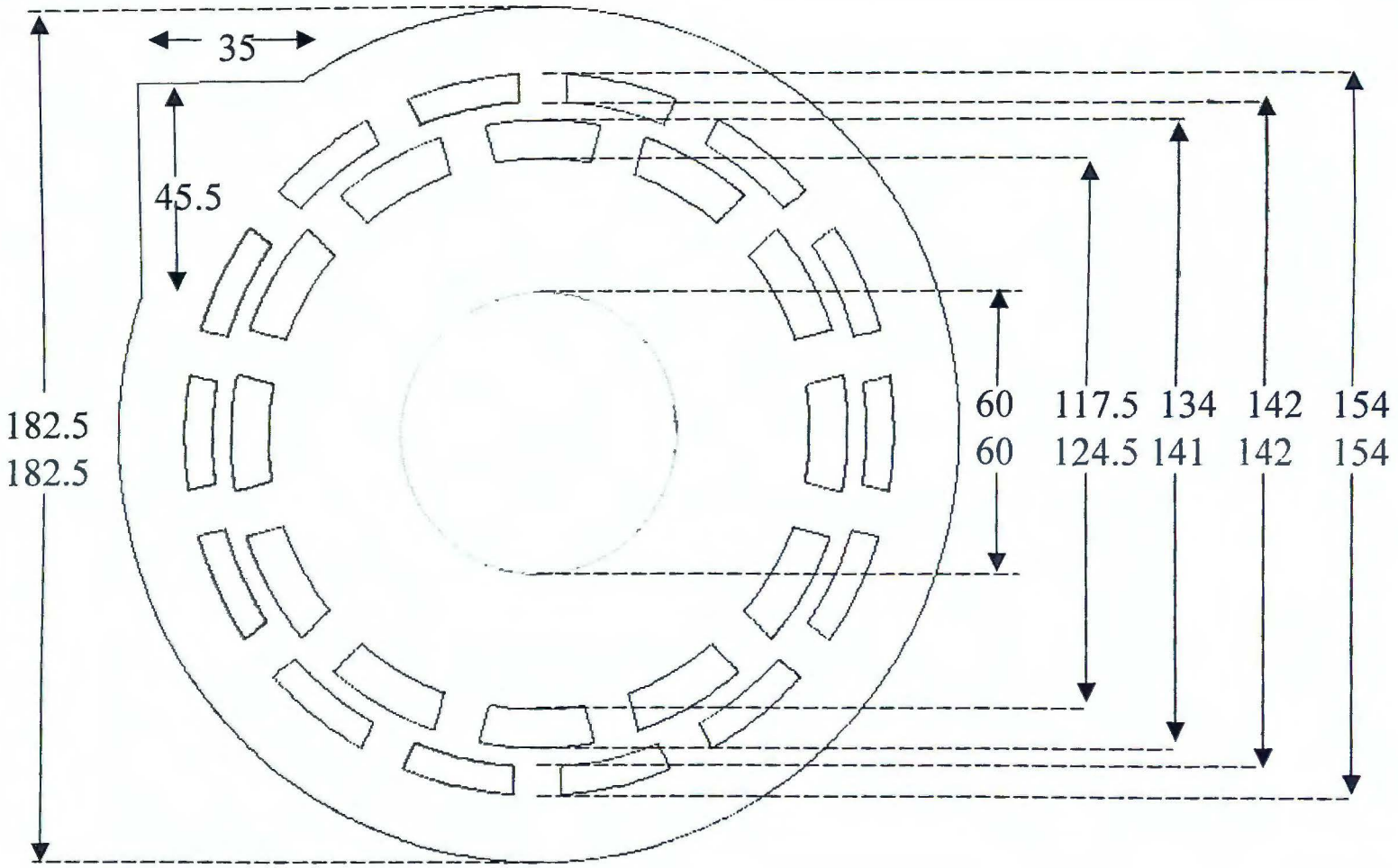

Figure 1-4. Model dimensions used for CFD simulation in millimeters. Top values are for the wide gap (4 mm) model, lower values are for the standard gap (0.5 mm) model.

Two different geometrical configurations of the rotor-stator are used for both simulation and experimental LDA measurements. In the first geometry, the shear gap or region between the rotor and stator teeth, has a width of 4 mm, and is referred to as the wide gap device or model. In the second configuration, the gap has a width of 0.5 mm, which is more typical of actual industrial equipment, and is referred to as the standard gap device or model.

1.4 Frames of Reference for Velocity Fields in Stirred Tanks and Rotor-Stator Devices

In both stirred tanks and rotor-stator mixers, there is always one portion of the device that moves with respect to the 'inertial' laboratory frame of reference (i.e. the rotor in a rotor-stator device or the impeller in a stirred tank) and one portion that is stationary. This fact can make computation and measurement of the flow in them somewhat complicated.

Methods for finite difference and finite volume simulations of flow in these systems can be divided into four major categories. The first method, which was quite common in the early days of stirred tank CFD, is probably not applicable to rotor-stator simulations. In this method, the entire domain is treated as existing in the laboratory or fixed frame of reference. Action of the tank impeller is modeled by treating the surface of the impeller sweep volume as a 'black box' source of momentum. Boundary conditions for the surface are obtained either by experimental measurements or simple empirical formulas. Measurements of velocities in the fixed frame of reference ignore the passage of stirrer blades or rotor teeth.

The other three CFD methods are based on solving the equations of motion in one or more rotating reference frames. In the rotating reference frame (RRF) method, the equations of fluid motion are solved in a frame of reference stationary with respect to the rotor or impeller. The tank wall or stator then moves relative to this frame. Extra terms are added to the equations of motion to account for the rotation. If there is no periodic interaction between walls of the rotating and stationary frames (as is the case in an unbaffled, cylindrical stirred tank), then solving the resulting steady state equations will in principle yield an exact solution (ignoring discretization error). Even when the flow is periodic in the inertial frame due to the presence of baffles in the tank or a stator, RRF is sometimes used if the interaction between the stationary and moving walls is expected to be weak, thus yielding an approximate solution.

The third method, the multiple reference frame method (MRF), yields an exact solution under the same conditions as the rotating reference frame method. In MRF, the fluid domain is divided into two (or more) regions. In the region(s) bounding rotating wall(s), the equations of motion are written and solved for a rotating frame of reference. In region(s) bounding stationary wall(s), the equations are written in a stationary frame of reference. During the solution process, fluxes of flow variables are interpolated across the boundaries between the regions, taking into account the difference in the equations for the zones. Like RRF, MRF methods are solved using a steady state discretization.

The most accurate, and computationally intensive, methods are those based on the sliding mesh technique. Sliding mesh simulations are fully time dependent and do not require empirical boundary conditions. In this method, the domain is divided into

a moving and stationary zone. Discretization of the governing equations is time dependent. At the end of each time step, the mesh attached to rotating walls rotates with the wall. In order to do this, the interface between the stationary and moving mesh is broken and reformed. The interface itself must thus consist of non-conformal cells. Fluxes across the interface are computed by interpolation. Measurements of velocity fields corresponding to this frame of reference are referred to as angularly correlated. These types of measurements are accomplished by synchronizing the output of a shaft mounted encoder with the instantaneous measurements. More will be said about this later in the manuscript.

1.5 Review of CFD for Stirred Tanks and Rotor-Stators

To date, the author knows of only two published works involving CFD simulations of rotor-stator mixers that are applicable to the chemical and process industries. One of these is the work by Epee-Bounya mentioned above. The other (LeClaire, 1995) simulated a KADY Mill Model 4C rotor-stator device which has one row of rotor and stator teeth and looks similar to the IKA type device of this study, but the rotor slots are slightly off angle (i.e. the slots have a cut angle that is opposed to the direction of rotor rotation). The simulation incorporated a two-dimensional approximation with a Newtonian fluid (5,000 cps). It assumed a laminar flow regime even though the rotor tip speed was set at 50 m / sec which probably results in turbulent flow. Almost no other details concerning the device geometry, boundary conditions, type of computational model, reference frame, or mesh details was given in this paper. There was also no comparison of simulation results to experimental

data. LeClaire's main inference from this work was that details of rotor-stator flow fields that are counterintuitive may be found through CFD simulation: His simulation showed that immediately after passage of a rotor slot by a stator slot, the flow in the shear gap near the downstream side of the stator slot may move in a direction opposed to the natural motion imposed on it by the rotor.

The literature on CFD of stirred tanks is much more extensive and includes simulations of both laminar and turbulent, steady-state and time dependent, and two and three-dimensional studies. Kuriyamam et. al. (1982) made a two-dimensional approximation and solved for the laminar flow field in an anchor-impeller unbaffled stirred tank using the stream function formulation of the flow equations. They obtained good agreement with experimental measurements for the radial and tangential velocities as well as the agitation power. Their results were also qualitatively comparable with experimental data on the variation of the streamline patterns with the tank Reynolds number.

In more realistic three-dimensional simulations it is not possible to use the stream function approach. Hiraoka et. al. (1988) used the rotating reference frame method was used for three-dimensional simulations of laminar flow in stirred tanks without baffles and good agreement between simulation and experimental laser Doppler Anemometry (LDA) data was obtained, except near the impeller shaft. Similar work by Abid et. al. (1994) also showed promising results in comparison to experimental data.

Although in baffled stirred tank reactors (BSTRs) the flow field is not steady in any reference frame, the earliest attempts at CFD in BSTRs attempted to simulate the

fixed frame flow by modeling the baffles as a momentum sink or pressure-induced drag and then solving the steady state equations (Harvey and Greaves, 1982) . In the work of Harvey and Greaves, the turbulent flow field in a baffled, 6-blade impeller agitated tank was simulated using the k-ε turbulence model and a two-dimensional approximation. In addition to modeling rather than directly computing the effect of baffles, they also treated the impeller blades as a 'black box' source of momentum by assigning specific, steady values for the velocities in computational cells bounding the geometric surface defined by the impeller. The velocities on the surface were chosen based on simple physical arguments. Because no experimental data were available for the values of k and epsilon at the impeller surface, Harvey and Greaves assigned fairly arbitrary values there. The numerical results they obtained for the mean velocity field and turbulent kinetic energy were compared to experimental data and only a qualitative similarity was found which is attributable, at least in part, to the gross simplifications of the model: Note that the modeling of baffles as a momentum drag implies perfect symmetry in the tangential direction which clearly cannot be the case near the outer baffled wall.

Attempts at three-dimensional modeling of BSTRs included several studies where the time averaged velocity profile and turbulent kinetic energy on the surface of the impeller swept volume was assigned based on experimental LDA measurements (Middleton et. al., 1986). Middleton and co-workers specifically modeled the baffles as solid walls with a no-slip boundary condition, and then solved the steady state equations in a fixed reference frame to obtain the time-averaged solution. Very good agreement between the simulated and experimental velocity

fields were found. Further simulations of mixing phenomenon using the simulated velocity field results obtained by Middleton also compared well with experimental data and offered insight into the inadequacy of scale-up rules then in use.

Ranade and Joshi (1989, 1990) also performed a series of fixed frame three-dimensional BSTR simulations using experimental and semi-empirical boundary conditions on the impeller swept volume surface and directly modeling the baffles as solid walls. Their work was motivated in part by the practical need to find which numerical algorithms and empirical model parameters were best suited to modeling turbulent flow in stirred tank reactors. In their study they introduced a numerical code called FIAT (Flow in Agitated Tanks) that was specifically tailored to time averaged three-dimensional simulations of stirred tanks and employed the std k-ε turbulence model. From their parametric studies, they concluded that fixed frame BSTR simulations are fairly sensitive to the boundary conditions applied on the impeller swept volume, as well as the value of the empirical parameters which appear in the k-ε turbulence model equations.

More work to simulate BSTRs in the spirit of the time averaged approach utilized by Middleton was performed by several other researchers, who proposed their own modifications to methods for specifying boundary conditions on the impeller control volume surface (see for instance Kresta and Wood, 1991). Later simulations compared results based on this method using three different turbulence models: the std k-ε model, the Reynolds stress model (RSM), and the Algebraic stress model (ASM) (Sturesson and Rasmuson, 1995). Sturesson et. al. found little difference in the averaged velocity fields predicted by the turbulence models.

Sheng et. al. (1998) performed a series of fixed frame simulations on a stirred tank with baffles and compared their results to Particle Image Velocimetry (PIV) data. PIV is a method where the instantaneous flow field over a given area (or volume) of fluid can be photographed to yield velocity and turbulent kinetic energy information. These simulations were performed in a stationary frame and used experimental PIV or LDA data to apply boundary conditions on the surface of the impeller sweep volume. In these simulations, the Renormalized k-ε turbulence model (RNG k-ε, a more sophisticated variation of the standard k-ε model) was compared to results obtained through the RSM model. They found the mean velocity field to be predicted fairly well by both models. The turbulent kinetic energy was underpredicted by up to one order of magnitude in both models. Further, the turbulent kinetic energy prediction of both models was worse in the impeller flow discharge region (below the impeller) than in the plane of the impeller itself.

Sheng et. al. (1998) also studied the effect that impeller boundary conditions have on the simulated field and concluded similarly to Ranade et. al. (1990) that simulation results are sensitive to the impeller swept volume boundary conditions, but primarily the turbulent kinetic energy and its dissipation, not the mean velocity field. This conclusion is not certain, however, because the simulations with different boundary conditions also used different turbulence models: RNG k-ε or RSM.

A slightly different approach to the problem was used to obtain time averaged results for BSTRs without the need for experimental input by Harvey et. al. (1995). Their method was essentially a variant of the RRF treatment. Both the baffles and impeller were included as solid surfaces and the steady-state, laminar flow equations

were then solved in the reference frame of the rotating impeller. Relative motion between the impeller and baffles was neglected, although computationally the fluid velocities computed at the baffled wall were based on a relative motion so that the no-slip wall boundary condition (based on a relative angular motion) was still satisfied. Although this model is physically unrealistic (i.e. a relative motion that does not exist in one sense but does in another), they obtained surprisingly good agreement with experimental LDA measurements of the time averaged velocity field by spatially averaging (in a tangential sense) their numerical results after simulation. The largest discrepancies were in tangential velocities close to the impeller.

To this author's knowledge, the first fully time dependent three-dimensional simulation of a BSTR was performed by Luo et. al. (1993) for a tank with a pitched blade impeller and six baffles. They used the std. k-ε model in conjunction with the sliding mesh technique. The computational domain was divided into two separate zones. Zone 1 was cylindrical, ran the entire axial length of the mixing vessel, and had a diameter just slightly larger than that of the impeller. Zone 2 was an annular cylindrical region encompassing the remainder of the vessel. In the computations, zone 1 rotated with the explicitly modeled impeller while zone 2 remained stationary with the tank wall / baffles. At the end of each time step, the impeller along with the inner mesh was rotated a slight amount corresponding to the mixer rotational speed. Fluxes of momentum were interpolated across the interface between zones 1 and 2 during the calculation of each time step. Luo et. al. time averaged their unsteady results and compared the resultant velocity field to experimental LDA data. They found fairly good agreement with experimental data. Further, comparison of their

velocity field results with those from a steady state approximate simulation showed fairly large discrepancies, indicating that time dependant calculations may be essential for a complete understanding of the flow in these systems. They did not perform any analysis of the turbulence parameters.

Bakker et. al. (1997) performed sliding mesh simulations of laminar flow in a pitched blade stirred tank for several tank Reynolds numbers by varying the fluid viscosity (Re between 40 and 1200). Here Re is based on the turbine size and rotational speed and defined as $Re = \rho ND/\mu^2$ where ρ is the fluid density, N the impeller rotational speed, D the impeller diameter, and μ the fluid viscosity. They found a good qualitative prediction of the Reynolds Averaged velocity field when compared to the experimental data of Wang et. al. (1995). The pumping number, which is defined as $N_q = Q_1 / N D^3$ where Q_1 is the volumetric flow rate of fluid leaving a control surface surrounding the impeller, was also well predicted as a function of Reynolds number.

Std. k-ε turbulence model sliding mesh simulation of a BSTR with comparison to LDA measurements performed by Ng et. al. (1998) also found a good prediction for the mean velocity field, but, as was the case for steady state studies (Sheng, 1998), the turbulent kinetic energy field was underpredicted.

Most recently, attention has shifted to turbulence models called Large Eddy Simulation (LES). These models attempt to directly simulate large turbulent eddies occurring in a flow and model those that are smaller than the computational grid size using what is called a subgrid scale model. LES is inherently an unsteady calculation requiring an extremely fine mesh. In one study where a tank driven with a Rushton

turbine was simulated using a Lattice-Boltzmann discretization in combination with LES (Derksen et. al., 1999), very good agreement was found when simulation was compared to LDA data for both the ensemble averaged velocity field and the turbulent kinetic energy, however there were still some deviations in the region of outflow from the impeller.

In summary, computational fluid dynamics in stirred tanks has progressed considerably since the 1970's, starting with stationary reference frame simulations, and moving on to RRF and sliding mesh methods. For laminar flow, there is no great difficulty in carrying out simulations that correlate well with experimental data. Until recently, turbulent flows have always been modeled with RANS equations. RANS models have been good for predicting mean velocity fields, but not the turbulent kinetic energy. In general, the RSM model predicts the turbulent kinetic energy pattern qualitatively better than k-ε models, but still underpredicts the turbulence. LES methods are now being used for simulations of stirred tanks and have shown better prediction of turbulence quantities, but the amount of computational power required for these types of simulations is beyond the reach of most engineers, both industrial and academic.

Work on simulation of the types of rotor-stator mixers used in the process industry is far behind that for stirred tanks, primarily because sliding mesh techniques, which are most appropriate for them, have only recently become available with commercial CFD codes. Although RANS methods may not be ideal for turbulent simulations of rotor-stator mixers, they are adequate for initial work. Results with stirred tank simulations seem to indicate that RANS simulations of rotor-stator devices

may be able to predict the mean velocity field and qualitative patterns of the turbulent kinetic energy, even if absolute magnitudes are incorrect.

1.6 Layout of Manuscript

Chapters two and three cover, in-depth, the methods used in this study: boundary conditions, grid generation and quality, computers, and computational algorithms. The first part of chapter two summarizes important characteristics for the five simulations that form this work. It also covers the two geometrical configurations of the inline rotor-stator that were simulated, the simplifying assumptions used for simulation and why they were chosen, the computational meshes, and it introduces the std k-ε turbulence model.

The second part of chapter two explains the several different sets of boundary conditions used for simulation, why they were chosen, and justifies their use. In the case of the turbulence boundary conditions, some detail is gone into as to how their values were computed.

Chapter three contains an overview of the grid generation process, computer resources and compute times, and specific computational algorithms used by the Fluent code for the simulations. This includes a fairly detailed discussion of the discretization, pressure-momentum coupling, turbulence modeling, treatment at walls, time stepping, and judgment of convergence.

Chapter four is an analysis of simulation results for the first geometrical configuration of the rotor-stator, the wide gap model. Chapter five is an analysis of simulation results for the second geometrical configuration, the standard gap model.

A detailed comparison to the wide gap results is also presented. In chapter six there is a brief comparison of experimental LDA data, obtained elsewhere, with the results presented in chapters four and five. Chapter seven draws final conclusions and proposes recommendations for further work.

Chapter 2 Simulation Models

With the exception of details concerning the computational algorithms, types of computers utilized, and CPU times required, the methods and models employed for this work are reported in this chapter. As stated in chapter 1, both a wide shear gap (4 mm) and standard shear gap (0.5 mm) IKA type inline rotor-stator mixer are simulated (Figs. 1-1 through 1-4). Additionally, 3 more simulations are performed of the wide gap model in order to gain insight into the effect that grid size, outlet boundary conditions, and operating conditions have on simulation results. Important parameters concerning differences between the five simulations are summarized in Table 2-1 which is a useful reference throughout this chapter. In Table 2-1, the number of mesh elements does not include cells in the extended outlet region for simulations 2 and 5 (see section 2.5).

Table 2-1. Model Parameters for CFD Simulations

	Simulation				
	Wide Gap				Standard Gap
	1	2	3	4	5
Mesh elements (thousands)	73.6	73.6	125.3	125.3	322.4
Gap width (mm)	4	4	4	4	0.5
Rotor speed	50	50	50	30	30

(rps)					
Gap Reynolds Number	83,800	83,800	83,800	50,300	6,600
Inlet velocity (m/sec)	2.64	2.64	2.64	1.52	1.52
Inlet flow rate (gpm)	78.8	78.8	78.8	45.4	45.4
Inlet TKE (m^2/sec^2)	0.01	0.01	0.01	0.006	0.006
Inlet ε (m^2/sec^2)	0.007	0.007	0.007	0.002	0.002
Outlet pressure (Pa)	0	N/A	0	0	N/A
Fluid density (kg/m^3)	998.2	998.2	998.2	998.2	998.2
Fluid viscosity (kg/m sec)	0.001	0.001	0.001	0.001	0.001

2.1 Model Geometry

For purposes of simulation, it was assumed that flow in the axial direction of the IKA rotor-stator mixer would be negligible after fluid entered the device and was forced to move in a primarily radial direction towards the rotor teeth. This assumption allowed the device to be approximated as an axisymmetric two-dimensional cross section as previously shown in Fig. 1-4. The reader is reminded that the rotor slot length in the simulated model is 8.25 mm while in the actual rotor-stator it is 11 mm (compare Fig. 1-4 with Table 1-1) due to an error during the mesh generation process.

In the two-dimensional model, the working fluid, water, enters the rotor-stator mixer normal to the circular inlet region, flows through the rotor teeth slots, into the

shear gap region and stator slots, enters the volute, and then exits the device in the upper left hand corner.

A two-dimensional approximation was justified because the rotor and stator slots of the physical rotor-stator have depths of only 10 and 12 mm respectively. Since the radial dimension of the device is more than 180 mm, it is reasonable to expect that the flow is *primarily* two-dimensional. It is clear from Fig. 1-2 that the depth of the rotor and stator teeth are very small in comparison to the radial dimension. Further, time dependent Reynolds averaged turbulent flow simulations using a finite volume method (the method employed in the FLUENT^{TM} code) in conjunction with the sliding mesh technique are extremely computationally intensive. Compute times would be prohibitively long if a full three-dimensional simulation were performed with present technology. Analysis of two-dimensional simulation results will provide a starting point for an understanding of the fundamental physics of rotor-stator flows. Further, comparison of the simulations with experimental measurements will hopefully elucidate where and in what manner the two-dimensional approximation may break down and also provide direction for experimental programs and future three-dimensional simulations.

Two different shear gap geometries are used for both CFD simulation and experimental LDA measurements. In the first geometry, the gap has a width of 4 mm and will be referred to as the wide gap model. In the second geometry, the gap has a width of 0.5 mm and will be referred to as the standard gap model.

There are several reasons for simulating a wide gap model before the more industrially applicable standard gap model. These include meshing constraints

(resulting in an extremely large mesh for the standard gap model) and larger expected velocity gradients encountered in the standard gap model but not, to the same extent, in the wide gap model. Both of these factors have an effect on computational intensity and may influence the ability to converge to a solution. It is therefore desirable to make certain that the wide gap model converges to a physically realistic solution in a reasonable time before attempting simulation of the standard gap model.

Figure 2-1 shows a close up of the meshes used for simulation of both the wide and standard gap models in the vicinity of the gap and a stator slot and may be a helpful aid in order to make the following discussion clear. Meshing constraints in the standard gap model are due to large differences in geometric length scales between the gap region (0.5 mm width) and adjacent stator slot regions (10 mm width). In order to obtain an accurate solution on a block structured quadrilateral mesh (the type of mesh employed) using the finite volume method, adjacent mesh elements should ideally be as similar in size as possible and should never vary by more than a factor of about 1.5. Additionally, for complex flows where there is no way to design the mesh before simulation so that the flow field is predominantly aligned with the mesh elements, or for flows where the field is expected to have significant curl, it is essential that quadrilateral elements are as close to square as possible. The element aspect ratio, a measure of its closeness to being square, is defined as the ratio of its adjacent sides and should have a value between 1 and 10, but should be at the high end only at points where the flow is aligned with the mesh. Finally, in order to resolve the flow field sufficiently in the gap region, it is necessary to have as many elements as possible spanning the gap width.

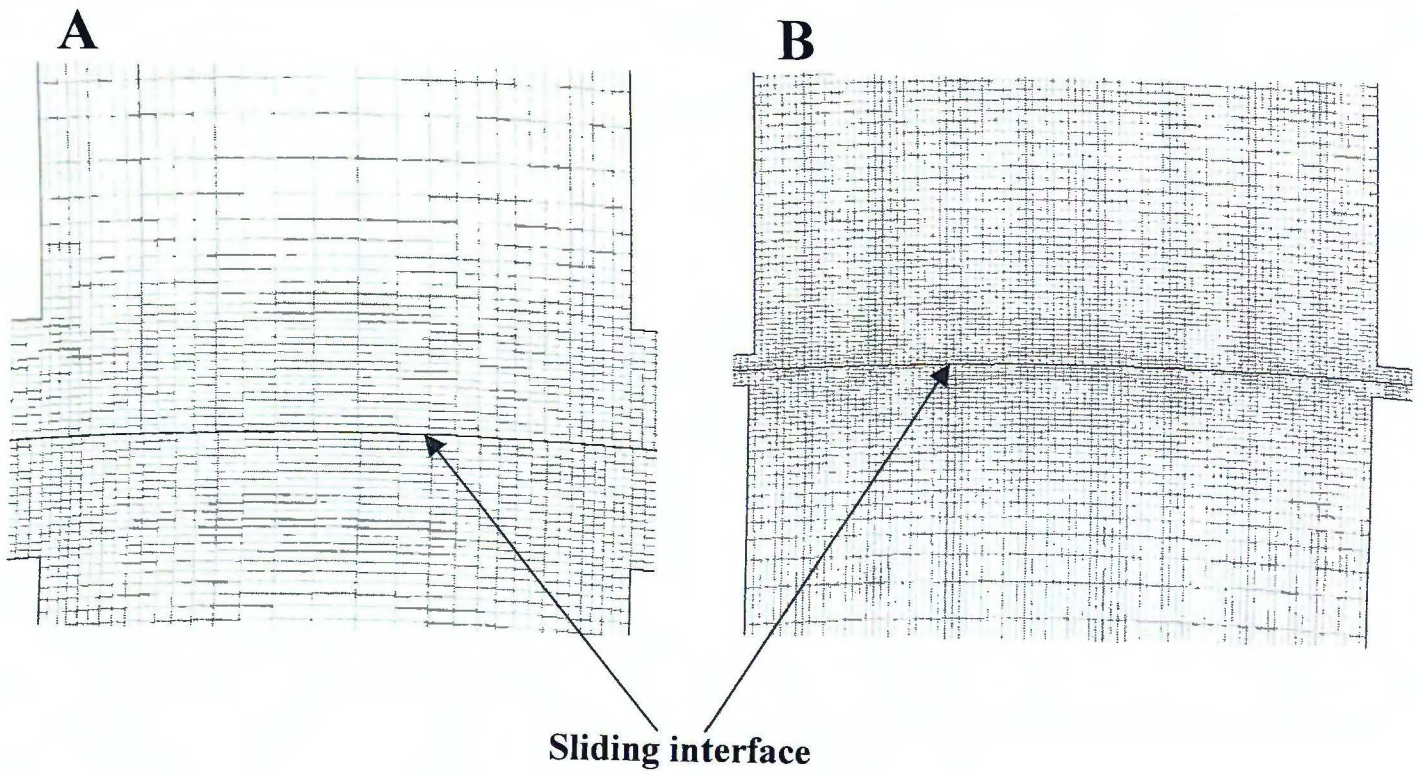

Figure 2-1. Close up of the computational mesh used for wide gap model simulations 3 and 4 (**A**) and standard gap model simulation 5 (**B**) in the vicinity of the shear gap when a rotor and stator slot are aligned.

In order to simultaneously meet these three meshing requirements of small element size changes, unity aspect ratio, and large number of elements across the gap , it is clear that, as the model gap width decreases, smaller elements will be required in the gap region. This will force the size of adjacent elements in the stator slots to be smaller, which will in turn force elements in the volute region to be smaller. By grading elements to larger sizes as the mesh moves further from the gap region through the stator slots and into the volute, it is possible to minimize the total mesh elements. However, element sizes far from the gap will ultimately be limited due to the aspect ratio constraint. Thus, as the gap size decreases, the number of mesh elements increases rapidly even in areas such as the volute where one would not expect a need for a greater number of elements in the standard gap over the wide gap model.

The second reason for simulating a wide gap model is because experimental LDA measurements in a 0.5 mm gap region are not possible at the present time. Thus, in order to validate CFD's predictive value in the gap region, where the highest shear and turbulence are expected to exist, it is necessary to use the wide gap model.

Finally, a wide gap device was simulated because it is desirable to compare the flow fields between the wide and standard gap models. To gain the greatest insight from this comparison all other simulation variables, such as rotor speed and inlet mass flow rate, would ideally be held constant during simulation or experimental measurement. By detailed comparison of flow field solutions (or measurements), it may then be possible to find some sort of quantitative dependence of flow variables in

the gap region, such as turbulent kinetic energy and turbulent energy dissipation rate, on gap width.

2.2 Computational Meshes

Grids for both the standard and wide gap models were created using the Geomesh module of the FLUENT™/UNS 4.4 software. For both models, all grids were two-block structured and utilized quadrilateral control volumes. The first block, called the rotor block, consists of an annular region with a radius extending from the circular inlet to one half the shear gap width (Fig. 2-2). The second block, called the stator block, is essentially an annular region consisting of the remainder of the computational domain (Fig. 2-3). The two blocks were fused at the interface between them (the middle of the shear gap region) in the FLUENT™ program. At the end of each time step, the interface between the two blocks is 'broken' and the rotor block 'slides' a small angle, θ, the value of which depends on the rotational speed of the simulation. After movement, the block interface is reformed and new momentum fluxes are computed across its boundary. Computation continues in this manner after each time step.

Four distinct meshes were created for a total of five simulations. Table 2-1 summarizes important differences between the simulations. Simulation 1, 2, and 3 are simulations of the wide gap model and were all run at operating conditions corresponding to a rotor speed of 50 rps and an inlet volumetric flow rate of 78.8 gpm. Differences between these simulations lie in the size of the mesh used (for grid independence studies) or the type of outlet boundary condition applied.

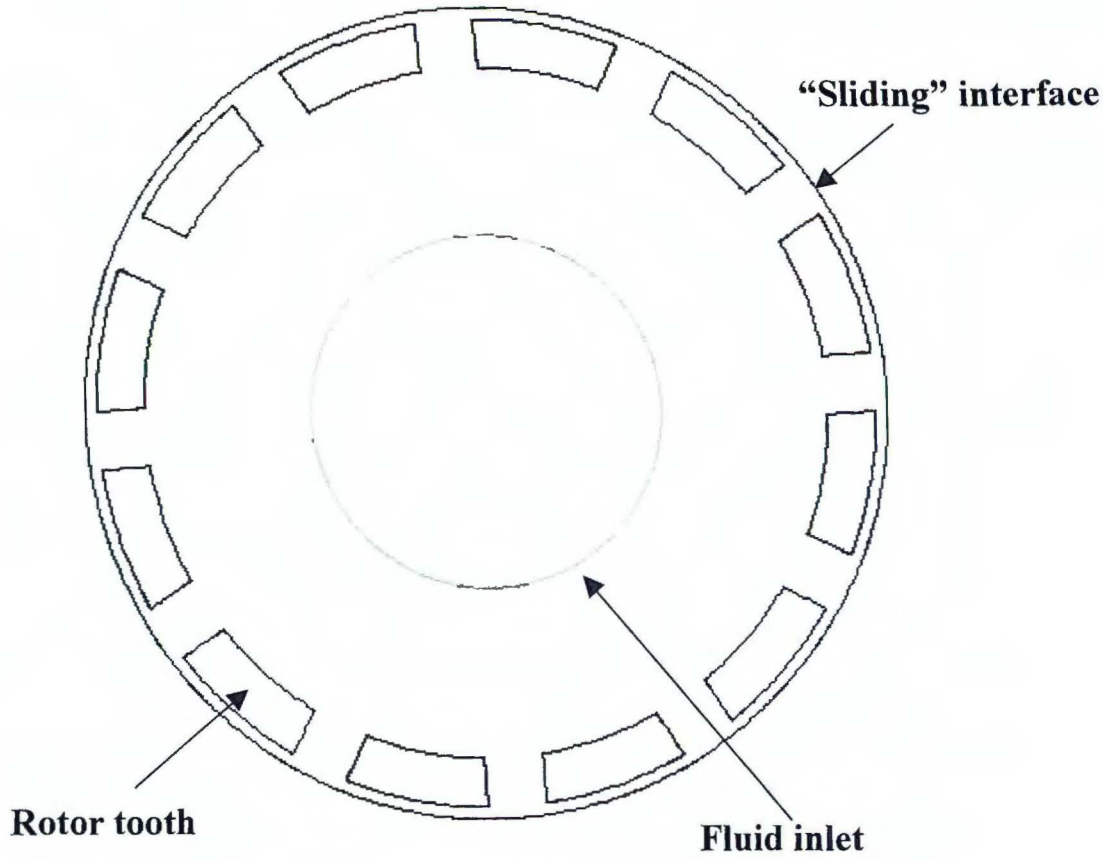

Figure 2-2. Rotor block portion of the computational domain. The sliding interface is topologically coincident with the interface on the stator block portion of the domain.

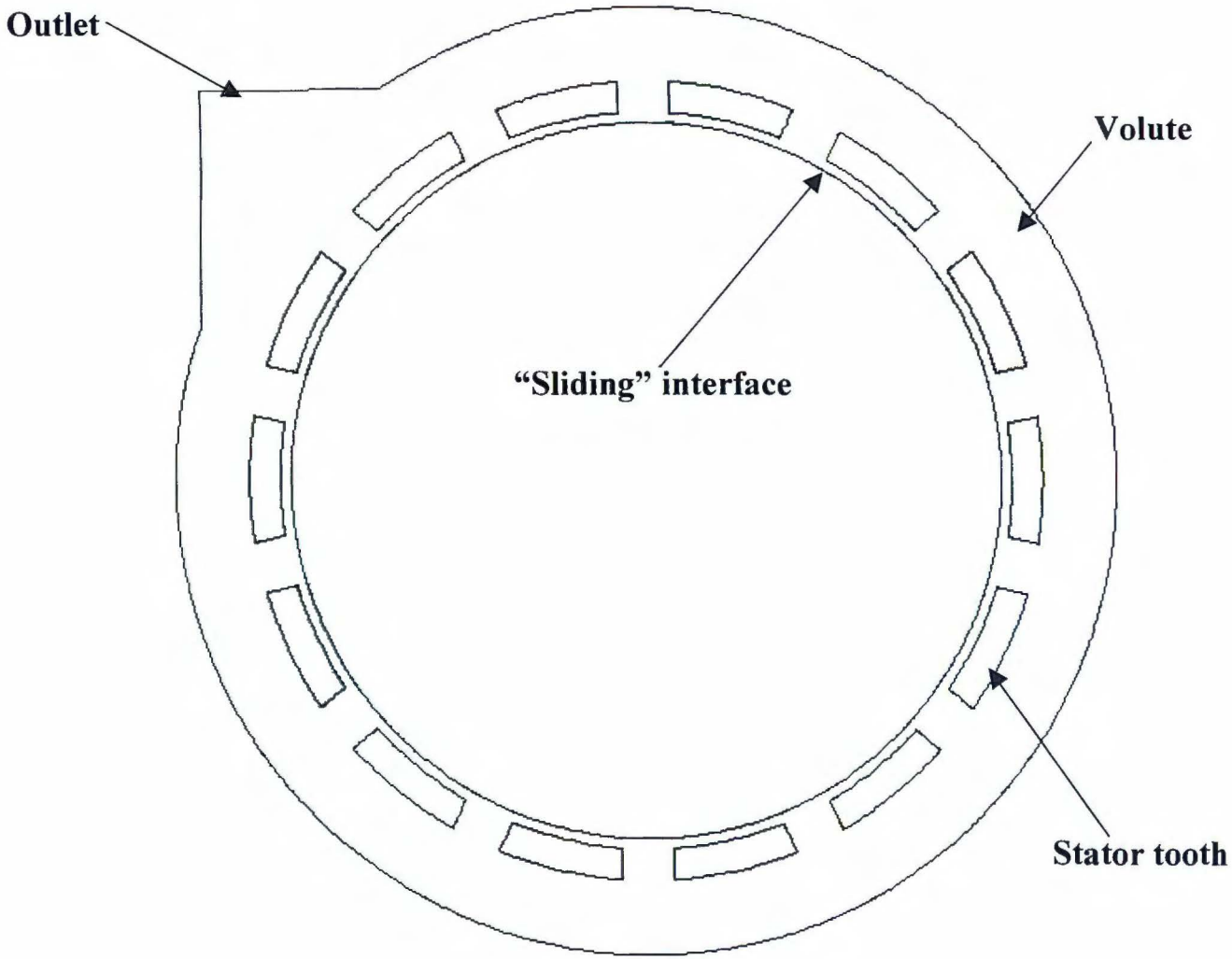

Figure 2-3. Stator block portion of the computational domain. For simulations 2 and 5, the outlet is extended an additional 0.25 m beyond the volute.

Simulation 1 utilized a 'coarse' mesh consisting of 73,600 quadrilateral cells and its overall domain was truncated at the outlet where a constant pressure boundary condition was applied (see Fig. 1-3 and section 2.5). Simulation 2 utilized the same coarse mesh of 73,600 cells, but the outlet was extended 0.25 m beyond that for simulation 1 so that a 'fully developed flow' boundary condition could be applied there (see Fig. 2-4 and section 2.5). The mesh for simulations 3 is a refined version of the mesh used for simulation 1 and consists of 125,300 cells. The coarse mesh has 26 elements spanning the 4 mm shear gap while the refined mesh has 30 elements. The primary difference between the coarse and fine meshes, however, is in the aspect ratio of these cells: It is closer to unity in the refined mesh. The mesh for simulation 4 is identical to that used for simulation 3. Simulation 4 was run at operating conditions corresponding to a rotor speed of 30 rps and an inlet volumetric flow rate of 45.4 gpm, which are the only operating conditions that were used for experimental LDA measurements of the wide gap device. The coarse and fine meshes used for the wide gap simulations are shown in Fig. 2-5.

The mesh for simulation 5, the standard gap simulation, has an extended outlet (and outlet boundary condition) identical in dimensions to that used for simulation 2. This mesh consists of 322,400 cells, with 8 cells spanning the 0.5 mm shear gap. This mesh is shown in Fig. 2-6.

2.3 Model Operating Conditions

In the wide gap model, simulations were performed for two distinct sets of operating conditions which are outlined in Table 2-1. Experimental LDA

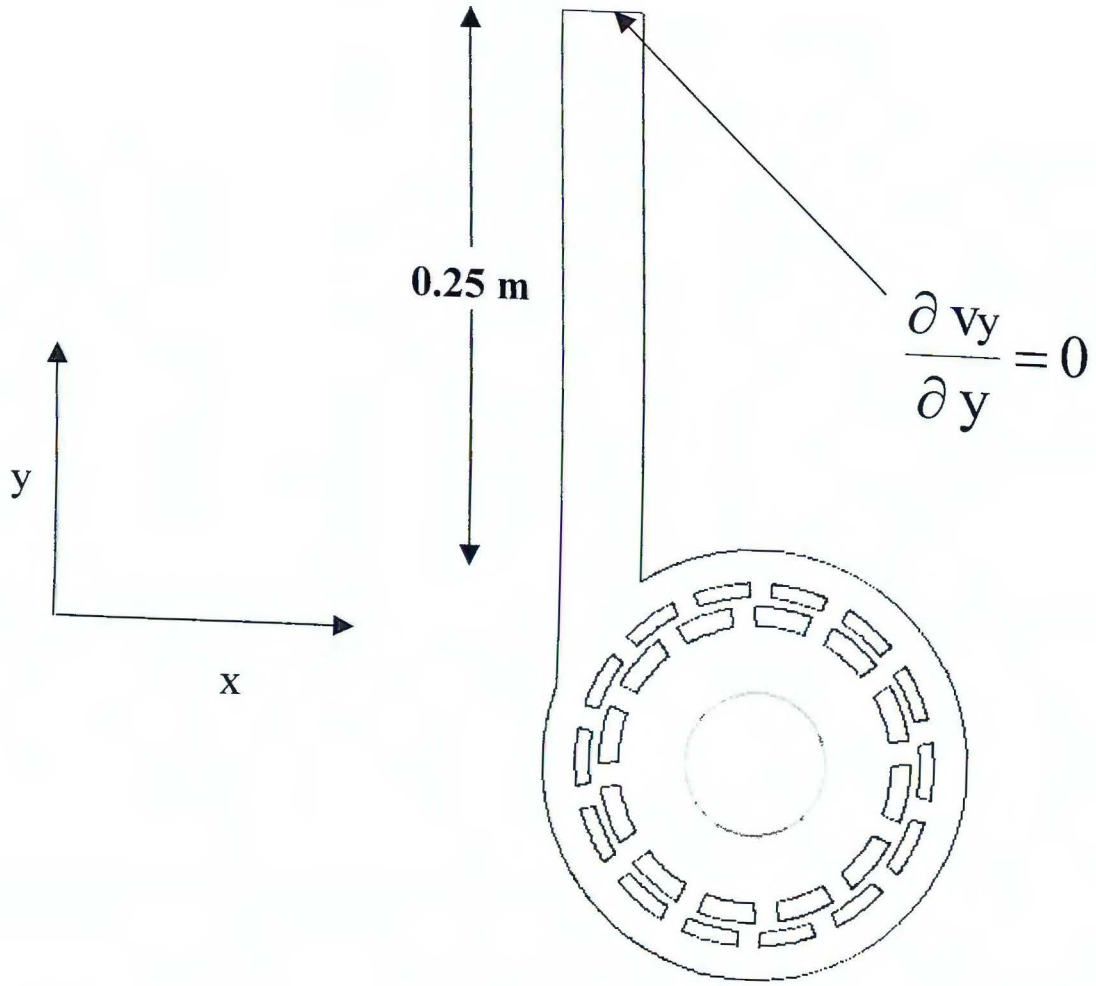

Figure 2-4. The computational domain used to simulate the rotor-stator with an outflow boundary condition (simulations 2 and 5). Domain shown after fusion of rotor and stator blocks.

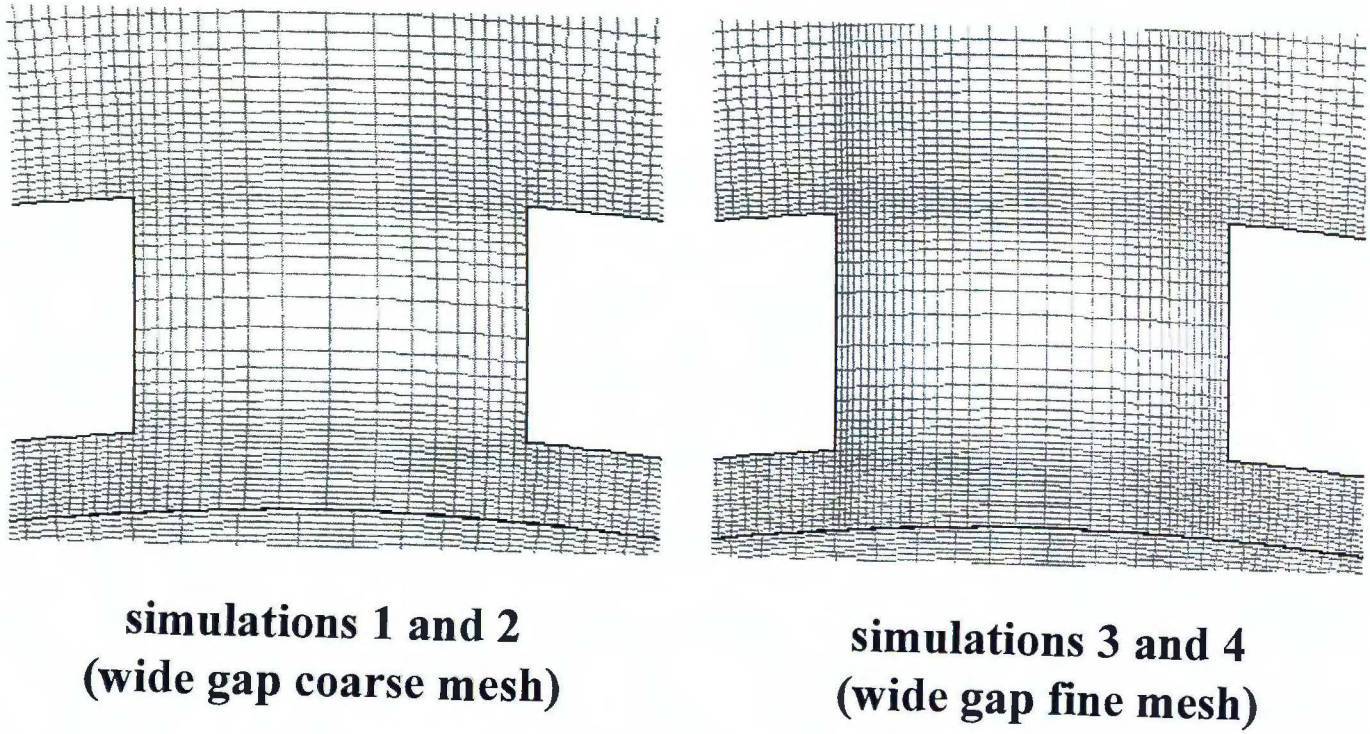

Figure 2-5. Close up of the mesh used for the wide gap model simulations in the vicinity of a stator slot and the adjacent shear gap and volute regions.

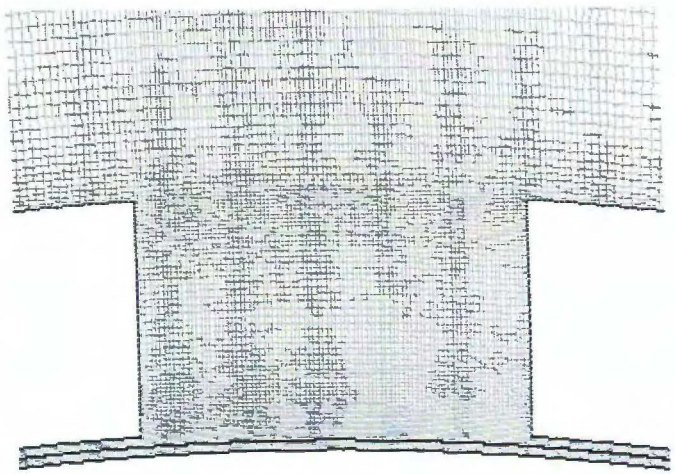

simulations 5
(standard gap mesh)

Figure 2-6. Close up of the mesh used for the standard gap model simulation in the vicinity of a stator slot and the adjacent shear gap and volute regions.

measurements were made for one of these sets of conditions. Specifically, only for a rotational speed of 30 revolutions per second (rps) and an inlet volumetric flow rate of 45.4 gallons per minute (gpm). The other operating condition simulated was 50 rps and an inlet volumetric flow rate of 78.8gpm.

Initially it was intended to simulate the wide gap device only at conditions for which experimental LDA measurements would be taken. However, simulations were begun before LDA measurements, and, when measurements commenced, it was found that the supply pump for the rotor-stator mixer was not capable of supplying an inlet flow of 78.8 gpm. Nevertheless, simulation at different sets of operating conditions may be useful for performing a parametric analysis of flow field dependence on operating conditions. Unfortunately, in the case of the two sets of operating conditions used, two variables (inlet flow rate and rotational speed) were varied simultaneously. This makes it somewhat difficult to determine exactly which operating condition variable causes an observed change in the simulated flow field, although careful physical reasoning does allow some discrimination between which operating condition variable causes an observed effect on the simulated field. In the future, it may be useful to run a simulation at 50 rps and 45.4 gpm so that a set of three simulations can be compared where only one operating condition variable is changed between each of them. This will allow a more rigorous analysis of flow dependence on operating conditions.

Only one set of operating conditions were used for both simulation and experimental measurements of the standard gap model (Table 1-2) : 30 rps and 45.4 gpm inlet flow rate. These are the same conditions used for both experimental

measurements and simulation in the wide gap model and allows for a direct qualitative and quantitative comparison between the solution fields for the two geometries.

2.4 Turbulence Model

The Reynolds number (Re) is a dimensionless group which is a measure of the ratio of inertial forces to viscous forces present in a flow field. When inertial forces are large, the flow is almost always turbulent. The definition of the Re number is different for different flow geometries. For the simple rotor-stator geometries simulated here, the Re number may be defined as

$$\mathrm{Re} \equiv \frac{\rho \, \delta \, V_{tip}}{\mu} \qquad (2.4\text{-}1)$$

Where δ is the gap width, V_{tip} is the tangential velocity of the rotor tip, and ρ and μ the density and viscosity of the working fluid respectively. It should be noted that the Reynolds number for a given system may be defined in several ways. Equation 2.4-1 is only one possibility. At the operating conditions used for the simulations (Re > 50,000 for the wide gap model) the flow should be highly turbulent. Turbulent flow differs from smooth flow, also known as laminar flow, in that the fluid velocity and pressure at a given point fluctuate rapidly in time. These fluctuations occur even though velocity and pressure values, averaged over a time scale much longer than that of the fluctuations, may be constant. For example, when flow through a long tube is laminar then, after an initial start-up time, the flow no longer evolves with time and the velocity and pressure are constants at each point in the tube. Turbulent flow in a tube, on the other hand, will technically never reach a steady state. Rather, a steady

average value of the velocity and pressure will be reached after an initial start-up time, this average being relative to the fluctuations. Turbulence is fundamentally a three-dimensional phenomenon, meaning that when present, fluctuations always occur in three directions.

Since turbulent flow fields are three-dimensional and involve extremely steep velocity and pressure gradients with respect to time and space (the fluctuations), it is nearly impossible at present to solve the flow equations precisely for any geometry. To do so using a finite volume model would require mesh element sizes and time steps prohibitively small.

Some CFD codes have been written that attempt to directly simulate turbulence introduced at the boundaries of a computational domain. For most practical engineering applications, however, it is not presently possible to perform direct calculation. Rather, the turbulence is *modeled* by the addition of extra equations coupled to those for the flow field. These equations are based on semi-empirical reasoning rather than being completely derived by first principles.

Of the several turbulence models available for use in CFD, the simplest ones are based on the eddy viscosity hypothesis. This hypothesis assumes that the effect of turbulence on the ensemble averaged flow is to increase the apparent viscosity of the fluid. This is based on the reasoning that there is an increased transport of the mean momentum in a direction perpendicular to the flow, above that occurring by molecular viscous effects, in turbulent flow. The increased transport is due to the turbulent fluctuations or 'eddies'.

The eddy viscosity model chosen for the simulations presented here is known as the standard k-epsilon (k-ε) model. In the k-ε model, it is assumed that the eddy viscosity, μ_t, is the same in all three spatial directions. In this sense, the k-ε model is isotropic and less sophisticated than the RSM model which accounts for differences in the value of μ_t for each spatial dimension. The k-ε model involves two additional equations, one for k and one for ε. Here k stands for the turbulent kinetic energy per unit mass (TKE) contained in the flow field fluctuations and ε is the rate at which this energy is dissipated. A brief description of the mathematical derivation of this model is given in chapter three.

2.5 Inlet and Outlet Boundary Conditions

The RANS equations are a system of partial differential equations and therefore require a set of boundary conditions for all variables in order to describe how the system interacts with its external environment. Some of these boundary conditions, like the fluid velocity at the inlet, are simply an expression of the conditions at which the device is operated. Other boundary conditions derive from physical principles of fluid flow and include concepts like that of no fluid slip at solid boundaries. Table 2-1 summarizes the boundary conditions for the five separate CFD simulations to be presented.

For all simulations, the velocity at the circular inlet is defined to be in the normal (radial) direction. Its magnitude is constant and determined by assuming that

the inlet is actually a cylinder with an axial depth of 10 mm, this being the actual depth of the rotor portion of the device (Table 1-1). By use of the equation

$$Q = V\ A \tag{2.5-1}$$

where Q is the inlet volumetric flow rate to be simulated and A is the surface area of the cylindrical inlet, the appropriate velocity, V, is calculated. The two volumetric flow rates simulated of 45.4 and 78.8 gpm correspond to inlet velocities of 1.52 and 2.64 m / sec respectively.

Values at the inlet must also be assigned for the turbulence variables k and ε. The inlet to the rotor-stator device is the outlet of a cylindrical pipe 60 mm in diameter. Turbulent quantities in fully developed pipe and duct flow are known to depend only on the upstream characteristics of the flow. This fact is useful for simulation since it is not known a-priori what values k and ε may take in the interior of the device.

On the other hand, it is to be expected that significant additional turbulence, beyond that due to simple pipe flow, will be created at the inlet of the actual (physical) device due to impingement of the fluid on a plane surface as the average fluid motion undergoes a sudden violent change of 90° from an axial to radial direction. Since the simulation model is two-dimensional and does not contain an axial dimension there is no way for the computation to predict the affect that this flow characteristic will have, which in all likelihood is the primary turbulence source at the inlet.

There is thus no way at present to accurately determine appropriate inlet values for k and ε with a two dimensional geometry. Fortunately, however, the turbulence at the inlet should be very small compared to that produced within the gap, especially

near the stator teeth where the fluid impinges at high velocity. For this reason computation of k and ε in these areas should be relatively insensitive to the much smaller values occurring at the inlet. In any case, turbulence characteristics at the inlet region before the gap is of relatively little interest. It may therefore be reasonable to simply assign values for k and ε based on those known to occur in the core (i.e. the center) of pipe flow.

Experimental research has resulted in empirical relationships which can be used to determine realistic values for turbulence parameters in pipes. Specifically, the turbulence intensity, I, which is defined to be the ratio of the root mean square of the velocity fluctuations, u', at a point to the average velocity, u, at the same point, at the core of fully developed pipe flow is found to be given approximately by the relation

$$I \approx 0.16\,Re^{-1/8} \tag{2.5-2a}$$

$$Re \equiv \frac{D\,V_a\,\rho}{\mu} \tag{2.5-2b}$$

where D is the tube diameter, V_a is the average axial velocity through a cross section of the pipe, ρ is the fluid density, and μ is the fluid viscosity (Fluent Inc., 1997). The core value of k in the pipe can then be computed by its definition

$$k = \frac{3}{2}(u\,I)^2 \tag{2.5-3}$$

which implicitly assumes that the TKE is isotropic. This is approximately true for core pipe flow (Hinze, 1975). The value for the turbulent dissipation rate at the pipe core can be related to the TKE using a semi-empirical relationship if a value for the turbulent length scale, l, is known. The turbulent length scale is a quantity describing

the size of the largest turbulent fluctuations in the flow. In pipe flow fluctuation size is limited by the pipe diameter. An empirical relation for l is

$$l \approx 0.07\, D \tag{2.5-4}$$

(Fluent Inc., 1997). The core turbulent dissipation rate can now be approximated from Eqs. 2.5-2 through 2.5-4 as

$$\varepsilon \approx C_{\mu}^{3/4}\, k^{3/2} / l \tag{2.4-5}$$

where C_{μ} is an empirical constant with a value of approximately 0.09 (Fluent Inc., 1997). Application of the above equations for the operating conditions used in the simulations results in rather small values for k and ε to be used at the inlet (Table 2-1).

Boundary conditions must also be set at the outlet region. The commercial CFD code used for simulation allows for two different outlet boundary conditions which may be appropriate for the model being simulated. These conditions are called either pressure outlet or outflow. Both were used in separate simulations (Table 2-1).

The pressure outlet boundary condition defines the gauge static pressure along the outlet (Fig. 1-3) to be 0. All pressures within the domain are then computed with respect to this value. A constant pressure outlet would seem to be reasonable for a rotor-stator that expels its working fluid to the atmosphere. In the simulations that were performed with this boundary condition it should be noted that the outlet is contiguous with the volute region rather than having a length of pipe running between the volute and outlet. This somewhat artificial condition may have an affect on the accuracy of the simulated flow field near the outlet as compared to the true physical flow.

In order to determine if a pressure outlet results in unrealistic flow in the volute region immediately adjacent to it, another simulation was performed with an outflow boundary condition. The outflow condition, in the case of the simulated device, is similar to, but not exactly, that found in the physical situation of fully developed pipe flow. For the outflow condition, the computational domain is extended an additional 0.25 m beyond the volute (Fig. 2-4), and the gradient of all flow variables in the y-direction (direction normal to the exit) are defined to be zero. The pressure is not defined on the outlet.

An extension value of 0.25 m in the outflow model was chosen on the basis of an empirical rule which states that length of piping necessary for turbulent flow to become fully developed, assuming that the flow at the entrance of the pipe has a flat profile, is 50 times the pipe diameter (Geankopolis, 1993). Since the outlet diameter is 0.035 m, application of this rule gives 1.75 m. Ideally the pipe extension would be even greater than 1.75 meters because the flow is not expected to have a flat profile at the extension inlet. Unfortunately it is not feasible to use such a long extension because it would make the mesh the too large. However, even though the length of 0.25 m is not sufficient to completely justify outflow conditions, it is so far removed from the volute region that if a pressure outlet boundary condition does significantly alter results in the adjacent volute region, a difference between the two simulations should be obvious.

2.6 Wall Boundary Conditions

A no-slip condition was applied at all solid walls. At rotor boundaries, the no-slip condition corresponds to a relative motion in the stationary frame of reference, dependant on the radial position. Standard wall functions (default in FLUENT^{TM} for turbulent flow) were used in wall adjacent cells in order to decrease the required computation time. The mathematical implementation used for the wall functions can be found in chapter three.

2.7 Summary

Five different simulations are to be presented (Table 2-1). Only results from simulations 4 and 5 will be examined and compared in depth, these being simulations of the wide and standard gap geometries respectively at operating conditions for which experimental LDA measurements were performed.

Results from the remaining simulations are presented in an abbreviated fashion as an in depth examination would be redundant. These simulations were performed primarily for comparison purposes. Specifically, grid independence of the simulations will be evaluated by comparison between simulations 1 and 3. Flow field differences due to the type of boundary condition at the outlet will be determined by a comparison of simulations 1 and 2. The effect of inlet volumetric flow rate and rotor speed will be established by comparison of simulations 3 and 4.

Chapter 3 Computational Methods

Problems in computational fluid dynamics are solved by discretized methods where the domain of interest is divided into a mesh of finite volumes and discretized equations describing the flow are written for each element. The equations are then assembled into a non-linear system which is usually solved by iterative linearization methods. Issues related to specifics of the actual computation of solutions to the Navier-Stokes and k-ε equations are covered in this chapter. Important numerical parameters for the rotor-stator mixer simulations, including discretization schemes, pressure treatment, residual reduction, and time step size are shown in Table 3-1.

Table 3-1. Solver Settings for CFD Simulations

Time step size for simulations 1, 2, 3	5.9525e-4 seconds (1.07 °)
Time step size for simulations 4, 5	1.0032e-4 seconds (1.07 °)
Solution initialization	Zero for all variables; full rotor speed and inlet mass flow rate
Pressure treatment	PRESTO (Staggered grid)
Pressure-velocity coupling	SIMPLE algorithm
Time discretization	1st order implicit
Momentum discretization	2nd order upwind
Turbulence (k and ε) discretization	2nd order upwind
Wall treatment	Standard wall functions
Residual reduction criteria	1e-4 (All variables)

The computational details covered in sections 3 through 11 of this chapter are specific to the implementation chosen for this study and come from the FLUENT™ manuals (Fluent Inc., 1997).

3.1 Computer Resources and Computational Expense

All simulations were begun in serial processing mode on a 195 MHz Silicon Graphics Octane workstation with 256 Mbytes of RAM made available for use by the Procter and Gamble Company.

Later, the meshes were partitioned into two domains utilizing the FLUENT™ program so that the simulations could be run using a parallel version of the CFD code. The simulations were then continued on a 500 MHz Pentium III dual processor Dell Precision 410 workstation with 1.0 Gigabyte of RAM running Windows NT 4.0. On the Dell workstation, each time step required approximately 5 or 20 minutes for the wide and standard gap simulations respectively (time step size corresponding to 1.07° of rotor rotation). The wide gap simulations required about 40 linearized outer iterations per time step while the standard gap simulation required up to 100 (see section 3.3). In general, each time step required considerably more CPU time at the beginning of simulation than at the middle or end.

3.2 Equations of Motion

The Navier-Stokes equations describe the flow of an incompressible fluid. For a simple Newtonian fluid moving in two directions, as in the rotor-stator mixer model, they may be written in cartesian coordinates as (Bird et. al., 1960)

$$\rho\left(\frac{\partial V_x}{\partial t}+V_x\frac{\partial V_x}{\partial x}+V_y\frac{\partial V_x}{\partial y}\right)=-\frac{\partial P}{\partial x}+\mu\left(\frac{\partial^2 V_x}{\partial x^2}+\frac{\partial^2 V_x}{\partial y^2}\right)+\rho g_x \qquad (3.2.1a)$$

$$\rho\left(\frac{\partial V_y}{\partial t}+V_x\frac{\partial V_y}{\partial x}+V_y\frac{\partial V_y}{\partial y}\right)=-\frac{\partial P}{\partial y}+\mu\left(\frac{\partial^2 V_y}{\partial x^2}+\frac{\partial^2 V_y}{\partial y^2}\right)+\rho g_y \qquad (3.2.1b)$$

where V_x and V_y are the x and y velocities respectively, P is the fluid pressure, μ the fluid viscosity, ρ its density, and g_i the gravitational force in the i direction. The variables to be solved for include the two velocities and pressure. Closure is obtained by the continuity equation which expresses conservation of mass

$$\frac{\partial V_x}{\partial x}+\frac{\partial V_y}{\partial y}=0 \qquad (3.2.2)$$

Equations 3.2.1 and 3.2.2 describe the flow for a given system exactly. As stated in chapter two, it is not presently practical to solve them when the flow is turbulent. Instead, another set of equations may be derived by taking the time average (for statistically steady flow), on a scale longer than the fluctuations, or the ensemble average (for statistically unsteady flow) of the equations after making the substitutions $V_i=\overline{V}_i+V'_i$ and $P=\overline{P}+P'$ where $\overline{V}i$ and $\overline{P}$ are the time (ensemble) averaged velocity in the i direction and pressure respectively, V_i and P their instantaneous values, and V'_i and P' the instantaneous magnitudes of their turbulent fluctuations. Equations 3.2.1 and 3.2.2 may now be written in summation notation as

$$\rho\left(\frac{\partial \overline{V}_i}{\partial t}+\overline{V}_j\frac{\partial \overline{V}_i}{\partial x_j}\right)=-\frac{\partial \overline{P}}{\partial x_i}+\mu\frac{\partial}{\partial x_j}\left(\frac{\partial \overline{V}_i}{\partial x_j}\right)+\rho g_i-\rho\frac{\partial}{\partial x_j}\left(\overline{V_j'V_i'}\right) \qquad (3.2.3)$$

$$\frac{\partial \overline{V}_i}{\partial x_i}=0 \qquad (3.2.4)$$

The last term in Eq. 3.2.3 is known as the Reynolds stress term and is the only mathematical difference between it and Eq. 3.2.1. There are a total of 4 Reynolds stresses in two-dimensional flow. The Bousinesq Hypothesis (not necessarily the best theory) states that the Reynolds stress has a form similar to ordinary viscous stress, being proportional to the gradient of the averaged velocities. This 'constant' of proportionality, called the turbulent or eddy viscosity and abbreviated μ_t, actually varies with the characteristics of the flow and is thus a function of both position and time. Using this hypothesis, Eq. 3.2.3 becomes

$$\rho\left(\frac{\partial \overline{V}_i}{\partial t}+\overline{V}_j\frac{\partial \overline{V}_i}{\partial x_j}\right)=-\frac{\partial \overline{P}}{\partial x_i}+(\mu+\mu_t)\frac{\partial}{\partial x_j}\left(\frac{\partial \overline{V}_i}{\partial x_j}\right)+\rho g_i \qquad (3.2.5)$$

3.3 The Standard k-ε Model Equations

The k-ε model is used to determine the value of μ_t to be used in the computation of a solution for Eq. 3.2.5. It models turbulent kinetic energy throughout the flow field by use of a general transport equation

$$\rho\left(\frac{\partial k}{\partial t}+\overline{V}_i\frac{\partial k}{\partial x_i}\right)=\frac{\partial}{\partial x_i}\left(\left(\mu+\frac{\mu_t}{\sigma_k}\right)\frac{\partial k}{\partial x_i}\right)-\rho\left(\overline{V_i'V_j'}\right)\frac{\partial \overline{V}_j}{\partial x_i}+\rho\varepsilon \qquad (3.3.1)$$

The second to last term in Eq. 3.3.1 is the production of k and the last term is its dissipation rate. Again using the Bousinesq hypothesis, the production term can be rewritten to give

$$\rho\left(\frac{\partial k}{\partial t}+\overline{V}i\frac{\partial k}{\partial x_i}\right)=\frac{\partial}{\partial x_i}\left(\left(\mu+\frac{\mu_t}{\sigma_k}\right)\frac{\partial k}{\partial x_i}\right)+\mu_t\frac{\partial \overline{V}_j}{\partial x_i}\frac{\partial \overline{V}_j}{\partial x_i}+\rho\varepsilon \qquad (3.3.2)$$

The dissipation rate of k is modeled by a similar equation

$$\rho\left(\frac{\partial \varepsilon}{\partial t}+\overline{V}i\frac{\partial \varepsilon}{\partial x_i}\right)=\frac{\partial}{\partial x_i}\left(\left(\mu+\frac{\mu_t}{\sigma_\varepsilon}\right)\frac{\partial \varepsilon}{\partial x_i}\right)+1.44\frac{\varepsilon}{k}\mu_t\frac{\partial \overline{V}_j}{\partial x_i}\frac{\partial \overline{V}_j}{\partial x_i}-1.92\rho\frac{\varepsilon^2}{k} \qquad (3.3.3)$$

Where σ_k and σ_ε are the turbulent Prandtl numbers for k and ε and have values of 1.0 and 1.3 respectively. These values, along with the other constants in Eq. 3.3.3, were determined experimentally from turbulent shear flows. Note that the second to last term also contains the Bousinesq formulation for the production of k. Both Eqs. 3.3.2 and 3.3.3 are special cases of the k and ε transport equations, valid only for incompressible isothermal flows.

The solution of Eqs. 3.3.2 and 3.3.3 allow the turbulent viscosity to be computed from the relation

$$\mu_t=\rho C_\mu\frac{k^2}{\varepsilon} \qquad (3.3.4)$$

where C_μ is an empirical constant with a value of 0.09.

Together Eqs. 3.2.4, 3.2.5, and 3.3.2 through 3.3.4 constitute a closed system of equations which are used to compute a flow field solution inside the computational domain. The FLUENT™ solver is a finite volume code that allows the user to choose

from among several algorithms to solve these equations. The specific ones used for this study are discussed below.

3.4 Overview of the Numerical Algorithm

Eqs. 3.2.4, 3.2.5, 3.3.2, and 3.3.3 are each discretized in time using a first order implicit formulation and in space using a 2^{nd} order method. The approach used for computation in this study may be summarized as follows:

1. The momentum equations are discretized for each (two-dimensional) mesh cell in a manner such that the nonlinearity of the velocity components does not explicitly appear. This yields a separate system of linear equations for each velocity component.
2. The x-momentum equations from step 1 are solved for $\overline{V}_x$. Implicit in the coefficients for each cell equation are the mass flow rates through each of the 4 cell boundaries, $\dot{m}$, and the pressures, $\overline{P}$, and turbulent viscosities, μ_t, from both the cell of interest and its neighbors. During solution, the x-momentum equations are uncoupled from these variables by using their most recently known values rather than solving for them simultaneously. The computed x-velocity field satisfies the x-momentum equation but not the continuity equation.
3. Step 2 is repeated for the y-momentum equation
4. The continuity equation is discretized in a manner that introduces the pressure to yield a system of linear equations which is solved to give a pressure correction. The x and y-velocities are present in the system coefficients and

must be uncoupled. This is accomplished by using velocity values computed in steps 1 and 2.

5. The pressure correction computed in step 4 is used to calculate an updated pressure field and mass flow rates through each cell boundary. These updated values do satisfy continuity, but may not satisfy the momentum equations.
6. The turbulent kinetic energy equation is discretized and solved using the current values for μ_t, ε, velocities, and face mass flow rates.
7. The turbulent kinetic energy dissipation rate equation is discretized and solved using the present values for μ_t, k, velocities, and mass flow rates.
8. A new turbulent viscosity, μ_t is computed using equation 3.3.4.
9. Convergence of all equations is tested. If the solution has converged to a desired level, the time step is advanced and the rotor portion of the computational mesh is moved. Otherwise, steps 1-9 are repeated using the updated field variables.

The above algorithm is known as a segregated method since both the non-linearity and coupling of the equations is treated through an iterative process. One completion of the above algorithm constitutes an 'outer' iteration as opposed to the 'inner' iterations, which refer to the algorithms used for solution of the large systems of linear equations produced in each of steps 2, 3, 4, 6, and 7.

3.5 Spatial Discretization of Momentum Equation

The FLUENT^{TM} code discretizes all the partial differential equations of flow using a control volume technique. Each cell (control volume) in the computational

domain yields an equation for the dependent variable of interest at the cell centroid. The primary difference between this and finite difference methods is that integrals are approximated rather than derivatives. Interpolation is used in the control volume technique to calculate variable values at, or fluxes across, cell boundaries during assembly of the discrete equations.

The momentum equation can be cast in integral form for a control area (CA) by considering the convective fluxes of momentum across its boundaries (also called faces), the stresses at the faces, and the body force acting within it. Equation 3.2.5 may then be written as

$$\frac{\partial}{\partial t}\iint_{\Omega}\rho\,\overline{V}_i\,d\Omega = -\oint_f \rho\,\overline{V}_i\,\overline{\mathbf{V}}\cdot\mathbf{n}\,df + \oint_f \tau_{ij}^{t}\,\hat{\mathbf{i}}\cdot\mathbf{n}\,df - \oint_f \overline{P}\,\hat{\mathbf{i}}\cdot\mathbf{n}\,df + \iint_{\Omega}\rho\,g_i\,d\Omega \qquad (3.5.1)$$

where Ω is the CA's surface area, f its boundary, τ_{ij}^{t} the turbulent stress tensor (containing both the viscous and Reynolds stress terms), $\overline{\mathbf{V}}_i$ the Reynolds averaged velocity vector, $\hat{\mathbf{i}}$ the basis vector in the i direction, and $\mathbf{n}$ the unit vector normal to the cell boundary.

The first term on the right of Eq. 3.5.1 represents the momentum flux into the CA due to convection by the bulk fluid velocity. Assuming that the $\overline{V}x$ values may be approximated as a constant along each of the four cell boundaries, which is true in the limit of an infinitely fine mesh, the x-component of the convection term is discretized for each cell as

$$\oint_f \rho\,\overline{V}_x\,\overline{\mathbf{V}}\cdot\mathbf{n}\,df \approx \sum_{f=1}^{4}\left(\overline{V}_{x,f}\int_f \rho\,\overline{\mathbf{V}}\cdot\mathbf{n}\,df\right) = \sum_{f=1}^{4}\dot{m}_f\,\overline{V}_{x,f}\,l_f \qquad (3.5.2)$$

where $\dot{m}_f$ is the mass flow rate through face f, $V_{x,f}$ the x-velocity at face f, and l_f the length of the face.

Since the discrete equations are solved for velocity values only at the cell centers it is necessary to interpolate values to the faces in order to apply Eq. 3.5.2. This is done using an upwind scheme meaning that interpolation is performed from the cell adjacent to the face that is upwind of the flow. For instance, Fig. 3-1 shows a schematic of 12 computational cells labeled 1 through 12 neighboring a primary cell c_p for which it is desired to write Eq. 3.5.2. If the present flow field at the center of c_p is in the North-West direction then $\overline{V}x$ at face 1 (f1) would be computed by interpolation from the center of cell 7. The least accurate approximation for $\overline{V}x$ at f1 would be that its value is equal to that at the center of cell 7. This approximation is a first-order upwind scheme and is the method that was used in previous rotor-stator simulations (Epee-Bounya, 1998). Discretization error introduced using this very simple interpolation can be significant, and it has the effect of increasing the 'apparent' diffusivity of momentum.

A better, 2nd order, approximation for $\overline{V}x$ at f1 and the one used in these simulations is obtained by using a scheme based on the $\overline{V}x$ value in the center of the upwind cell and its neighbors. In the 2nd order method, $\overline{V}x$ at f1 (Fig. 3-1) is approximated using a linear combination of its cell centered values in the primary cell and cells 4, 7, 8, and 11. Specifically

$$\overline{V}_{x,f1} \approx \overline{V}_{x,c7} + \nabla \overline{V}_{x,c7} \cdot \Delta \mathbf{S} \qquad (3.5.3)$$

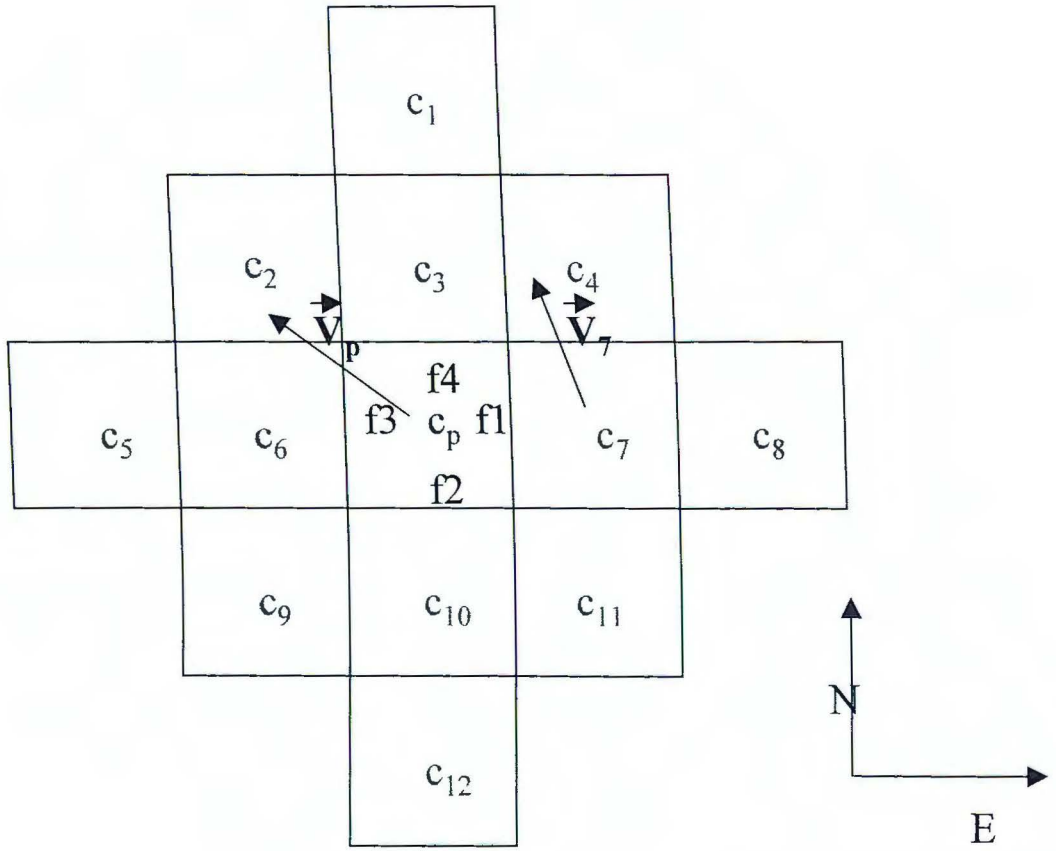

Figure 3-1. Discretization of a primary cell, c_p, on the computational mesh.

where $\nabla \overline{V}_{x,c7}$ is the gradient of $\overline{V}_x$ evaluated at cell 7's centroid and ΔS is the displacement vector from the cell centroid to face 1's centroid. The gradient term is approximated using a discrete form of the divergence theorem

$$\nabla \overline{V}_{x,c7} = \frac{1}{\Omega_{c7}} \sum_{f=1}^{4} \tilde{\overline{V}}_{x,f} l_f \tag{3.5.4}$$

where $\tilde{\overline{V}}_{x,f}$ is the mean of the cell centered $\overline{V}x$ values adjacent to face f. In Eq. 3.5.4 the summation is taken over the faces bounding cell 7, not the primary cell.

Discretization of the shear stress term in Eq. 3.5.1 is also 2nd order and proceeds in a similar manner. The body force term may be written in discrete form exactly as

$$\iiint_{\Omega_p} \rho \, g_i \, d\Omega_p = \rho \, g_i \, \Omega_p \tag{3.5.5}$$

and the pressure term is discretized according to

$$\oint_f \overline{P} \, \hat{i} \cdot \mathbf{n} \, df = \sum_{f=1}^{4} \overline{P}_f \mathbf{n} \cdot \hat{i} \, l_f \tag{3.5.6}$$

As with the convective term, the pressure is assumed constant on each of the four faces, and the present values of pressure at the cell centroid must be interpolated to the faces. Since the pressures are actually solved for in step 4 of the algorithm (i.e. during solution of the continuity equation, see sections 3.4 and 3.7), this is accomplished indirectly by staggering the mesh for the continuity equation so that its cell centers correspond to the faces in the mesh used for the momentum equation. This scheme is called PRESTO (PREssure STaggering Option) in the FLUENT™ code.

Substitution of the shear stress discretization (not shown) and Eqs. 3.5.2 – 3.5.6 into 3.5.1 yields a 'linear' equation for each mesh cell

$$\frac{\partial}{\partial t}\iint_{\Omega_p}\rho\,\overline{V}_{x,p}\,d\Omega_p = a_p\,\overline{V}_{x,p} + \sum_{nb=1}^{12} a_{nb}\,\overline{V}_{x,nb} + \sum_{f=1}^{4}\overline{P}_f\,\mathbf{n}\cdot\hat{\mathbf{i}}\,l_f + \rho\,g_i\,\Omega_p \qquad (3.5.7)$$

where the subscript nb refers to values at the centroids of cells neighboring the primary cell (subscript p). Note that for this 2nd order discretization up to 12 neighboring cell values may be required yielding a linear system with a bandwidth of about 12. The coefficients a_p and a_{nb} contain contributions from values of $\dot{m}$ at the primary cells faces as well as contributions due to the primary and neighboring cell geometries (Eqs. 3.5.2 and 3.5.3).

3.6 Temporal Discretization of Momentum Equation

Equation 3.5.7 is discretized implicitly in time for step size Δt at time step n to yield the final form of the x-momentum equations

$$\overline{V}_{x,p}^{n} = \overline{V}_{x,p}^{n-1} + \frac{\Delta t}{\rho}\left(a_p\,\overline{V}_{x,p} + \sum_{nb=1}^{12} a_{nb}\,\overline{V}_{x,nb} + \sum_{f=1}^{4}\overline{P}_f\,\mathbf{n}\cdot\hat{\mathbf{i}}\,l_f + \rho\,g_i\,\Omega_p \right)^{n} \qquad (3.6.1)$$

Equation 3.6.1 is solved using a Gauss-Seidel solver in combination with multigrid methods.

Since the rotor-stator model has 12 rotor teeth and 14 stator teeth, a temporally periodic flow pattern with 12 periods per revolution of the rotor is expected. On the basis of CFD research on stirred tanks by Ng et. al. (1998), a time step size corresponding to 1.07° was deemed to be small enough to resolve details of the time dependent flow and was used for all simulations. This step size corresponds to 28

time steps per period, or 336 time steps per complete revolution of the rotor. For simulations 1, 2, and 3, this translates to 5.9525×10^{-5} seconds per time step, and for simulations 4 and 5 it corresponds to 1.0032×10^{-4} seconds per time step.

3.7 Pressure-Momentum Coupling (Continuity Discretization)

When the solution process advances to a new time step, n, the mass flow rates and pressures implicitly appearing in Eq. 3.6.1 (a_p, a_{nb}, and P_f) are evaluated using their most recently known values. The continuity equation is then used to update their values for use in the next outer iteration by calculating a pressure and mass flow rate correction. The discrete form of mass conservation (Eq. 3.2.4) may be written for each cell as

$$\sum_{f=1}^{4} \dot{m}_f \approx \sum_{f=1}^{4} \rho \, \overline{V} \, l_f = 0 \tag{3.7.1}$$

where $\overline{V}$ is the Reynolds averaged velocity magnitude at the centroid of face f. The right side of Eq. 3.7.1 is then written in a manner that introduces the pressure

$$\sum_{f=1}^{4} \dot{m}_f \approx \sum_{f=1}^{4} \left(\hat{J}_f + d_f \left(\overline{P}_{c0} - \overline{P}_{c1} \right) \right) \tag{3.7.2}$$

where $\hat{J}_f$ contains the influence of the velocities in the cells adjacent to face f and the $\overline{P}_c$'s are the pressures at the center of those cells . The calculation of $\hat{J}_f$ is done using a non-linear averaging of the two adjacent velocities in order to eliminate checker-boarding of the pressure field which has been found to result when simpler schemes are used. The coefficient d_f is obtained from an algebraic combination of the current

a_p coefficients on either side of the face appearing in the momentum equation and the face length (Fluent Inc., 1997)

The SIMPLE algorithm (Semi-Implicit Method for Pressure Linked Equations) is used to compute a pressure and mass flow rate correction. In brief, Eq. 3.7.2 is evaluated for each (non-boundary) face in the domain using the current value of the velocity field obtained from the preceding iteration of the momentum equations and the current pressure field. This results in values for the face mass flow rates , $\dot{m}_f^*$ which do not satisfy the continuity equation. A mass flow rate which does satisfy continuity, $\dot{m}_f$, may be written as the sum of the incorrect value and a correction, $\dot{m}_f'$

$$\dot{m}_f = \dot{m}_f^* + \dot{m}_f' \tag{3.7.3}$$

It is postulated that the mass flow rate correction be written as

$$\dot{m}_f' = d_f (P_{c0}' - P_{c1}') \tag{3.7.4}$$

where P' is a pressure correction. Substitution of Eqs. 3.7.3 and 3.7.4 into the left side of Eq. 3.7.1 yields an equation for each cell. For a given cell, p, the resulting pressure correction equation may be written as

$$c_p P_p' = \sum_{nb} c_{nb} P'_{nb} + \sum_{f=1}^{4} \dot{m}_f^* \tag{3.7.5}$$

where the c's are coefficients and the summation notation and solution method is the same as that for the discretized momentum equation. After solution, an updated mass flow rate for each face, $\dot{m}_f$, is calculated from Eqs. 3.7.3, 3.7.4, and the pressure corrections which gives

$$\dot{m}_f = \dot{m}_f^* + d_f (P_{c0}' - P_{c1}') \tag{3.7.6}$$

The updated mass flow rates calculated by Eq. 3.7.6 satisfy continuity however they no longer satisfy the momentum equations. During the next outer iteration, corrected pressures and mass flow rates are used in the momentum equation to solve for the velocities. After enough outer iterations, the corrected mass flow rates computed from Eq. 3.7.6 will satisfy both the continuity and momentum balances, to within a desired level of tolerance, and the solution proceeds to the next time step.

3.8 k and ε Discretization

After solving the discrete continuity equation to yield updated pressures and face mass flow rates, the turbulence equations, k and ε, are discretized and solved sequentially in order to compute a new value for μ_t to be used in the next outer iteration. The procedure is very similar to that for the momentum equation and will not be discussed further.

3.9 Treatment at Inlet and Outlet Boundaries

The velocities and turbulence values defined at the inlet faces are used for interpolation of values to the cells bounding the inlet.

For pressure-outlet conditions the discrete equations for the cells bounding the outlet are set up by interpolation of values from the interior of the domain, except for the static pressure which uses the value set at the outlet (0 bar). When backflow occurs, the values for k and ε set at the outlet are used.

Calculation for an outflow boundary condition is only slightly more complicated due to the fact that the static pressure is not explicitly defined anywhere on the computational domain. All values in the boundary cells are interpolated from within the domain. In order to keep the static pressure from floating as the simulation advances in time, a reference cell is chosen by the solver and at the end of each time step, the value of the pressure in this cell is subtracted from the entire domain. The pressure field is thus relative to the (arbitrary) reference cell.

3.10 Treatment at Walls

Near the walls the flow can be divided into three regions: A viscous sublayer where turbulent effects are not important, a buffer region where molecular viscosity and turbulence are both important, and a fully turbulent region. With the k-ε turbulence model it is possible to simulate the flow all the way to the walls, however the model must be modified in the near wall region so that it is valid in the viscous and buffer sublayers. Further, cells near the wall would be required to be very small, since these sublayers exist only very close to the wall, and this would increase computational cost dramatically.

Thus, rather than attempting to integrate the flow equations all the way to the wall, standard wall functions were used to compute velocities and turbulence values in the wall adjacent cells. Wall functions provide formulas, based on semi-empirical results, for the mean velocity and turbulence parameters in wall adjacent cells (Mohammadi, 1995). Specifically, the mean velocity, U_p, is calculated by

$$U^* = \frac{1}{\kappa} \ln(E\, y^*) \tag{3.10.1a}$$

$$U^* \equiv \frac{U_p C_\mu^{1/4} k^{1/2} \rho}{\tau_o} \tag{3.10.1b}$$

$$y^* \equiv \frac{U_p C_\mu^{1/4} k^{1/2} y \rho}{\mu} \tag{3.10.1c}$$

where κ is Von Karman's constant (0.42), E has a value of 9.81 obtained empirically, k is the turbulent kinetic energy in the cell, τ_o is the wall shear stress, and y is the distance from the cell center to the wall.

In order to apply Eq. 3.10.1, the value of k in the wall adjacent cell is obtained by integrating the k equation all the way to the wall. The boundary condition is

$$\frac{dk}{dn} = 0 \tag{3.10.2}$$

where n is the unit vector in a direction normal to the wall. The production of k and its dissipation are assumed to be at equilibrium in the wall adjacent cells and are calculated using empirical formulas.

It should be noted that the use of these wall functions is strictly valid only when applied to shear layers adjacent to flat walls where there is no pressure gradient normal to the wall. Nonetheless, wall functions have been used extensively for flows where this does not hold because without them computation is generally too expensive.

3.11 Convergence Criteria

At the end of each outer iteration, the level of convergence is tested by evaluating a residual for each equation. The discretized transport equation of a scalar quantity ϕ may be written

$$a_p \phi_p = \sum_{nb=1}^{12} a_{nb} \phi_{pnb} + b \tag{3.11.1}$$

The residual for the entire solution is defined as a scaled sum of individual residuals evaluated at each cell in the domain

$$R^{\phi} \equiv \frac{\sum_{\text{All cells}} \left| \left(\sum_{nb=1}^{12} a_{nb} \phi_{pnb} + b - a_p \phi_p \right) \right|}{\sum_{\text{All cells}} |a_p \phi_p|} \tag{3.11.2}$$

In Eq. 3.11.2 the numerator provides a measure of how close the computed value of ϕ_p is to actually satisfying Eq. 3.11.1. The denominator acts as a scaling factor. Equation 3.11.2 is applicable to the momentum, k, and ε equations. The residual for the continuity equation is defined as

$$R^{c} = \frac{\sum_{\text{All cells}} |\text{Rate of mass creation in cell, present iteration}|}{\sum_{\text{All cells}} |\text{Rate of mass creation in cell, iteration 5}|} \tag{3.11.3}$$

In the rotor-stator simulations, all residuals were required to reach a value of $\leq 10^{-4}$ before proceeding to the next time step.

Chapter 4 Wide Gap Results

In this chapter, detailed results for all simulations run for the wide gap model are covered. Sections 4.1 through 4.4 present results obtained exclusively from simulation 4. Recall that simulation 4 was run on a mesh consisting of approximately 125,000 elements at operating conditions of 30 rps and 45.4 gpm with a constant pressure outlet boundary condition (Table 2-1). Also recall that that the computational domain implies a periodic flow pattern with 12 periods per revolution of the rotor. All simulations were run using a time step that resulted in 28 time intervals per period which corresponds to 1.07° of rotor rotation / time step. In the vector and contour plots of sections 4.2 – 4.4, only every fourth time step is presented for each field variable.

In the remainder of the chapter, results between simulations 3 and 4; 1 and 2; or 1 and 3 are compared in order to examine the effects that operating conditions, mesh size, and outlet boundary condition have on the simulated flow field.

4.1 Approach to Periodic Steady State

In previous CFD work to simulate rotor-stator flow fields it was assumed that the solution process reaches a periodic steady state after 10 full revolutions of simulation (Epee-Bounya, 1998). The usual method to monitor for periodicity is to choose a point in the computational domain where a moderate to strong periodic

behavior is expected and record the values of a flow variable there. In the present simulations, the mass flow rate across lines in each of the stator slots was monitored as shown in Fig. 4-1. Mass flow rates across lines in stator slot 1 and 6 as a function of time step are shown in Fig. 4-2. After approximately 9 revolutions, the mass flow rate through stator slot 1 is fully periodic while the value through slot 6 is still decreasing. Four revolutions later, all 14 stator slot mass flow rates are periodic (result shown at 9 and 26.6 revolutions).

From the above results it would appear that flow in the region of stator slot 6 takes the longest time to develop, and it is fully developed after 13 revolutions. Using the methods described above, however, it is impossible to test for periodicity everywhere in the domain. A more unambiguous way to judge periodicity is to compare the difference in the solution at two different simulation times by contour plots.

Rather than do this comparison for each of the 28 time intervals in a full period, a program was written in Matlab to take the simulation solutions for an entire flow period (29 distinct solution fields) after a given revolution and time average the Reynolds averaged field variables. This was accomplished by taking the FLUENT™ data files for 29 consecutive time steps of simulation and using them to write what are known as interpolation files. An interpolation file consists of the x and y spatial coordinates for the center of each cell in the computational domain, along with the corresponding values of the solution variables for the x-velocity, y-velocity, TKE, and turbulent energy dissipation rate. The program 'AVERAGE' was then used to

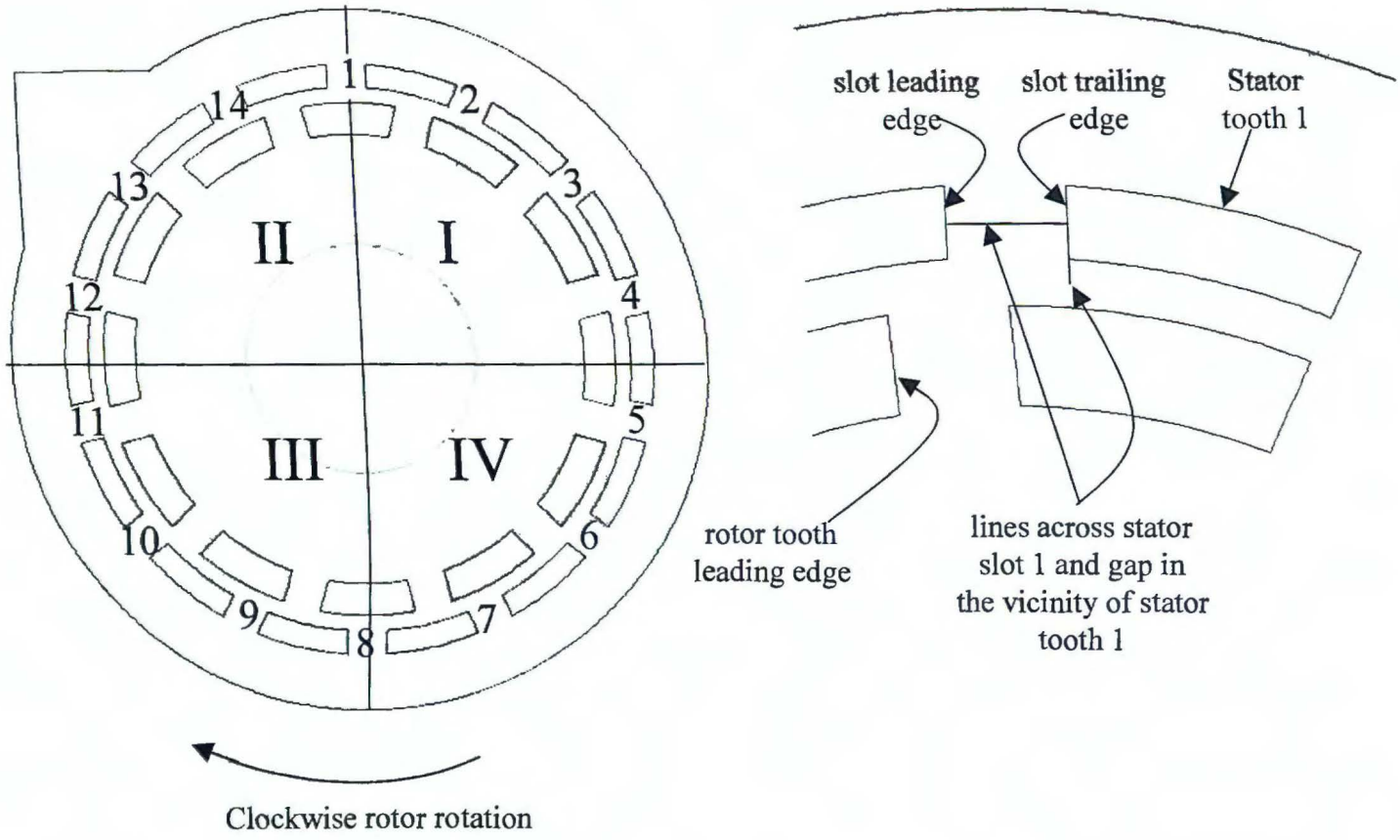

Figure 4-1. Numbering of stator slots and domain quadrants I - IV (left) and close up of stator slot 1 (right). All 14 stator slot regions have lines across the slot and extending 2 (or 0.25) mm into the gap region in order to monitor flow variables.

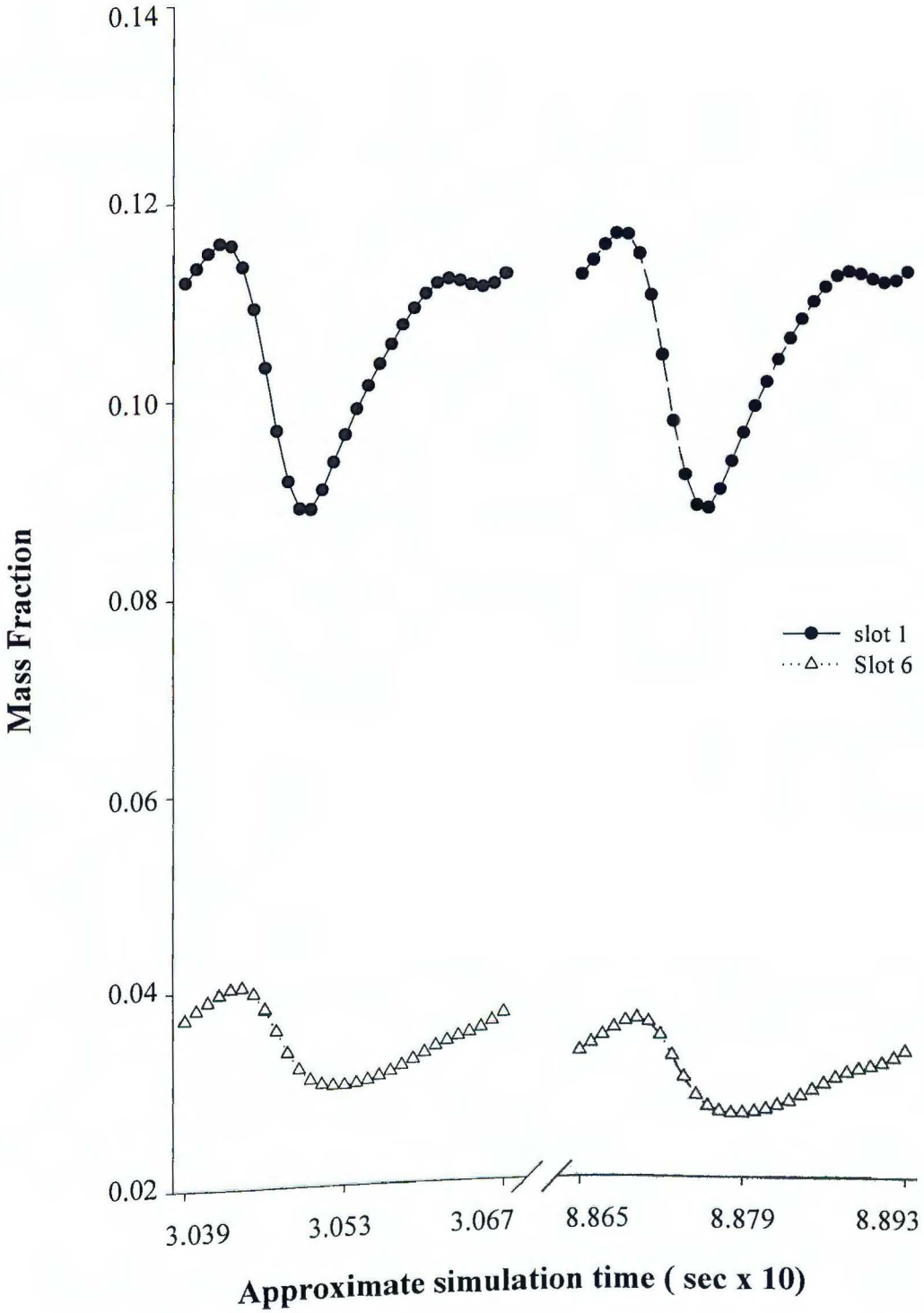

Figure 4-2. Time dependent mass flow rates through stator slots 1 and 6 after approximately 9 and 26.6 revolutions of simulation. Simulation 4.

compute the time average value of each flow variable for each computational cell according to the equation

$$\bar{v}_{ff} = \frac{1}{\Delta t} \int_{t1}^{t29} s(\bar{v}(t1), \bar{v}(t2), \ldots \bar{v}(t29))\, dt \qquad (4.1.1)$$

Where v_{ff} is the time averaged variable of interest, Δt is the time interval of one period, and $s(\bar{v}(t1), \bar{v}(t2), \ldots \bar{v}(t29))$ is a spline formed by evaluating the Reynolds averaged variable of interest, $\bar{v}$, at the 29 discreet time steps in one period of simulation.

Averaged solutions obtained by Eq. 4.1.1 were manipulated using one of two other Matlab programs ('PercentDifference' or 'MagnitudeDifference') to yield interpolation files which were plotted in FLUENT™ as contour plots and show the percent or absolute difference in the time averaged flow variables between either 28 and 9.1 or 28 and 15.3 revolutions of simulation. Simulation times at these revolutions correspond to 0.30, 0.51, and 0.93 seconds for 9.1, 15.3, and 28 revolutions respectively.

Equation 4.1.1 transforms the simulated flow variables into what is called the fixed frame of reference. In early LDA studies of mixing equipment, data was always collected in the fixed frame. In fixed frame measurements of rotor-stator flows, data are taken at a fixed point relative to the laboratory and rotational motion of the rotor is ignored. The resulting measurements are then the average of their values for all possible positions of the rotor. A fixed frame value differs from its Reynolds averaged counterpart in that it is an average taken over a time scale that is long with respect to

the periodicity imposed by the rotor. In contrast, an angularly resolved measurement of a Reynolds averaged flow variable for a rotor-stator flow is, strictly speaking, not a time average. Rather, it is an ensemble average. In statistically steady turbulent flows, such as simple pipe flows, a Reynolds or ensemble average is equivalent to a fixed frame value. However, in a rotor-stator, due to periodicity, the Reynolds average must be defined more strictly as

$$\bar{v} = \lim_{N \to \infty} \frac{1}{N} \sum_{n=1}^{N} v(t) \tag{4.1.2}$$

where v(t) is the instantaneous value of a flow variable and "N is the number of members of the ensemble (an imagined set of flows in which all controllable variables are identical)" (Ferziger and Peric, 1999). In the case of a rotor-stator mixer, a very important 'controllable variable' in the computation or measurement of Eq. 4.1.2 is the angular position of the rotor with respect to the point of measurement: Each measurement in the summation term of Eq. 4.1.2 corresponds to the same distinct rotor position relative to the stator.

Throughout the remainder of this work, with the exception of the TKE and its dissipation rate ε, simulation results that have been computed after application of Eq. 4.1.1 are referred to as fixed frame results. TKE and ε results that are reported after application of equation 4.1.1 are referred to simply as 'time averaged'. This is because the TKE and ε, in contrast to the mean velocities and pressures, are modeled parameters in the simulations and therefore not directly comparable to fixed frame measurements. This distinction between simulated mean velocities and pressures

versus the TKE and its dissipation rate is related to the phenomenon of pseudoturbulence in LDA measurements and is discussed more fully in chapter 6.

The rotor-stator domain is divided into four quadrants and the stator slots are numbered for reference throughout the remainder of this work (Fig. 4-1). Figures 4-3a and b show difference plots of the fixed frame velocity vectors between solutions at 28 and 9.1 revolutions of simulation in quadrants II and IV. The maximum difference in quadrant I is only 0.8 m/sec and occurs in the portion of the volute adjacent to the stator teeth. In quadrant IV the maximum difference is about 4 m/sec and occurs in the volute region between stator slots 5 and 6. After 15.3 revolutions of simulation (Fig. 4-3b and c), the differences in the fixed frame velocity field are negligible in all areas of the domain (< 0.03 m/sec). The red areas in Fig. 4-3b and c are an artifact of the interpolation procedure used to calculate the fixed frame values, and occur in portions of the domain where the computational mesh moves with each time step.

Figure 4-4 shows difference contour plots for the time averaged TKE. After 9.1 revolutions the TKE is overestimated in the gap region as compared to the fully periodic solution at 28 revolutions. The percent difference in the gap varies from a minimum of close to zero near slots 1-5 and 14 to a maximum of about –25 % near slots 6-13 (plots not shown for all regions). The TKE field appears to be completely periodic in all stator slots after 9.1 revolutions except for slot 6, where its average value decreases by more than 30 % after 28 revolutions. The greatest deviation between the time averaged TKE field obtained at the two simulation times is, similarly to the fixed frame velocity field, in the volute region between slots 5 and 6 where there is up to a 100 % difference. There is also a difference of up to 30 % at the outer edge

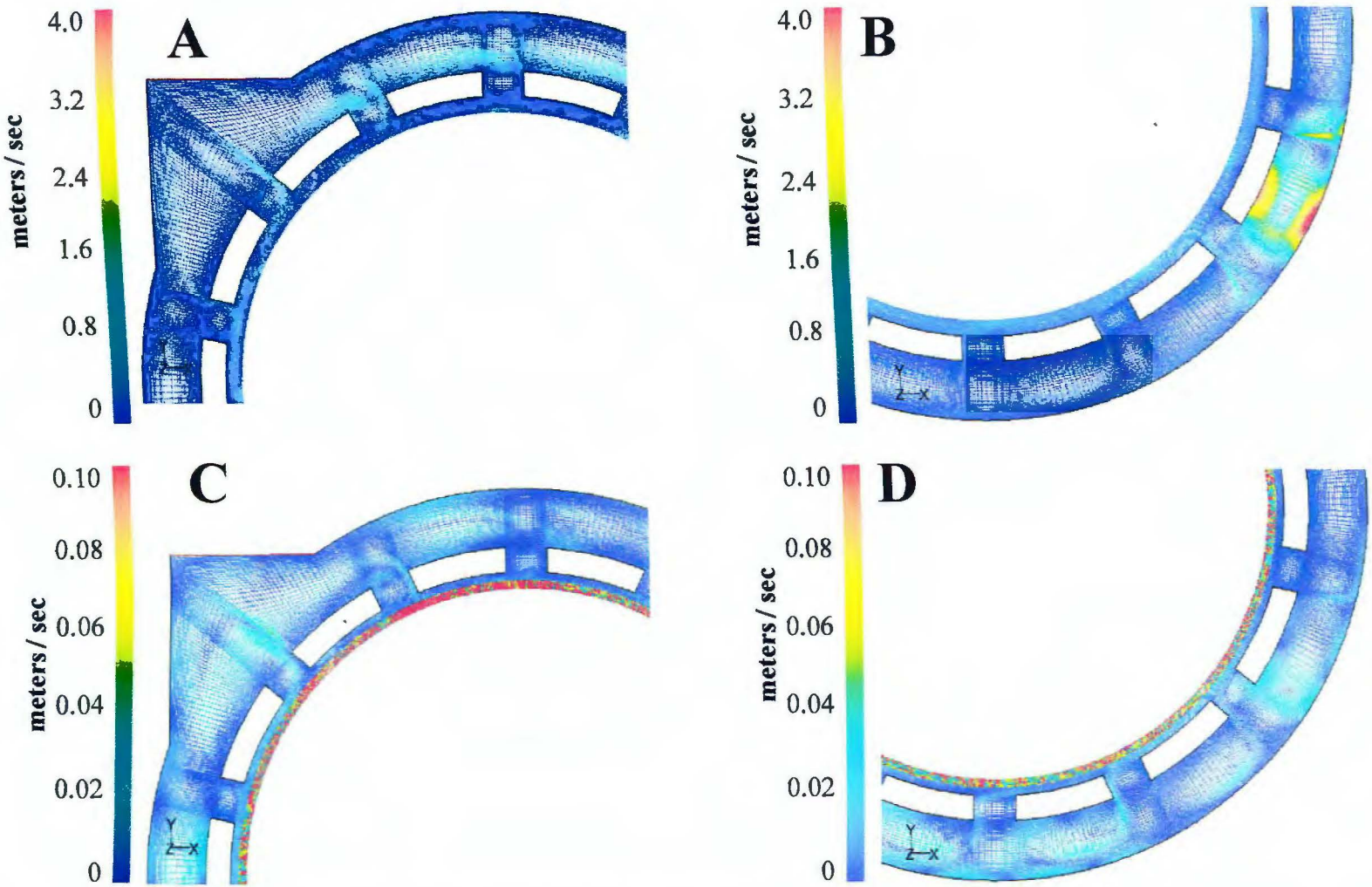

Figure 4-3. Difference between the fixed frame velocity magnitudes ($\| \mathbf{v}_2 - \mathbf{v}_1 \|$) for 28 versus 9.1 revolutions of simulation (**A**) and (**B**) and 28 versus 15.3 revolutions of simulation (**C**) and (**D**). Simulation 4.

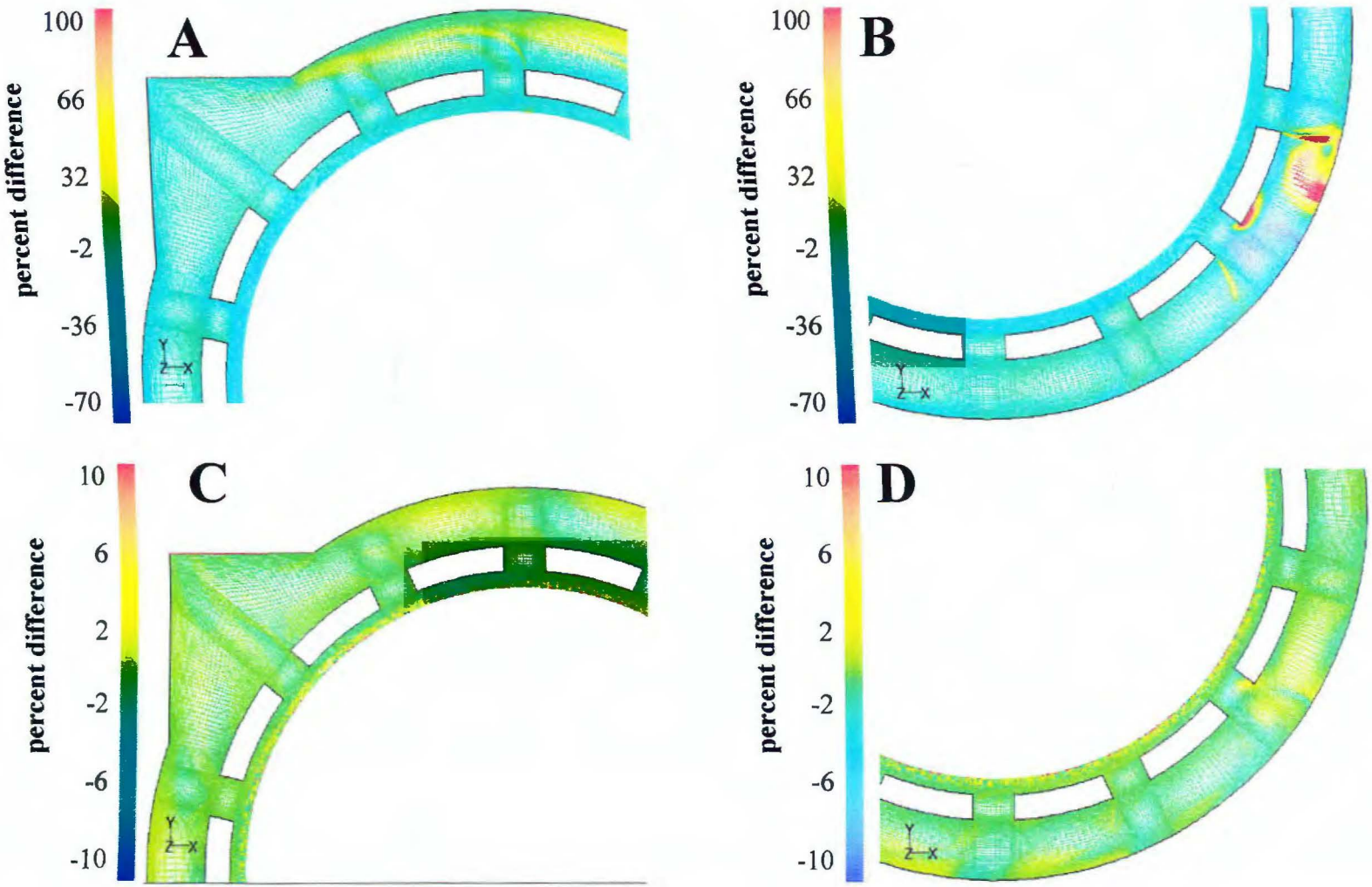

Figure 4-4. Percent difference between the time averaged turbulent kinetic energies for 28 versus 9.1 revolutions of simulation (**A**) and (**B**) and 28 versus 15.3 revolutions of simulation (**C**) and (**D**). Simulation 4.

of the volute region near slots 1, 2, and 14. Figure 4-4 b and c shows that the TKE field is fully developed after 15.3 revolutions (< 1% change everywhere).

The time averaged turbulent energy dissipation rate develops in a manner similar to the TKE field, however it does appear to be nearly fully periodic after 9.1 revolutions throughout the entire gap region, having a maximum difference of about – 5 % occurring in quadrant IV (Fig. 4-5). The volute region differences between 9.1 and 27 revolutions are identical to those for the TKE except that the magnitudes of change in the case of ε are much larger: up to 200 % in the volute region between slots 5 and 6 and up to 90 % in the outer volute region near slots 1, 2, and 14.

The mean static pressure develops to a periodic solution more rapidly than any other flow variable (Fig. 4-6). After 9.1 revolutions the fixed frame pressure is essentially constant in time. Changes with further simulation occur in slot 14 and again in the volute region near slots 5 and 6. Even in these areas, however, the magnitude of change is only about 10 %.

In summary, the difference plots show that a periodic solution is probably not reached after 10 revolutions. All flow variables take about 15 revolutions of simulation to develop in the volute region diametrically opposed to the outlet. The periodicity of the TKE and its dissipation rate also take 15 revolutions to develop in the volute region immediately above stator slot 1, and the TKE is significantly underdeveloped in the gap region near slots 6-13 and in stator slot 6. The large deviations of the time averaged turbulence parameters in the volute regions (30 – 200 %) between 9 and 15 revolutions of simulation may be due in part to their small values

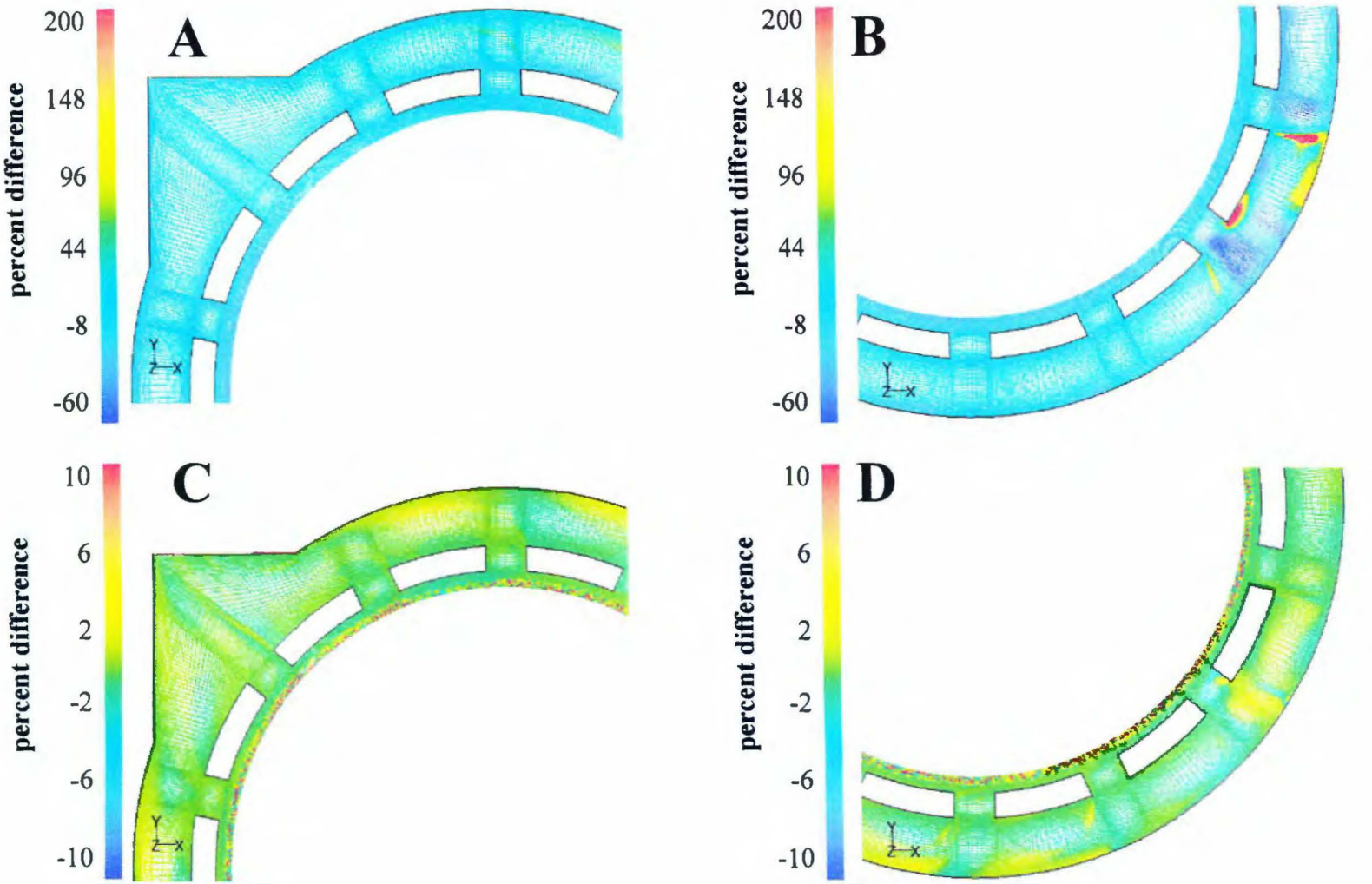

Figure 4-5. Percent difference between the time averaged turbulent dissipation rates for 28 versus 9.1 revolutions of simulation (**A**) and (**B**) and 28 versus 15.3 revolutions of simulation (**C**) and (**D**). Simulation 4.

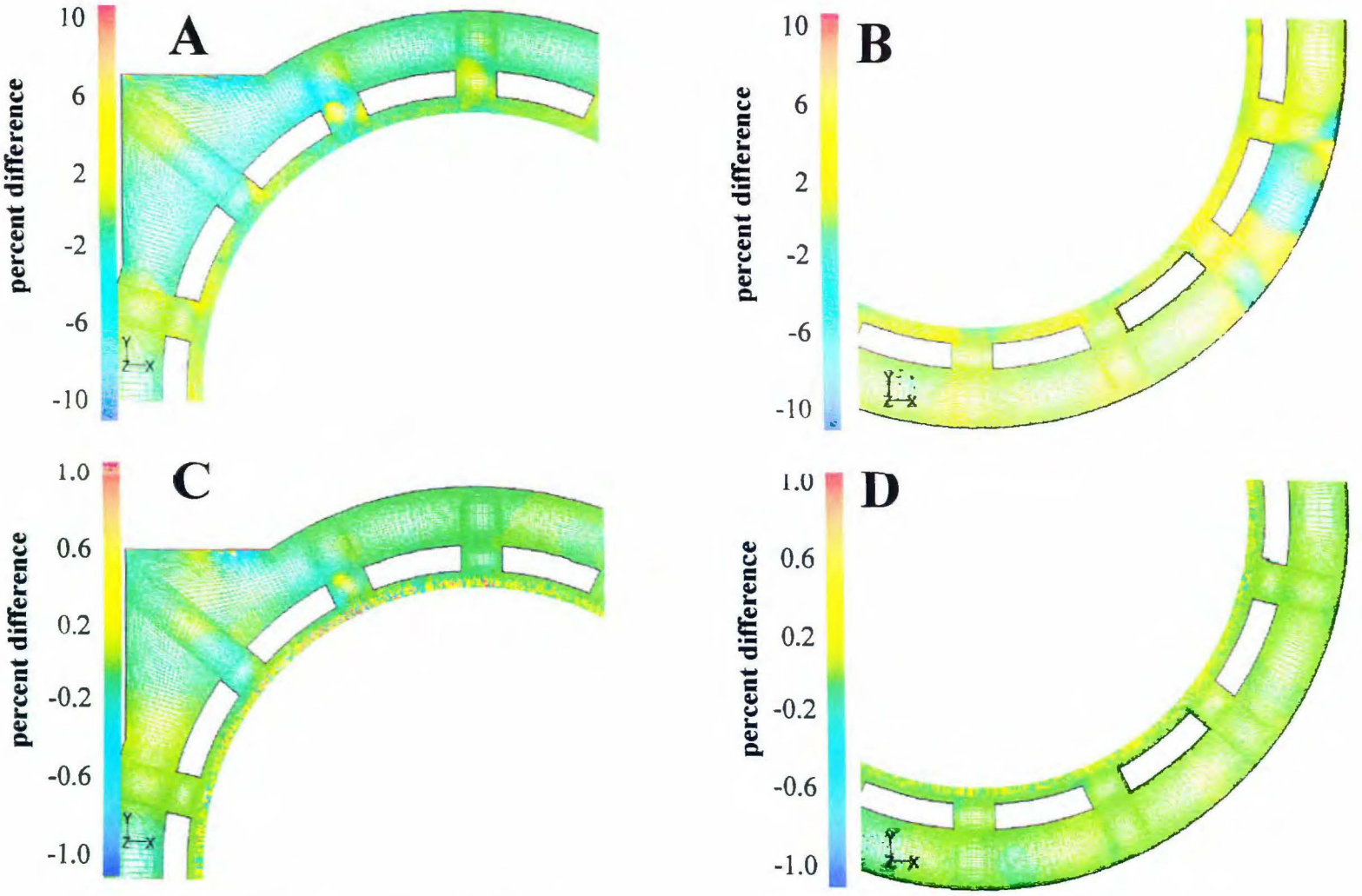

Figure 4-6. Percent difference between the fixed frame static pressures for 28 versus 9.1 revolutions of simulation (**A**) and (**B**) and 28 versus 15.3 revolutions of simulation (**C**) and (**D**). Simulation 4.

there (section 4.4). All results to follow come from simulations run for at least 15 revolutions.

4.2 Mean Velocity Field at 30 rps and 45.4 gpm Operating Conditions

Figures 4-7 through 4-13 show a linear sequence of the angularly resolved mean velocity vectors in the vicinity of stator slot 1 for simulation 4 after about 28 revolutions of simulation. When the leading edge of a rotor slot is aligned with the left edge of stator slot 1, the flow in the gap reaches its largest mean velocity of about 24 m/sec in a tangential direction, close to the stator side of the gap directly above the center of the rotor slot (Fig. 4-7). Flow in the gap region bounded on the left by the right edge of slot 14 and on the right by the left edge of stator slot 2 varies in magnitude from about 2 m/sec to 24 m/sec at any given instant of time. There is always a moderate to significant radial component to the gap flow directly above the left half of the rotor slot and extending about 2 mm into the gap. Gap flow above the right half of the rotor slot is always primarily tangential. When rotor and stator slots are aligned, the radial mean velocity component in the fluid directly above the rotor slot increases in magnitude and extends across the entire gap into the stator slot (Fig. 4-9). The highest gap mean velocities always occur directly above the rotor slot. While there is a variation of gap flow velocities above the rotor slot, the entire region above the rotor slot may be considered to behave like a turbulent jet.

The mean velocity in the turbulent jet in the gap never decreases below 18 m/sec. The jet velocity does decrease by about 5 m/sec when a rotor slot has passed stator slot 1 (Figs. 4-7 through 4-10). The increased radial velocity in the jet as slots

Figure 4-7. Angularly resolved mean velocity vectors near slot 1 at time step 9,236 (0.9266 seconds). Simulation 4.

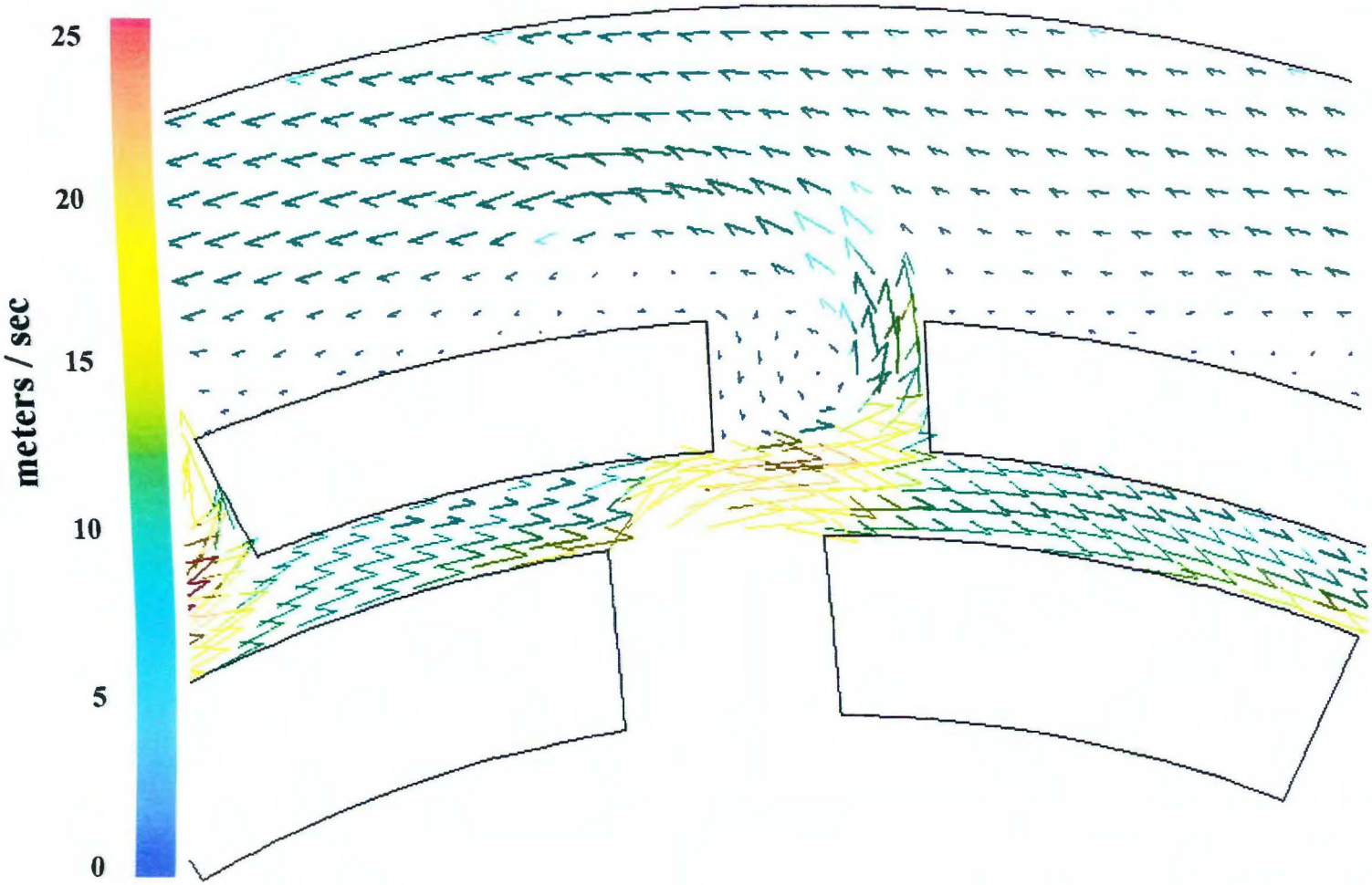

Figure 4-8. Angularly resolved mean velocity vectors near slot 1 at time step 9,240 (0.9270 seconds). Simulation 4.

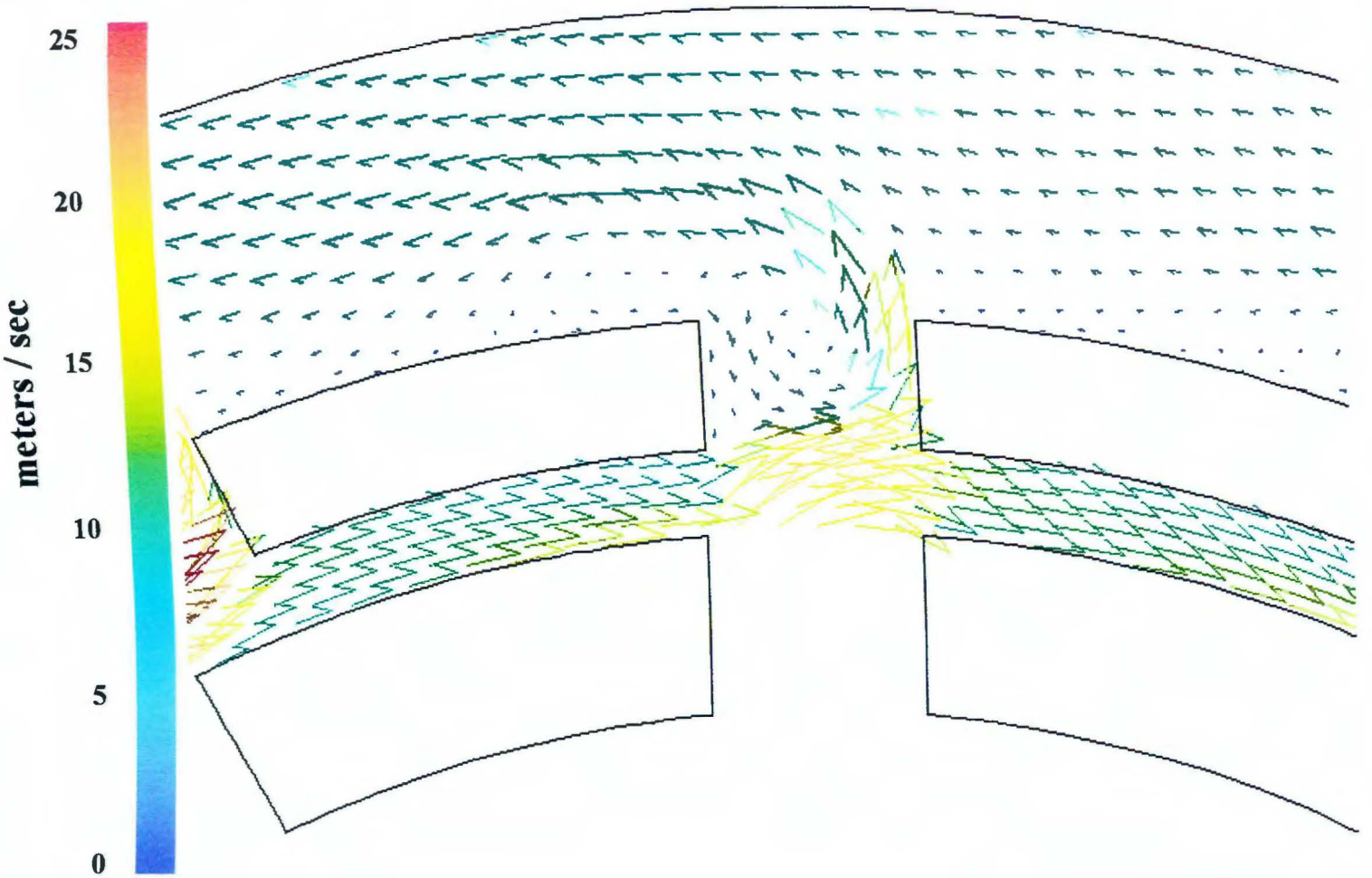

Figure 4-9. Angularly resolved mean velocity vectors near slot 1 at time step 9,244 (0.9274 seconds). Simulation 4.

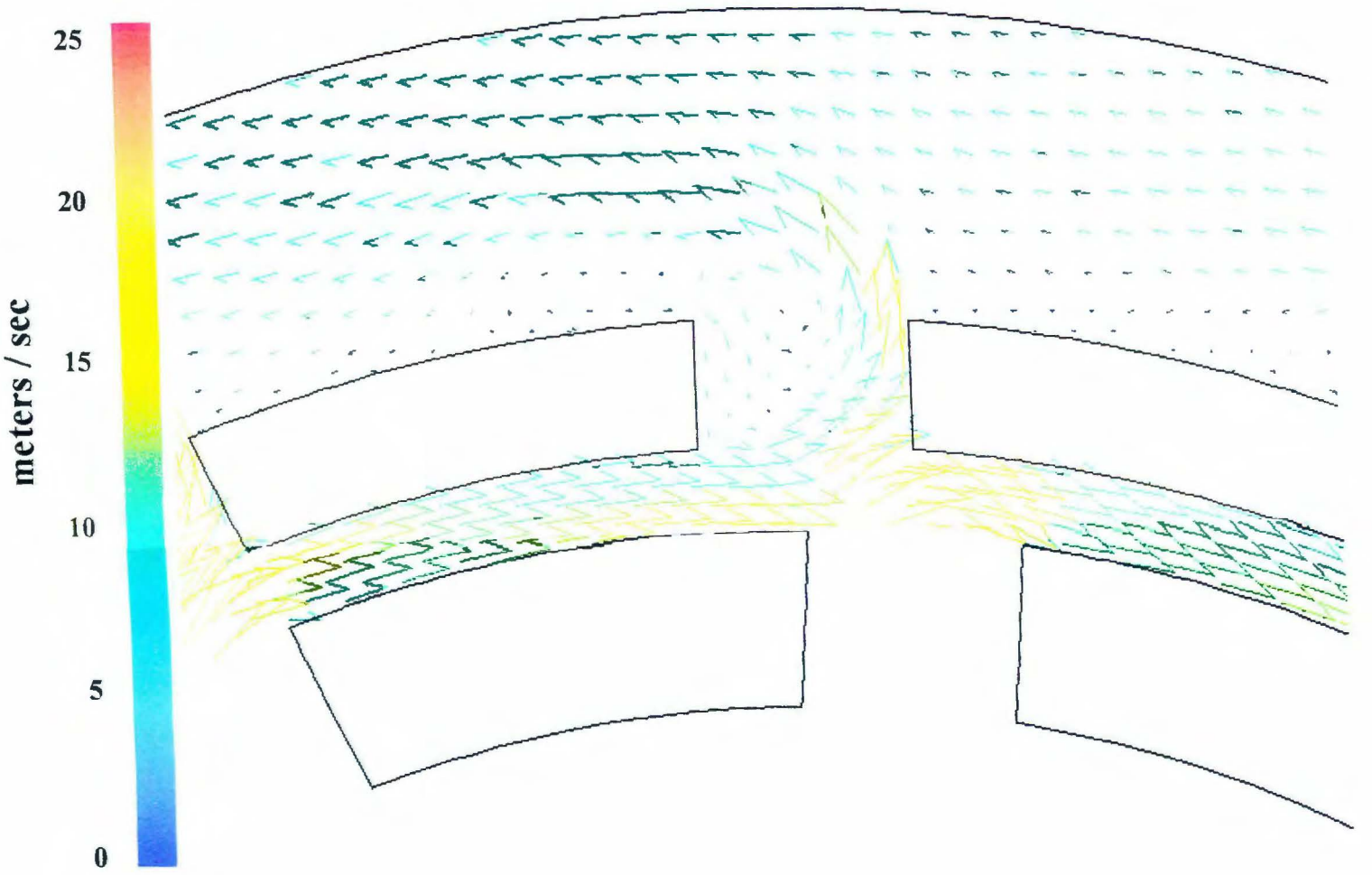

Figure 4-10. Angularly resolved mean velocity vectors near slot 1 at time step 9,248 (0.9278 seconds). Simulation 4.

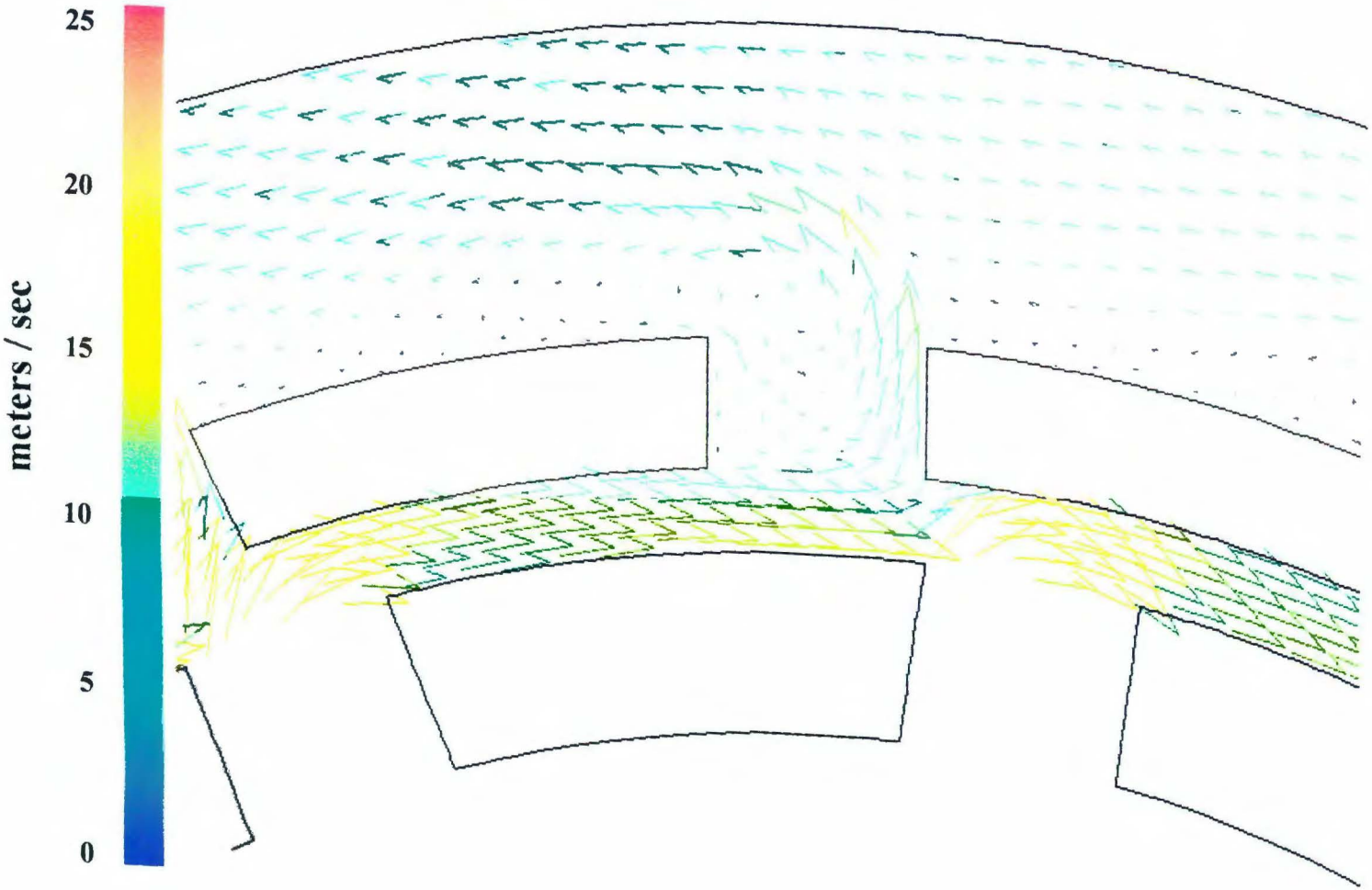

Figure 4-11. Angularly resolved mean velocity vectors near slot 1 at time step 9,252 (0.9282 seconds). Simulation 4.

Figure 4-12. Angularly resolved mean velocity vectors near slot 1 at time step 9,256 (0.9286 seconds). Simulation 4.

Figure 4-13. Angularly resolved mean velocity vectors near slot 1 at time step 9,260 (0.9290 seconds). Simulation 4.

move into alignment results in an increased mass outflow from the stator slot into the volute during this period. The radial (and absolute) magnitude change is probably due to the fact that slot alignment allows the system driving pressure, at the inlet, to push in its natural radial direction and force the fluid out of the gap toward the volute most easily during this period. Figure 4-14 shows the mass outflow from stator slots as a function of time step from alignment with a rotor slot. These plots clearly show that outflow in slot 1 is significantly higher during alignment, although the maximum outflow does occur when the slots are only half aligned, with the leading edge of a rotor tooth directly under the middle of slot 1 (Figs. 4-10 and 4-14).

The presence of a turbulent jet above the rotor slot in the simulation is an interesting phenomenon that has yet to be shown experimentally. Figures 4-12 and 4-13 show that flow in the gap region to the right of the lower right corner of stator slots 1 and 14 becomes stagnated and partially reversed after a rotor slot has completely swept past stator slot 1 (or 14). With some areas of the gap having close to zero flow at a given time, it is at least physically defensible on the basis of mass conservation arguments that there would be some areas of especially high velocity.

Due to the no-slip boundary condition at all walls, the spatially averaged or nominal shear rate, $\frac{\partial V_\theta}{\partial r}$, across the gap in areas and times when a rotor tooth is in partial or full alignment with a stator tooth is given by $\frac{V_{tip}}{\delta}$ where δ is the gap width and V_{tip} is the rotor tip speed. Flow in these regions can be very crudely compared to flow between concentric cylinders with the inner cylinder rotating (Couette flow). For

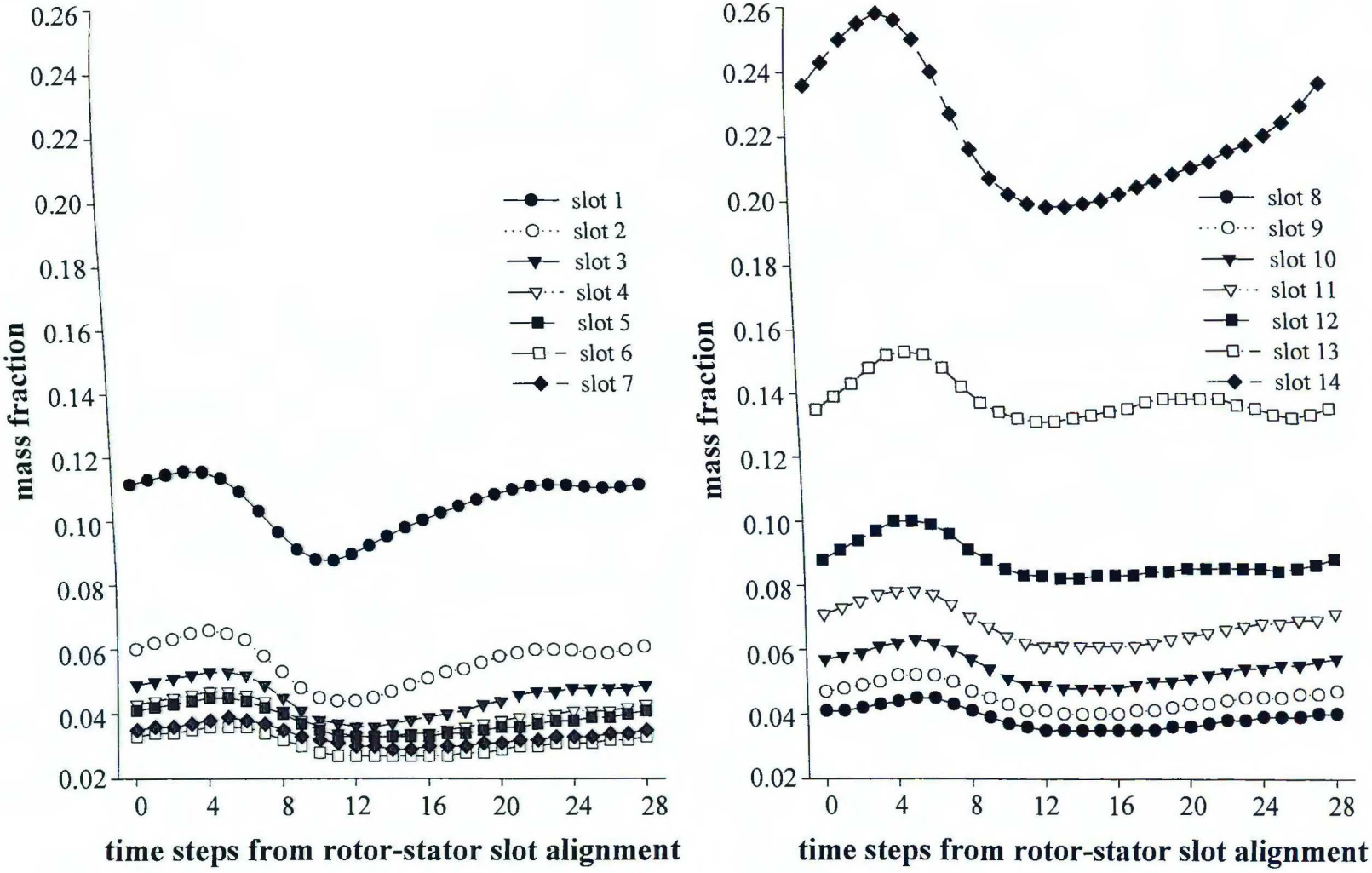

Figure 4-14. Time dependent mass flow rates through stator slots as a function of slot alignment beginning at approximately time step 9,236 (0.926 seconds). Simulation 4.

laminar Couette flow the equations of motion can be solved exactly and an approximately constant shear would be expected between walls. For turbulent Couette flow it is reasonable to expect that, in analogy with turbulent pipe flow, the mean tangential velocity would decrease very rapidly near the rotating cylinder and much less rapidly further away resulting in a very high shear rate near the inner cylinder and a substantially lower shear in the central region between the two walls, and also close to the stationary wall.

The numerical results show that, when a rotor tooth and stator tooth 1 are fully aligned (Fig. 4-9), the simulated gap flow appears to be plug. Clearly this pattern differs significantly from that hypothesized for turbulent tangential annular flow. The reason for this can be attributed partly to the presence of slots in both the rotor and stator, but the primary reason is probably that the gap flow is driven by both rotation and a mass source (i.e. the gap mass inlet is through the rotor slots). In the gap, stresses are the primary means of tangential momentum transport by the rotor, while convection is the primary means for transport due to mass inflow. A dimensionless parameter, which we can call the Gap Number, that acts as a measure of these two mechanisms may be useful for characterizing flow patterns in the gap. The simplest possibility is

$$Ga = \frac{V_{tip}}{\overline{V}_{inlet}} \qquad (4.2.1)$$

A small Ga indicates gap flow similar to that expected in turbulent duct flow while a larger Ga indicates flow more similar to that found in turbulent tangential annular flow.

For the simulation under consideration Ga = 8.3. When a rotor tooth is in perfect alignment with a stator tooth, the shear across the gap is most likely to be represented by duct or tangential annular flow depending on Ga. Figure 4-15a shows the tangential mean velocity, V_{tan}, normalized to the rotor tip speed, V_{tip}, across the gap from the azimuthal center of a rotor tooth when it is directly under stator tooth 1 and shows in detail that the profile is essentially plug except for a thin, very steep boundary layer at the stator tooth. Interestingly there is no boundary layer at the rotor tooth. It may be expected that if the volumetric flow rate were to decrease (smaller Ga) then a boundary layer would be present next to the rotor. The average shear in the gap due to the mean velocity field (at this instant in the simulation) excluding that in the stator boundary layer is approximately 850 sec^{-1}, which is the shear that the bulk of fluid crossing an imaginary line in the gap would experience. This is only 26 % of the value of the nominal shear rate of 3,150 sec^{-1}.

The numerical solution of turbulent flow bounding walls is difficult, and the lack of a boundary layer near the rotor wall in Fig. 4-15a, although plausible, is a surprising result. In addition to being most applicable for shear flows adjacent to flat walls, the Log Law of the Wall used for the wall function treatment in the simulations is not suitable for values of the dimensionless distance y+ less than 30 or greater than 300. Y+ at a given point is defined as

$$y+ = \frac{y \rho \sqrt{\tau_0 / \rho}}{\mu} \qquad (4.2.2)$$

where y is the distance from the point to the wall, τ_0 the shear stress at the wall, and the other variables are as previously defined. The value of y+ near the rotor tooth and

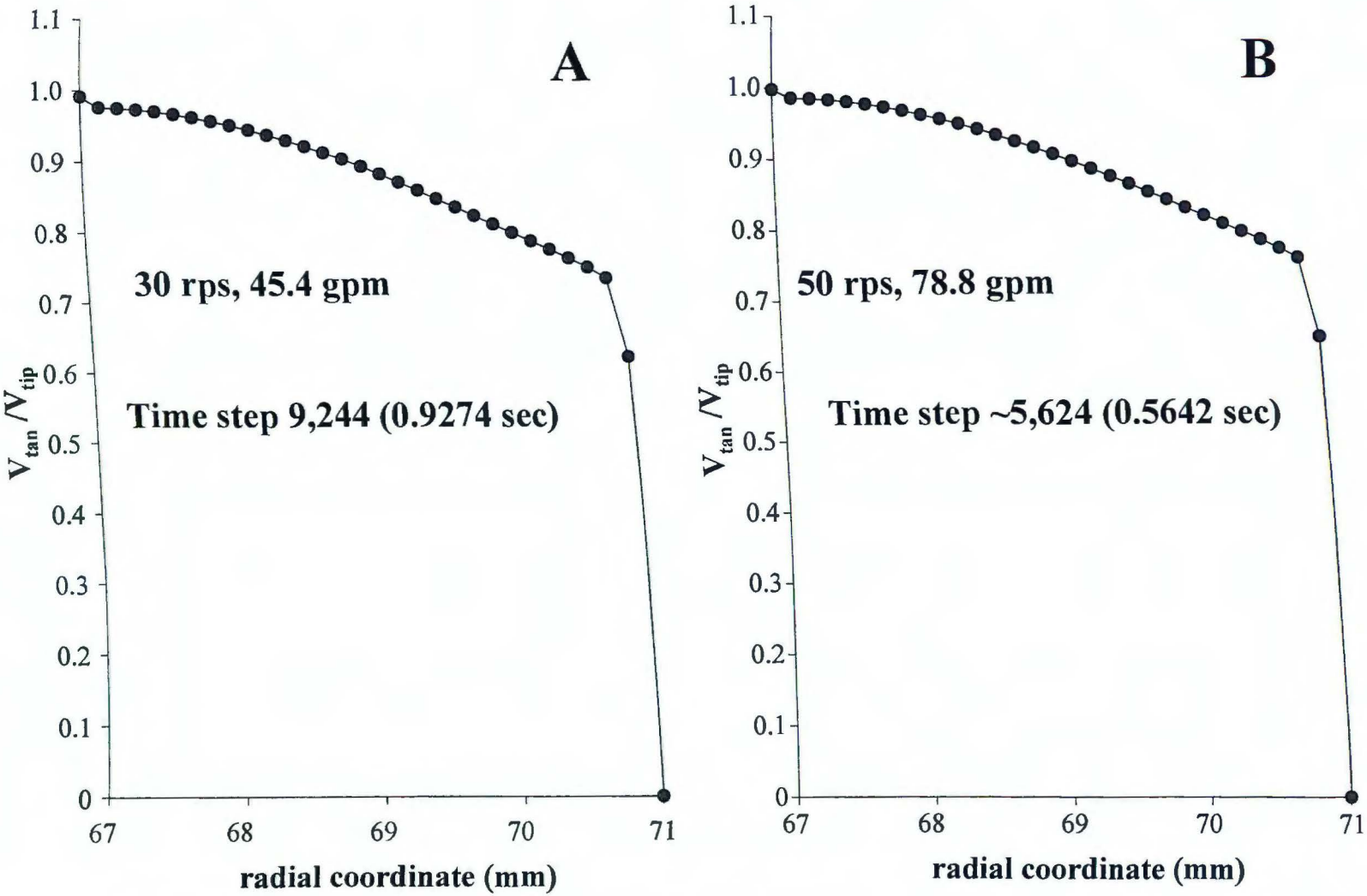

Figure 4-15. Reduced tangential mean velocity profiles across the gap at the azimuthal center of stator tooth 1 when in full alignment with a rotor tooth . Simulation 4 (**A**), and simulation 3 (**B**).

stator tooth 1 at the same time step corresponding to Fig. 4-15a is plotted in Fig. 4-16a. Y+ is about 50 in the computational cells bounding stator tooth 1 which is ideal for proper application of the wall functions. Near the rotor tooth y+ is too low, having a value anywhere from 5 to 20 which in principle could adversely affect the solution there.

Mean flow velocities in stator slot 1 are not as strongly periodic as those occurring in the gap. Outflow from the left side of the slot is essentially non-existent due to the formation of a very low velocity vortex. All mass outflow into the volute occurs on the right side of the stator slot and, as mentioned above, the mean velocity there correlates with the approach of the high-speed jet in the gap region. Fluid exiting the right side of slot 1, makes a half horseshoe, 90° turn extending into the central region of the volute above the right side of stator tooth 14.

Existence of a vortex in slot 1 may be explained as follows: Flow in the gap region has a very small radial component but, as fluid impinges on the right edge of the stator slot and moves toward the volute, the radial velocity becomes dominant. Once an element of fluid has reached the right top corner of slot 1 it is forced to curl further in a counterclockwise direction as it makes its way to the outlet. The simulated flow on the right side of slot 1 is due primarily to convective momentum transport from the gap region, and it transfers its counterclockwise motion to the left side of the slot through viscous effects resulting in the observed vortex. Since viscous effects are expected to be very small in comparison to convection for the large Reynolds number of the simulation, this explains the relatively small magnitudes of the mean velocities in the vortex as compared to those observed on the right side of the slot. The velocity

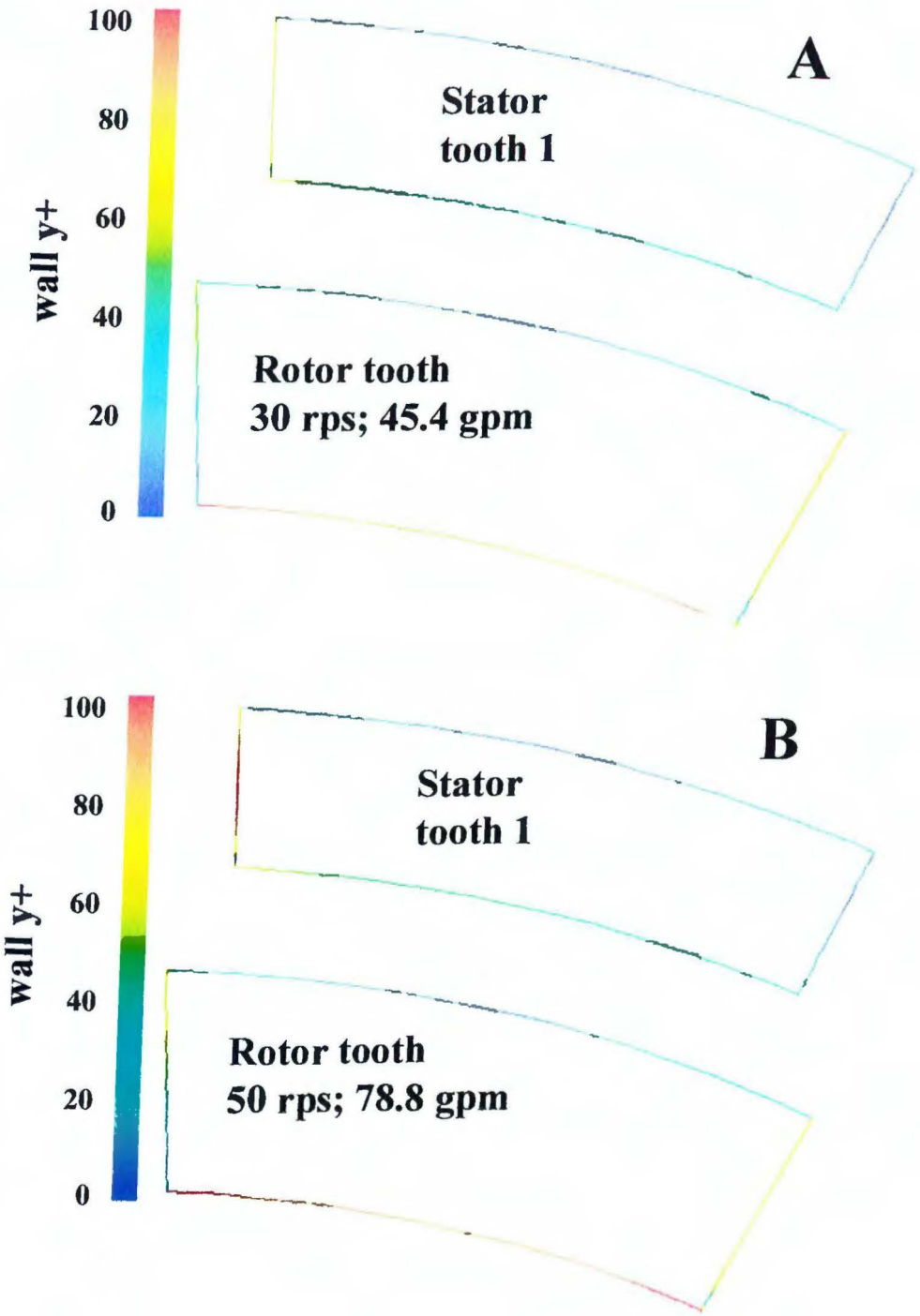

Figure 4-16. Wall y+ values at stator tooth 1 in the wide gap model. Simulation 4 at time step 9,244 (**A**), and simulation 3 at time step ~5,624 (**B**).

magnitudes in the vortex correlate weakly with the time dependent increases in velocity on the right side of slot 1 as would be expected (compare Figs. 4-7 and 4-9).

Time dependent flow in other stator slots and gap regions have very similar characteristics to those for slot 1. The primary difference is the magnitude of flow variables as is indicated by the instantaneous and fixed frame mass flow rates through each of the slots (Figs. 4-14 and 4-17a). According to the simulation, there is a strong correlation between slot distance from the outlet and mass flow rate. Of the slots in the half of the domain to the right of the outlet, slot 14 has by far the highest mass flow rate. Flow rates through slots 1 – 6 decrease in order and have from two fifths to one eighth that of slot 14. Beginning with slot 7 mass flow rates begin to increase again. Nearly 30 % of the total device mass outflow occurs through stator slot 14. It is interesting to note that the stator teeth bounding the slot nearest the exit (slot 14 for these simulations) are often the first to fail in industrial equipment.

Volute flow is most strongly periodic directly above each stator slot. Even here, however, the periodicity is for all practical purposes restricted to changes in magnitudes, in synchronization with those found in slot 1, rather than any changes in direction. For this reason it is justified and more succinct to visualize the volute flow using fixed frame simulation results after 28 rotor revolutions (Figs. 4-18 through 4-22).

The fixed frame volute velocity field magnitudes in the area bounded by stator tooth 14 below and the horseshoe outflow region above are very small, and near the tooth the fluid reverses direction (Fig. 4-18). The reversed flow in this region then feeds back into the vortex on the left side of slot 1 which shows that the slot vortex is

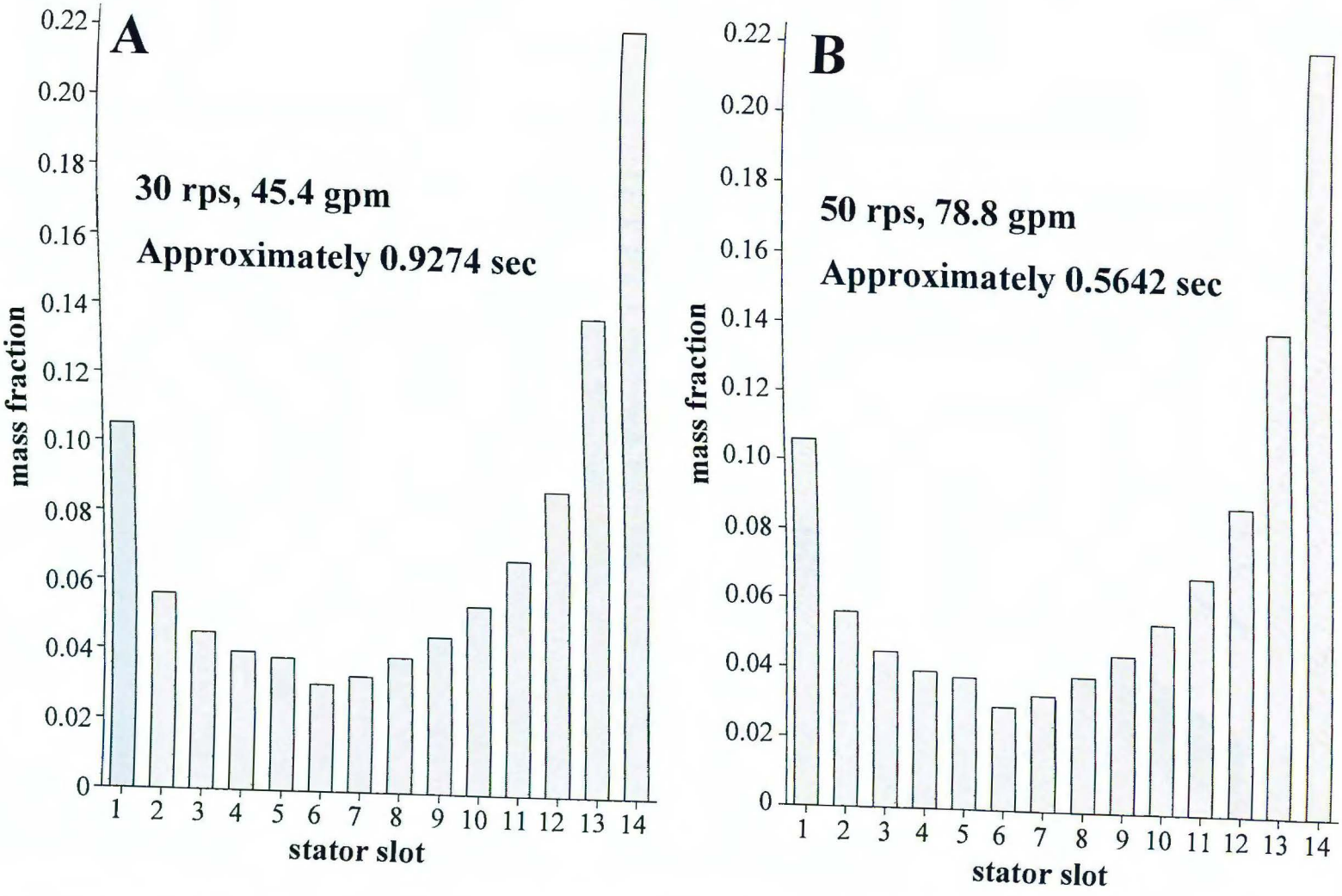

Figure 4-17. Fixed frame mass flow rates through stator slots for simulations of the wide gap model. Simulation 4 after more than 9,244 time steps (**A**), and simulation 3 after more than ~5,624 time steps (**B**).

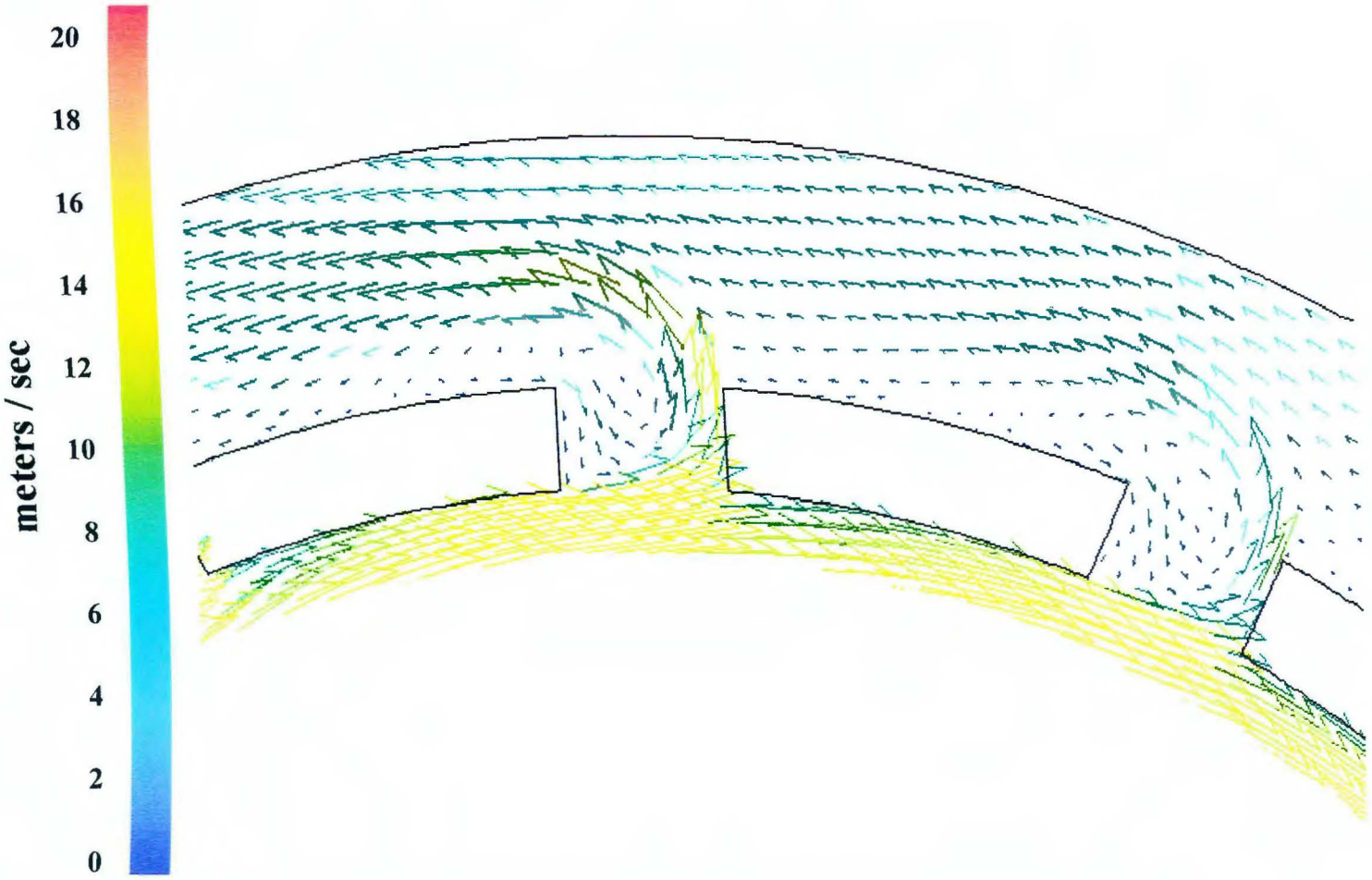

Figure 4-18. Fixed frame velocity vectors near slots 1 and 2 after 28 revolutions of simulation. Simulation 4.

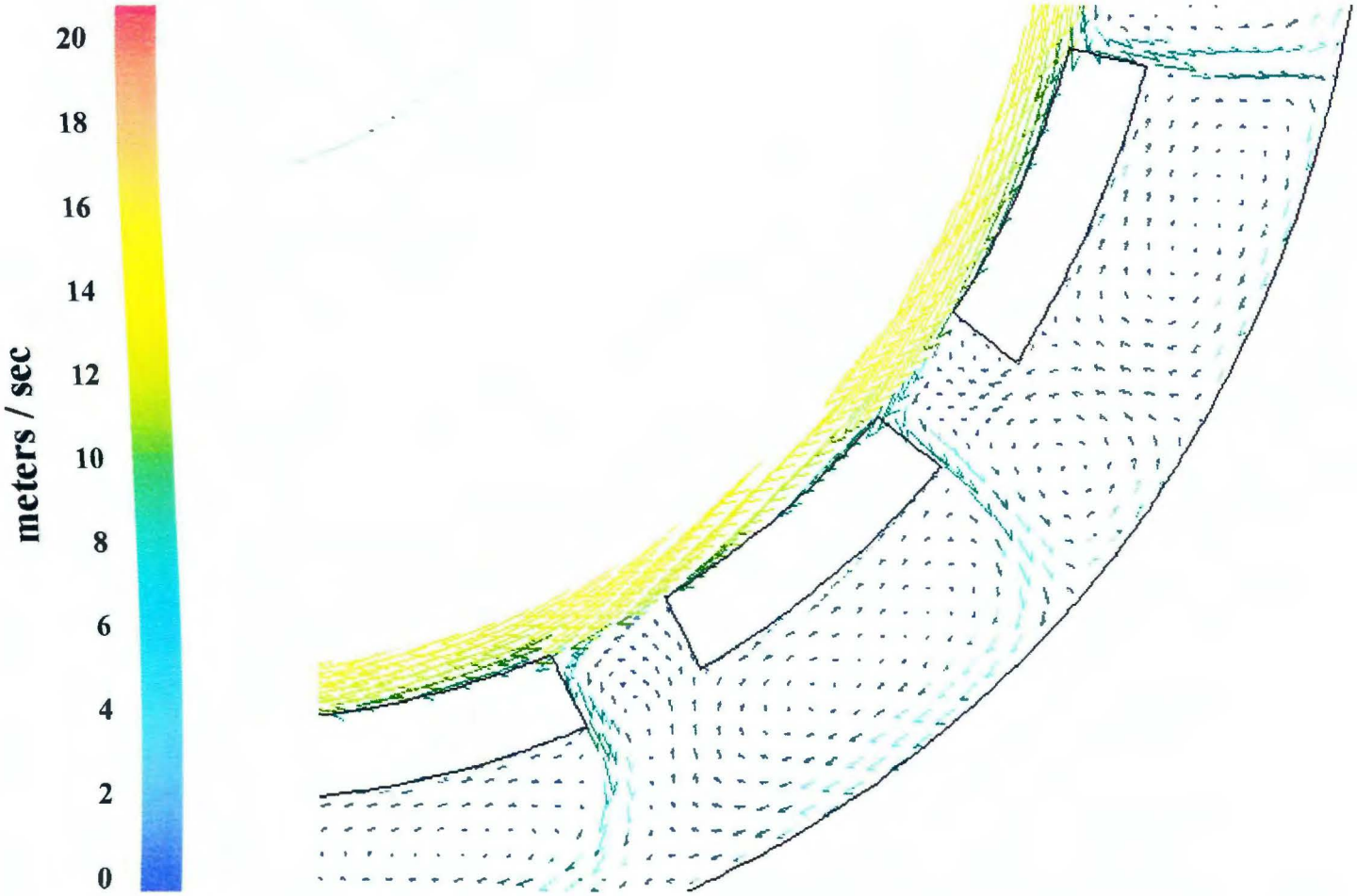

Figure 4-19. Fixed frame velocity vectors near slots 6 and 7 after 28 revolutions of simulation. Simulation 4.

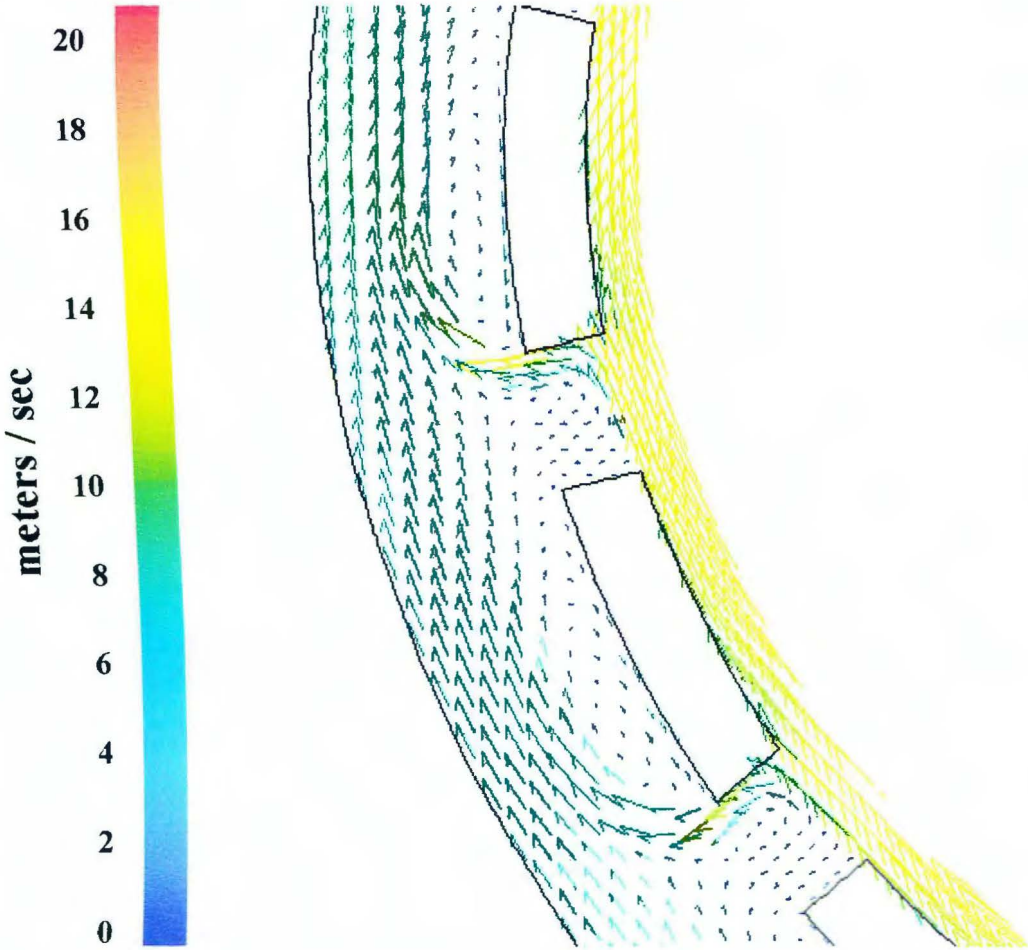

Figure 4-20. Fixed frame velocity vectors near slots 10 and 11 after 28 revolutions of simulation. Simulation 4.

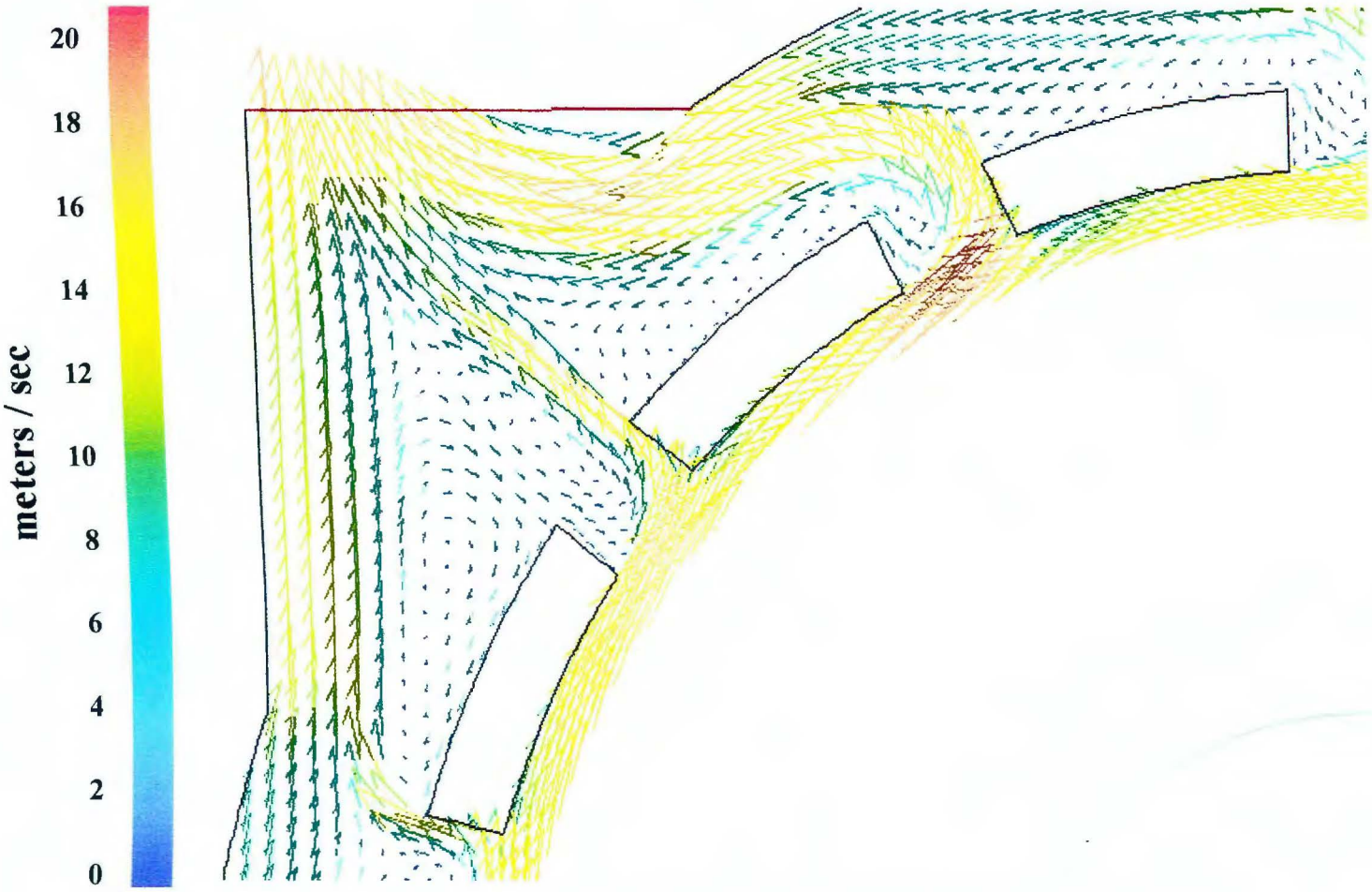

Figure 4-21. Fixed frame velocity vectors near slots 13 and 14 after 28 revolutions of simulation. Simulation 4.

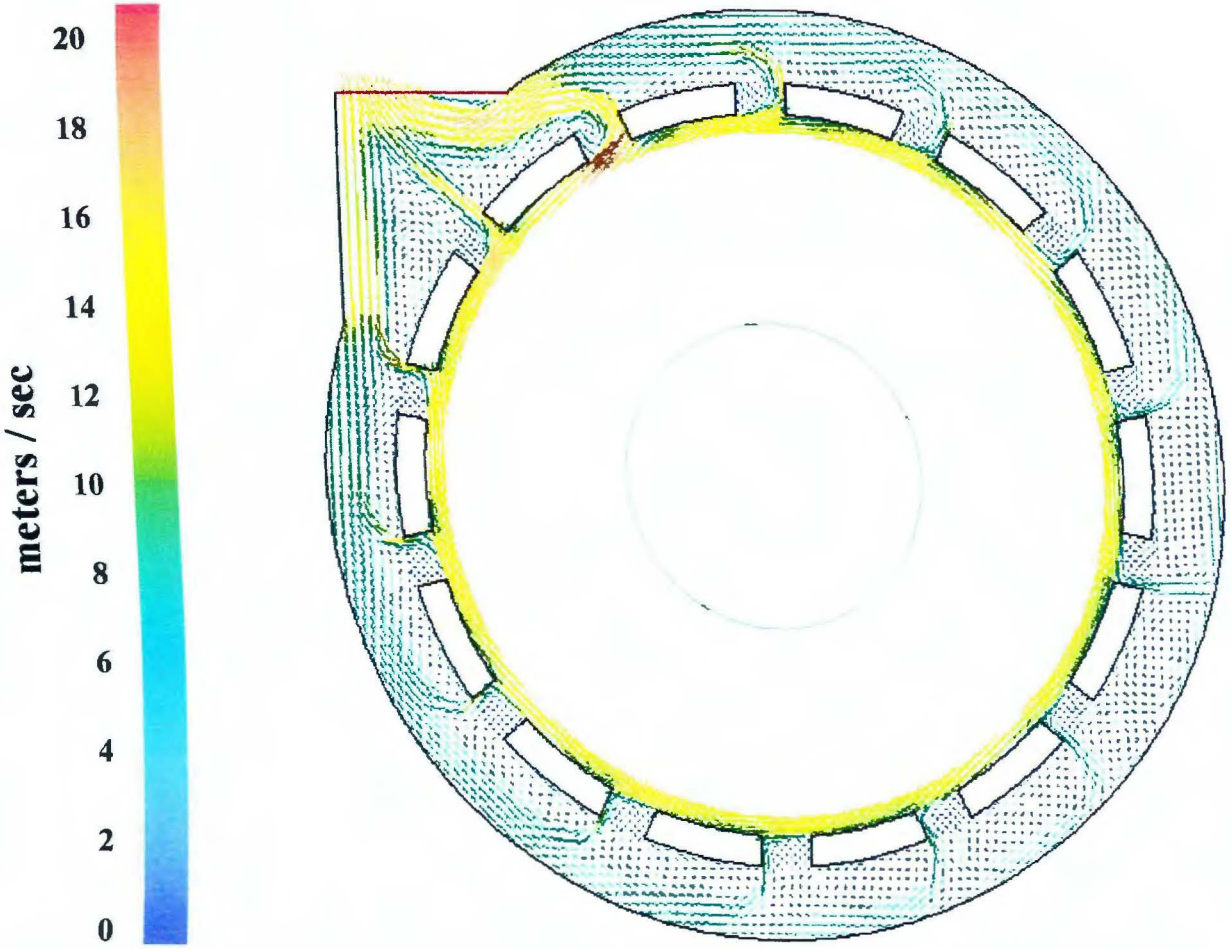

Figure 4-22. Fixed frame velocity vectors in the entire domain after 28 revolutions of simulation. Simulation 4.

not a completely stagnated area of flow but rather has a continuous mass source from the volute. Practically this means that a small fraction of mass flowing out the right one-fourth of slot 1 is recirculated back to the left side of the slot, and any particles following this trajectory will have an extended residence time.

Overall flow patterns throughout the volute may help explain the strong correlation between slot mass outflow and distance from the outlet. Consider again the fluid exiting from the right of stator slot 1 and the 90° turn it takes in the volute. This turn is an acceleration and must involve a concomitant loss of energy by conservation principles. Although only speculation, the source of energy for inducing the momentum change may be at the expense of the volute flow downstream of a given slot. The counterclockwise flow in the volute before slot 1 is responsible, through inertial transfer, for changing the momentum of the fluid leaving slot 1. The loss of inertia in the upstream volute flow incurred during this process manifests itself through a redistribution of mass outflow from the slots. Of slots 1-6 and 14, those further from the outlet will feel the effects of energy loss due to inertial transfer in the volute regions more than slots closer to the outlet. A similar argument applies to slots 7-13 where volute flow is in the clockwise direction. Outflow from slot 6 requires special consideration (see below).

Figures 4-23 and 4-24 show the pathlines followed by particles released from the gap due to the fixed frame velocity field. It should be noted that visualization of the flow field by this method ignores the effect of turbulent fluctuations on the pathlines that particles would be expected to take, but is nevertheless a very useful tool. The first stator slot where volute flow splits between a clockwise and

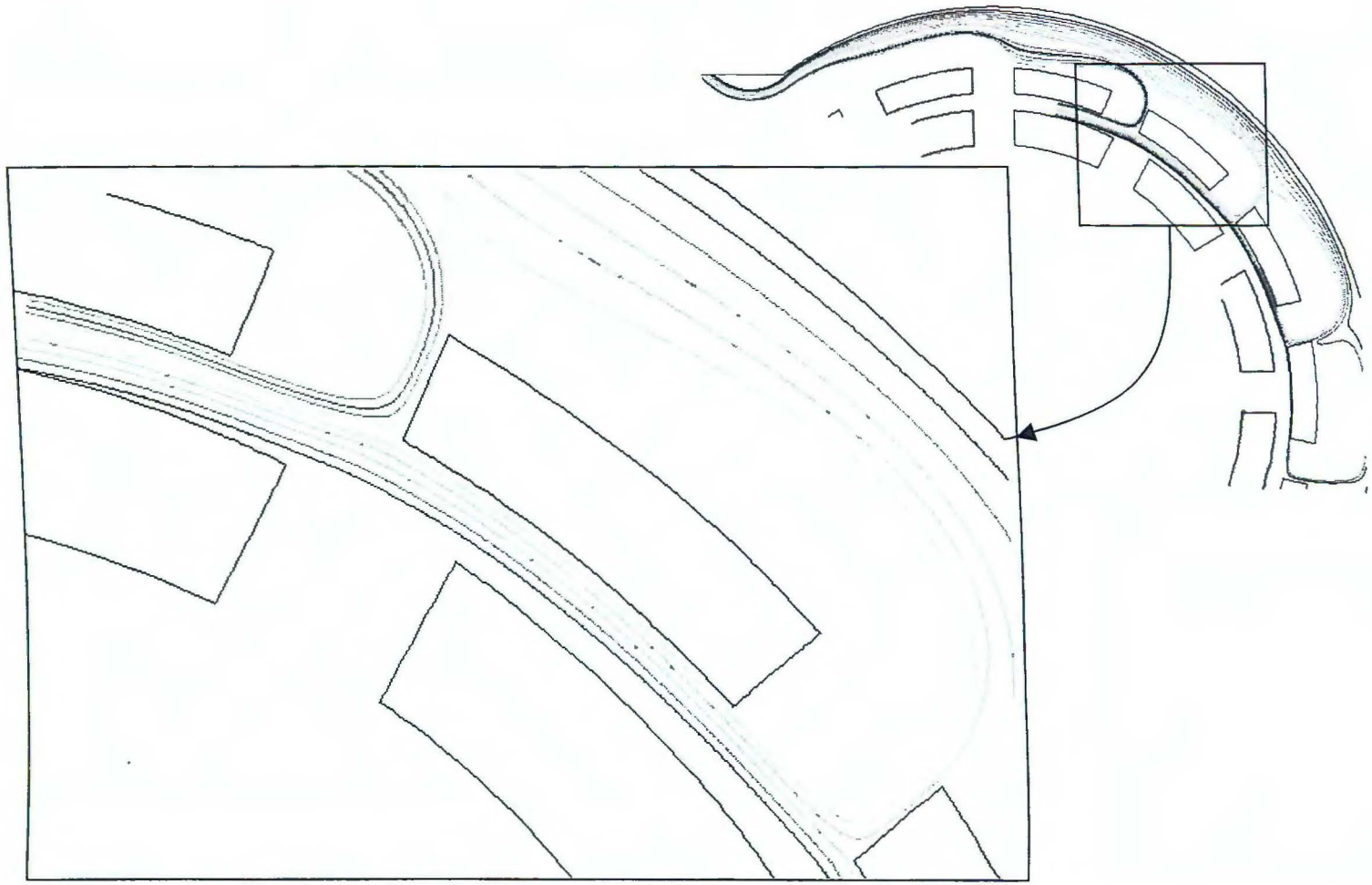

Figure 4-23. Pathlines near slots 2 and 3 due to the fixed frame velocity field after 28 revolutions of simulation . Simulation 4.

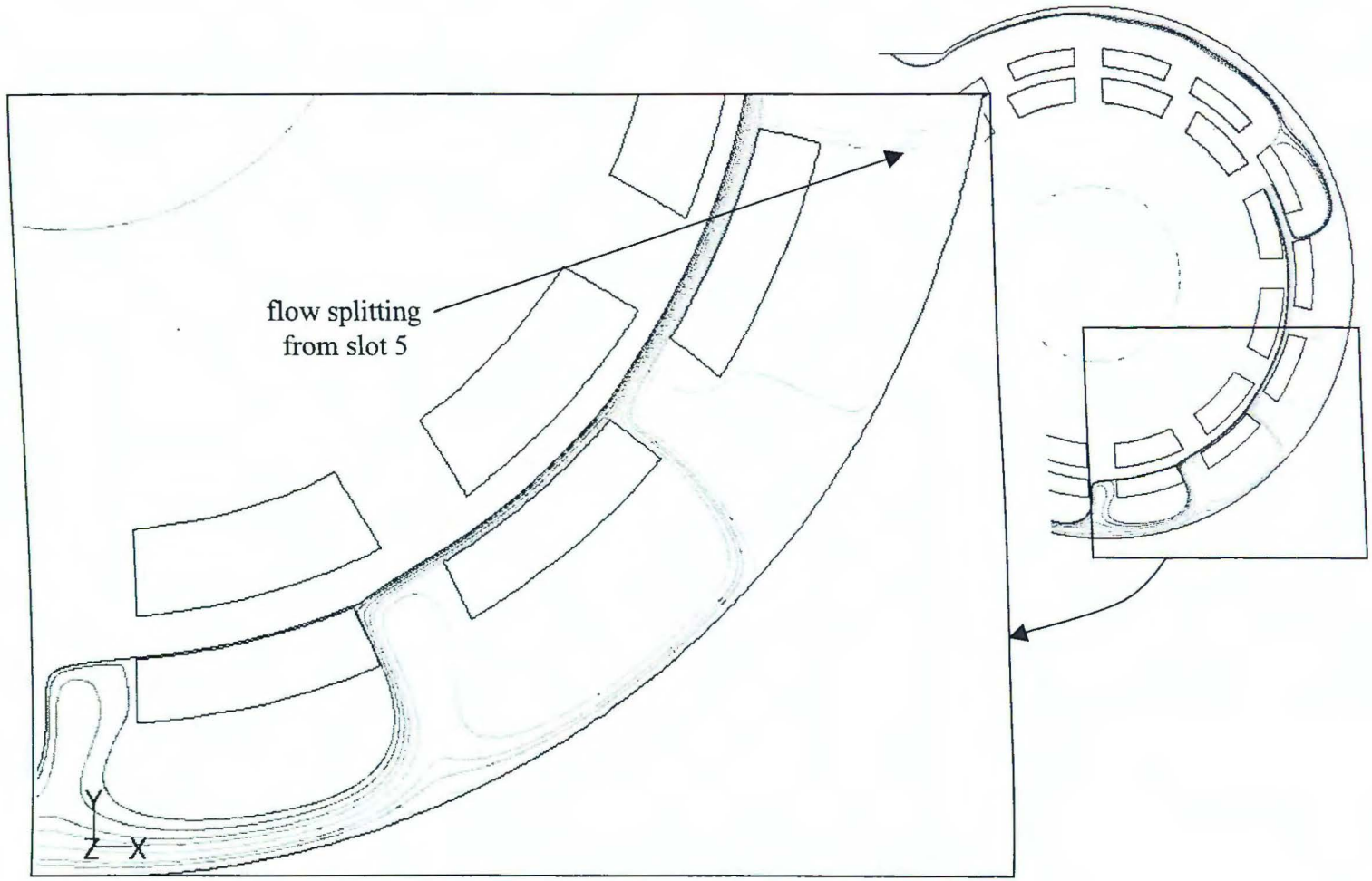

Figure 4-24. Pathlines near slots 6, 7, and 8 due to the fixed frame velocity field after 28 revolutions of simulation. Simulation 4.

counterclockwise direction is at slot 5, although for practical purposes the outflow from slot 5 may be considered to be quantitatively counterclockwise. Outflow from slots 6 and 7 are 100% in the clockwise direction. The very low outflow rates from these slots may be in part explained by the fact that there is no (slot 6) or very little (slot 7) inertial momentum transfer occurring in the volute to drive the flow from these slots toward the outlet. In the volute region adjacent to slot 6 this results in the 90° direction change being affected by the volute wall rather than upstream flow. Notice that the pathlines due to flow from slot 6 are much closer to the volute wall than those from slots where considerable inertial transfer is significant: Compare to pathlines above slot 1 or even slot 7. Practically, this results in extension of the recirculation areas near the stator teeth further into the volute region.

Since volute flow from slot 5 is predominantly counterclockwise and that from slot 6 is clockwise, the volute flow between these two slots is very highly recirculatory and stagnated. Between the slots there are two vortices: one directly below slot 6 which moves in a clockwise direction and one closer to slot 5 moving in a counterclockwise direction. The directional splitting explains the reason that the simulation takes so long to develop in this area (section 4.2): There is no convective momentum transport of the Reynolds averaged velocity field here.

The pathlines also clearly show that flow from the volute back into stator slots is significant for slots where the adjacent volute flow is in the clockwise direction (Fig. 4-24). Backflow also occurs in the other slots, however for these slots the backflow occurs from a fluid element that has left the slot to which it flows back into (see analysis of slot 1 above). For slots 6-12, the backflow occurs from fluid that left

slots upstream. This distinction may be irrelevant, however, the pathlines seem to indicate that backflow into slots 7-12 is much greater than that occurring in slots 1-5 and 14. In fact, backflow in slots 1-5 and 14 is not even apparent from the pathlines, but was deduced for slot 1 from an analysis of the mean velocity field near the left top corner of slot 14 (Fig. 4-18).

Flow in the volute region near slot 13, which is closest to the exit, is quite different than in other areas of the volute (Fig. 4-21). Essentially, fluid leaving slot 13 travels straight to the exit with no change in direction. There are low velocity vortices adjacent to the teeth bounding slot 13. If backflow occurs into this slot, it appears that it would be due to a mechanism similar to that described for slot 1 rather than that for slots 7-12.

4.3 Mean Pressure Field at 30 rps and 45.4 gpm Operating Conditions

Figures 4-25 through 4-31 show how the mean static pressure field changes throughout a period in the vicinity of stator slot 1. The mean pressure spans a range of about 4 bar throughout the device (1 bar = 0.99 atm). The highest mean pressures in the gap close to slot 1 occur in two areas. The first region is roughly semi-circular in shape with a radius of about 2 mm and extends from either stator tooth 14, 1, or both, depending on the rotor position, halfway into the gap. When the leading edge of a rotor slot is aligned with the left edge of stator slot 1 (Fig. 4-25) this high-pressure area is about 3 bar and located directly above the left edge of the rotor slot. Comparison with Fig. 4-7 shows that it is due to impingement of fluid leaving the left

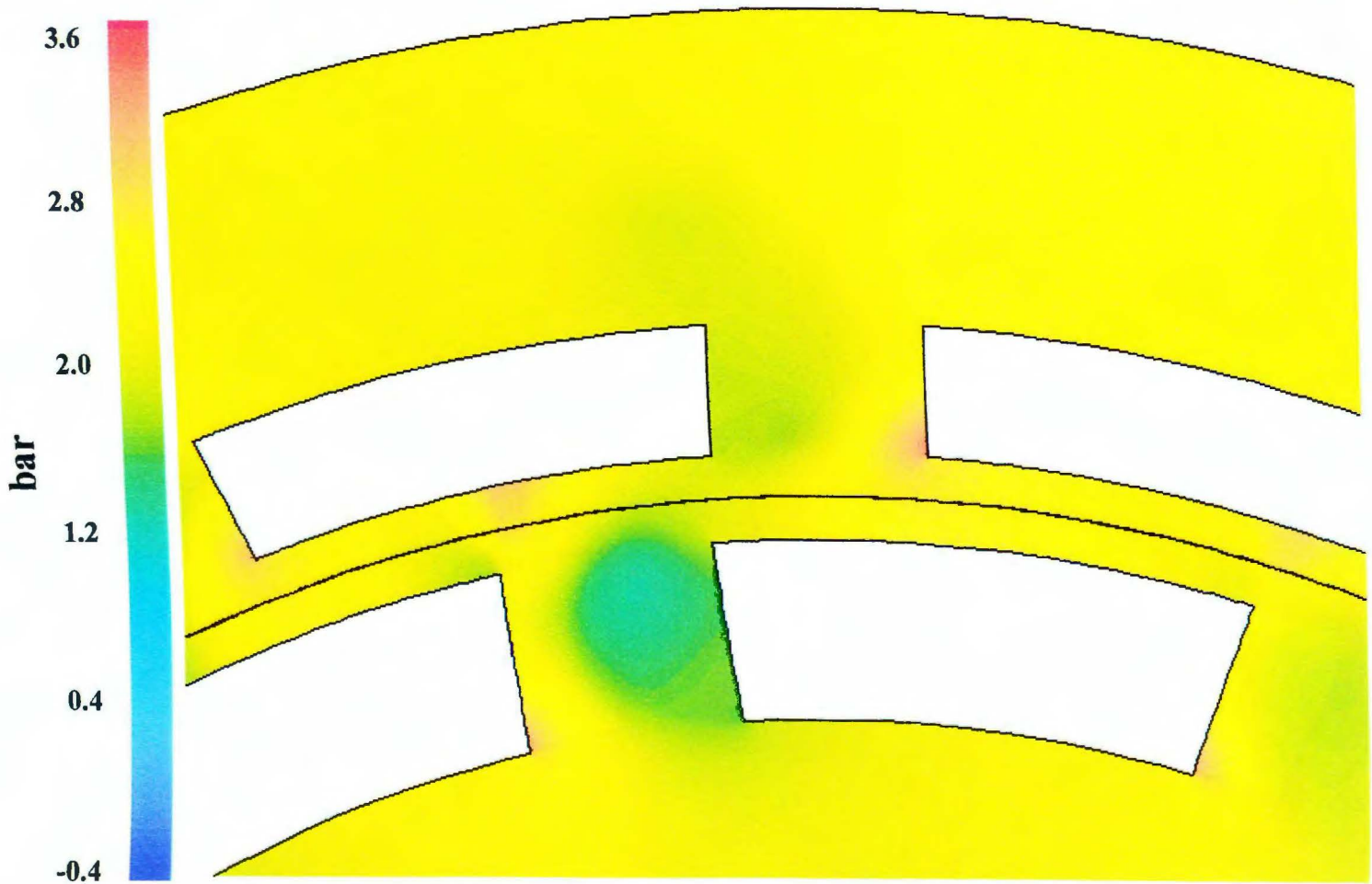

Figure 4-25. Angularly resolved mean static pressure near slot 1 at time step 9,236 (0.9266 seconds). Simulation 4

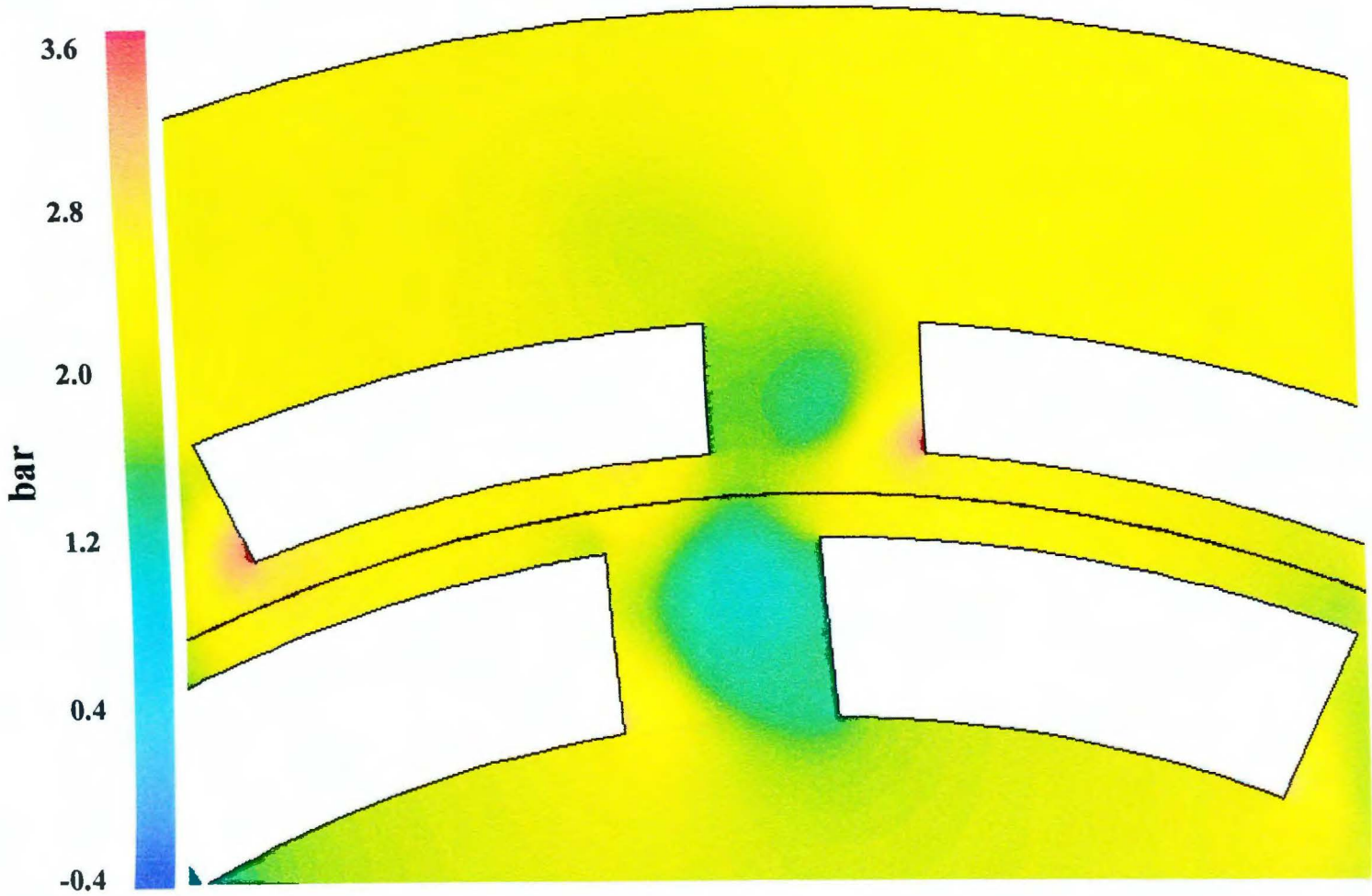

Figure 4-26. Angularly resolved mean static pressure near slot 1 at time step 9,240 (0.9270 seconds). Simulation 4

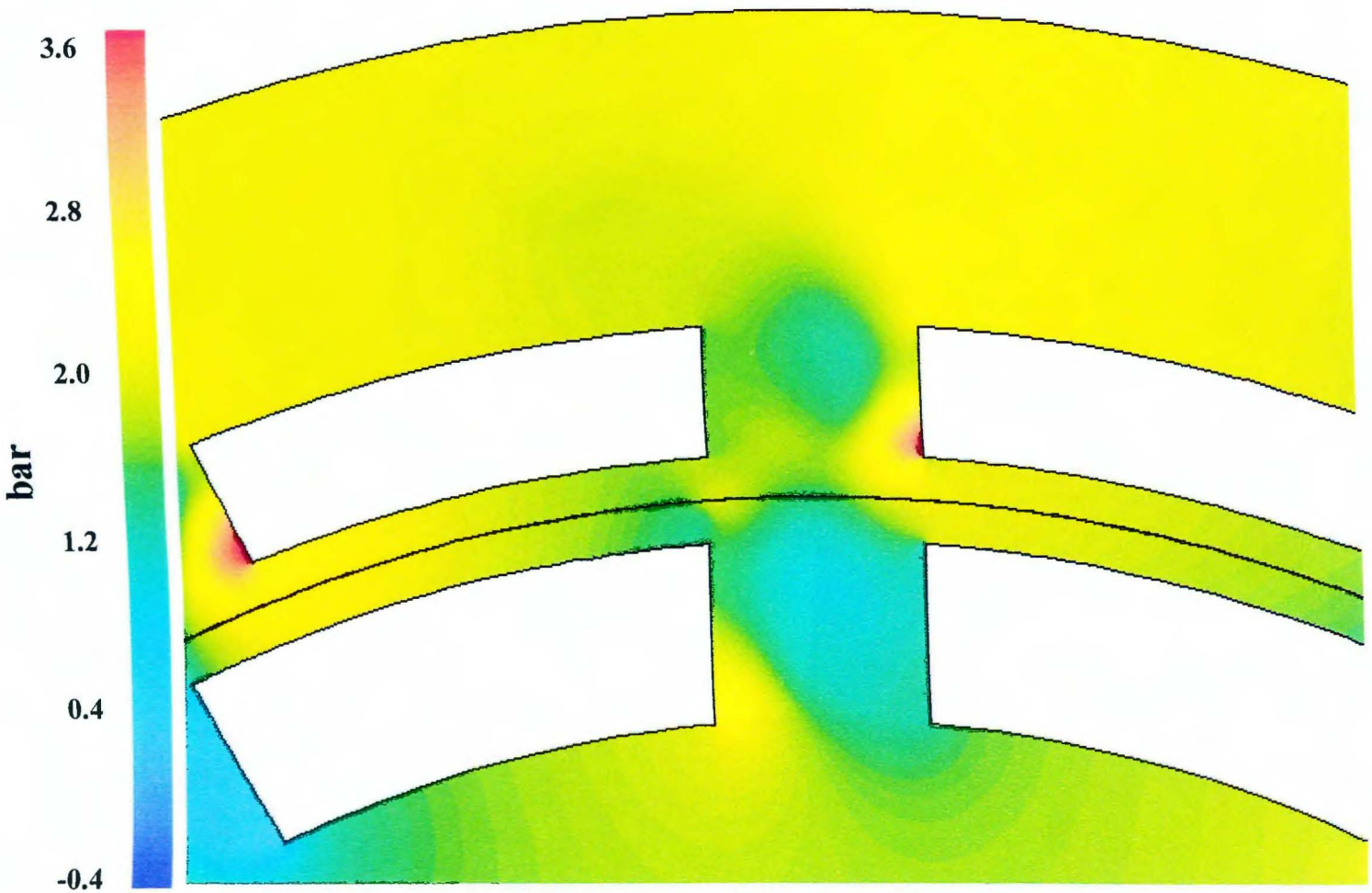

Figure 4-27. Angularly resolved mean static pressure near slot 1 at time step 9,244 (0.9274 seconds). Simulation 4

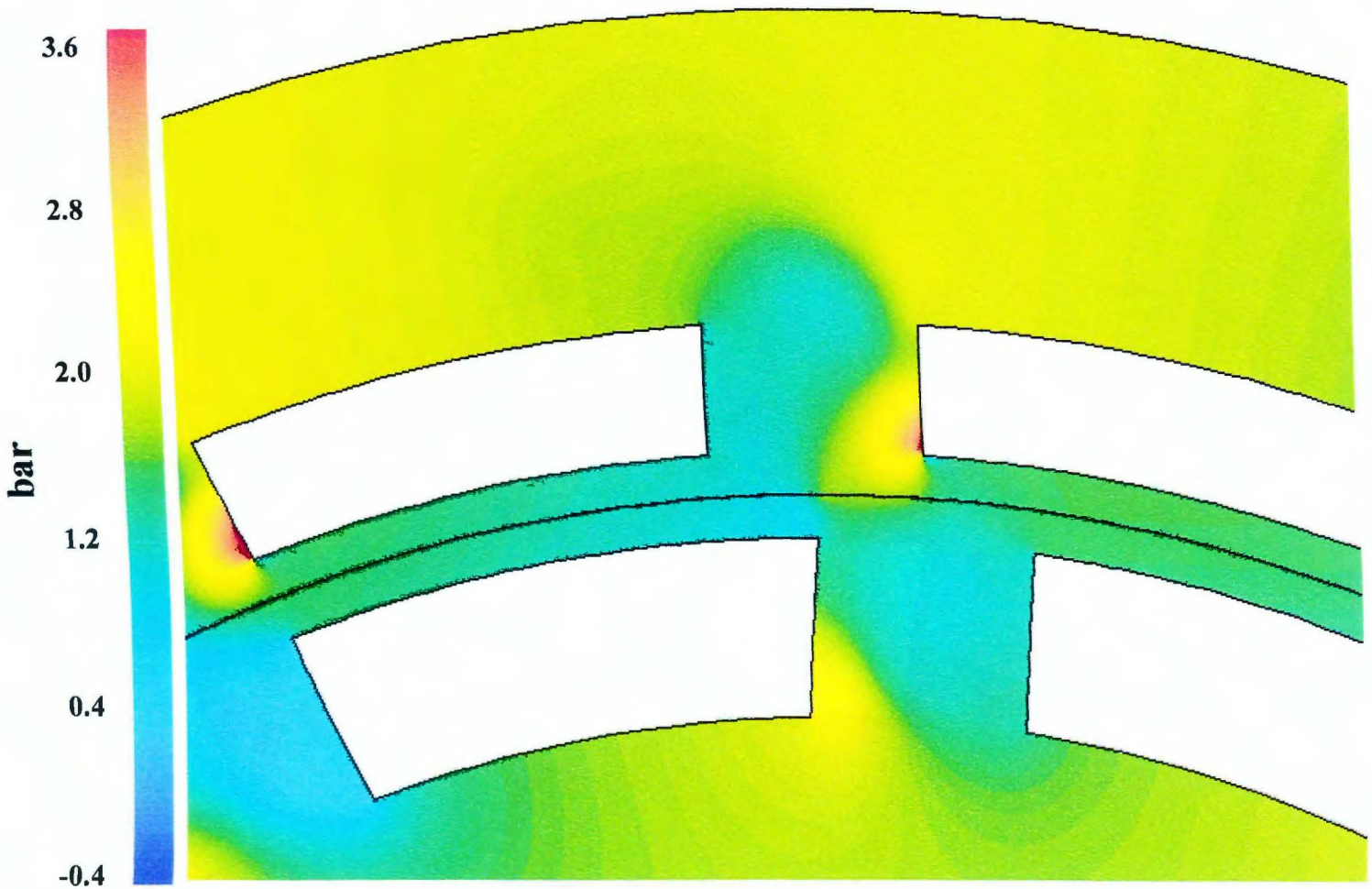

Figure 4-28. Angularly resolved mean static pressure near slot 1 at time step 9,248 (0.9278 seconds). Simulation 4

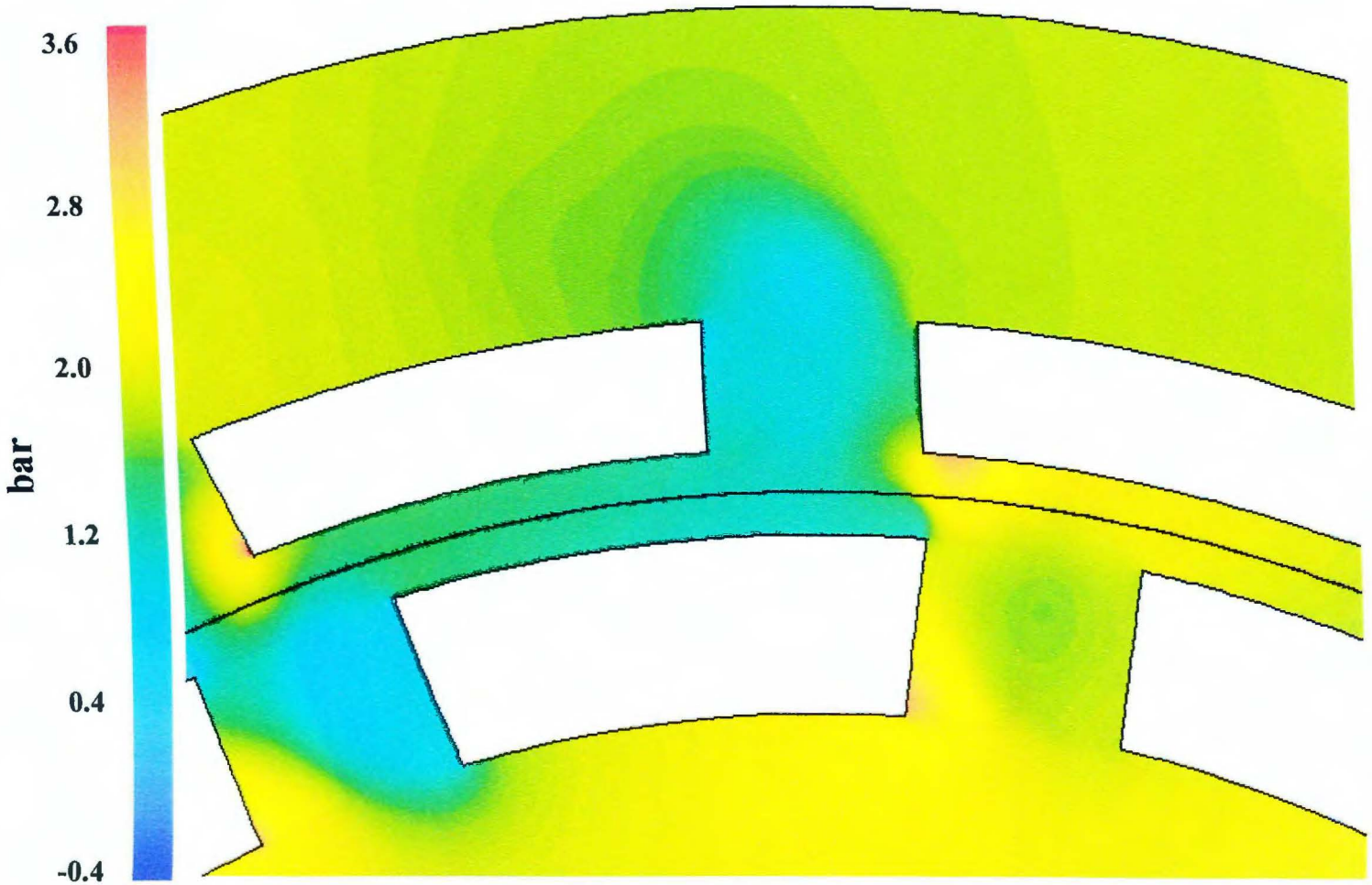

Figure 4-29. Angularly resolved mean static pressure near slot 1 at time step 9,252 (0.9282 seconds). Simulation 4

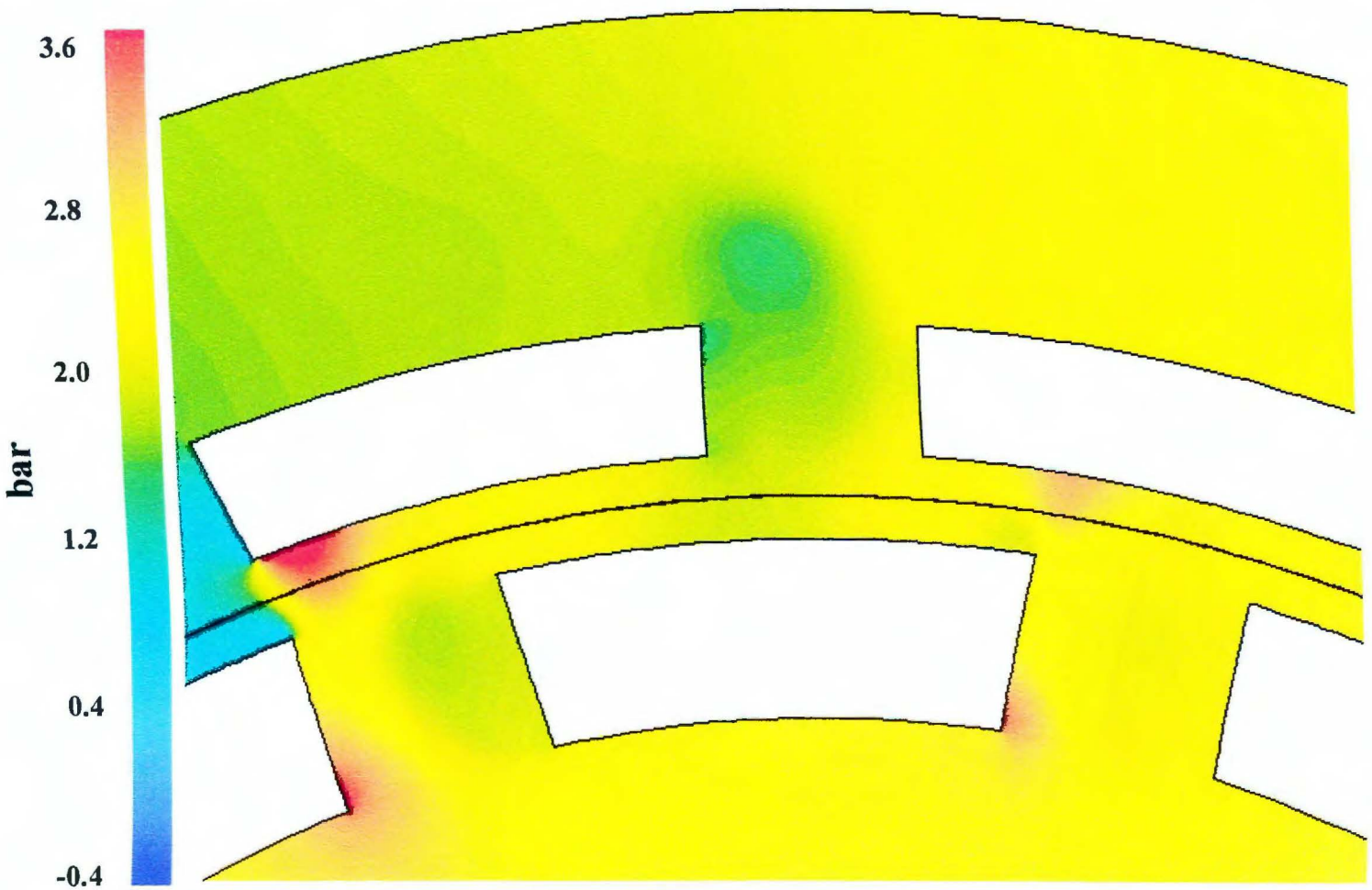

Figure 4-30. Angularly resolved mean static pressure near slot 1 at time step 9,256 (0.9286 seconds). Simulation 4

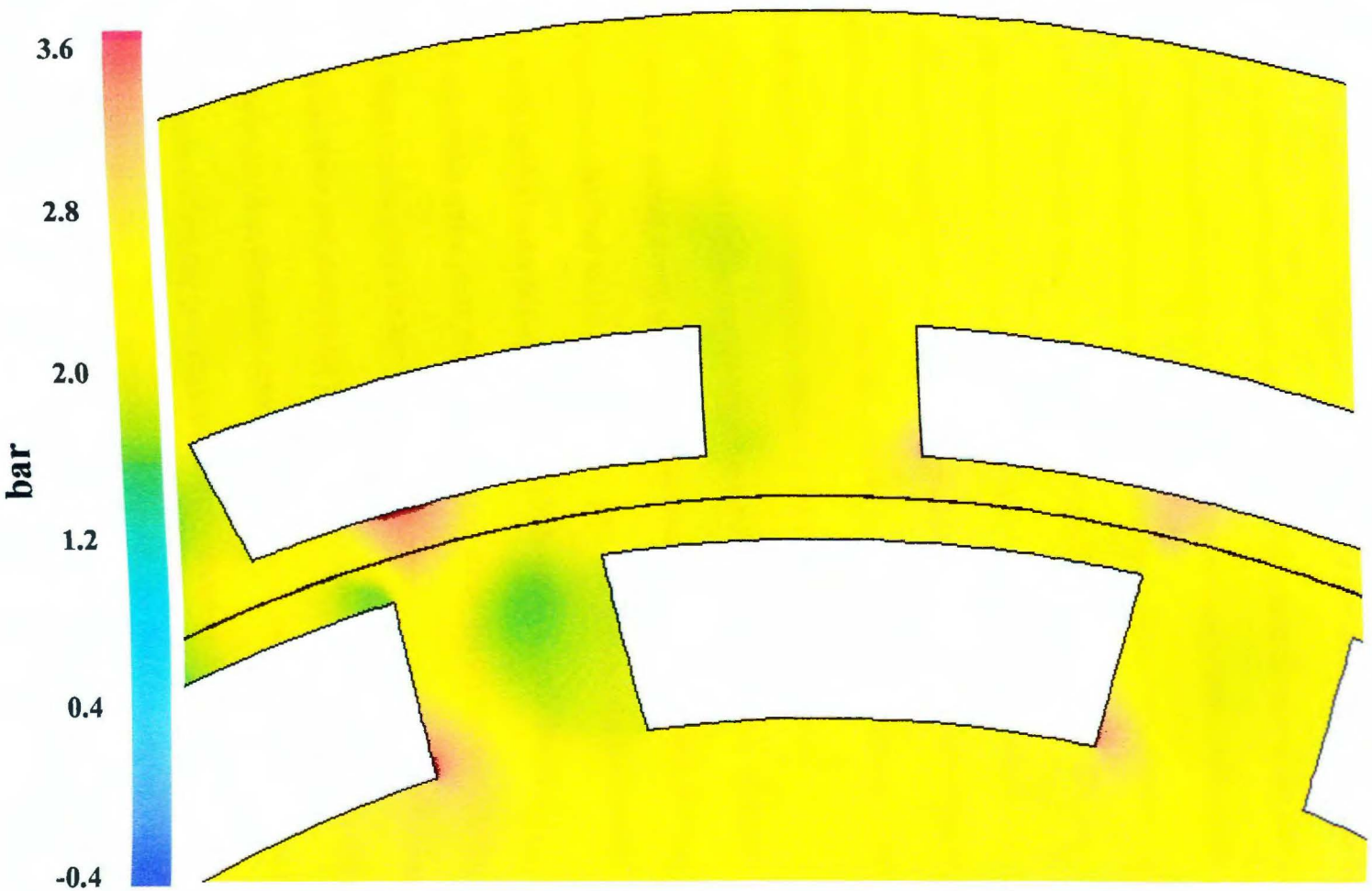

Figure 4-31. Angularly resolved mean static pressure near slot 1 at time step 9,260 (0.9290 seconds). Simulation 4

side of the rotor slot with the stator tooth: Recall that the fluid exiting the left side of a rotor slot always has the strongest radial component relative to other gap velocities.

The high-pressure region on stator tooth 14 moves clockwise along the tooth edge as the rotor slot sweeps by and always remains directly above the left edge of the rotor slot as would be expected. The mean pressure magnitude, however, does decrease to about 2 bar as the rotor and stator slots become more aligned (Figs. 4-8 and 4-26). When the slots are completely aligned (Figs. 4-9 and 4-27), the high-pressure area under stator tooth 14 completely disappears, and the gap region under the tooth has a tangential mean pressure gradient very roughly resembling that which would be expected for duct flow due to an imposed pressure: a higher pressure to the left (about 2.5 bar) decreasing to about 1.5 bar on the right.

The second high-pressure region occurs on the right corner of stator slot 1 and is observed at almost every time step of the simulation. In actuality, this region may be considered identical to the high-pressure area that follows the lower edge of the stator tooth throughout a period. Figure 4-25 shows that, with the leading edge of a rotor tooth under stator tooth 14, the mean pressure at the corner is only slightly greater than that observed in the high-pressure regions underneath teeth 1 and 14 (~3 bar). As the rotor and stator slots become aligned and the jet approaches the right edge of stator tooth 1, the mean pressure at the corner increases commensurately, and it is a maximum when the two slots are directly under each other (Fig. 4-27). Note that when the two slots are in complete alignment, the fluid impinging on the corner of tooth 1 is flowing in a primarily tangential direction (Fig. 4-9). Four time steps later, the fluid in this region still has a strong tangential direction, but it does appear to be

slightly less so. Further, the mean velocity in the jet has decreased in magnitude (compare Figs. 4-9 and 4-10). Clearly the high mean pressure at the corner of tooth 1 is due to impingement on it by the jet. Changes in jet velocity and direction account for the concomitant decrease in mean pressure, as well as the apparent paradox of the smaller mass outflow from slot 1 when rotor and stator slots are completely aligned compared to four time steps later when the slots are only half aligned (Fig. 4-14).

As the rotor slot moves from a position of 4.3° past full alignment with slot 1 (Fig. 4-28) to being completely underneath stator tooth 1 (Fig. 4-29), the high-pressure region on the tooth moves around the corner to the bottom edge of stator tooth 1 inside the gap, and also decreases about 0.5 bar in magnitude. After moving around the corner, this high-pressure region and the one discussed previously may be considered one and the same. The high-pressure area follows the leading edge of the rotor tooth throughout its passage by stator tooth 1, increasing slightly in size as it moves from the left to right edge of the tooth.

Regions of relatively low mean pressure exist inside slot 1 on the left where the vortex is present. The low-pressure region is smallest (~ 0.5 bar) when a rotor slot has just passed the stator slot and high-pressure region number 2 has rounded the tooth corner (Fig. 4-29). At this time, the low-pressure region also reaches its greatest size, extending all the way across the slot and well into the volute. As the rotor continues its passage, the low-pressure region in the slot slowly increases in magnitude and recedes from the volute. The slot mean pressure increase continues until the lagging edge of the rotor tooth is aligned with the left edge of slot 1, after which time it begins to decrease and the cycle begins again. The time of lowest mean pressure on the left

side of the slot (Fig. 4-29) corresponds to time step 8 in Fig. 4-14. Comparison shows that at this time the mass outflow from slot 1 is close to a minimum. However, the mean pressure there is also fairly low 4 time steps previously (Fig. 4-28) and at this time the slot mass outflow is nearly maximal. Additionally, when a rotor tooth completely blocks slot 1 (Fig. 4-31), the outflow is nearly equivalent to that which occurs during the period of lowest slot mean pressure, yet at this time the mean pressure on the left of the slot is nearly at its highest level (~2.4 bar). There appears to be no simple correlation between stator slot mean pressure and mass outflow.

The mean pressure field in the inlet region before the rotor and also in the volute undergoes a periodic shocking. Figure 4-32b shows the pressure distribution when it is at its overall lowest throughout the volute and inlet (about 1.7 bar) while Fig. 4-33b shows the distribution when it is at its highest (about 3.0 bar). Figures 4-32a and 4-33a are plots of the relative mass outflow from each of the stator slots at these instants of time. The scale in Figs. 4-32a and 4-33a is not straightforward: On average, the difference between mass flow rates from any two given stator slots does not change greatly. For this reason, a bar chart of stator mass flow rates at any given instant will always have the same general shape as that for their fixed frame mass flow rates (Fig. 4-17). In order to discriminate between the relative slot flow rates at different rotor positions, it is necessary to use a scale that is normalized to each slot individually. For instance, in Fig. 4-32a a value of zero on the y-axis represents the minimum value for the mass flow rate through a given slot and a value of 1 represents the maximum value through that slot. If the maximum total mass fraction of flow through stator slot 1 is 0.116 and the minimum value is 0.09, then in Fig. 4-32a, a

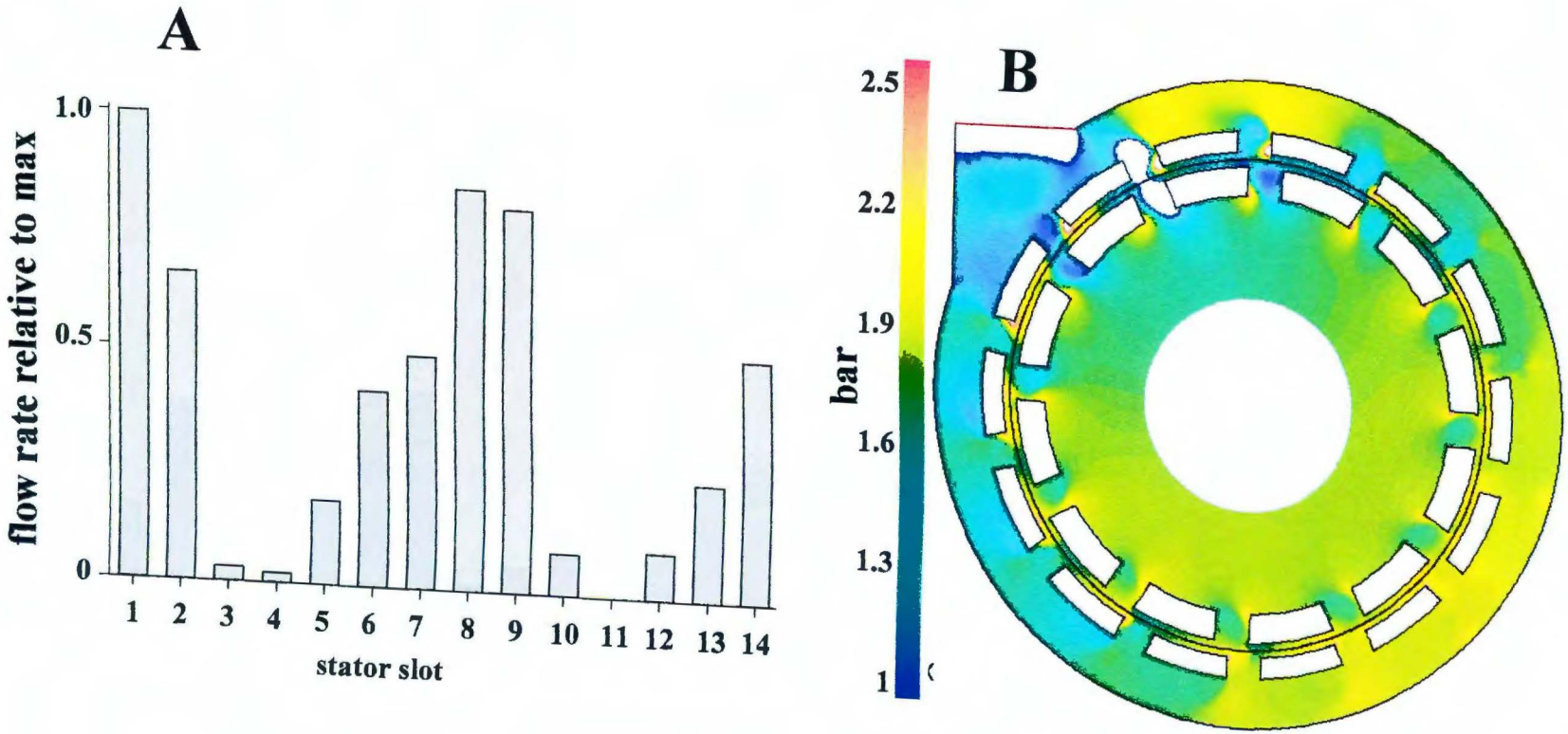

Figure 4-32. Instantaneous mass flow rates from stator slots relative to maximum for given slot (**A**) and the corresponding mean static pressure field (**B**). Time step 9,248 (0.9278 seconds). Simulation 4.

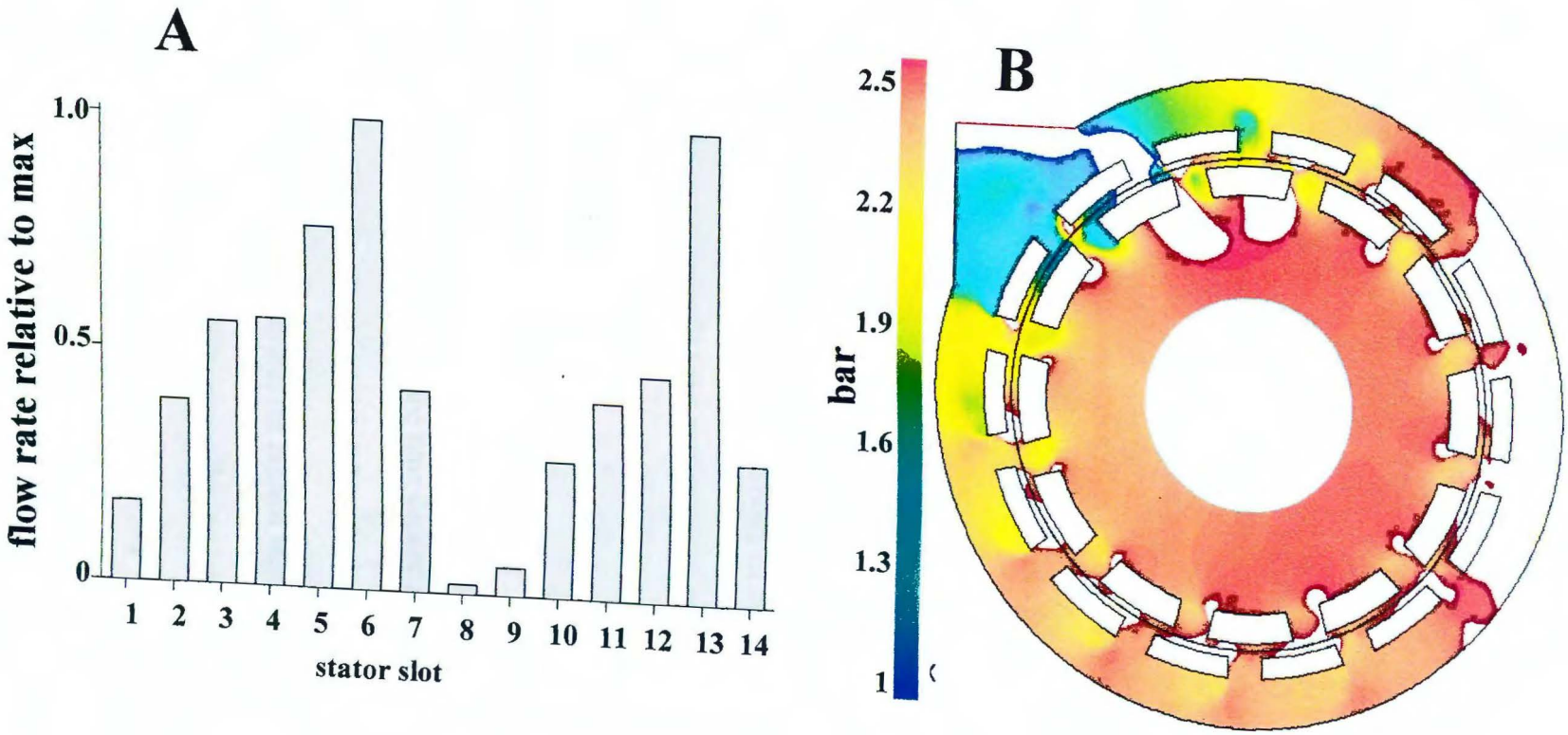

Figure 4-33. Instantaneous mass flow rates from stator slots relative to maximum for given slot (**A**) and the corresponding mean static pressure field (**B**). Time step 9,256 (0.9286 seconds). Simulation 4.

value of 1.0 for stator slot 1 would correspond to a mass fraction of 0.116 while a value of 0 would correspond to a mass fraction of 0.09. Each slot is normalized to its own maximum and minimum so that a value of 1.0 for stator slot 2 corresponds to a mass fraction of 0.065, not 0.116.

When the mean pressure is low in the volute and inlet (Fig. 4-32), the mass outflow from stator slots 1 and 8 is maximal. When the volute and inlet pressure is maximum (Fig. 4-33), the mass flow rate from slot 6 and 13 is maximal. In fact, there is a very strong correlation between which slots have maximal outflow and the volute / inlet pressure. Specifically, as the simulation advances forward in time, the slots which have maximum outflow move sequentially from numbers 6 to 1. The mean pressure is highest when slot 6 is maximum, considerably less when slot 5 is maximum, and so forth all the way to when slot 1 has maximum outflow, after which time the cycle repeats itself. Note that the geometry of the device implies that the two stator slots opposite each other will have maximum (or minimum) flow rates simultaneously.

4.4 Turbulence Field at 30 rps and 45.4 gpm Operating Conditions

Figures 4-34 through 4-40 show the time dependent evolution of turbulent kinetic energy in the vicinity of stator slot 1. When the leading edge of a rotor slot is aligned with the left edge of stator slot 1, the highest region of turbulent kinetic energy is about 38 m^2 / sec^2 and occurs directly above the top left corner of the rotor slot, extending approximately 2 mm into the gap (Fig. 4-34). Comparison with the mean velocity and pressure fields at this time (Figs. 4-7 and 4-25) show that this is the same

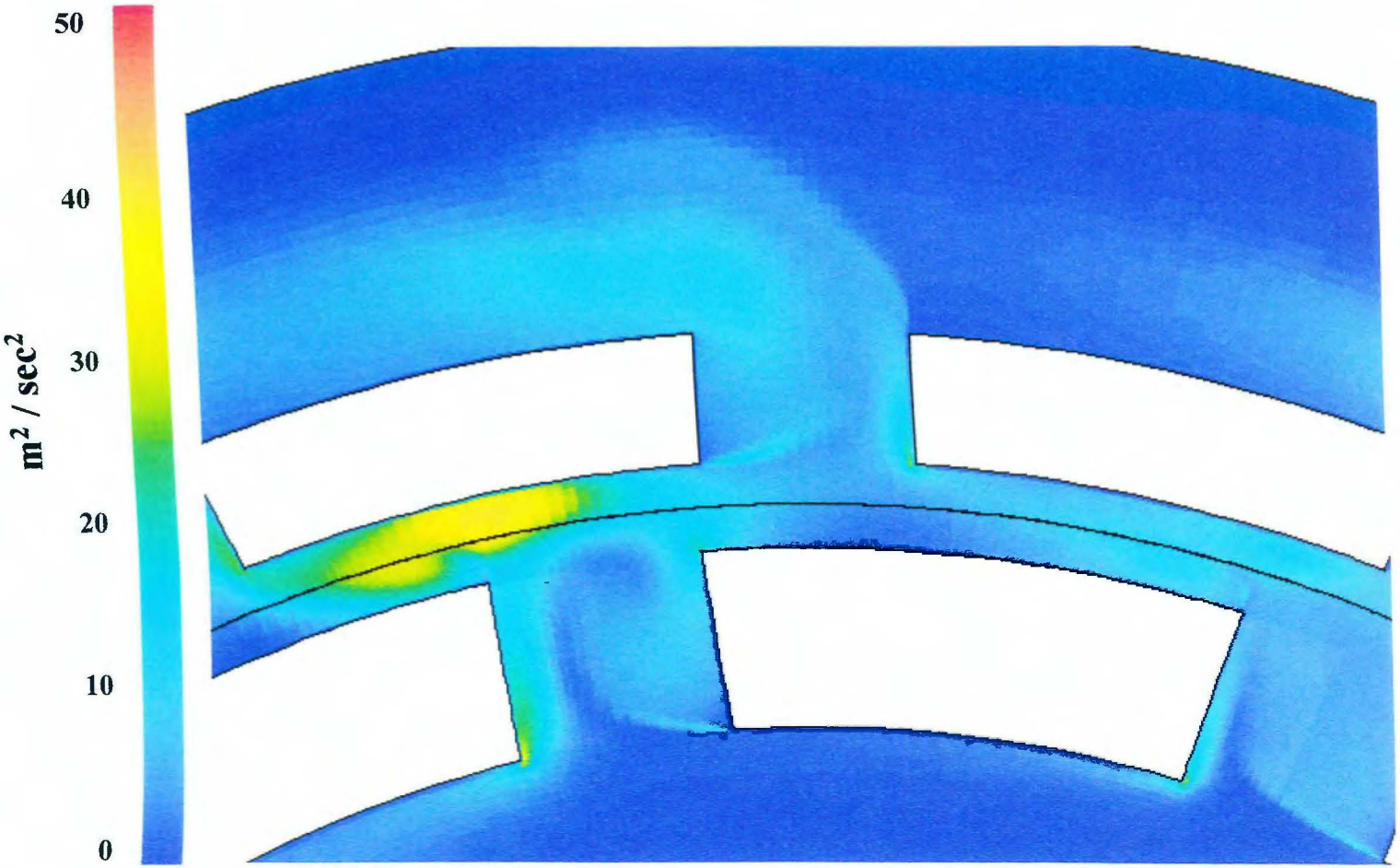

Figure 4-34. Angularly resolved turbulent kinetic energy near slot 1 at time step 9,236 (0.9266 seconds). Simulation 4.

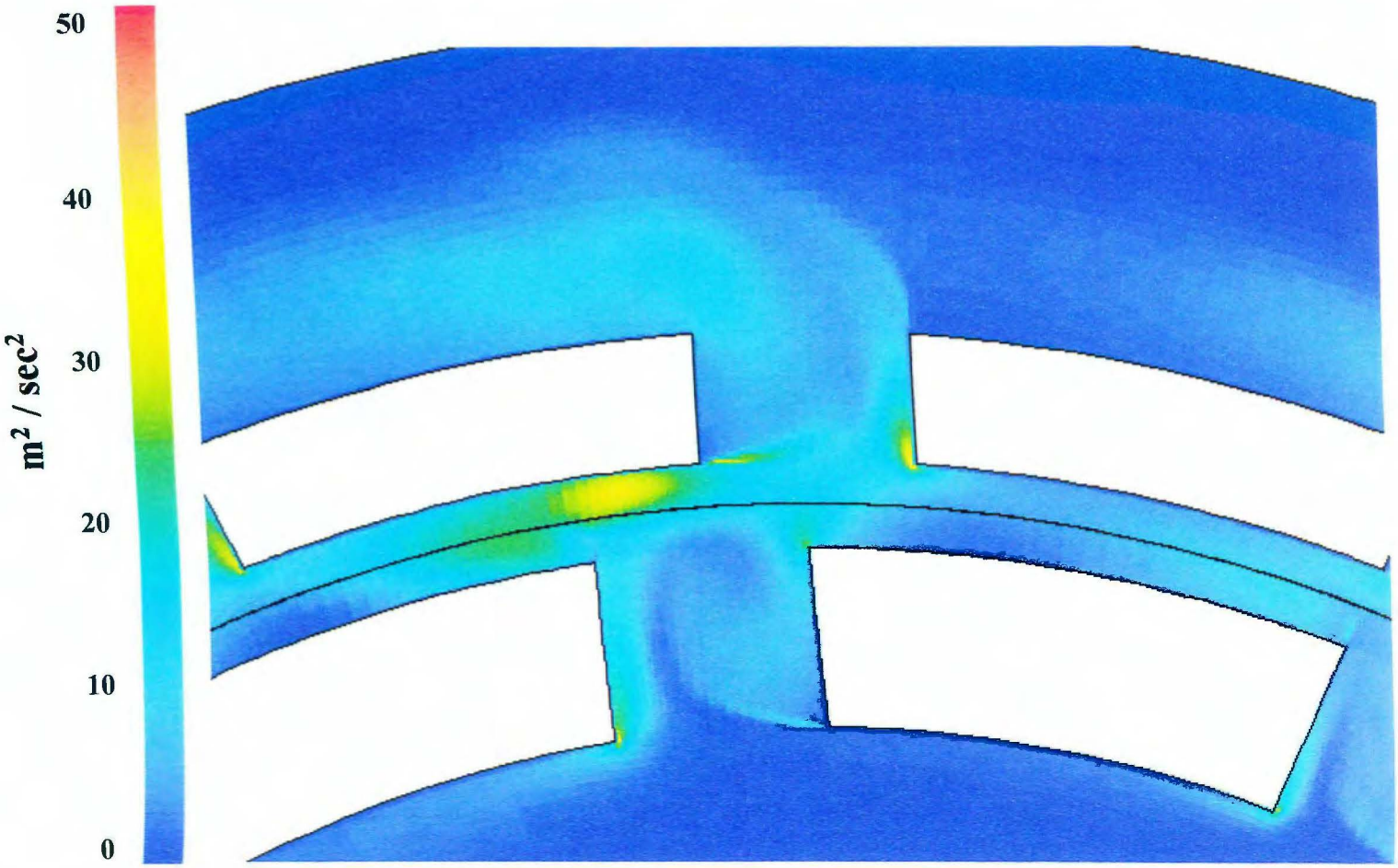

Figure 4-35. Angularly resolved turbulent kinetic energy near slot 1 at time step 9,240 (0.9270 seconds). Simulation 4.

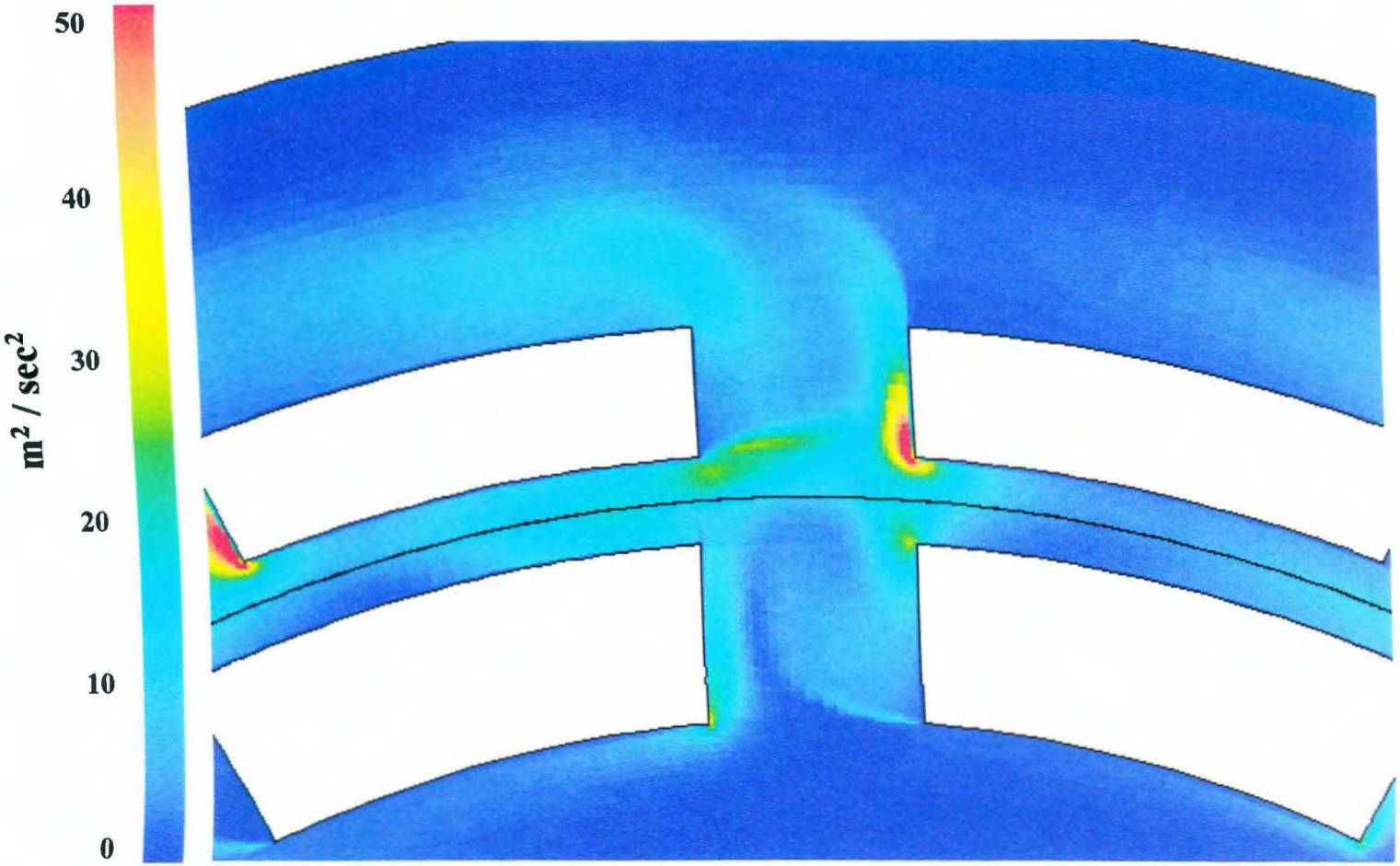

Figure 4-36. Angularly resolved turbulent kinetic energy near slot 1 at time step 9,244 (0.9274 seconds). Simulation 4.

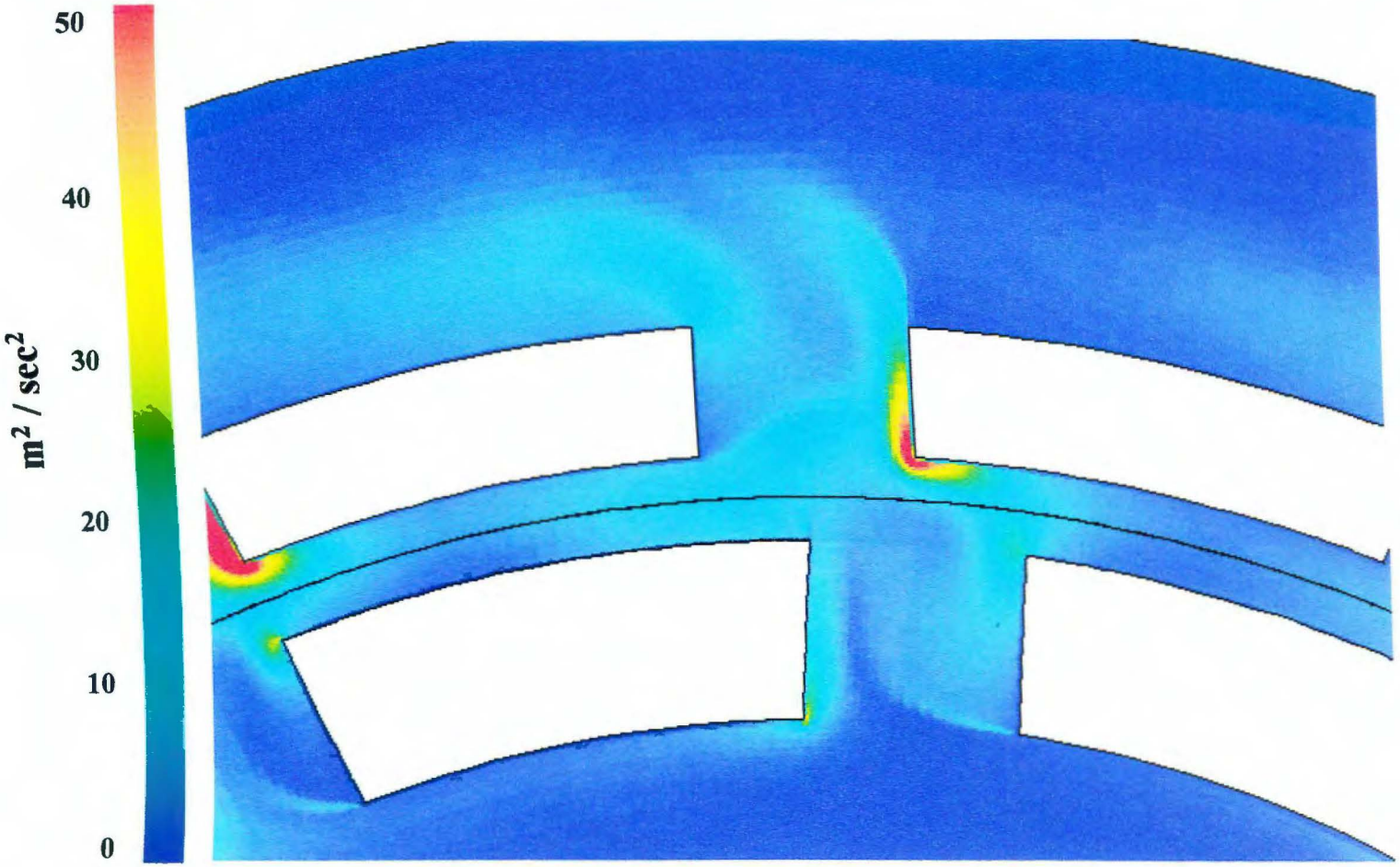

Figure 4-37. Angularly resolved turbulent kinetic energy near slot 1 at time step 9,248 (0.9278 seconds). Simulation 4.

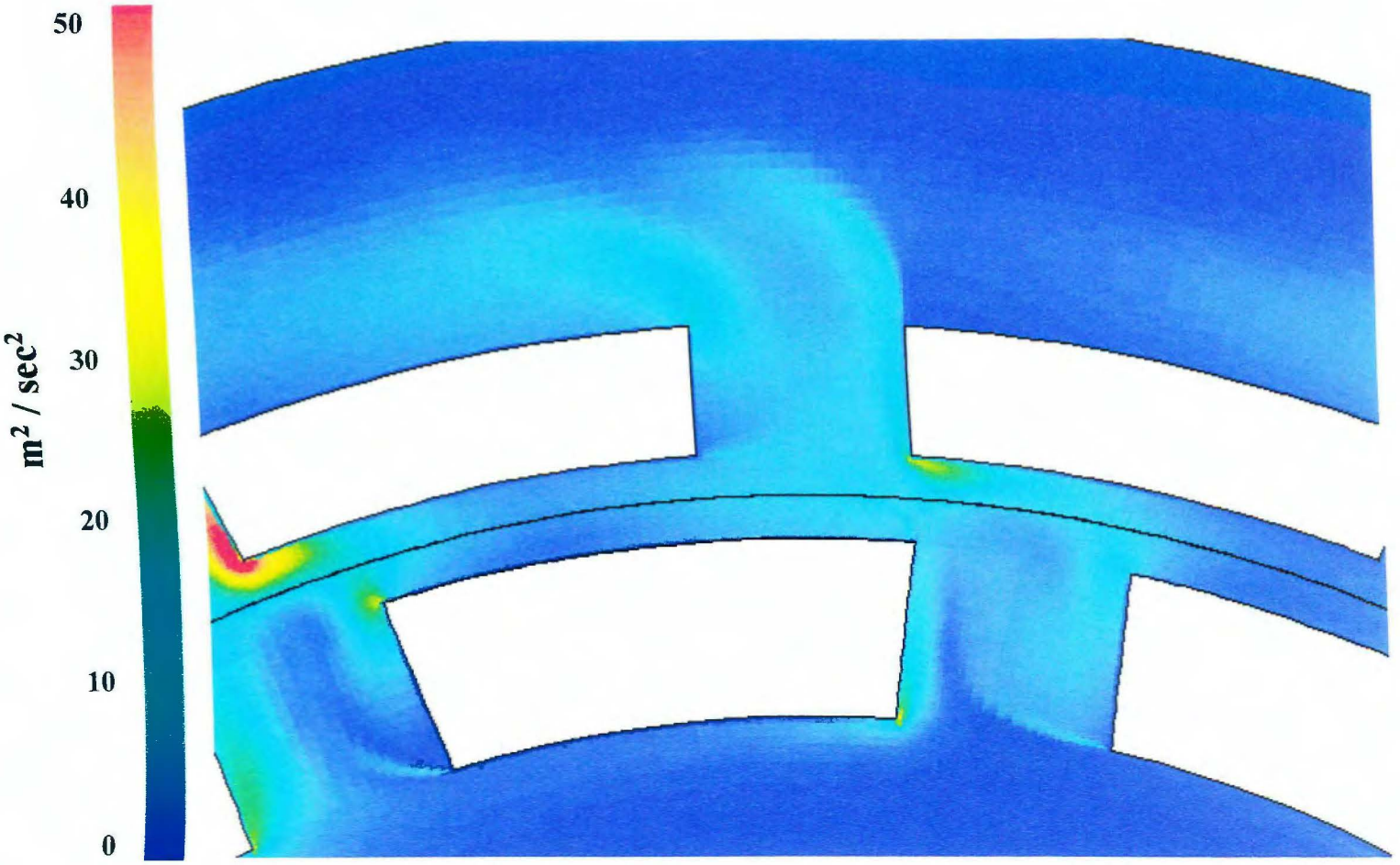

Figure 4-38. Angularly resolved turbulent kinetic energy near slot 1 at time step 9,252 (0.9282 seconds). Simulation 4.

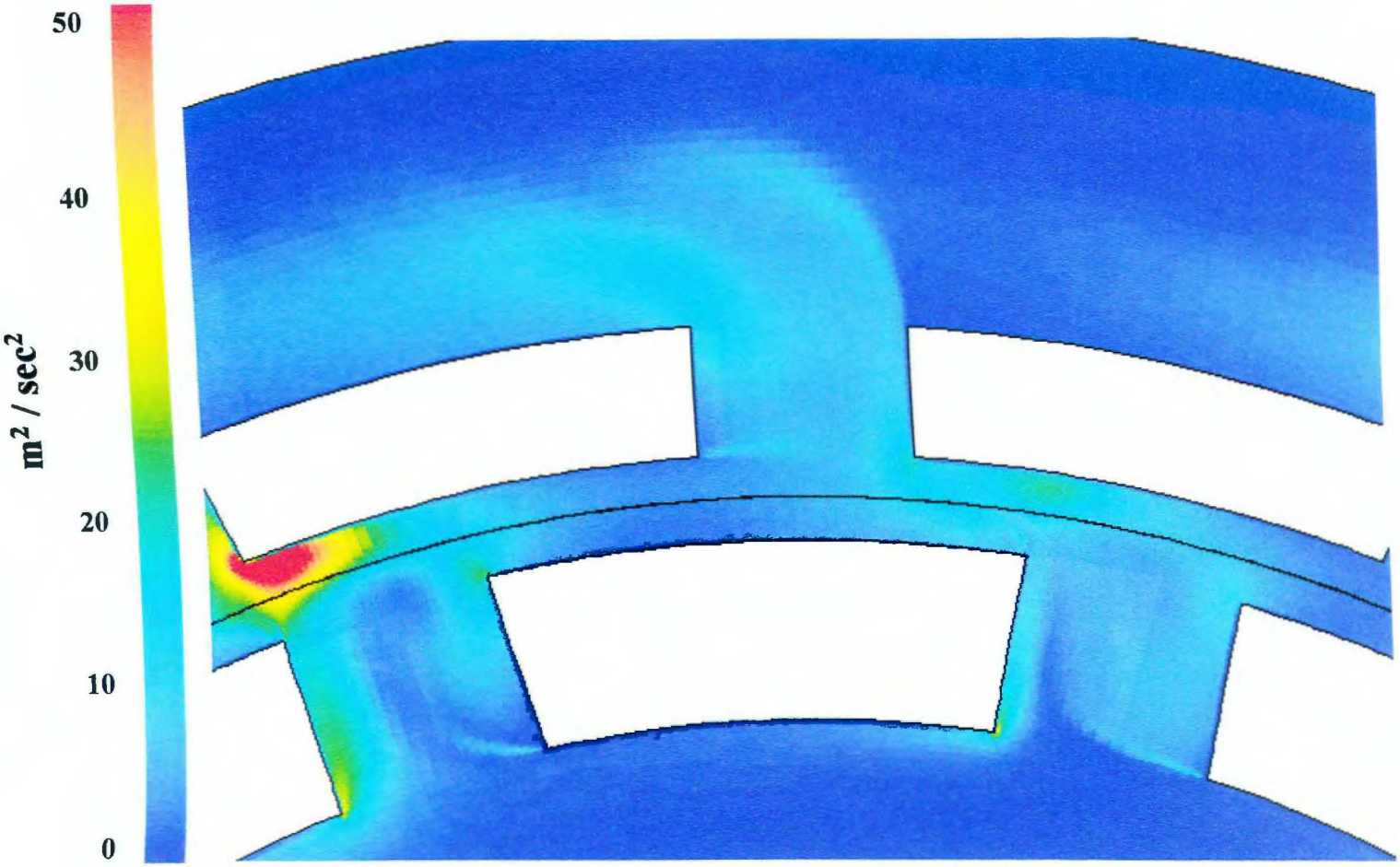

Figure 4-39. Angularly resolved turbulent kinetic energy near slot 1 at time step 9,256 (0.9286 seconds). Simulation 4.

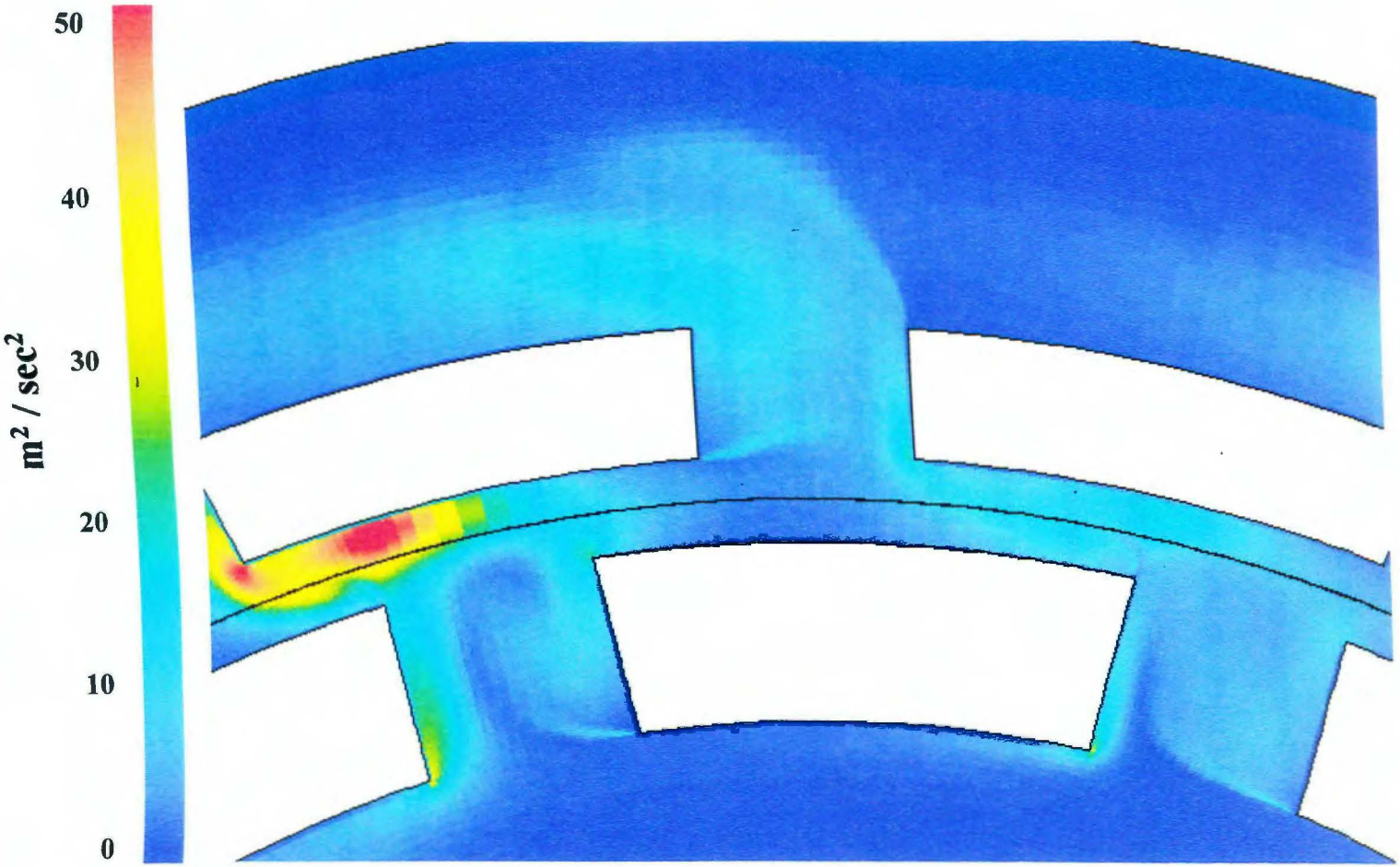

Figure 4-40. Angularly resolved turbulent kinetic energy near slot 1 at time step 9,260 (0.9290 seconds). Simulation 4.

time and location that fluid leaves the rotor slot radially and impinges upon the stator tooth. Four time steps later, the region of high turbulent kinetic energy has followed the lagging edge of the rotor slot, but it has decreased substantially in size (Fig. 4-35). When the rotor and stator slots are aligned (Fig. 4-36), the tangentially moving region has decreased to about 25 m^2 / sec^2 and extends well into stator slot 1 from the lower right corner of stator tooth 14. After an additional 4.3° of rotation (slot now half closed), the turbulent region has decreased in magnitude so that it is essentially indistinguishable from the background turbulence in slot 1 (Fig. 4-37).

While the turbulent region travels along the gap toward the left side of slot 1, a second area of even higher turbulence first appears on the right lower corner of tooth 1 when a rotor-slot is half aligned with stator-slot 1 (Fig. 4-35). This region grows in size and magnitude as the slots become more aligned, reaches a maximum of about 50 m^2/sec^2 when the rotor slot has moved 4.3° past complete alignment (Fig. 4-37), and then begins to decrease. During the time of increase, this turbulent region extends further up slot 1 toward the volute region, but its maximum appears to remain on the lower corner of stator tooth 1.

The highly turbulent region on the corner of tooth 1 correlates with impaction of the jet that follows each rotor slot throughout a period of simulation. Indeed its rise and fall in magnitude correlates well with mass flow rate out the right side of stator slot 1 (compare with Fig. 4-14). Further, it is clear that this turbulent region also correlates with the appearance of the high-pressure area on the corner of tooth 1 (section 4.4). As is the case with the two high-pressure regions in the gap, the high turbulence region at the corner of tooth 1 passes around the corner of the tooth (Fig. 4-

38) while undergoing a decrease in magnitude. At this point, it may be considered to be the region of turbulence which will follow the lagging edge of the adjacent rotor slot and increase in magnitude and size until it reaches the center of tooth 1 at which point it will begin to decrease until it finally disappears at slot 2.

The time dependent turbulent energy dissipation rate, ε, has a qualitative distribution very similar to the turbulent kinetic energy (Figs. 4-41 through 4-47). Regions of high energy dissipation exist in exactly the same locations as those of high turbulent kinetic energy. The maximum magnitude of region 1 for ε is approximately 80,000 m^2 / sec^3 and when the leading edge of a rotor slot is aligned with the left edge of stator slot 1 (Fig. 4-41). As the rotor continues its passage, the high energy dissipation region decreases in a manner similar to the TKE. Right before a rotor-slot moves into partial alignment with stator-slot 1 (Fig. 4-41), a thin wisp like region of very high energy dissipation is present at the corner of stator tooth 14 and extends tangentially about one quarter of the distance across slot 1. This wisp is present in the TKE field, although it is less distinguishable from the background slot turbulence. In the case of the energy dissipation rate, the wisp at the tooth corner is about 1.5 times the magnitude of the region approaching the slot, whereas in the case of the turbulent kinetic energy, the wisp has a magnitude equal to or less than the approaching high TKE region. Further, in the case of ε, the wisp increases in magnitude and stretches to a maximum distance of one-half the slot width as a rotor-slot moves into complete alignment with stator-slot 1 (Figs. 4-41 through 4-43). In the case of the turbulent kinetic energy, the wisp extends much less of the way into stator-slot 1 and it appears

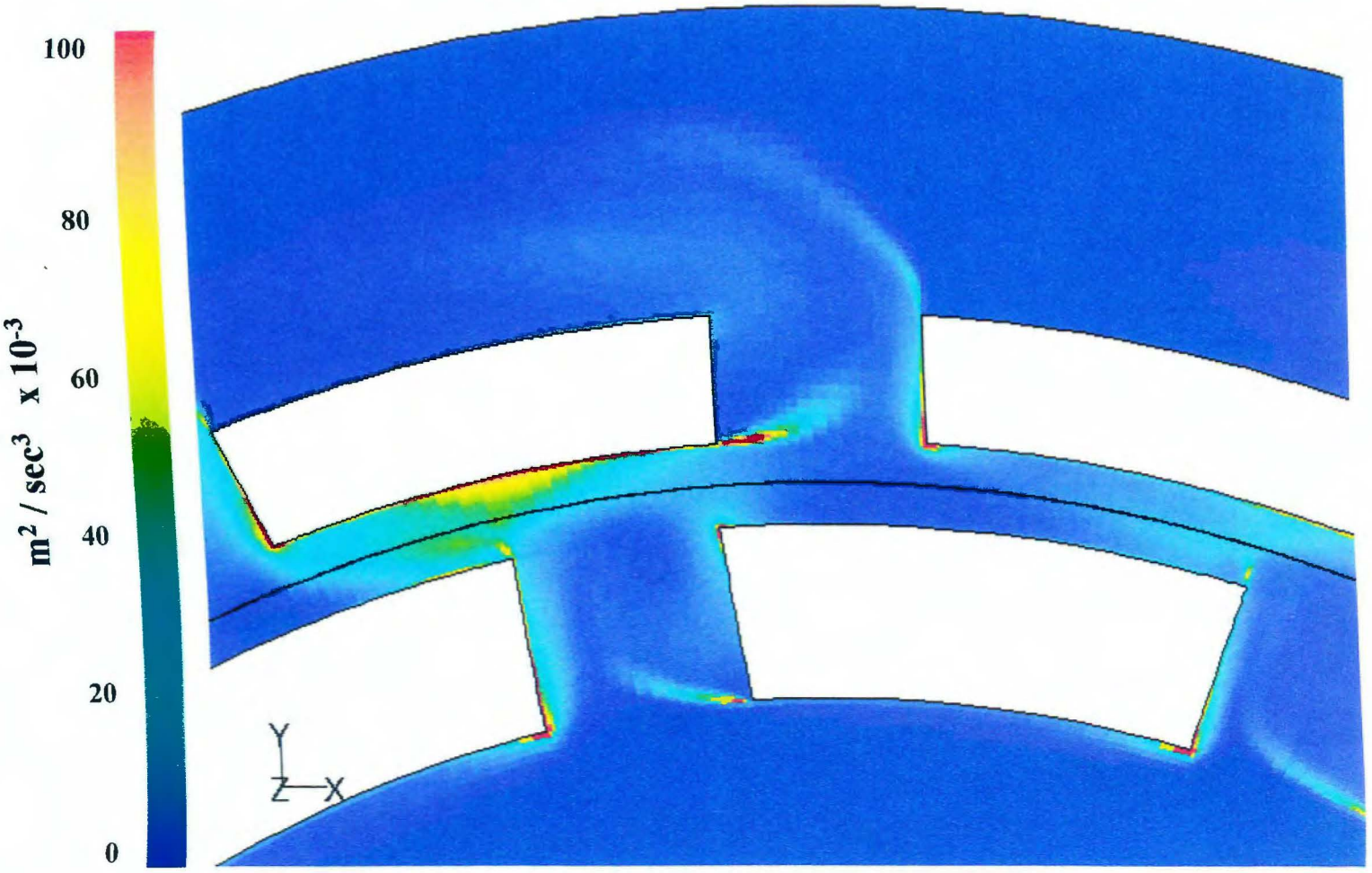

Figure 4-41. Angularly resolved turbulent kinetic energy dissipation rate near slot 1 at time step 9,236 (0.9266 seconds). Simulation 4.

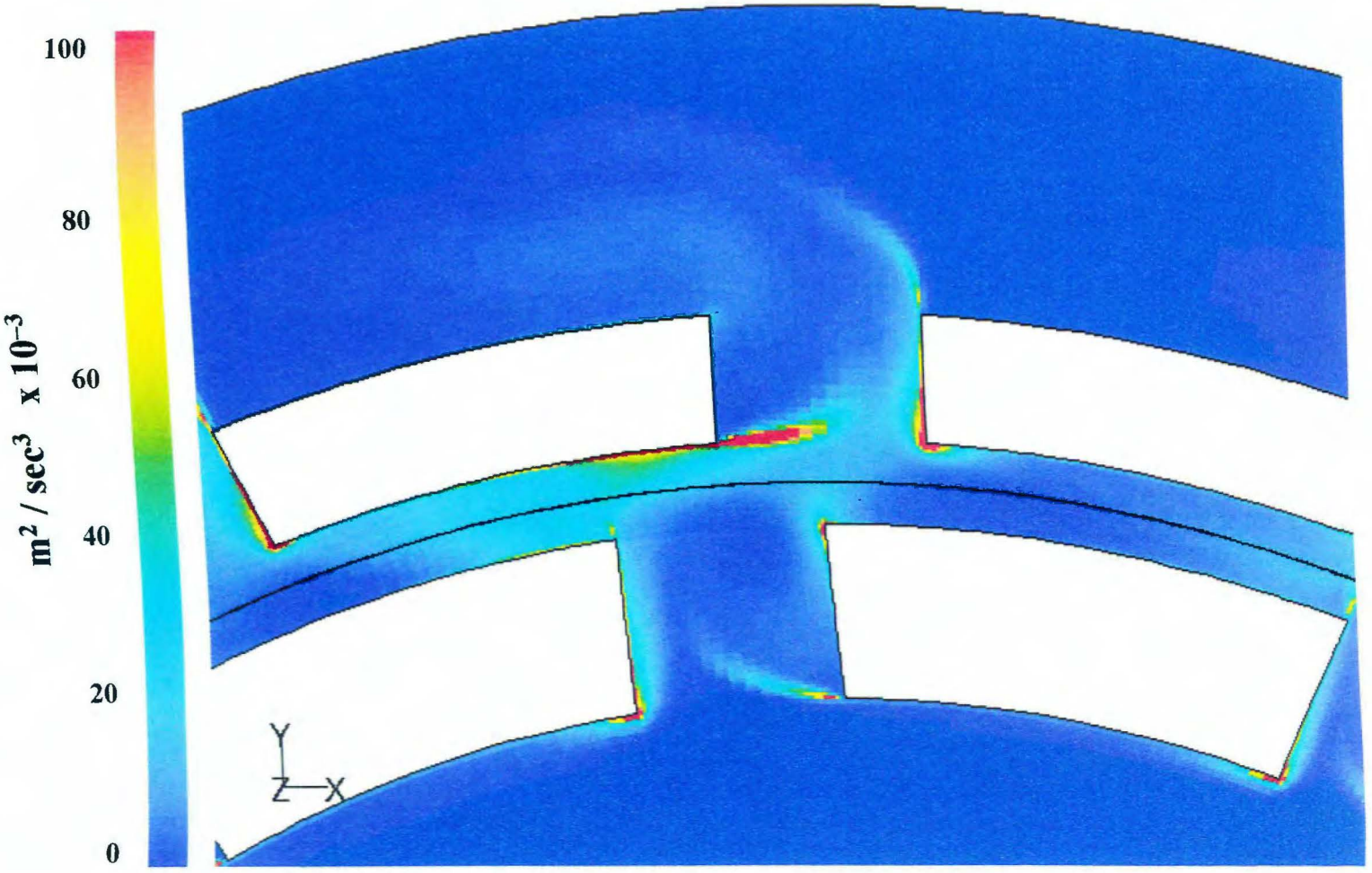

Figure 4-42. Angularly resolved turbulent kinetic energy dissipation rate near slot 1 at time step 9,240 (0.9270 seconds). Simulation 4.

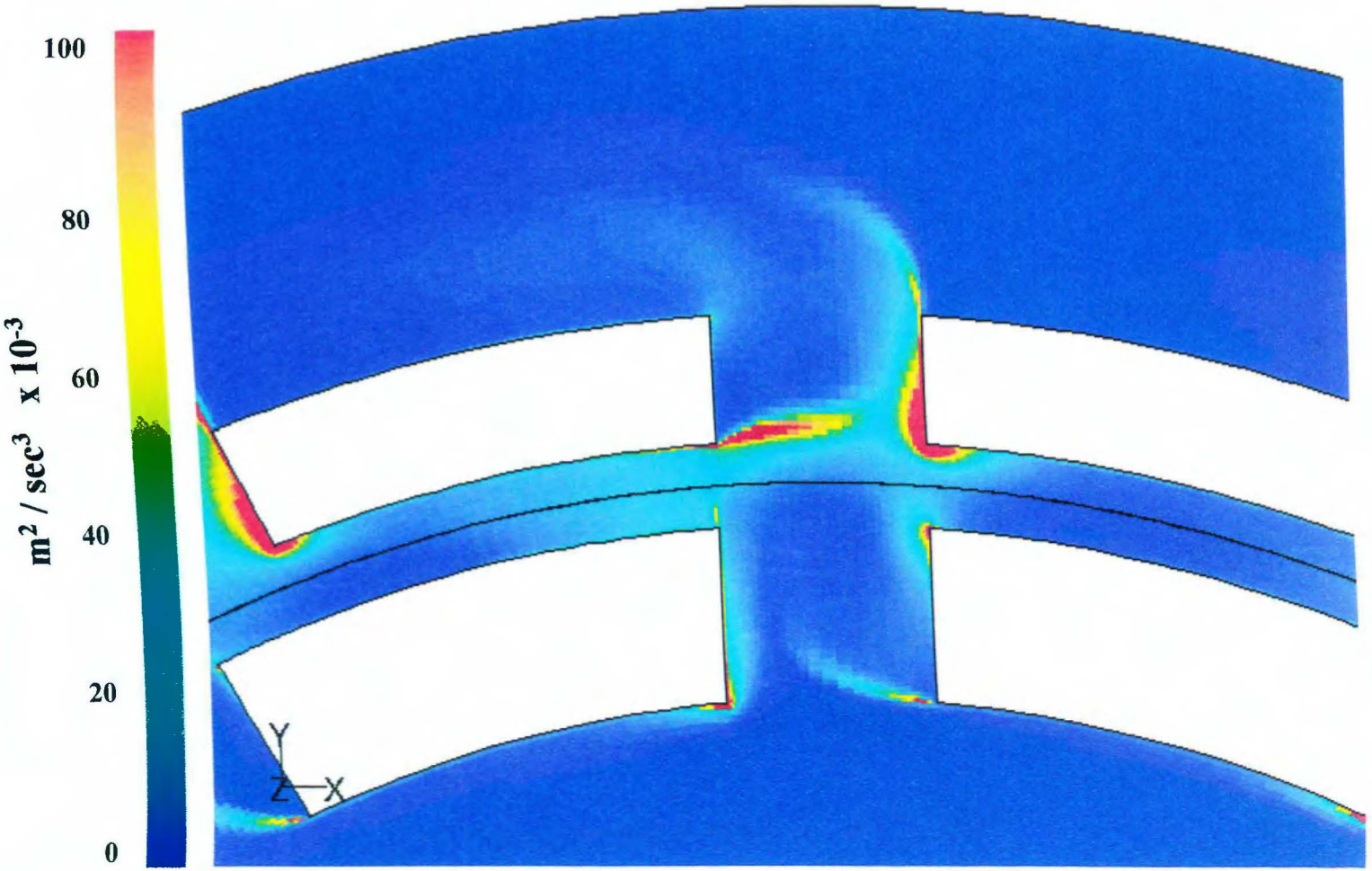

Figure 4-43. Angularly resolved turbulent kinetic energy dissipation rate near slot 1 at time step 9,244 (0.9274 seconds). Simulation 4.

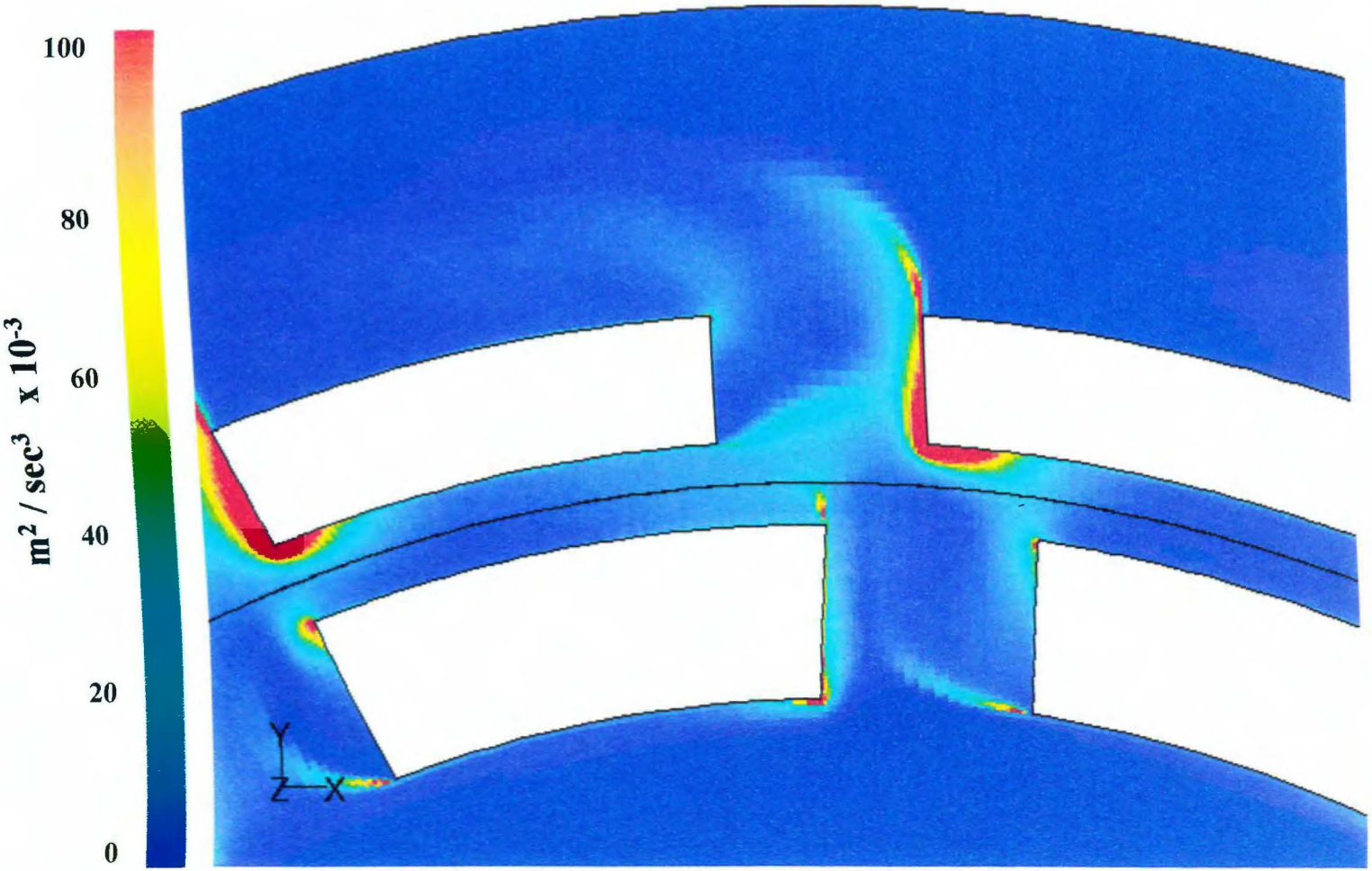

Figure 4-44. Angularly resolved turbulent kinetic energy dissipation rate near slot 1 at time step 9,248 (0.9278 seconds). Simulation 4.

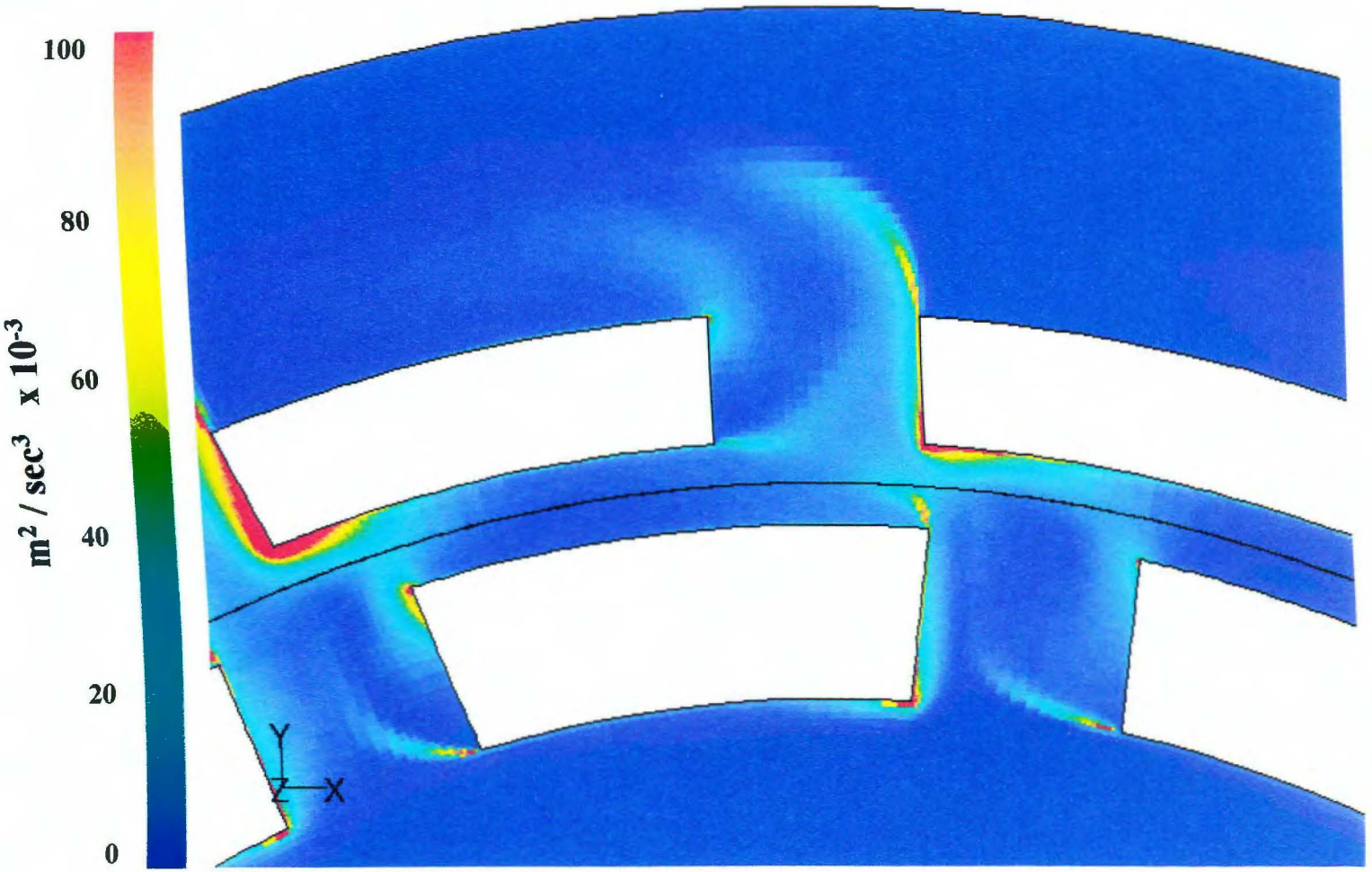

Figure 4-45. Angularly resolved turbulent kinetic energy dissipation rate near slot 1 at time step 9,252 (0.9282 seconds). Simulation 4.

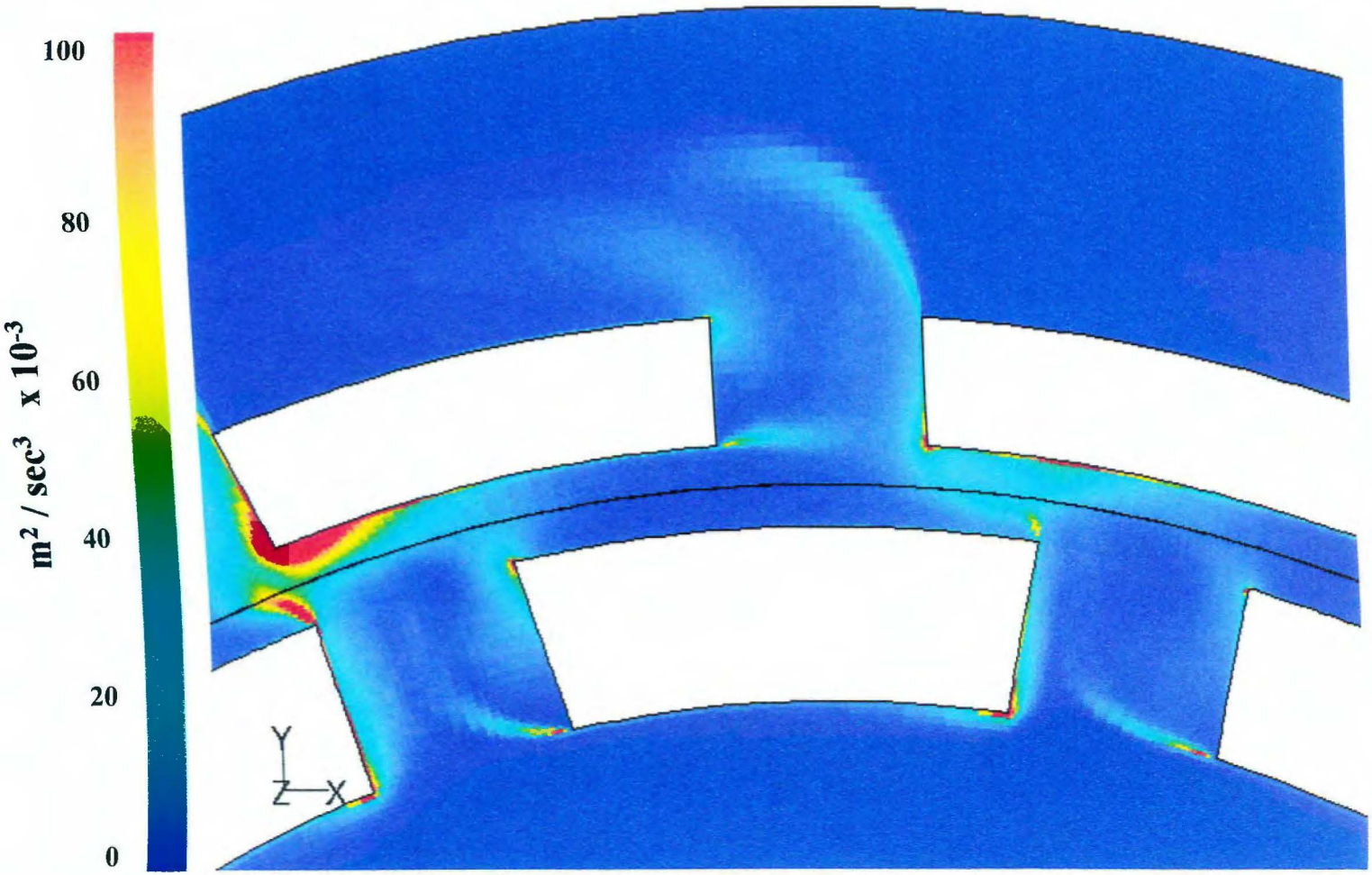

Figure 4-46. Angularly resolved turbulent kinetic energy dissipation rate near slot 1 at time step 9,256 (0.9286 seconds). Simulation 4.

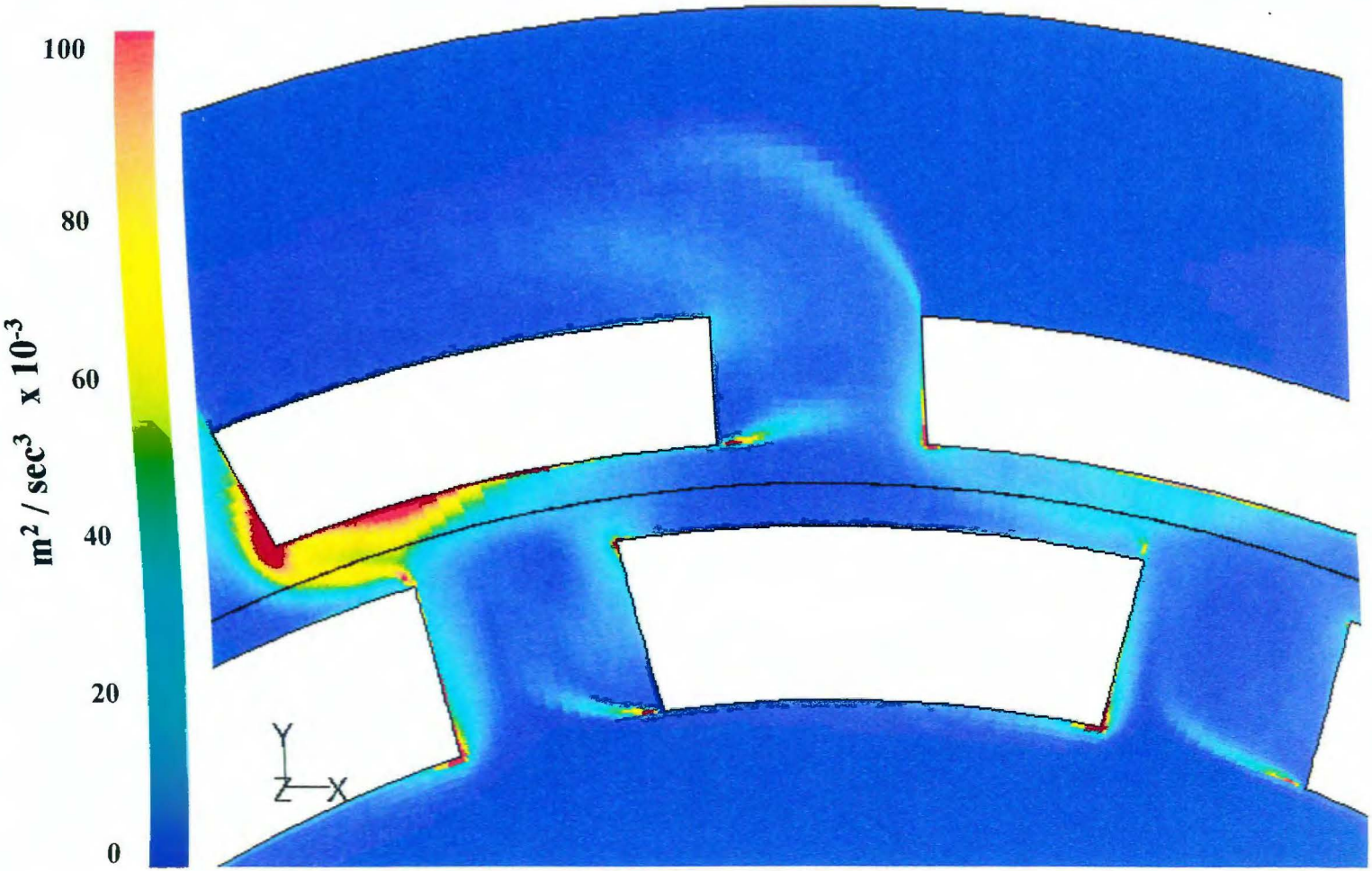

Figure 4-47. Angularly resolved turbulent kinetic energy dissipation rate near slot 1 at time step 9,260 (0.9290 seconds). Simulation 4.

to reach a maximum when the rotor-slot and stator-slot are only half aligned, and then decrease with further slot alignment.

As the wisp of turbulent dissipation appears on the left corner of tooth 14, the dissipation rate at the right lower corner of tooth 1 increases. In a manner similar to the turbulent kinetic energy, the energy dissipation rate at the right corner increases as the rotor-slot continues its passage by the stator slot. The area of high energy dissipation here appears to cover a larger area than the corresponding area of high turbulent kinetic energy. At one point, the high energy dissipation area extends from the lower corner of slot 1, all the way up its right side, and out into the volute while simultaneously extending around the corner along the wall of stator-tooth 1 and well into the gap region (Fig. 4-44).

The patterns of turbulence in the gap near all stator-slots is very similar, however, as with the velocity field, the absolute magnitudes vary considerably from slot to slot as would be expected since the "local" Reynolds numbers will vary around the domain. Figures 4-48 and 4-49 show the time dependent spatial average of either the turbulent kinetic energy or the turbulent energy dissipation rate on an imaginary line extending from the corner of each tooth halfway across the shear gap (see Fig. 4-1). This position was chosen for monitoring the time dependent behavior of turbulence around the domain because, from the above analysis, it is the region that appears to have the highest turbulent kinetic energies. The plots are normalized to either the nominal rotor tip kinetic energy of $\frac{1}{2}V^2_{tip}$ or the nominal gap viscous

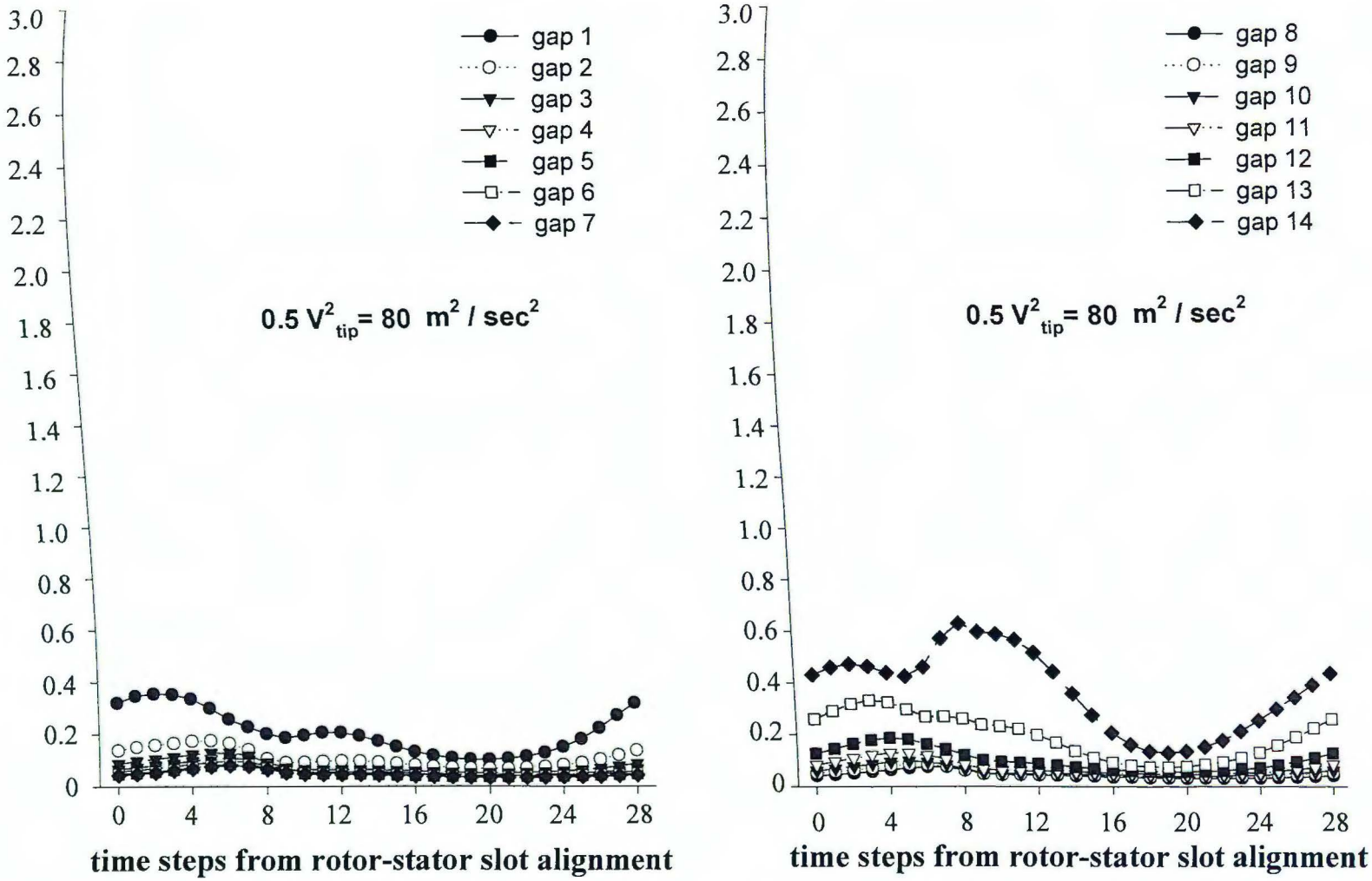

Figure 4-48. Time dependent turbulent kinetic energy (normalized to 0.5 V^2_{tip}), across lines spanning one-half the shear gap, as a function of slot alignment. Plots begin at approximately time step 9,236. Simulation 4.

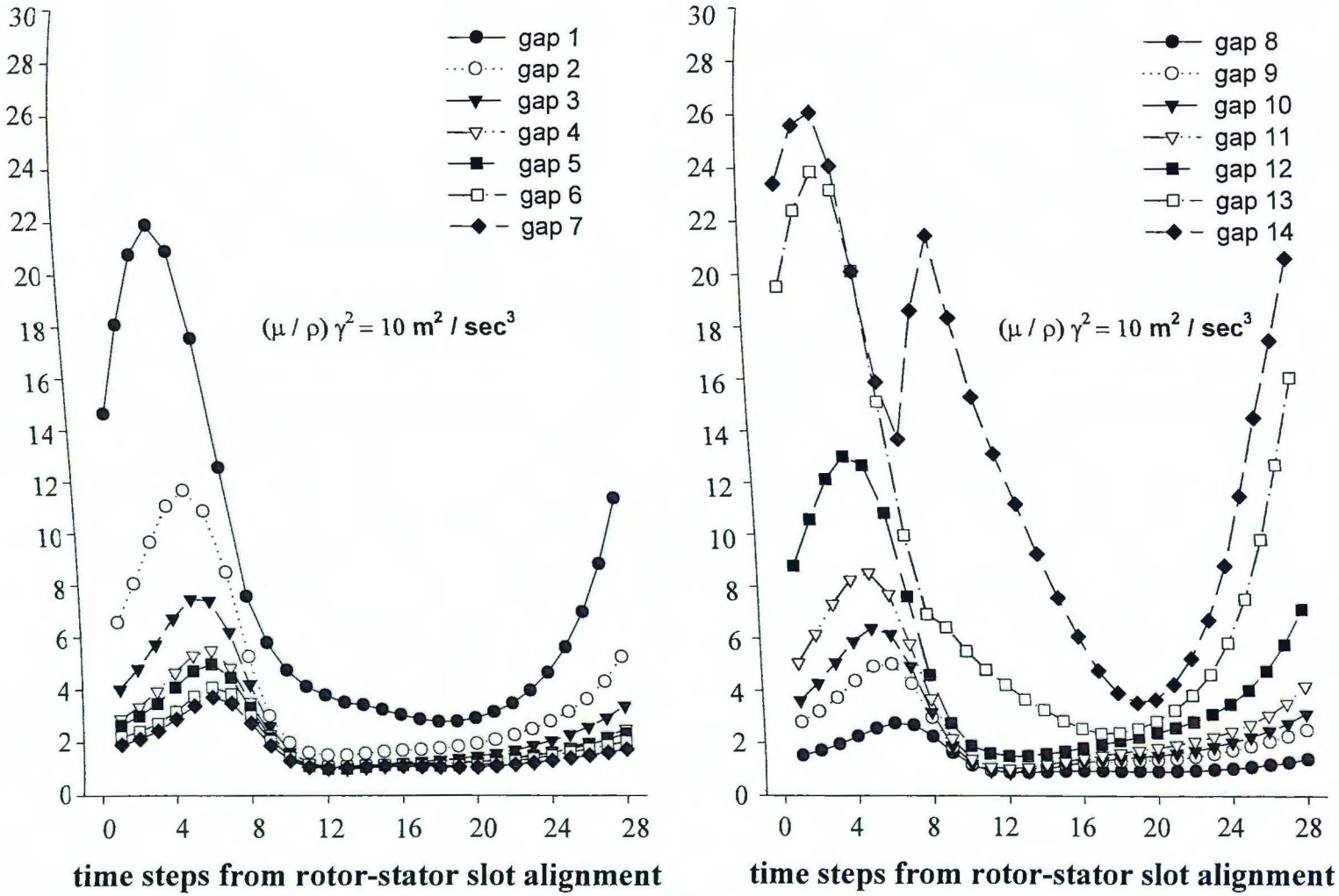

Figure 4-49. Time dependent turbulent energy dissipation rate (normalized to $(\mu/\rho)\,\gamma^2 / 10^3$), across lines spanning one-half the shear gap, as a function of slot alignment. Plots begin at approximately time step 9,236. Simulation 4.

dissipation rate of $\frac{\mu}{\rho}\dot{\gamma}^2$ where $\dot{\gamma}$ is the nominal gap shear rate previously defined. As expected, both the turbulent kinetic energy and its dissipation are highest on the line immediately to the right of stator slot 14 (called 'gap 14' in Figs. 4-48 and 4-49) followed by the lines near slots 1 and 13. The energies and dissipation near the remaining slots crudely follows a similar pattern observed for mass flow rates: The closer the slot is to the outlet, the higher its turbulence. The region near slot 14 has an interesting feature that is qualitatively different from the time dependent turbulence observed near the other slots. Specifically, the turbulence near all slots except 14 is an absolute maximum after a rotor-slot has moved about 4.3° from complete alignment with the stator-slot. A local maximum in the case of slots 13 and 1, or an apparent inflection point in the turbulence for slots 2-12, is then reached approximately 8.6° later. The angular location of a rotor-slot at the absolute maximum turbulence correlates well with its position at maximum mass outflow from the slots (compare to Fig. 4-14). However, in the case of slot 14, the pattern seems to be reversed from that in slot 1. An absolute maximum in the turbulence is observed for slot 14 at the same rotor-slot stator-slot alignment where a local maximum is observed for slot 1. Further, the rotor-slot position corresponding to an absolute maximum in turbulence near slot 1 results in only a local maximum near slot 14. Analysis of the mass flow rates through stator slot 14 (Fig. 4-14) shows no qualitative difference between it and slot 1 and the reason for the difference in their predicted turbulence patterns is not clear.

4.5 Comparison of 30 rps, 45.4 gpm and 50 rps, 78.8 gpm Operating Conditions

Simulation 3 was performed at operating conditions of 50 rps and 78.8 gpm inlet volumetric flow rate on the same mesh as simulation 4. The time dependent (not shown) and fixed frame mass flow rates through each of the stator slots is nearly identical to those for 30 rps and 45.4 gpm operating conditions when normalized to the overall mass flow rate (Fig. 4-17b). Since the Gap number is approximately the same for both simulations (19.7 vs. 18.9) this result is not surprising.

The overall patterns of time dependent mean velocity, mean static pressure, and turbulence are all identical between the two simulations. As is the case with volute flow patterns, it is most succinct to compare results between the two simulations using fixed frame solution fields since no qualitative difference was observed between the two simulations upon initial examination. The fixed frame velocity field obtained for the two different operating conditions is shown in Fig. 4-50. The maximum velocity at 50 rps / 78.8 gpm is about 35 m/sec and the maximum at 30 rps / 45.4 gpm is about 20 m/sec. The fixed frame static pressure fields are also identical except for absolute magnitudes (Fig. 4-51). The maximum pressures obtained are about 8.9 and 3.1 bar for 50 rps / 78.8 gpm and 30 rps / 45.4 gpm respectively. The minimum fixed frame pressure is identical for the two simulations because it occurs directly adjacent to the outlet that is set to 0 for both simulations.

The maximum value obtained for the time averaged turbulent kinetic energy field is about 50 m^2/sec^2 for 30 rps / 45.4 gpm and 160 m^2/sec^2 for 50 rps / 78.8 gpm. Both maximums occur in the right corner of slot 14 (Fig. 4-52). The maximum turbulent energy dissipation rate also occurs in the right corner of slot 14 and is about

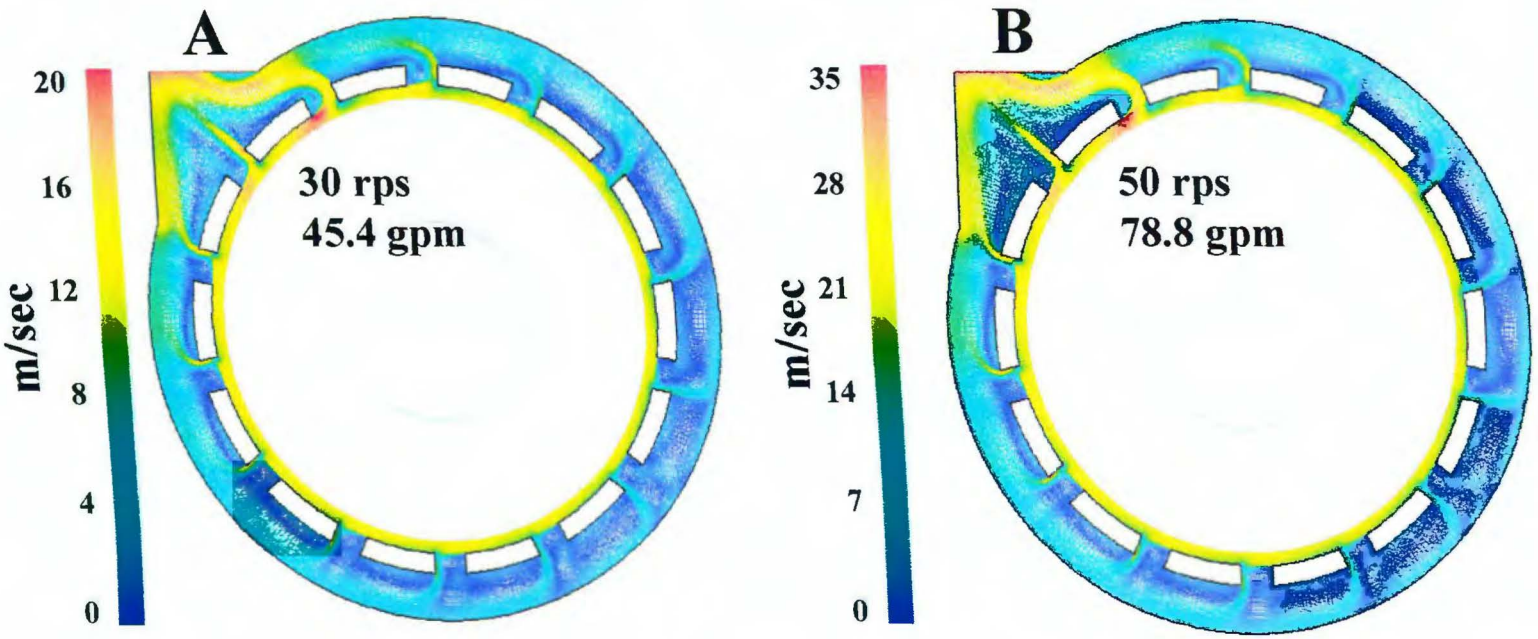

Figure 4-50. Fixed frame velocity field in the entire domain. Simulation 4 after 28 revolutions of simulation (**A**), and simulation 3 after 16.7 revolutions of simulation (**B**).

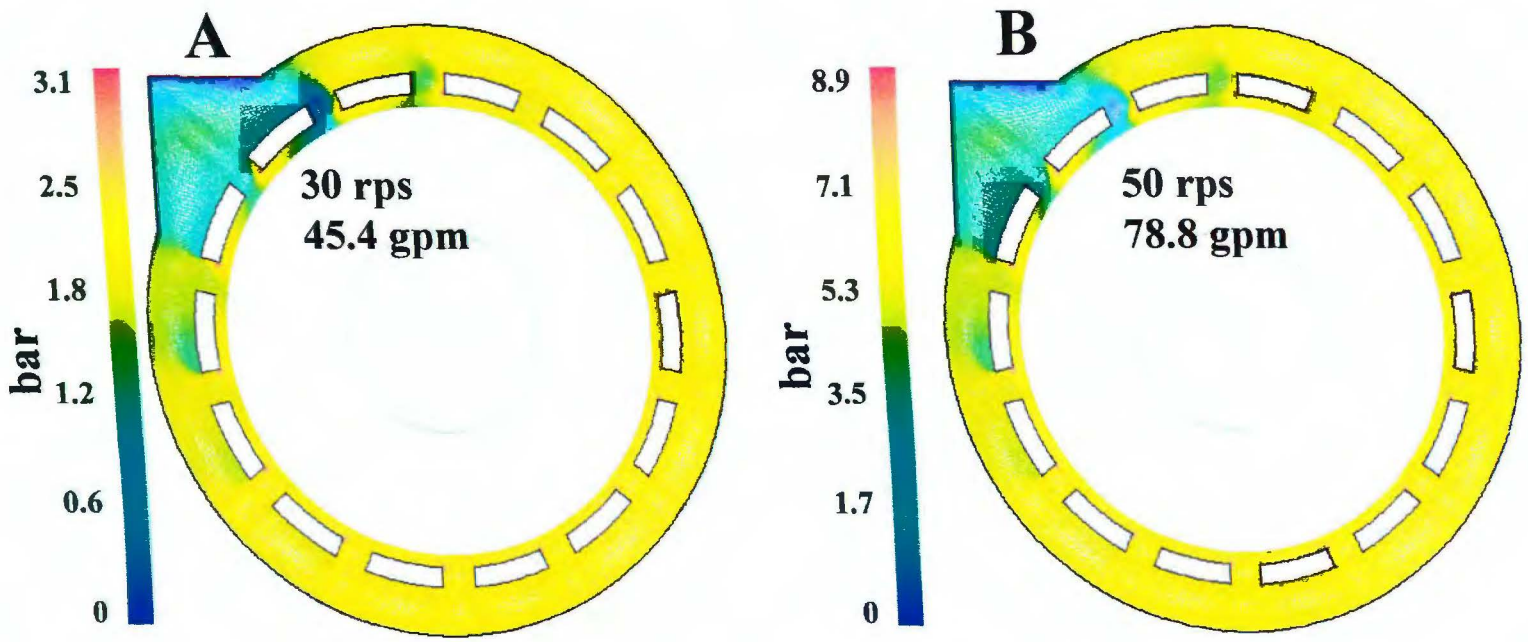

Figure 4-51. Fixed frame static pressure in the entire domain. Simulation 4 after 28 revolutions of simulation (**A**), and simulation 3 after 16.7 revolutions of simulation (**B**).

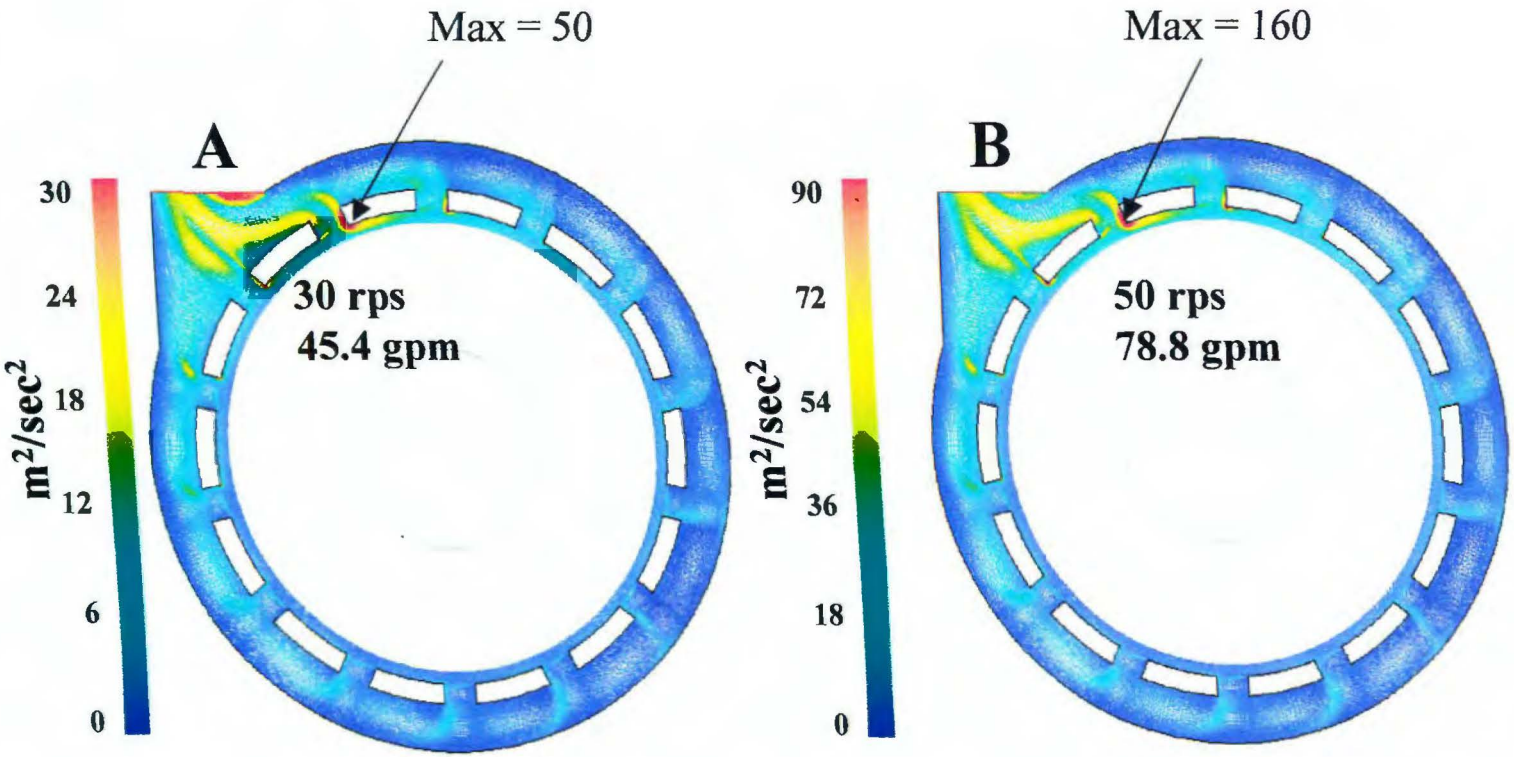

Figure 4-52. Time averaged TKE field in the entire domain. Simulation 4 after 28 revolutions of simulation (**A**), and simulation 3 after 16.7 revolutions of simulation (**B**).

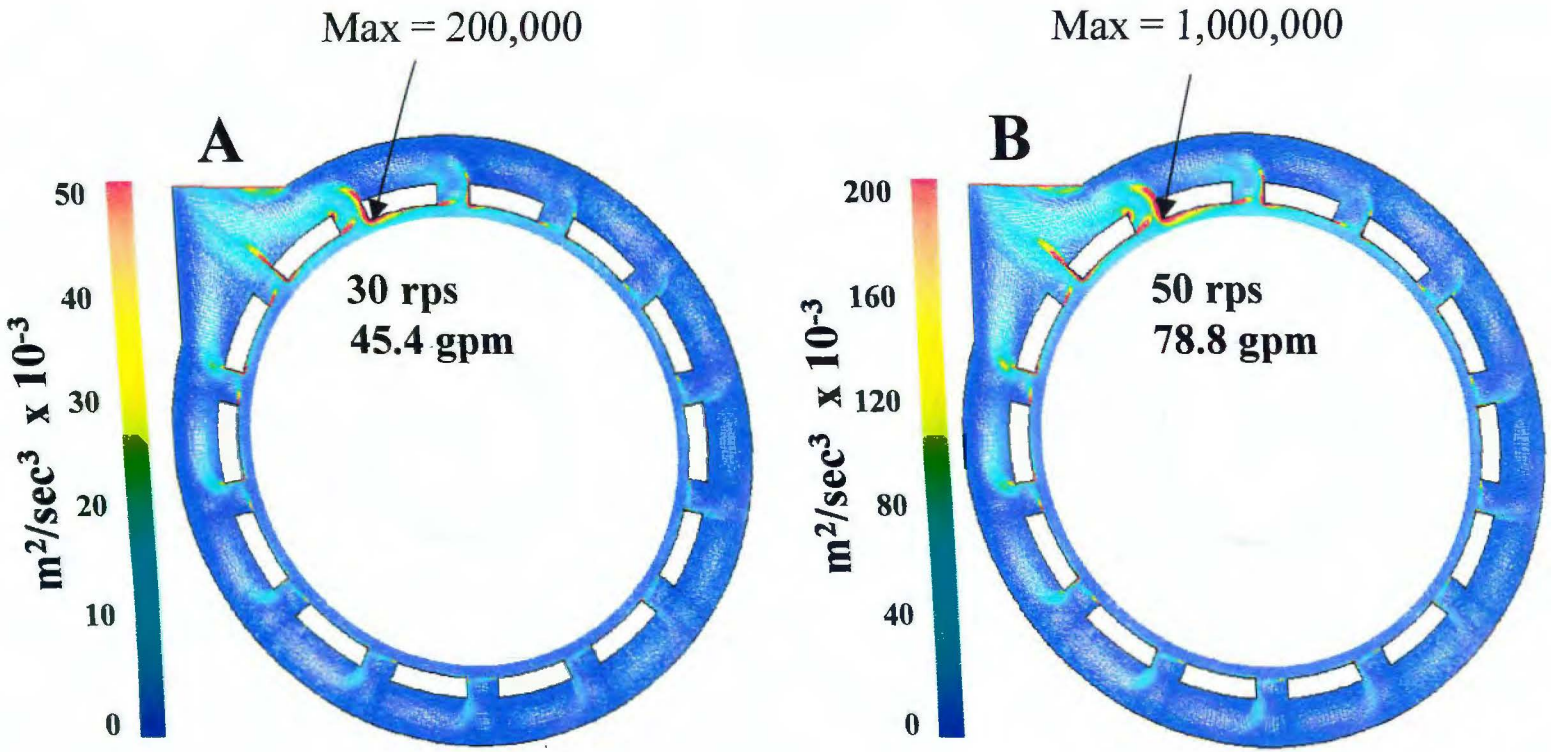

Figure 4-53. Time averaged turbulent dissipation rate in the entire domain. Simulation 4 after 28 revolutions of simulation (**A**), and simulation 3 after 16.7 revolutions of simulation (**B**).

200,000 and 1,000,000 m^2/sec^3 for the two simulations (Fig. 4-53). In general, the time averaged turbulent kinetic energy and its dissipation is higher near the leading edge of a stator tooth (where impaction of the turbulent jet occurs) rather than near the lagging edge of the adjacent tooth.

The tangential mean velocity profile across the gap for 50 rps / 78.8 gpm is shown in Fig. 4-15b. The profile is almost exactly the same as for 30 rps / 45.4 gpm when plotted as a reduced velocity: The flow in the gap is plug except for a very thin boundary layer near the stator wall. The average shear outside of the boundary layer (i.e. ignoring the 2 points nearest the stator wall in Fig. 4-15b) is 1320 sec^{-1} which is approximately 1.6 times that computed for simulation 4: 850 sec^{-1}. Since there is no change in the reduced velocity profile across the gap it is logical that the average shear outside the rotor boundary layer scale linearly with the overall mass flow rate:

$$\frac{78.8 \text{ gpm}}{45.4 \text{ gpm}} = 1.7 \approx 1.6 = \frac{1320 \text{ sec}^{-1}}{850 \text{ sec}^{-1}}$$

Perhaps if Ga of the simulations had been substantially different a much different reduced velocity profile and average gap shear outside of the boundary layer would have resulted at 78.8 gpm. The values of y+ near the rotor and stator tooth 1 are similar for the two simulations (Fig. 4-16), and the same caveats covered in section 4.2 apply.

4.6 Effect of Outlet Boundary Conditions: Constant Pressure Versus Outflow

Simulations 1 and 2 were both run at operating conditions of 50 rps / 78.8 gpm on coarse meshes of approximately 73,000 cells. However, the outlet for simulation 2

was extended an additional 0.25 m and set to an outflow boundary condition while simulation 1 had an outlet set to a constant pressure and cut off immediately adjacent to the volute (see Table 2-1). Direct visual comparison of the time dependant mean velocity, mean pressure, and turbulence fields did not reveal any difference between the two solutions, even in the region of the volute immediately adjacent to the outlet. Comparison of the fixed frame mass flow rates from the stator slots also did not show any difference (result not shown).

Since the magnitudes present in the different solution fields can span a wide range it is nearly impossible to know exactly how different the two simulations are using direct visual comparison. For this reason, percent difference plots for each of the fixed frame or time averaged fields between the two simulations were made (except for the mean static pressure), similar to those found in section 4.1 for the analysis of the approach to a periodic steady state.

The numerical treatment of an outflow boundary condition results in a mean pressure offset throughout the computational domain that is reset at each time step. Thus, the mean pressures between simulations 1 and 2 cannot be directly compared. In fact, the *time dependent* mean pressure results in simulation 2 are mathematically incorrect. The reason for this is that the 'true' mean pressure at the inlet is expected to change magnitude throughout a period of simulation (see Figs. 4-32 and 4-33). In the outflow boundary condition used, the mean static pressure of an (arbitrary) cell adjacent to the inlet is set to 0 gauge at the beginning of each time step so that any changes in pressure there are not captured. The lack of change in mean pressure at the inlet implies an incorrect pressure change (from time step to time step) anywhere in

the domain that 'sees' the inlet pressure field. Certainly it is reasonable to expect that the mean pressure field throughout the domain is dependent on the pressure at the inlet. The above argument, of course, does not imply that the solution obtained for simulation 2 for each *individual* time step is (mathematically) incorrect. The solution at each time step is in principle correct. To compare the pressure fields of simulation 1 and 2 all that would be needed is to determine an offset pressure to apply to the solution of one or the other solutions. The problem is that a different offset pressure will be needed for each time step. It is for this reason that a thorough analysis of the differences in the mean pressure field between simulation 1 and 2 was not attempted even though it is possible. Presently, it can be said that a superficial comparison of the mean pressure field for several time steps did not reveal any differences. In any event, the primary concerns of the simulations are mean velocities and turbulence, and their computation is not affected by relative offsets in mean static pressure.

Figure 4-54 is a percent difference plot of the fixed frame velocity magnitudes. The difference in mean velocity magnitudes is near zero throughout most of the domain. An exception to this is in each of the slots and the volute region where the fixed frame velocity field itself has a very small magnitude (see Fig. 4-50a). Also, near the outlet the difference in the two velocity fields is significant (up to 90 %) and is attributable to the different outlet boundary conditions rather than small mean velocity magnitudes.

Differences between the turbulent kinetic energy fields (Fig. 4-55a) are negligible almost everywhere except adjacent to the outlet. There are other regions, scattered evenly throughout the domain, where there is a moderate discrepancy

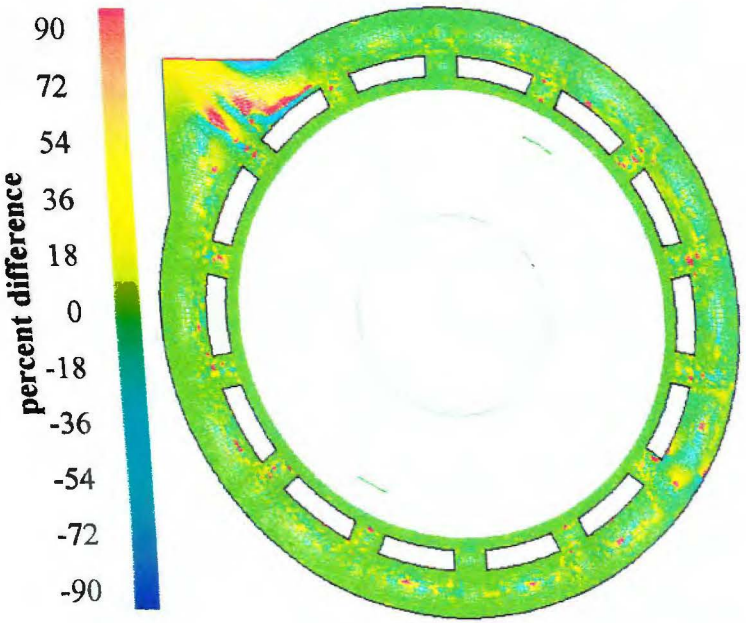

Figure 4-54. Percent difference between the fixed frame velocity magnitudes between simulation 1 (constant pressure outlet) and simulation 2 (extended outlet outflow). Simulation 1 after 17.9 revolutions and simulation 2 after 15.2 revolutions.

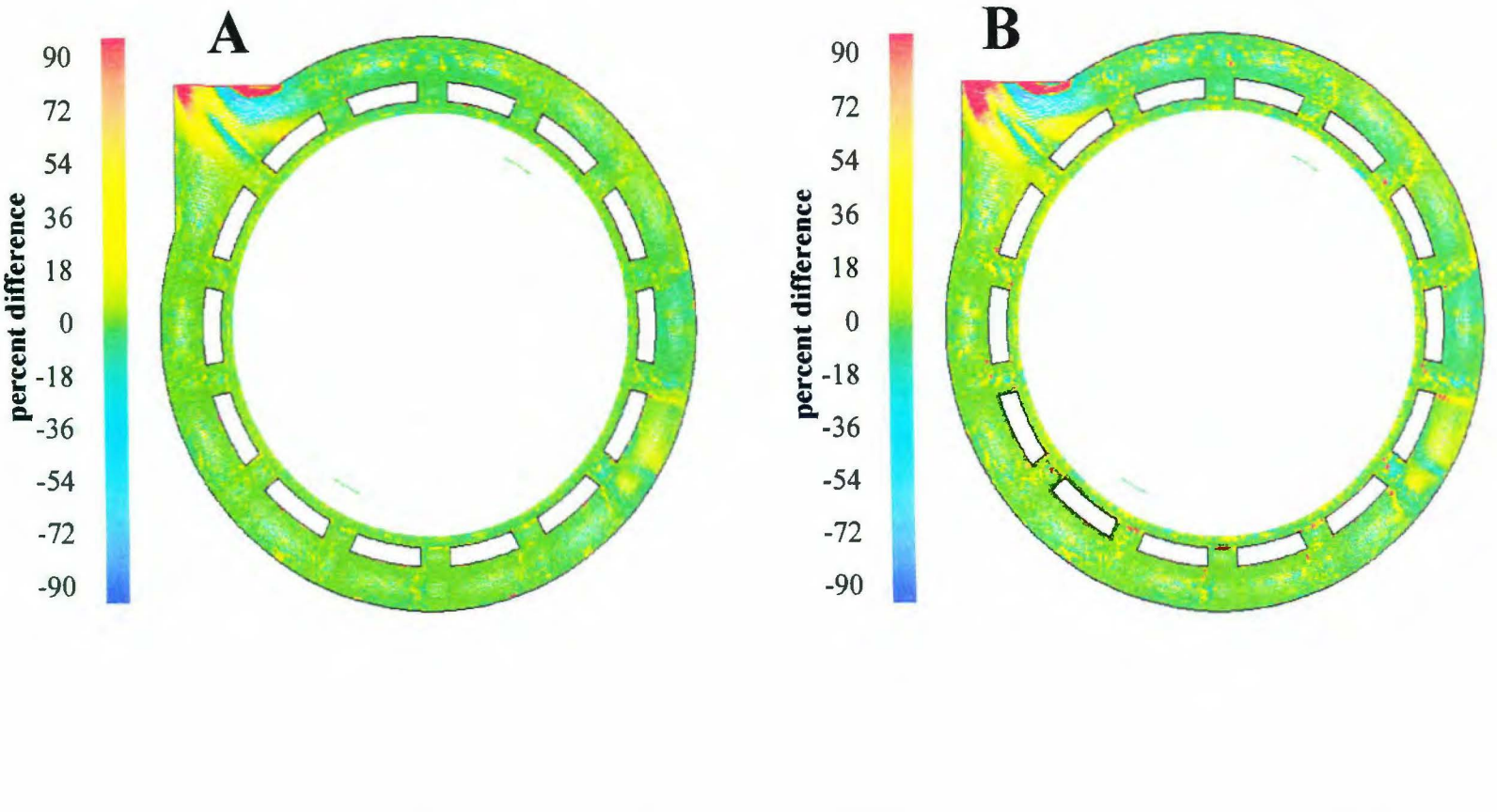

Figure 4-55. Percent difference between the time averaged TKE (**A**) and the turbulent dissipation rate (**B**) between simulation 1 (constant pressure outlet) and simulation 2 (extended outlet outflow). Simulation 1 after 17.9 revolutions and simulation 2 after 15.2 revolutions.

between the two simulations: This may be due to errors introduced during the averaging process. Differences in the turbulent energy dissipation rate are also most pronounced near the outlet (Fig. 4-55b). As with the turbulent kinetic energy, there are some very small regions of discrepancy in the computed energy dissipation rates (from 25 – 100 %) scattered more or less evenly throughout the domain. Often these regions occur where the simulated dissipation is small, but in some of these areas, like the boundary between stator-slots and the shear gap or extending from the leading edge of a stator tooth into the volute, the dissipation rate has a moderately large value (see Fig. 4-53b).

It appears that the major effect of cutting the outlet off at the volute is to overestimate the turbulent kinetic energy and its dissipation rate, and the mean velocity near the outlet when compared to the outflow boundary condition solution. There are, however, some regions near the outlet where the opposite holds true. Of the field variables, the turbulent dissipation rate seems to be most sensitive to changes in the outlet boundary condition.

4.7 Grid Independence of Simulations

Simulations 1 and 3 were run on meshes of 73.6 and 125 thousand elements respectively with pressure outlet boundary conditions, an inlet volumetric flow rate of 78.8 gpm, and a rotor speed of 50 rps. The primary difference between the two meshes is the element quality in the gap region. There are 30 elements spanning the gap in the 125 K mesh and 26 elements in the 73 K mesh. More importantly, the aspect ratios of the gap elements in the 125 K mesh are much less on average than

those in the 73 K mesh which was achieved by increasing the number of elements spanning the stator slot from 18 to 33. The 125 K mesh is also more dense near the slot and volute walls (Fig. 1-8).

Both the time dependent and fixed frame stator slot mass flow rates are identical for both simulations (result not shown). Figures 4-56a and b are percent difference plots of the fixed frame mean velocity magnitudes and static pressures. Figure 4-56a shows that the mean velocity fields for the simulations are identical. Regions of large discrepancy in Fig. 4-56a are areas where there is recirculation / stagnation of the fluid and the mean velocities are very small. There is essentially no difference in the fixed frame static pressure fields except close to the outlet and in stator slot 14. The reason for this is not clear, especially in stator slot 14 which is meshed the same as other stator slots in the two simulations.

The turbulence field differences (Figs. 4-57a and b) are most sensitive to changes in the mesh. For the most part, they are the same between the two simulations, however there are significant differences extending from the leading edge of some of the stator teeth (i.e. stator tooth 2) into the volute region. One possible reason for this is due to the use of the wall functions. The wall functions are valid at $y+ \sim 30\text{-}600$. On the right wall of the stator slots, y+ reaches a value of up to 150 whereas on the wall that forms a 90° angle with this edge, the value of y+ is only about 5. This is because most mass outflow from the stator occurs adjacent to the slot wall, while the other wall, which bounds the volute, is a region of very stagnated, recirculatory flow that may even be laminar. The very different flow regimes in cells

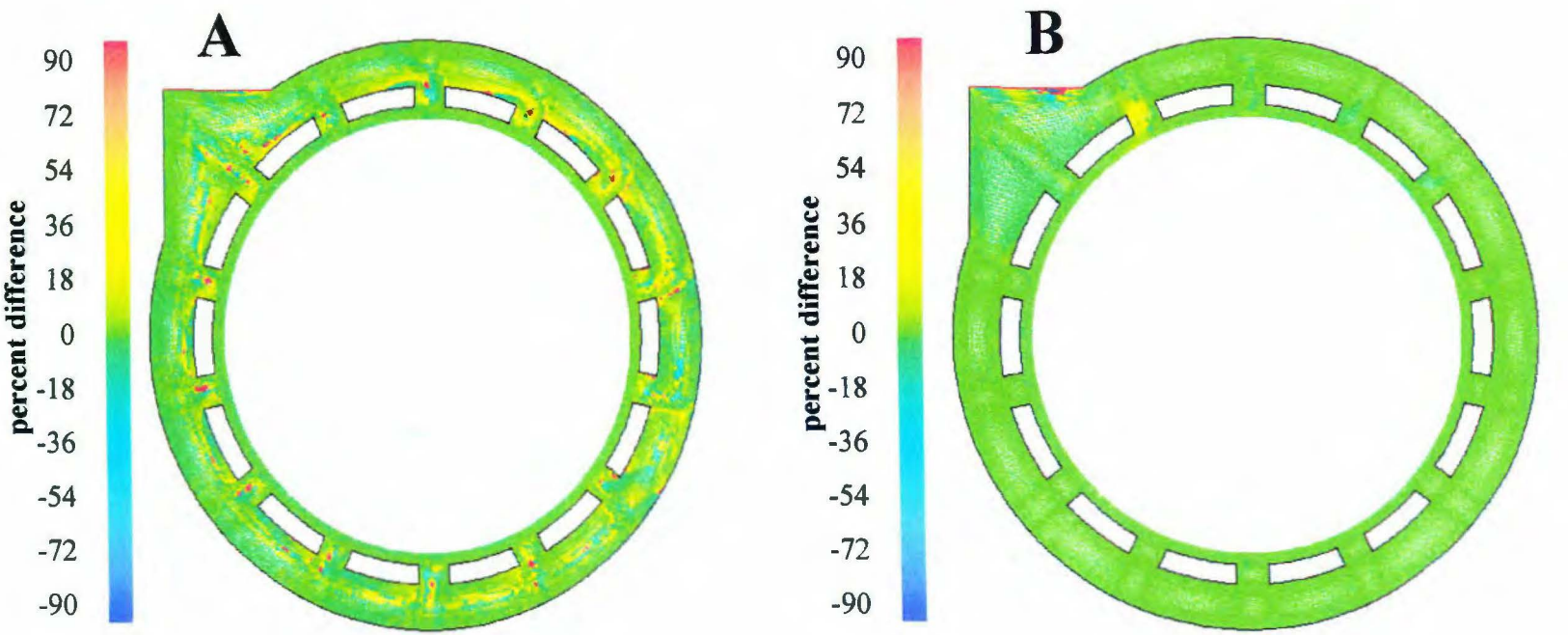

Figure 4-56. Percent difference between the fixed frame velocity magnitudes (**A**), and static pressures (**B**) between simulation 1 (73.6 K element mesh) and simulation 3 (125 K element mesh). Simulation 1 after 17.9 revolutions and simulation 3 after 16.7 revolutions.

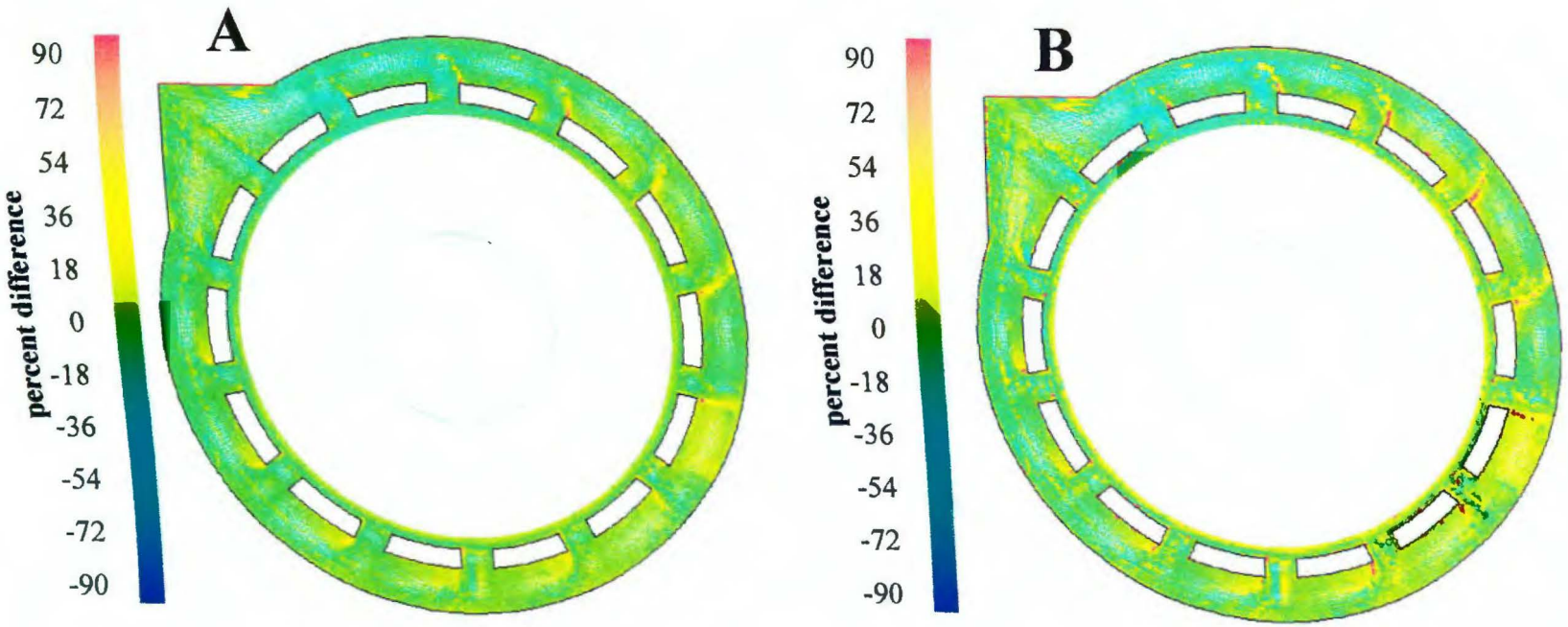

Figure 4-57. Percent difference between the time averaged TKE(**A**), and turbulent dissipation rate (**B**) between simulation 1 (73.6 K element mesh) and simulation 3 (125 K element mesh). Simulation 1 after 17.9 revolutions and simulation 3 after 16.7 revolutions.

bounding stator slot corners may be too much for the wall functions to handle properly.

Chapter 5 Standard Gap Results with Comparison to the Wide Gap Model

This chapter contains results from simulation 5, which is the standard gap model run with an outflow outlet boundary condition and operating conditions of 30 rps and 45.4 gpm (Table 2-1). Standard gap results are also compared with the wide gap model, simulation 4. Recall that both of these simulations were run at the same rotor speed and inlet mass flow rate.

Analysis and comparison of the time dependent mean velocity field for simulation 5 in the gap region near stator slot 1 as a rotor tooth sweeps out one period is found in sections 5.1.1 through 5.1.6. These results are illustrated graphically by the series of Figs. 5-1 through 5-21. The series is broken into sets of three (for instance Figs. 5-1 through 5-3) which each correspond to the same rotor position relative to stator slot 1. The next set of three (Figs. 5-4 through 5-6) illustrate the same location 4 time steps later (4.3° of rotor rotation) and so forth. It is necessary to break the presentation in this manner in order to blow up the region enough to see details of the mean velocity field in the very small shear gap. Each set of three figures corresponds to the same rotor positions for Figs. 4-7 through 4-13, respectively, presented for the wide gap model. The first figure in each set is the region directly under stator slot 1. The second figure is directly to the left of slot 1. The third figure covers the shear gap region directly to the right of stator slot 14. Since there are a total of seven rotor positions presented in the mean velocity field sequence of figures, each figure is

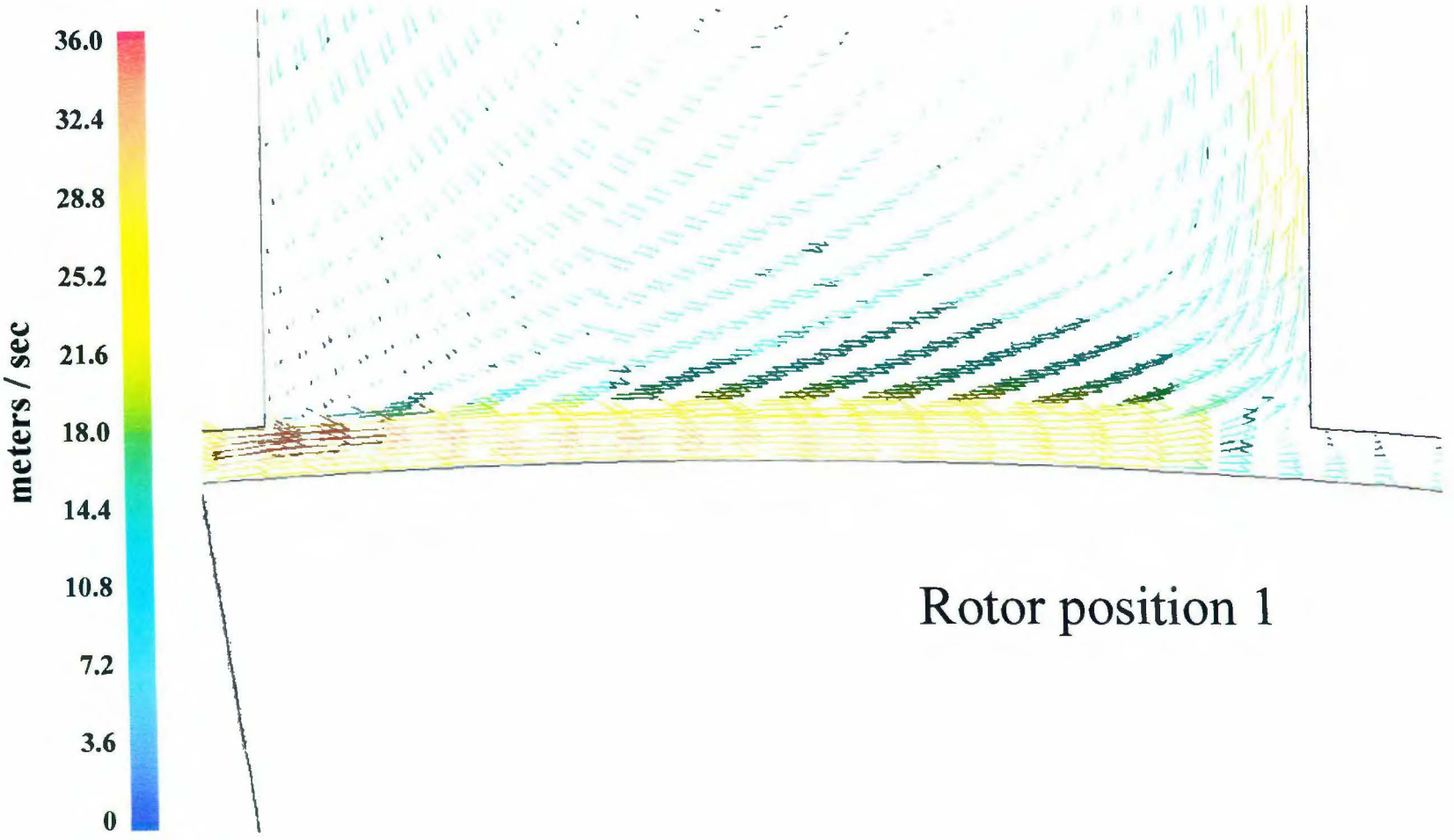

Figure 5-1. Angularly resolved mean velocity vectors in the gap under stator slot 1 at time step 6.412 (0.6432 seconds). Simulation 5

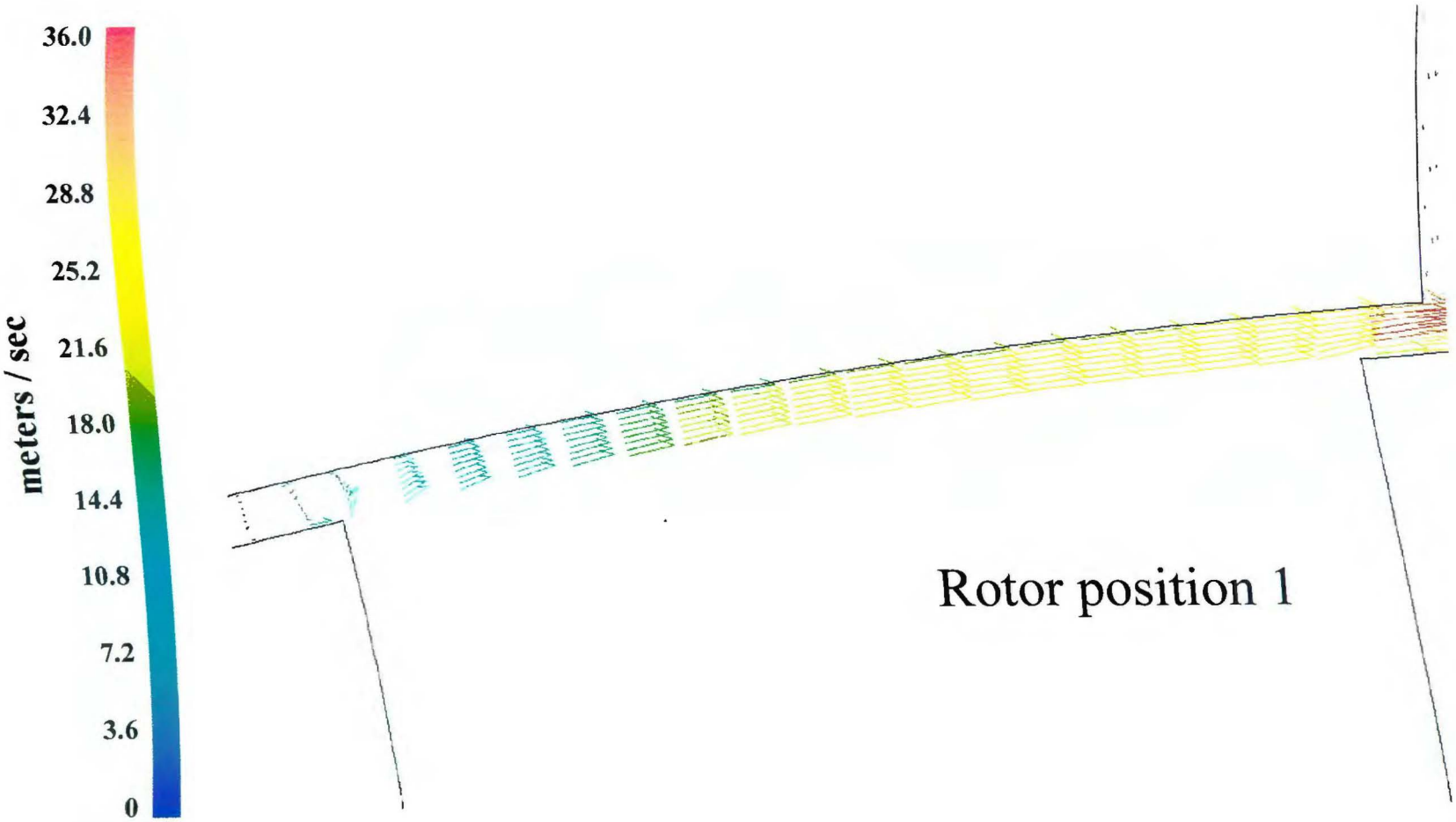

Figure 5-2. Angularly resolved mean velocity vectors in the gap to the left of stator slot 1 at time step 6,412 (0.6432 seconds). Simulation 5

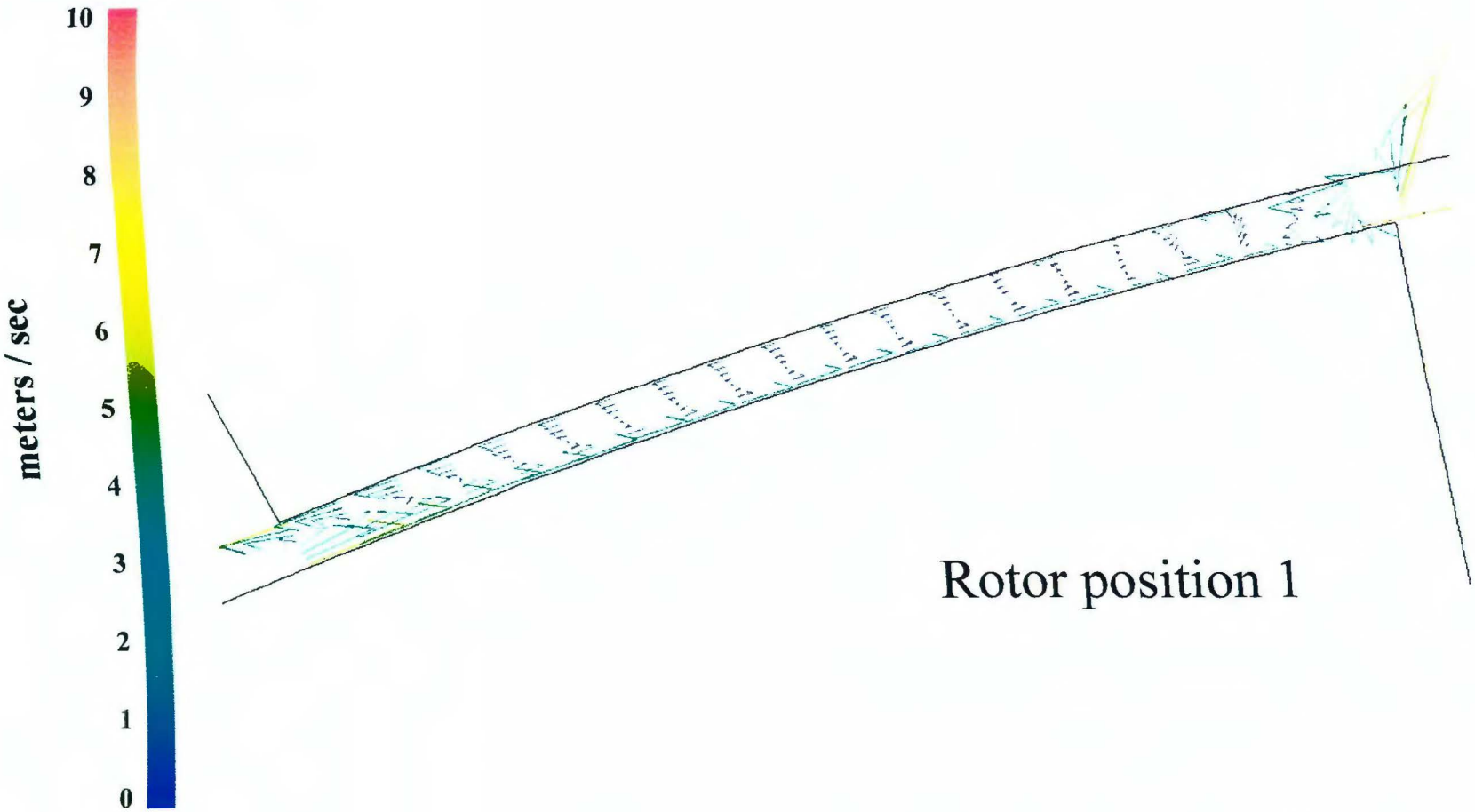

Figure 5-3. Angularly resolved mean velocity vectors in the gap to the right of stator slot 14 at time step 6,412 (0.6432 seconds). Simulation 5

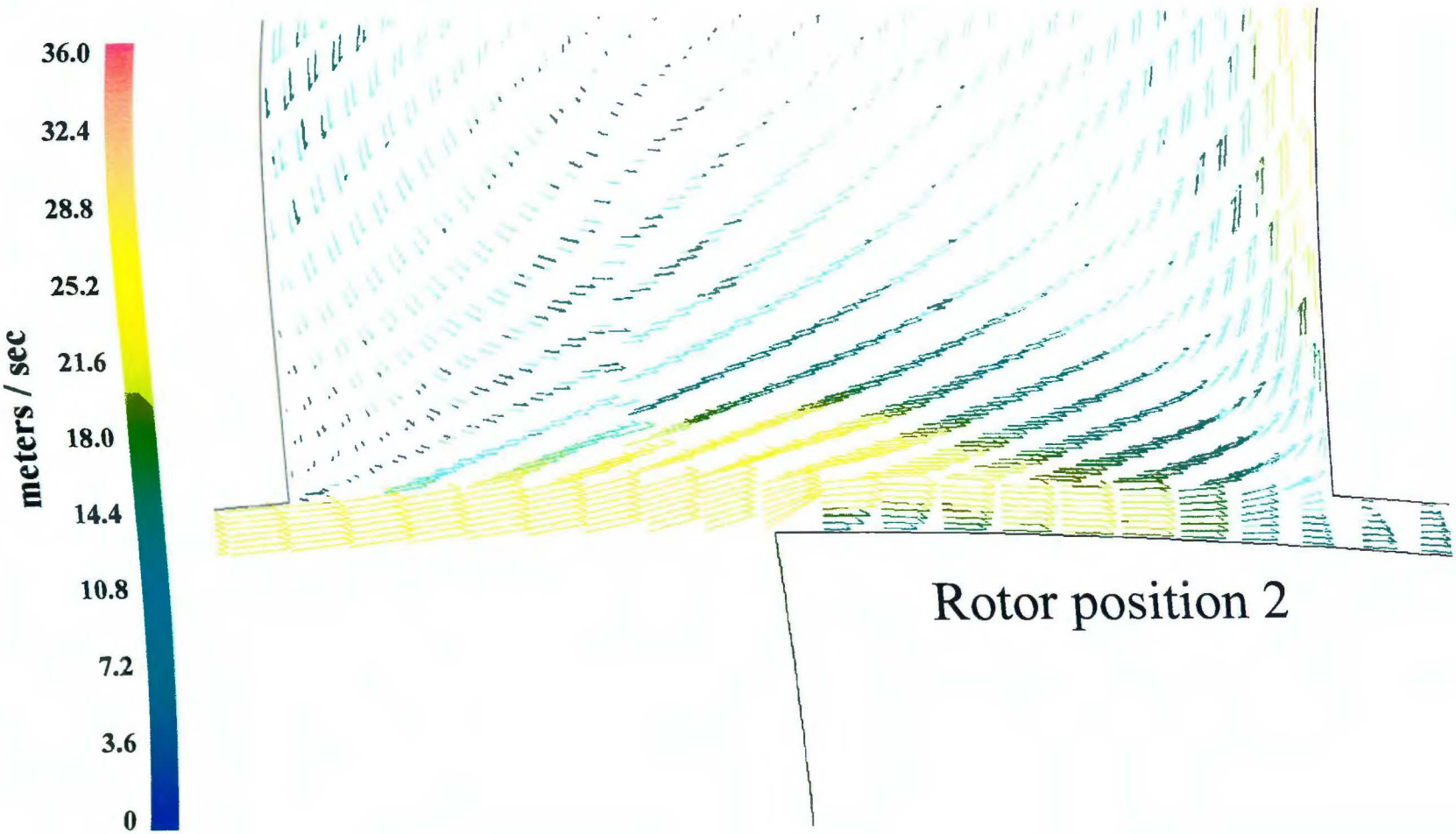

Figure 5-4. Angularly resolved mean velocity vectors in the gap under stator slot 1 at time step 6,416 (0.6436 seconds). Simulation 5

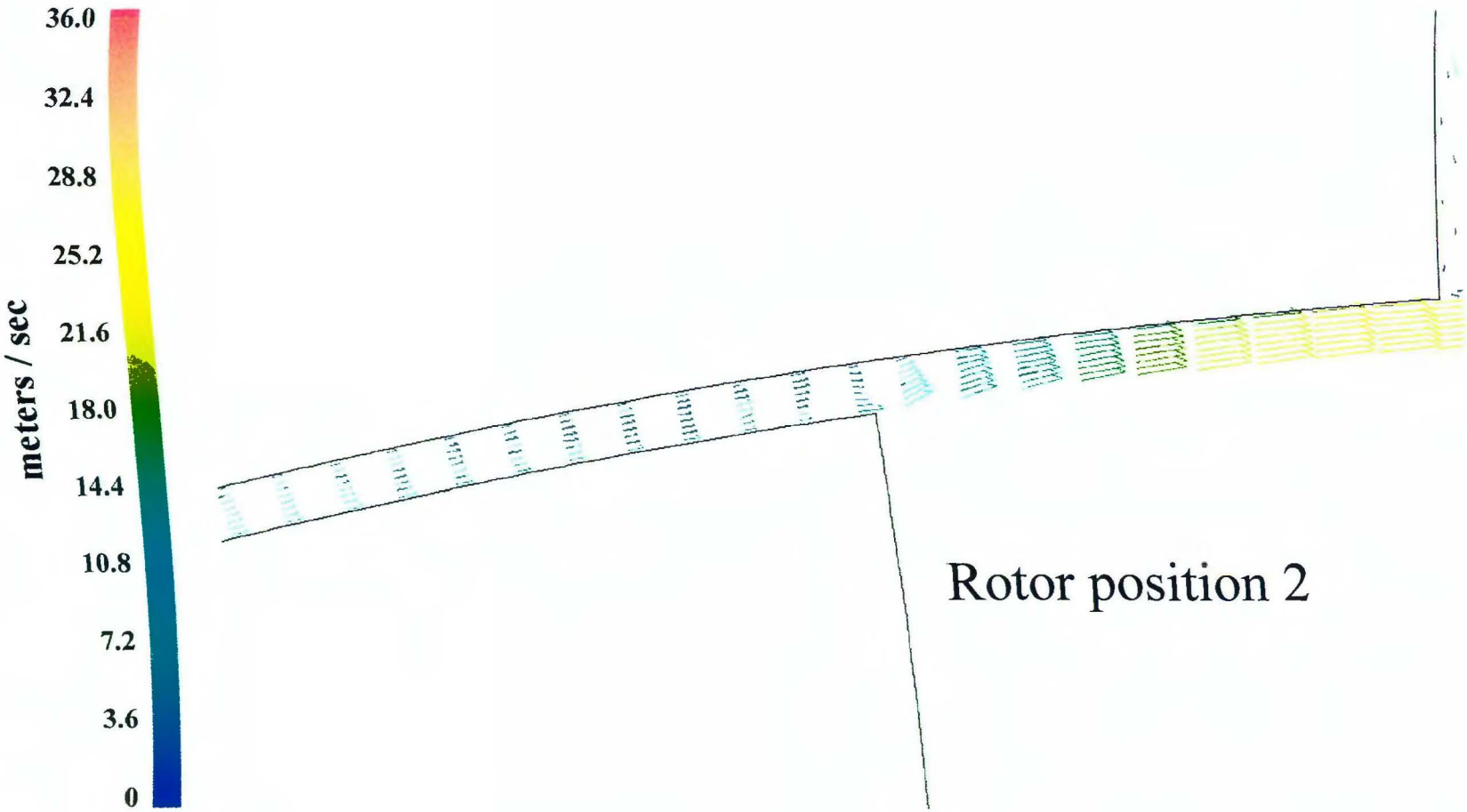

Figure 5-5. Angularly resolved mean velocity vectors in the gap to the left of stator slot 1 at time step 6,416 (0.6436 seconds). Simulation 5

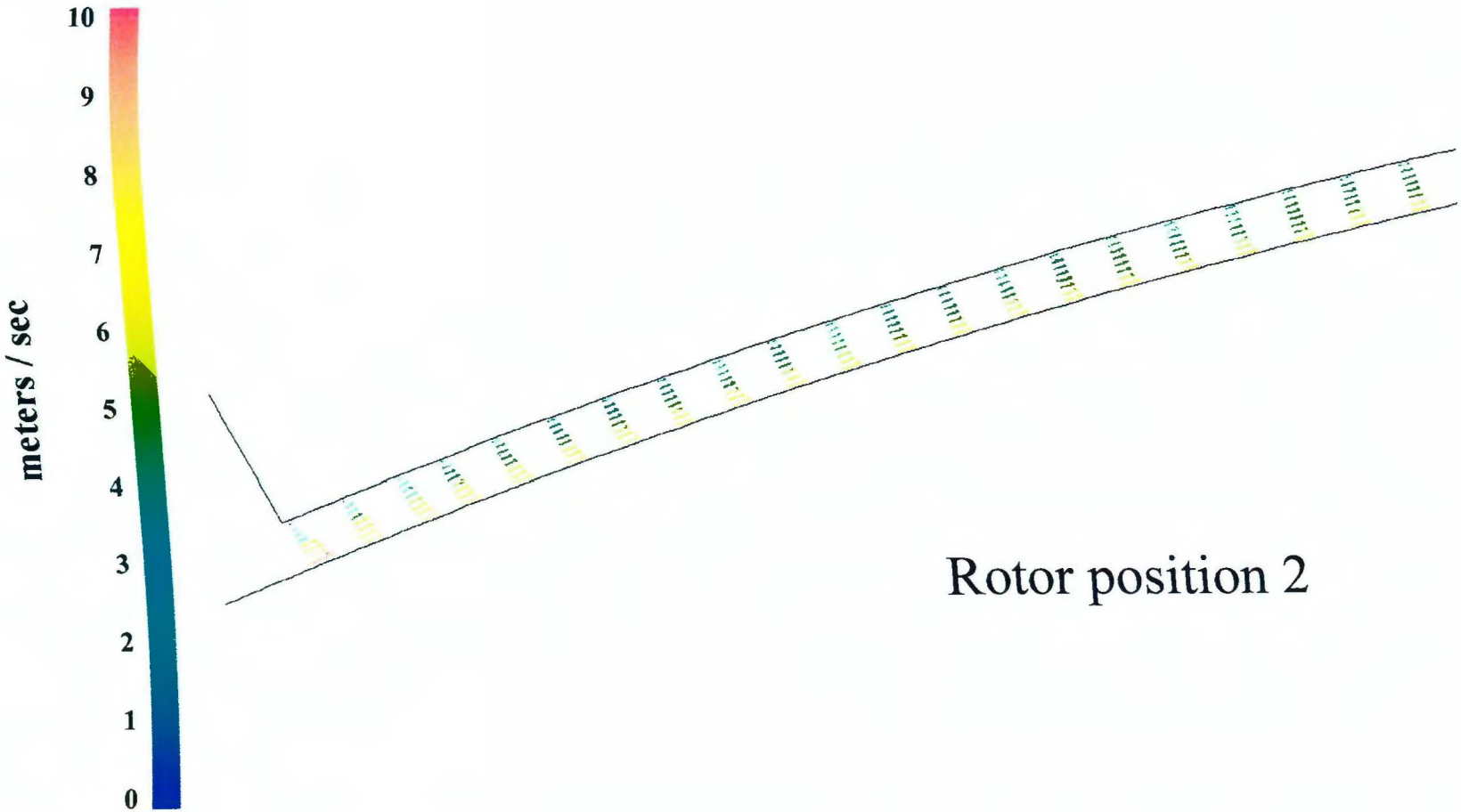

Figure 5-6. Angularly resolved mean velocity vectors in the gap to the right of stator slot 14 at time step 6,416 (0.6436 seconds). Simulation 5

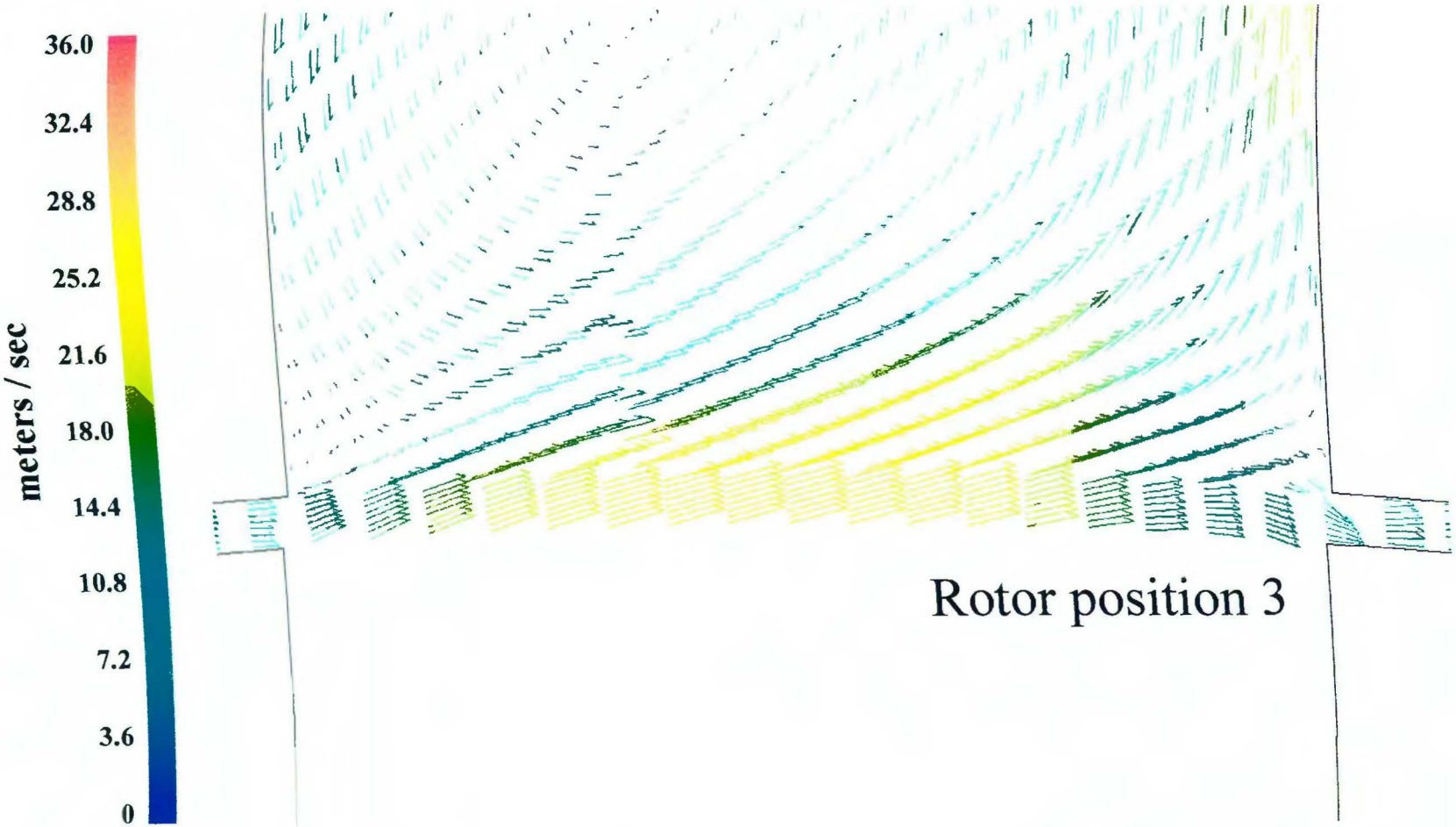

Figure 5-7. Angularly resolved mean velocity vectors in the gap under stator slot 1 at time step 6,420 (0.6440 seconds). Simulation 5

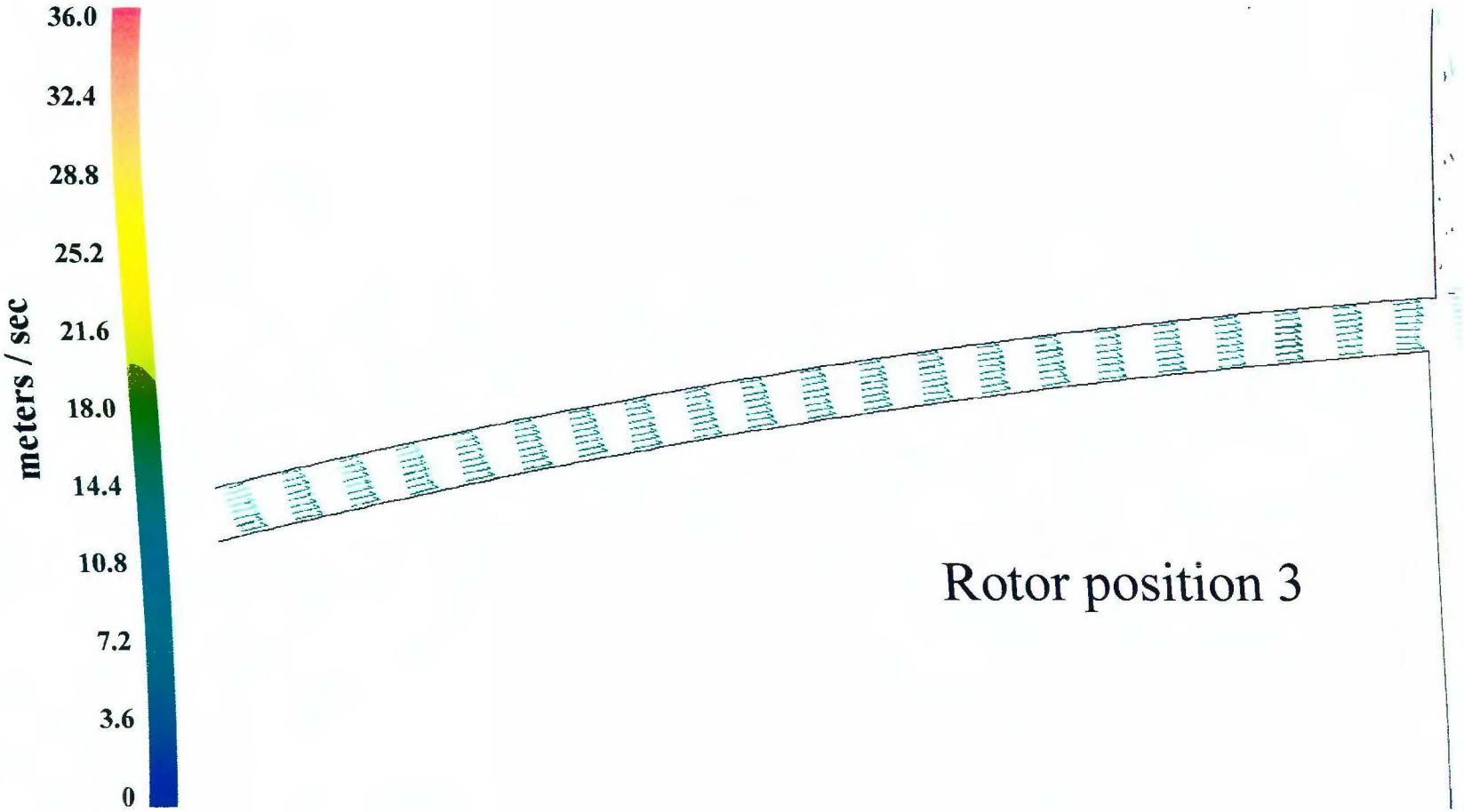

Figure 5-8. Angularly resolved mean velocity vectors in the gap to the left of stator slot 1 at time step 6,420 (0.6440 seconds). Simulation 5

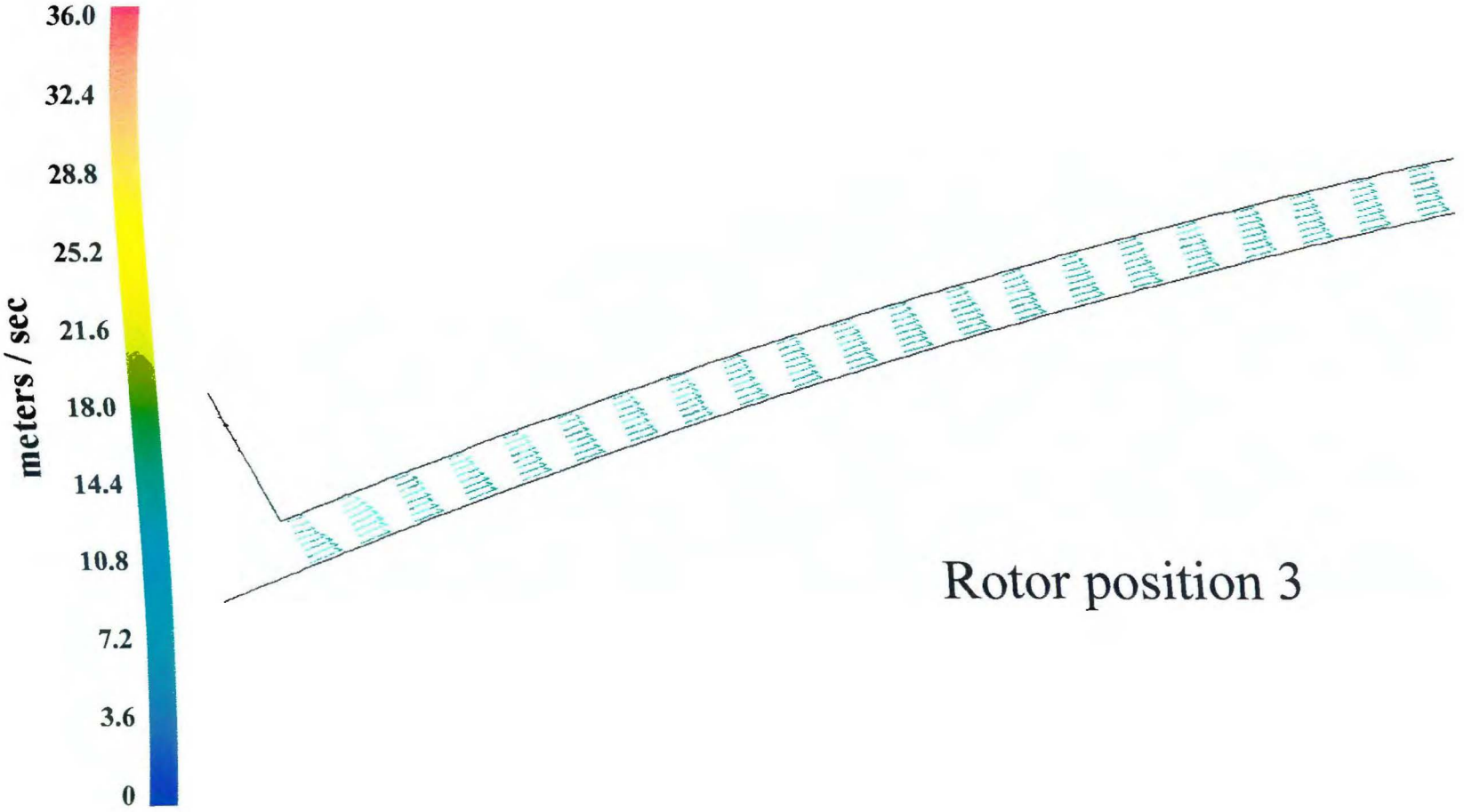

Figure 5-9. Angularly resolved mean velocity vectors in the gap to the right of stator slot 14 at time step 6,420 (0.6440 seconds). Simulation 5

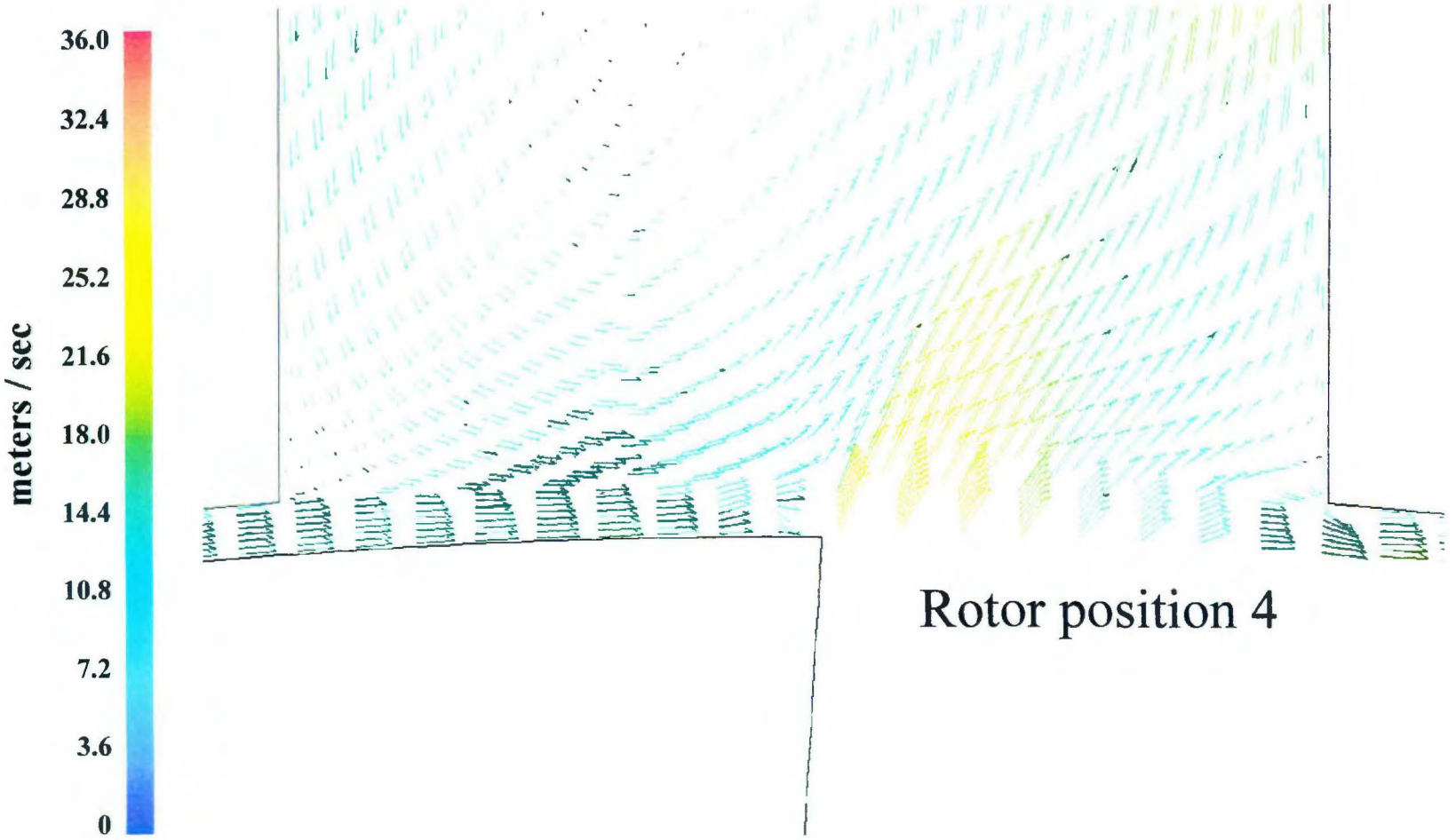

Figure 5-10. Angularly resolved mean velocity vectors in the gap under stator slot 1 at time step 6,424 (0.6444 seconds). Simulation 5

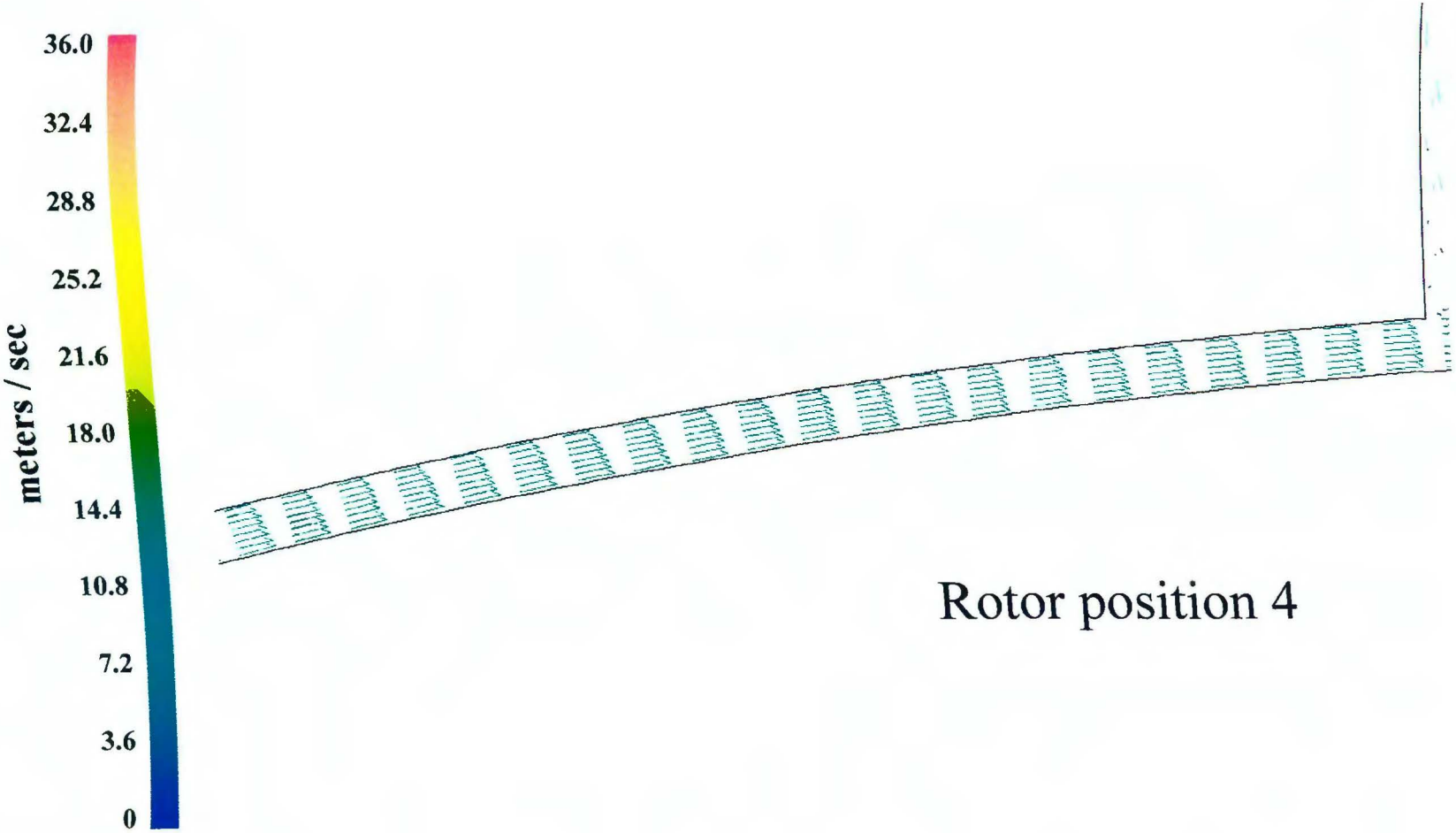

Figure 5-11. Angularly resolved mean velocity vectors in the gap to the left of stator slot 1 at time step 6,424 (0.6444 seconds). Simulation 5

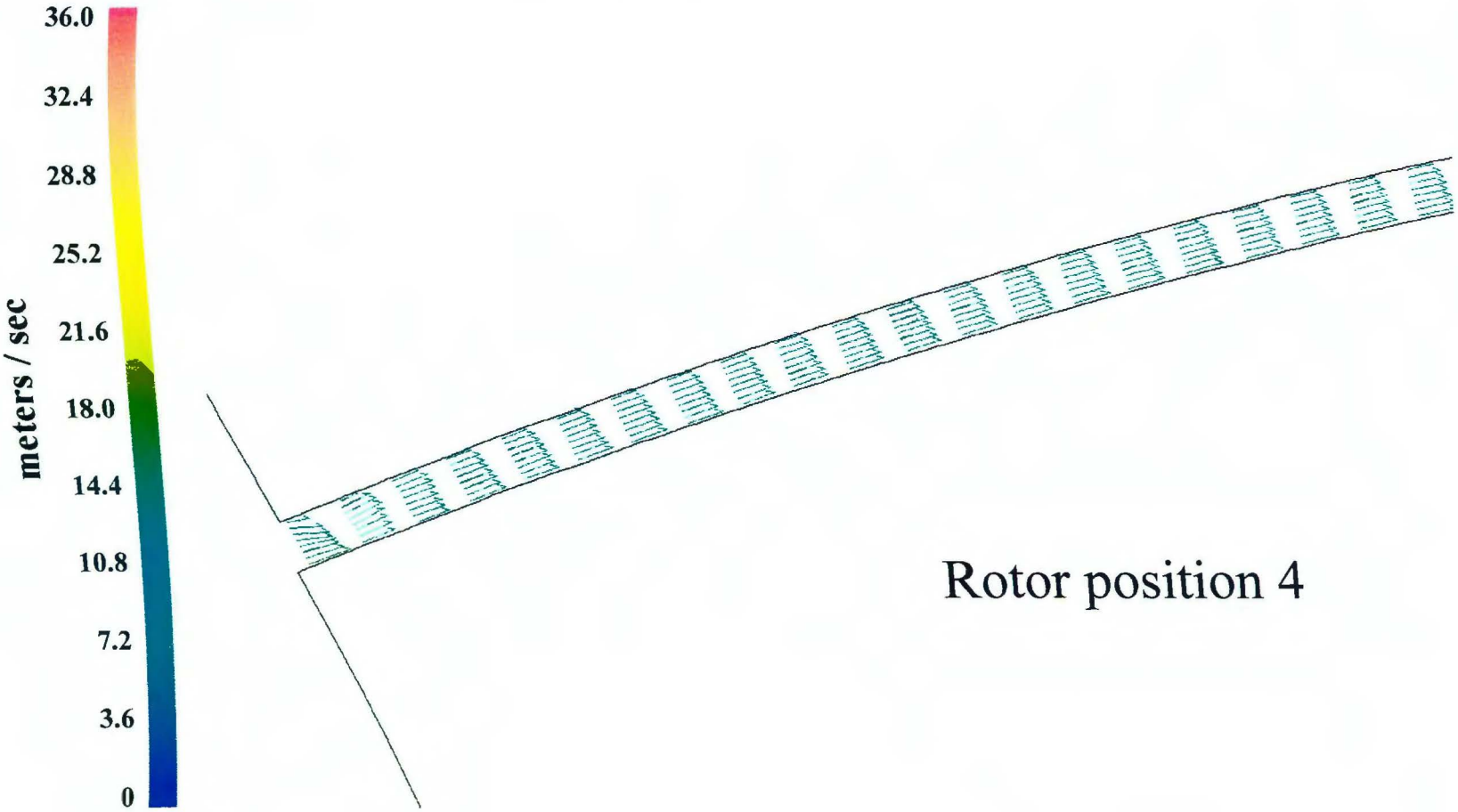

Figure 5-12. Angularly resolved mean velocity vectors in the gap to the right of stator slot 14 at time step 6,424 (0.6444 seconds). Simulation 5

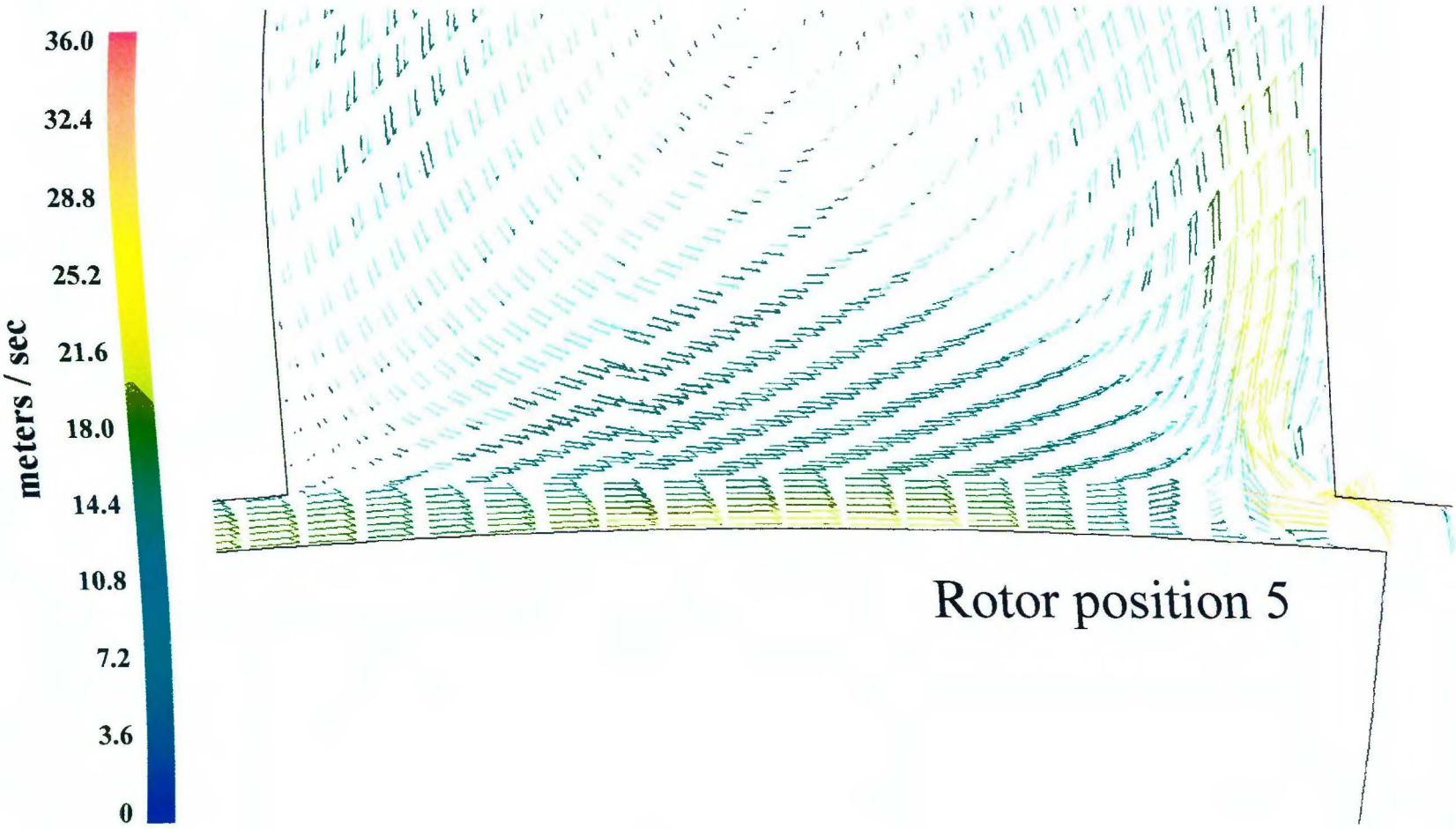

Figure 5-13. Angularly resolved mean velocity vectors in the gap under stator slot 1 at time step 6,428 (0.6448 seconds). Simulation 5

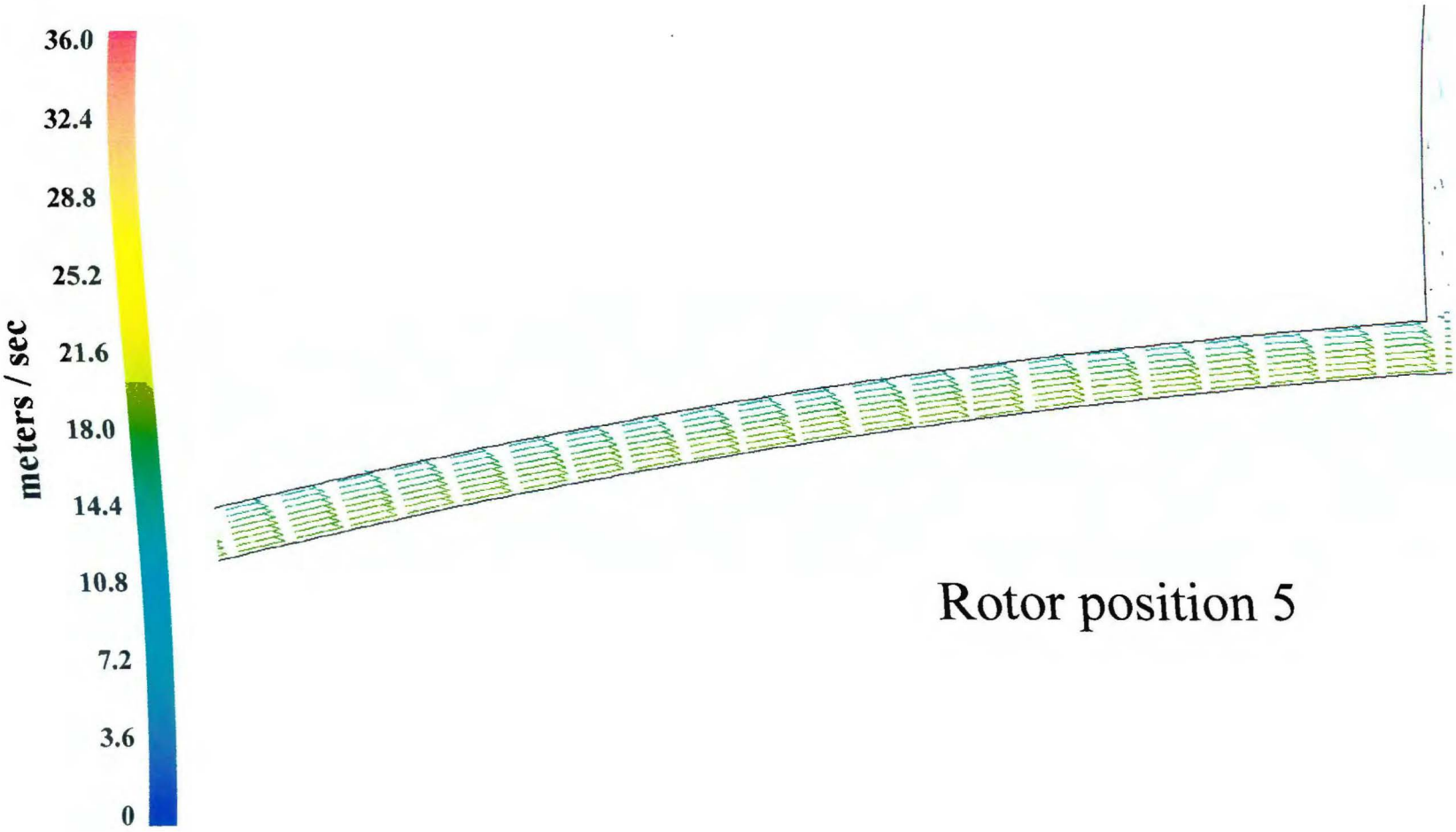

Figure 5-14. Angularly resolved mean velocity vectors in the gap to the left of stator slot 1 at time step 6,428 (0.6448 seconds). Simulation 5

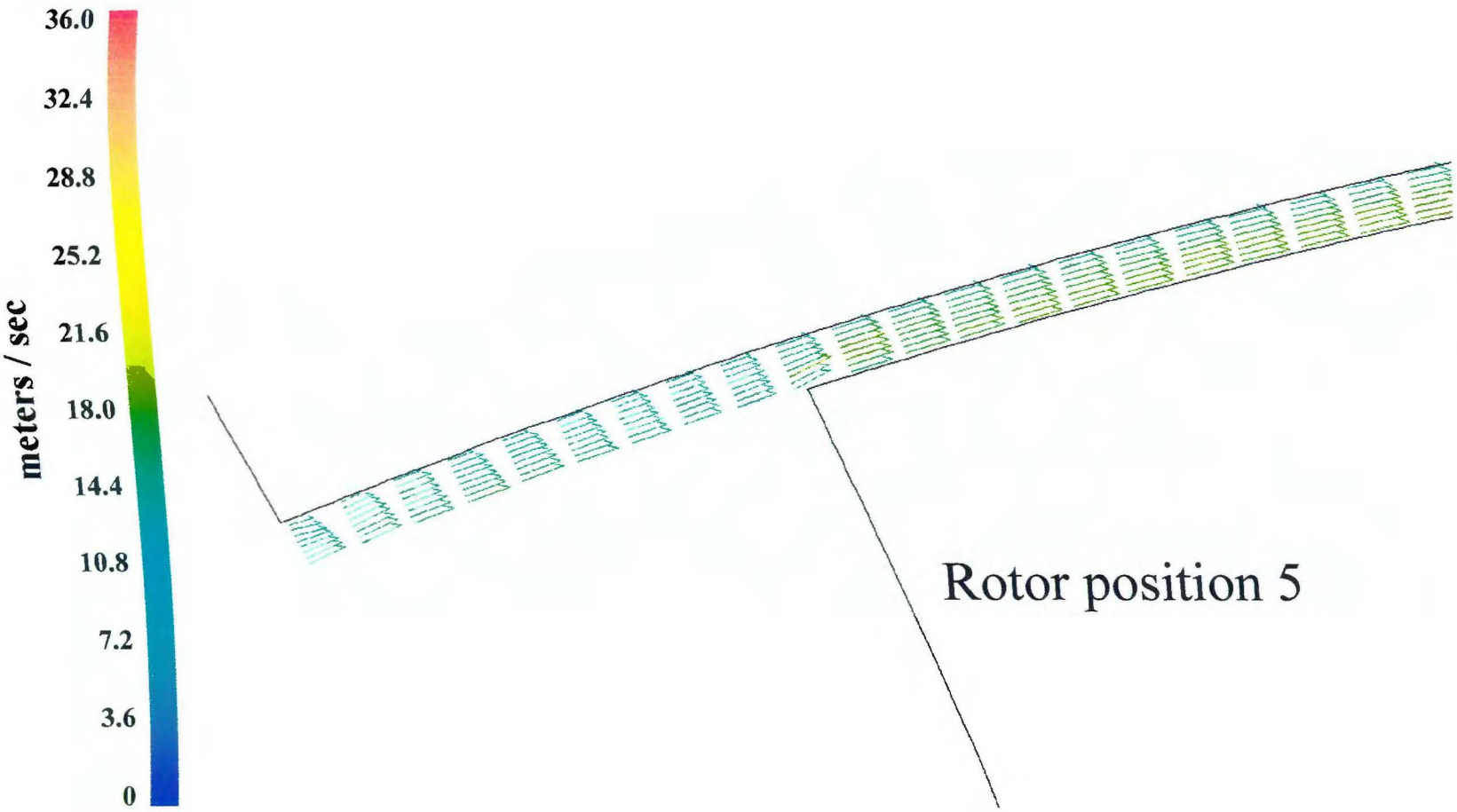

Figure 5-15. Angularly resolved mean velocity vectors in the gap to the right of stator slot 14 at time step 6,428 (0.6448 seconds). Simulation 5

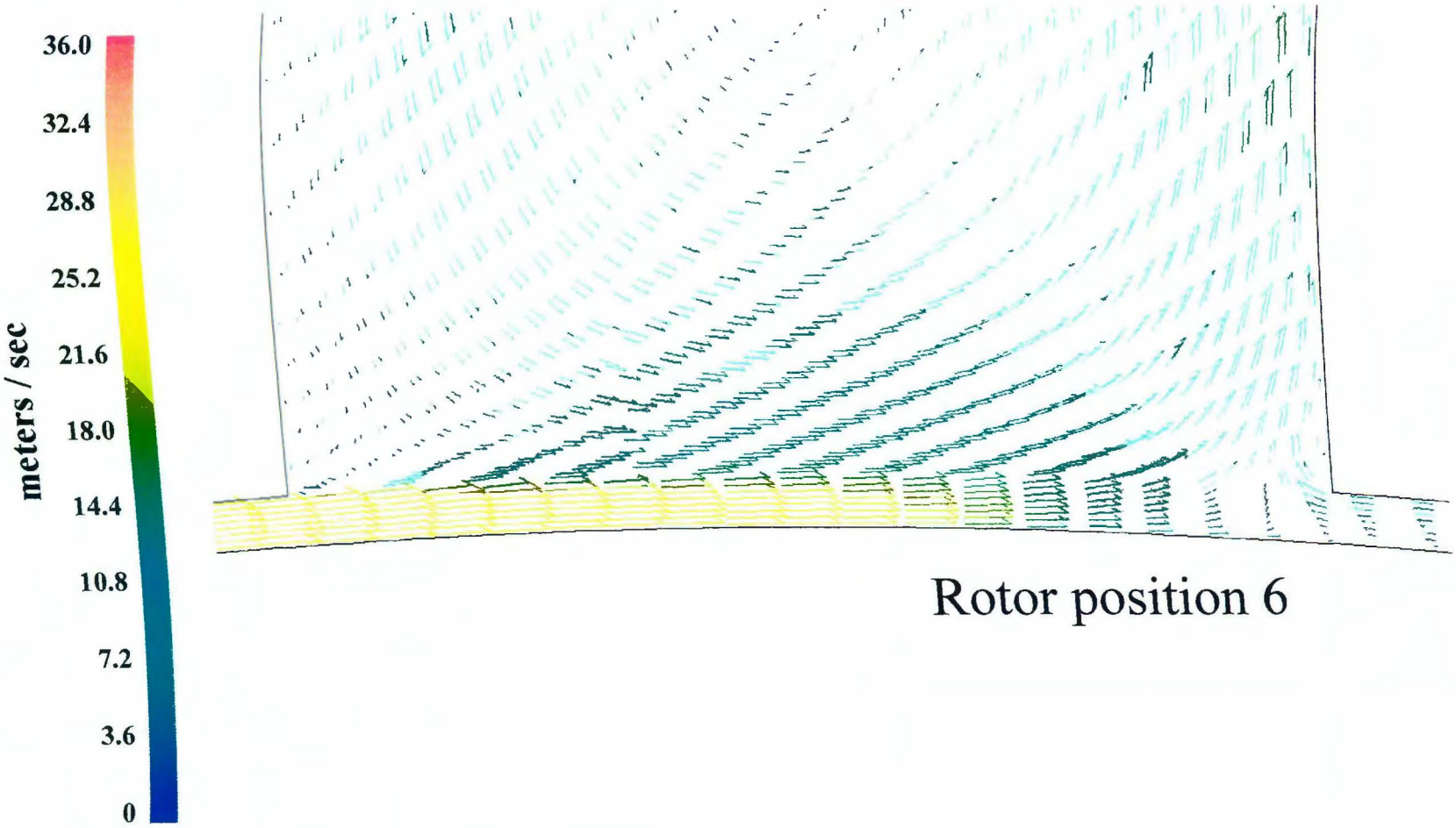

Figure 5-16. Angularly resolved mean velocity vectors in the gap under stator slot 1 at time step 6,432 (0.6452 seconds). Simulation 5

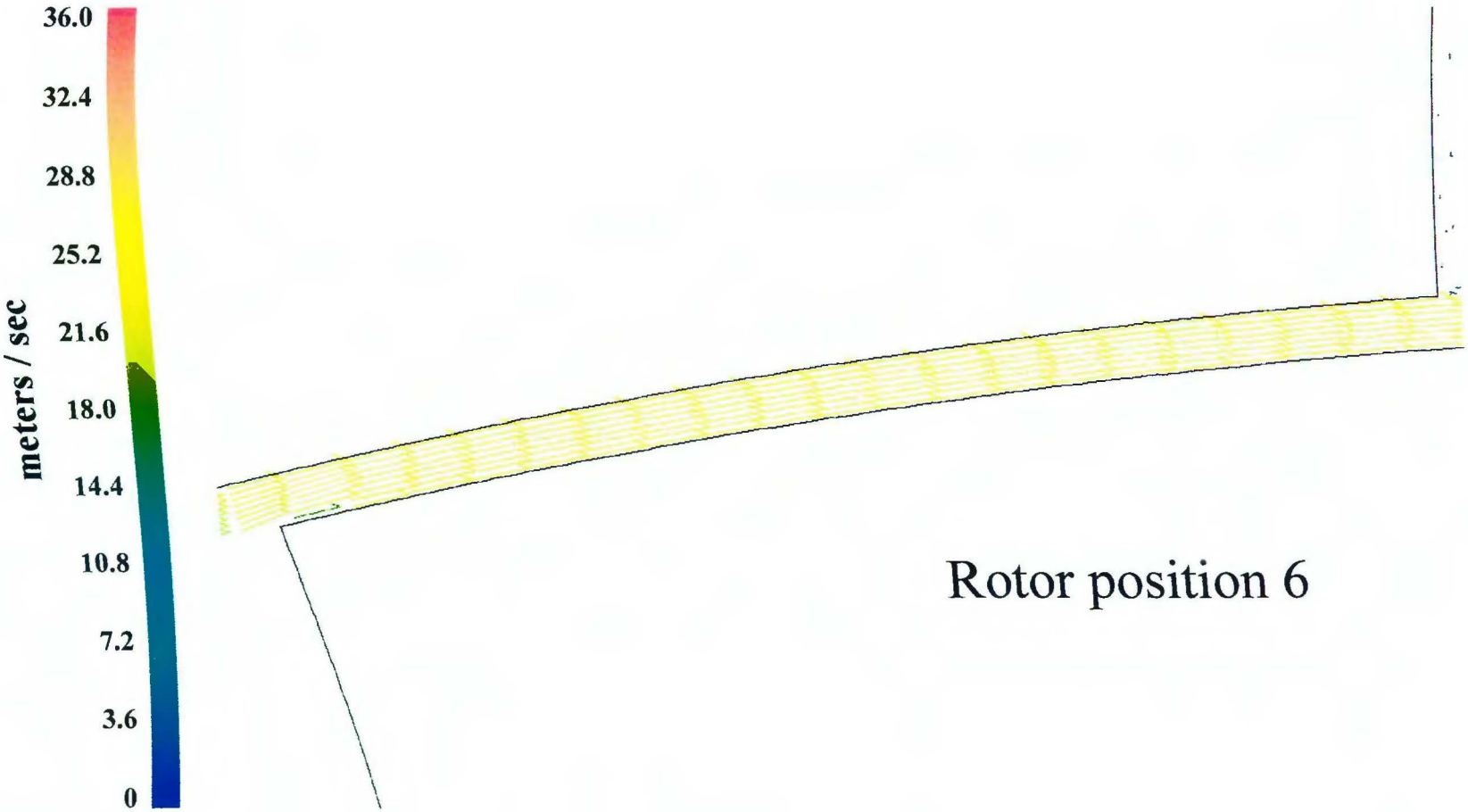

Figure 5-17. Angularly resolved mean velocity vectors in the gap to the left of stator slot 1 at time step 6,432 (0.6452 seconds). Simulation 5

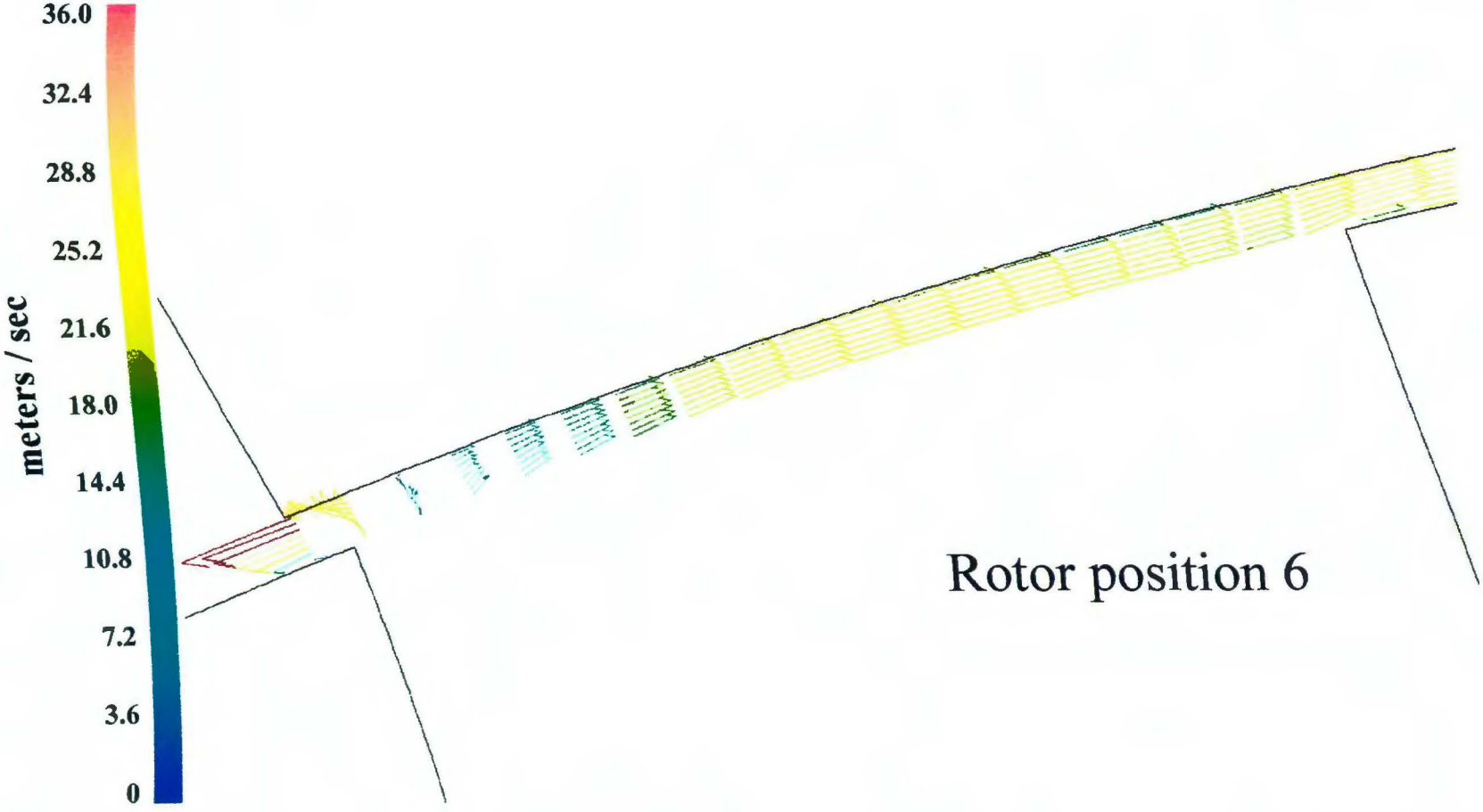

Figure 5-18. Angularly resolved mean velocity vectors in the gap to the right of stator slot 14 at time step 6,432 (0.6452 seconds). Simulation 5

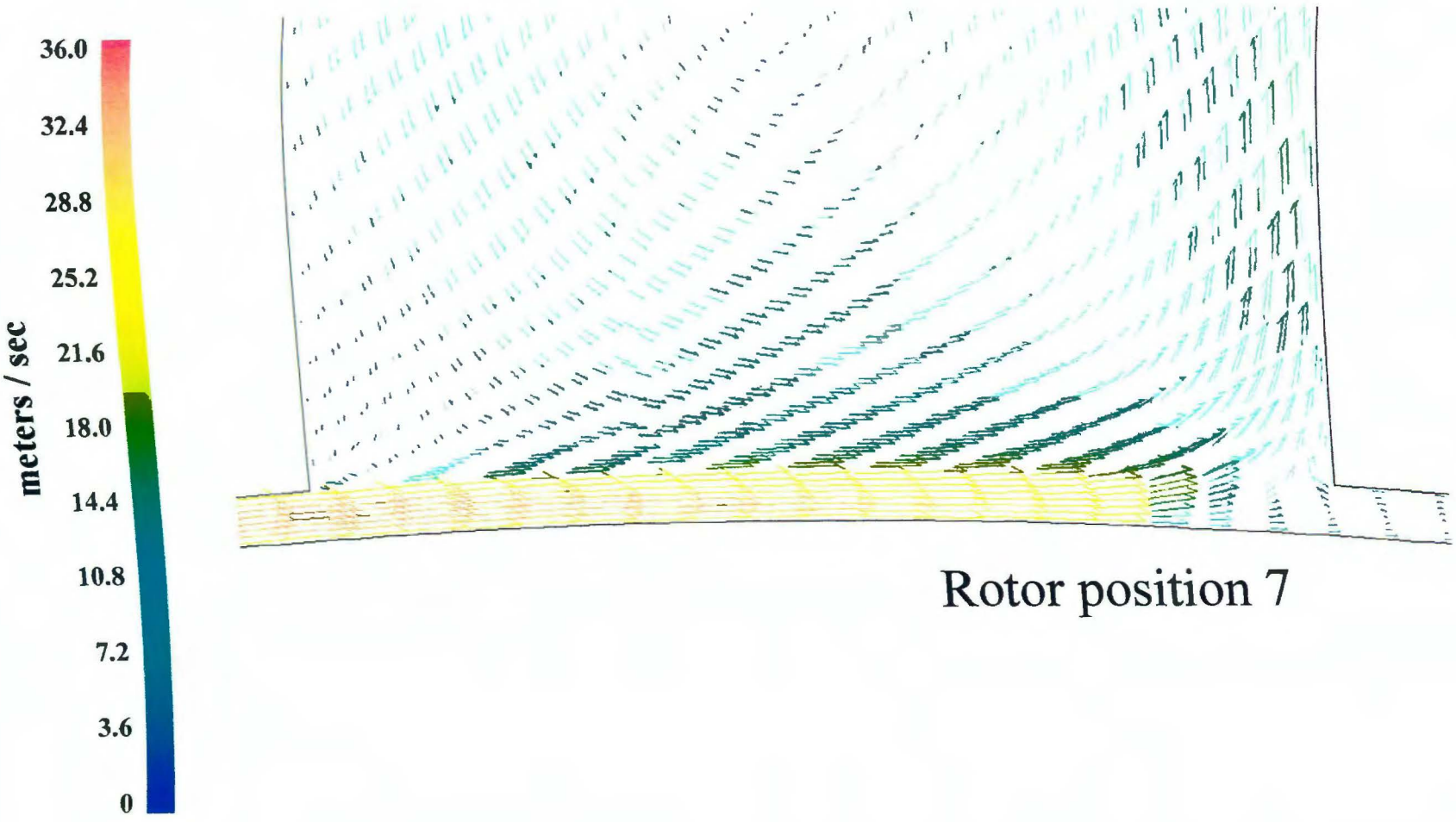

Figure 5-19. Angularly resolved mean velocity vectors in the gap under stator slot 1 at time step 6,436 (0.6456 seconds). Simulation 5

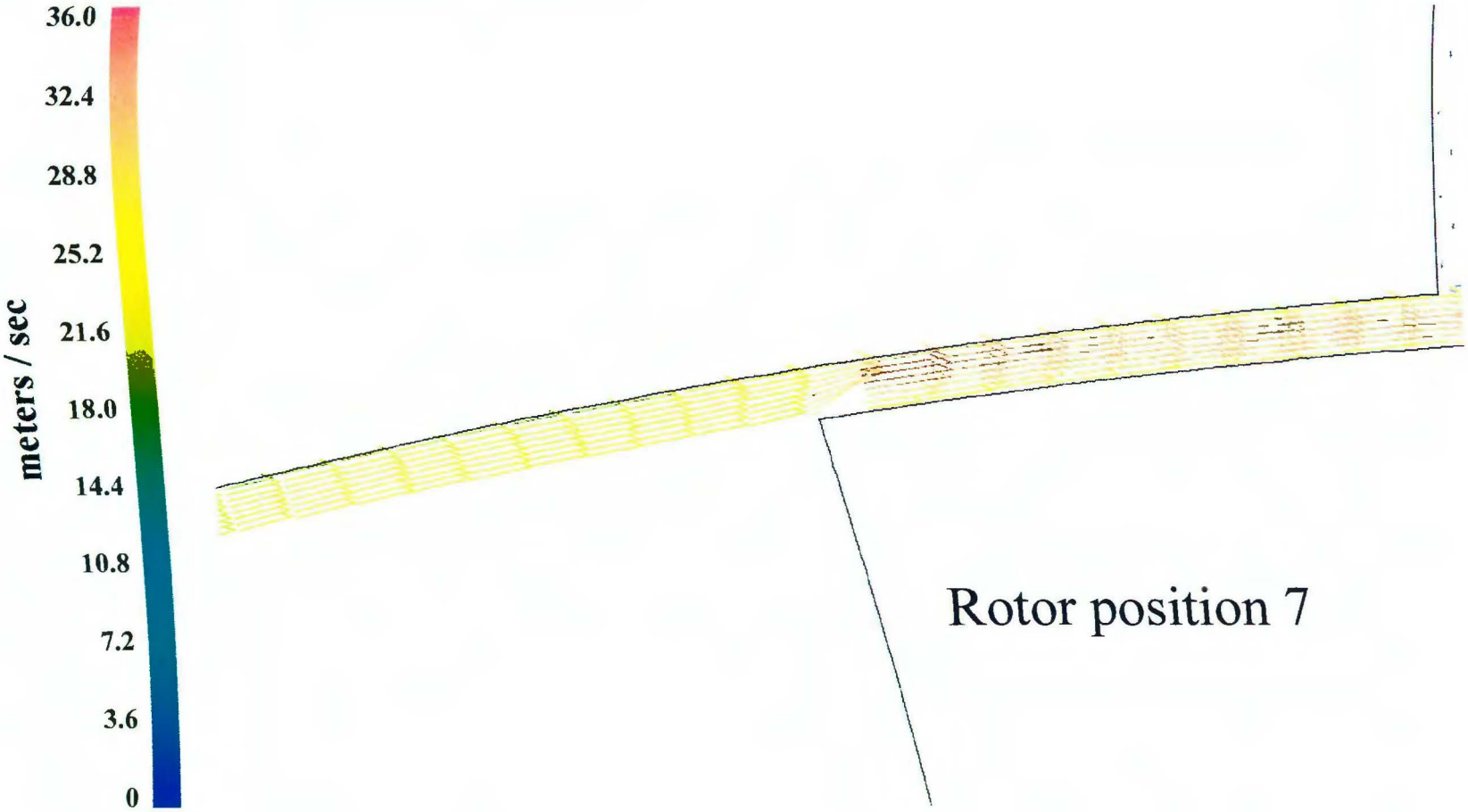

Figure 5-20. Angularly resolved mean velocity vectors in the gap to the left of stator slot 1 at time step 6,436 (0.6456 seconds). Simulation 5

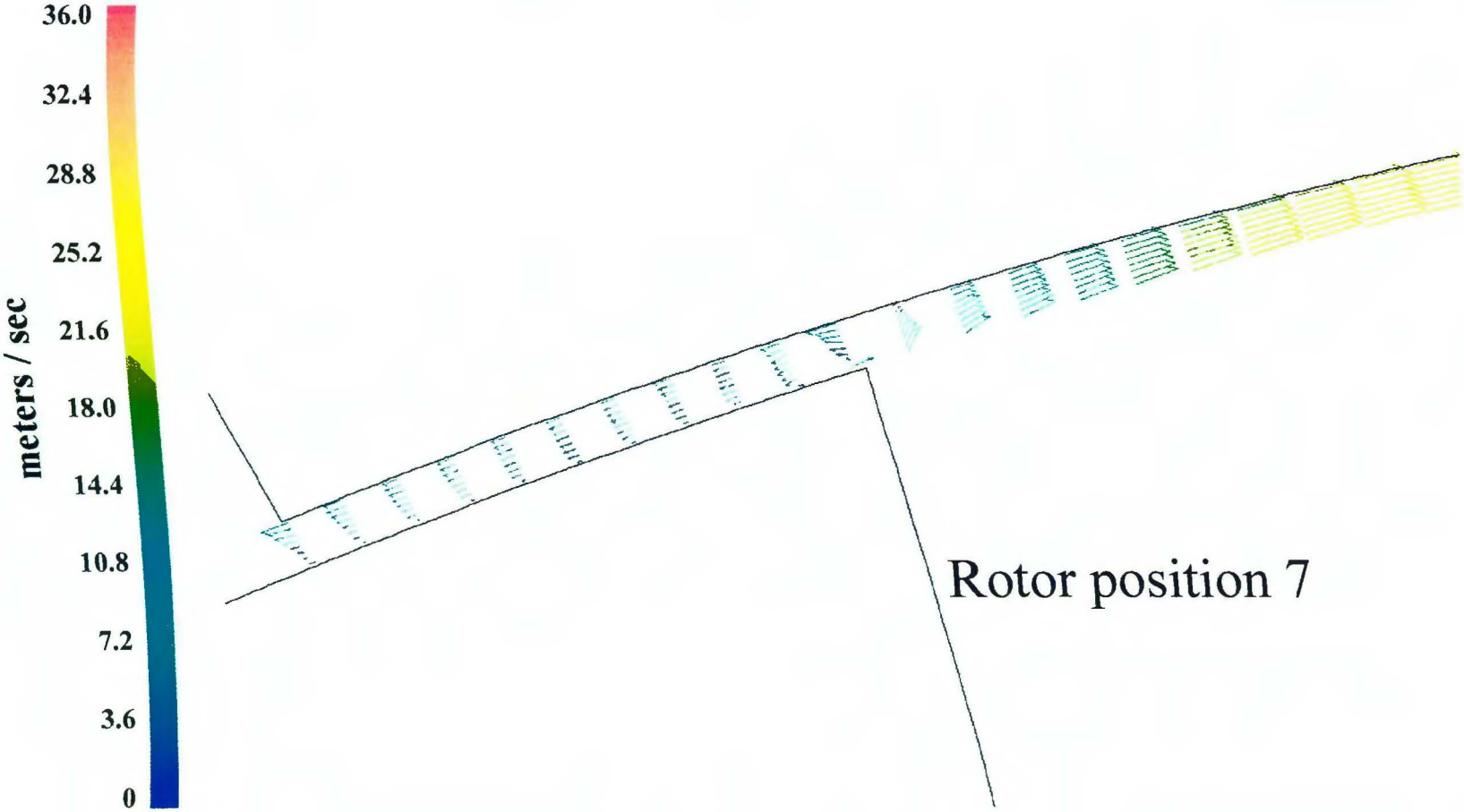

Figure 5-21. Angularly resolved mean velocity vectors in the gap to the right of stator slot 14 at time step 6,436 (0.6456 seconds). Simulation 5

labeled 'Rotor Position n' where n goes from 1 to 7. Shear patterns in the gap, mass flow rates, and fixed frame mean velocities are covered in the last part of section 5.1.

The remainder of the chapter contains an analysis and comparison of the mean static pressure and turbulence fields.

5.1.1 Gap Mean Velocity Field at Rotor Position 1

When the leading edge of a rotor slot is directly under the left edge of stator slot 1 (Figs. 5-1 through 5-3), a high speed tangential jet spans the width of the gap. This jet is similar to the one observed in the wide gap simulation (Fig. 4-7). In the standard gap simulation, the jet begins at the left edge of stator slot 1 and extends almost all the way across the stator slot. Its magnitude decreases from a maximum of about 34 m / sec at the left edge of slot 1 to about 21 m / sec at the right edge of slot 1. The position of the jet in the standard gap simulation is quite different from that observed in the wide gap simulation, where the jet maximum occurs directly above the center of the rotor slot approaching stator slot 1. The maximum jet mean velocity magnitude in the standard gap simulation is about 40% greater than that for the wide gap simulation.

Except for the shift in jet position, the mean flow velocities in the region of the gap directly above the rotor slot at the simulation time under consideration (Fig. 5-2) is qualitatively similar to results obtained for the wide gap model. Above the left edge of the rotor slot, the gap mean velocities have a moderate radial component to them that is converted to a tangential motion by impaction with the stator tooth. Moving more toward the center of the rotor slot, the gap mean velocities lose their

radial component and become purely tangential. This shift from a raidial to tangential direction does occur over a much shorter length than in the wide gap simulation (compare to Fig. 4-7), probably due to the much shorter width of the gap in the present simulation. Interestingly, the gap mean velocities on the left side of the rotor slot in the standard gap simulation are much smaller than the corresponding ones in the wide gap simulation, both in terms of absolute magnitude, and relative to the maximum obtained in the high speed jet.

Further left of the rotor slot (Fig. 5-3) the flow in the gap region is reciruclatory and almost stagnated relative to the mean velocity magnitudes present in other regions of the gap. Close to the rotor side of the gap the flow moves in a clockwise tangential direction as would be expected, and the mean velocity magnitudes in the computational cells bounding the rotor tooth are about 4 m/sec which implies a fairly steep gradient in the tooth boundary layer. This is in contrast to the corresponding mean velocities in the wide gap simulation, which were found to be about 10 -12 m / sec: roughly the same velocity as the rotor implying the absence of a boundary layer. On the stator side of the gap the flow actually moves in a counterclockwise direction in an attempt to exit from stator slot 14. Note the splitting of flow in the gap directly above the leading edge of the rotor tooth evident in both Figs. 5-2 and 5-3.

5.1.2 Gap Mean Velocity Field at Rotor Position 2

With the rotor advancing an additional 4.3° (Figs. 5-4 through 5-6), the rotor slot is now halfway aligned with stator slot 1 and the maximum jet mean velocity in

the gap decreases to about 24 m / sec and shifts slightly to the right. The gap mean velocities also take on a radial component towards the middle of stator slot 1. This shift in direction also occurs in the wide gap model, but at a later time when the rotor and stator slots are in complete alignment (Fig. 4-9).

To the right of stator slot 14, the recirculation in the gap that was evident at rotor position 1 is gone (Figs. 5-5 and 5-6): All fluid is now moving in a clockwise tangential direction, albeit very slowly. The steep boundary layer near the rotor side of the gap has also decreased, as evidenced by the larger mean velocity magnitudes (~7-10 m / sec) in the rotor adjacent cells (Fig. 5-6).

5.1.3 Gap Mean Velocity Field at Rotor Position 3

As the rotor and stator slots move into complete alignment, the maximal gap mean velocities are located tangentially further into stator slot 1, so that they occur directly at the angular center of the slot (Fig. 5-7). The gap velocities under the stator slot also take on a greater radial component. To the left of stator slot 1, the gap flow mean velocity is still small and appears to be nearly plug except very close to stator slot 14, where a slight gradient across the gap exists (Figs. 5-8 and 5-9).

5.1.4 Gap Mean Velocity Field at Rotor Position 4

When the rotor slot has moved an additional 4.3°, so that it is again only half aligned with stator slot 1 (Figs. 5-10 through 5-12), there is little change in the gap flow except in the 5 mm long span where the two slots are aligned (Fig. 5-10). In this region the flow takes on a nearly 100 % radial direction, and its mean velocity

magnitude is in the range of 18 – 25 m / sec. These are the highest radial mean velocities occurring in the gap bounding slot 1, and the mass flow rate out the slot is also highest at this time (Fig. 5-22: 4 steps from rotor-slot stator-slot alignment).

5.1.5 Gap Mean Velocity Field at Rotor Positions 5 and 6

4.3° of rotation later the rotor slot has completely passed stator slot 1 and the stator slot may be considered 'closed' (Figs. 5-13 through 5-15). It is evident that the gap flow near the right corner of stator slot 1 is beginning to undergo a flow reversal. Most of the fluid exiting the rotor slot into the gap at this point in time still attempts to exit the gap from stator slot 1, even though to do so it must move in a direction opposing the natural tendency imposed on it by rotor rotation.

The radial mean velocities in the lower portion of slot 1 have disappeared with the exception of those at the far right end. Concomitantly, the mass flow rate out the slot decreases significantly to near its minimum (Fig. 5-22: 8 steps from rotor-slot stator-slot alignment). An additional 4.3° later (Figs. 5-16 through 5-18), flow reversal is still evident at the right corner of stator slot 1, and it is beginning to develop at the corner of stator slot 14. Note that geometrically, the time step represented by Figs. 5-16 through 5-18 is identical, relative to slot 14, as the time step represented by Figs. 5-13 through 5-15 is relative to slot 1. Clearly the flow fields in these two regions at their relative time steps are qualitatively identical.

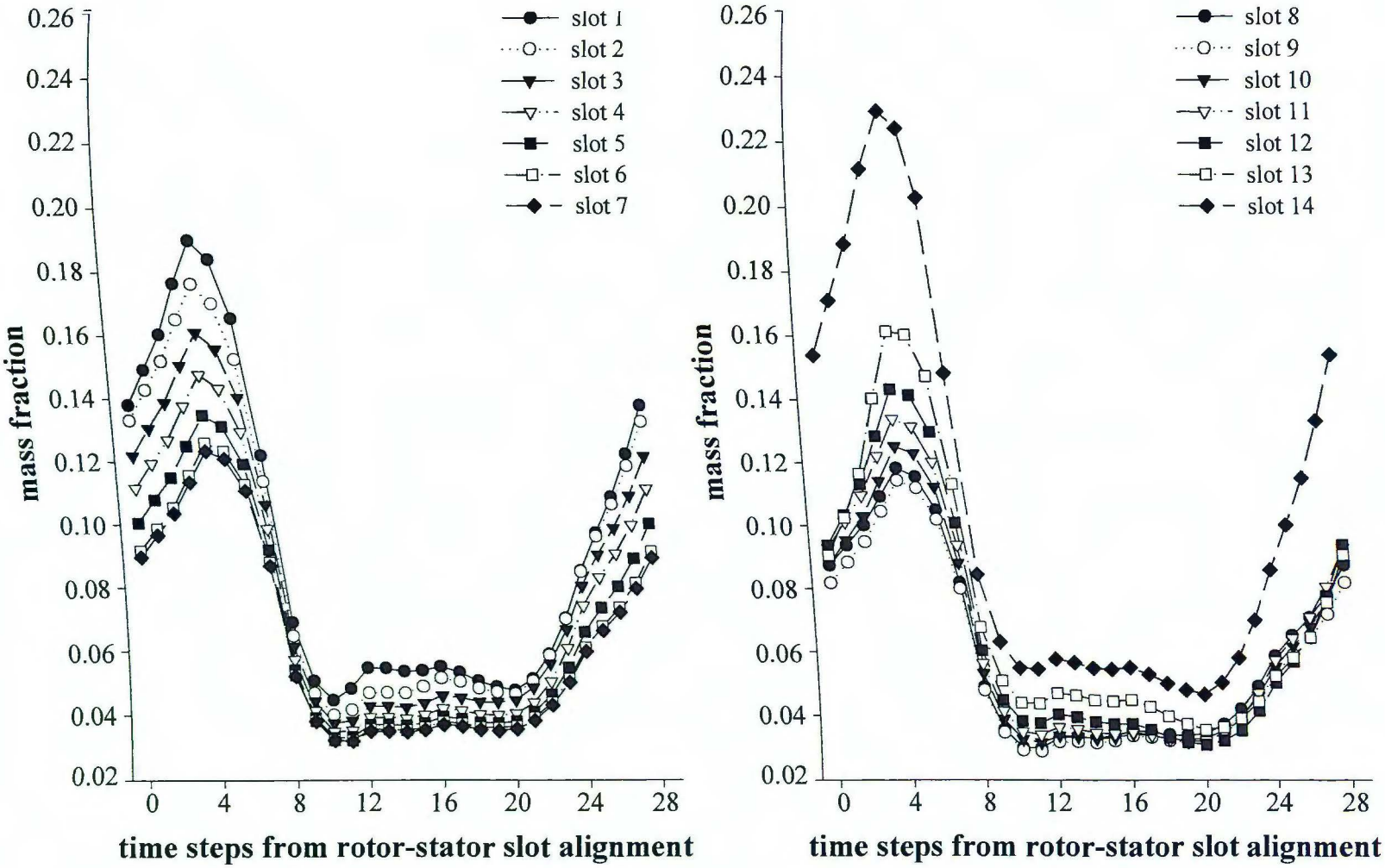

Figure 5-22. Time dependent mass flow rates through stator slots as a function of slot alignment beginning at approximately time step 6,412. Simulation 5.

5.1.6 Gap Mean Velocity Field at Rotor Position 7

The final set of figures for the gap mean velocity field (Figs. 5-19 through 5-21) show that the mean velocity in the high speed jet increases in magnitude directly above the leading edge of the rotor slot. Flow reversal is still evident to the right of stator slot 1, although the counterclockwise flow is now minor. The flow reversal near slot 14 is also still apparent. 4.3° or 8.6° more of rotation corresponds to rotor positions 1 and 2 respectively, at which times the flow reversal is no longer present near slot 1 (4.3°) or slot 14 (8.6°).

5.1.7 Mean Shear Patterns Across the Gap

The reduced mean tangential velocity profile across the gap from the azimuthal center of a rotor tooth when it is directly under stator tooth 1 is plotted in Fig. 5-23a. It is very similar in form to the profile obtained for the standard gap model (Fig. 4-15a) in that a well defined boundary layer is lacking at the rotor wall. The average shear experienced by the majority of fluid in this region of the gap at this time (outside of the boundary layer) is approximately 9,200 sec^{-1}, which is about 10 times greater than that in the corresponding wide gap simulation.

The original standard gap mesh (Table 2-1) consists of 8 elements spanning the gap. Since this is a fairly small number, it is possible that this could effect the flow field results there. Therefore, the mesh used for simulation 5 was adapted based on the value of y+ in wall adjacent cells after 6,428 time steps of simulation (19.1 revolutions). This yielded a mesh where every wall adjacent cell with a y+ value greater than 1 was split into four equal quadrants. Solution was continued on this

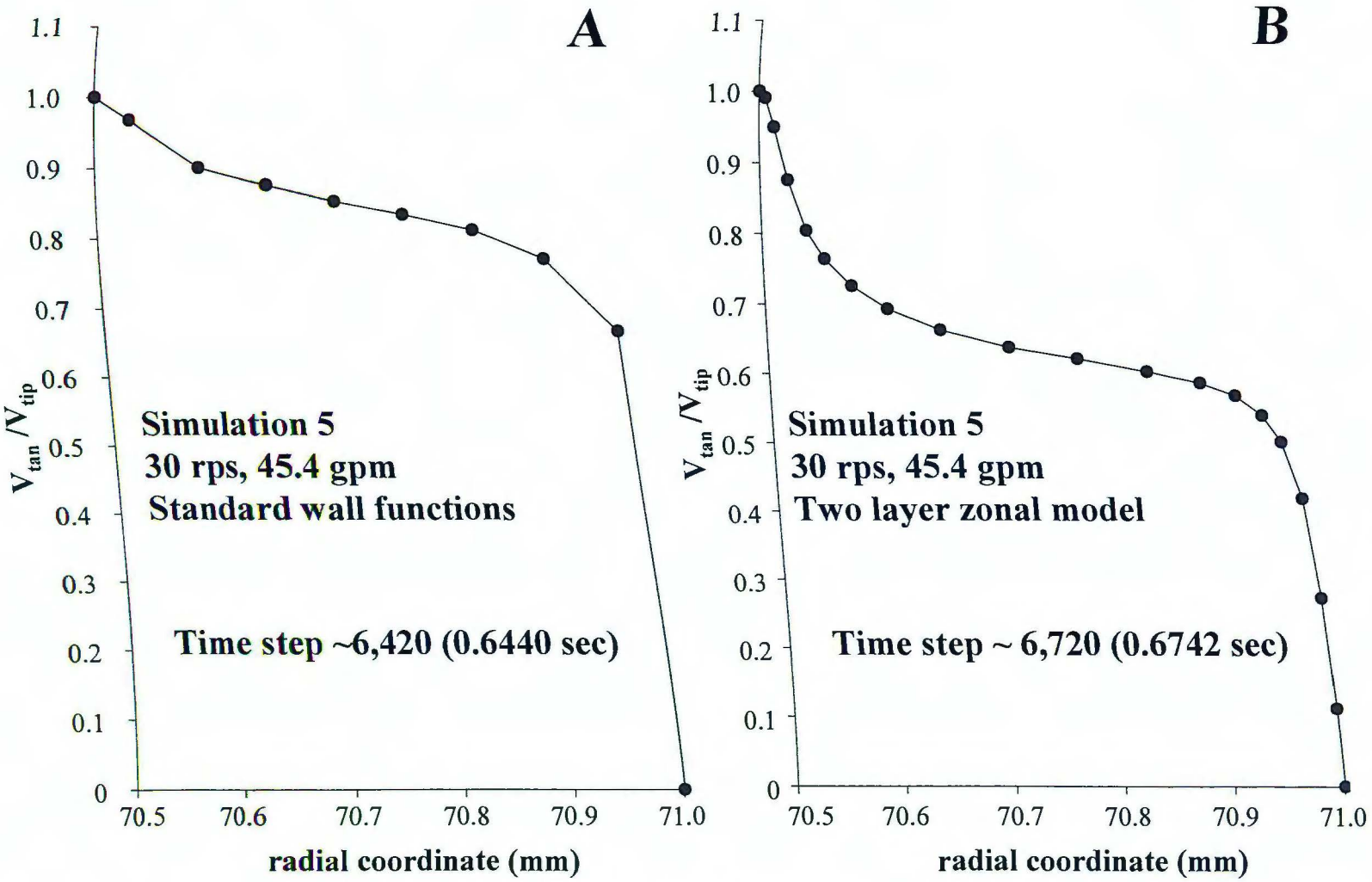

Figure 5-23. Reduced tangential velocity profiles across the gap at the azimuthal center of stator tooth 1 when fully aligned with a rotor tooth. Simulation 5 using standard wall functions (**A**), or two layer zonal model (**B**).

mesh for 40 time steps (~1.3 periods), and the adaption process was repeated. Solution then proceeded again for 32 time steps at which time a final y+ adaption was performed. This final mesh was very dense around the gap walls (Fig. 5-24) and consisted of 680,000 computational cells. Solution was continued on the final mesh for 230 time steps.

After the first adaption of the mesh, the wall function treatment was disabled in favor of the two-layer zonal model available in FLUENT™. The two layer zonal model attempts to solve the flow field all the way to the wall, using a low Reynolds number turbulence model in cells close to the wall. Details of the model can be found in the FLUENT™ manual (Fluent Inc., 1997).

Although 230 time steps may not be enough time steps to reach a fully periodic condition with the two layer zonal model, it is enough to see significant differences in changes to the simulated flow near the wall. Figure 5-23b shows the reduced mean tangential velocity profile across the gap obtained from the two layer zonal model. A very slight boundary layer is predicted near the rotor wall which, although considerably smaller than the boundary layer near the stator, is still noticeably different from results obtained with standard wall functions. Overall, however, it is arguable that the wall function approach yields results comparable to the two layer zonal model: Notice in Fig. 5-23a that there appears to be a very small and ill-defined boundary layer at the rotor wall, but it is not as noticeable as for the two layer zonal model because there are not as many mesh cells in the region.

On the other hand, Fig. 5-25a shows the wall y+ values near stator tooth 1 for the standard gap simulation using wall functions. The stator side, and to a greater

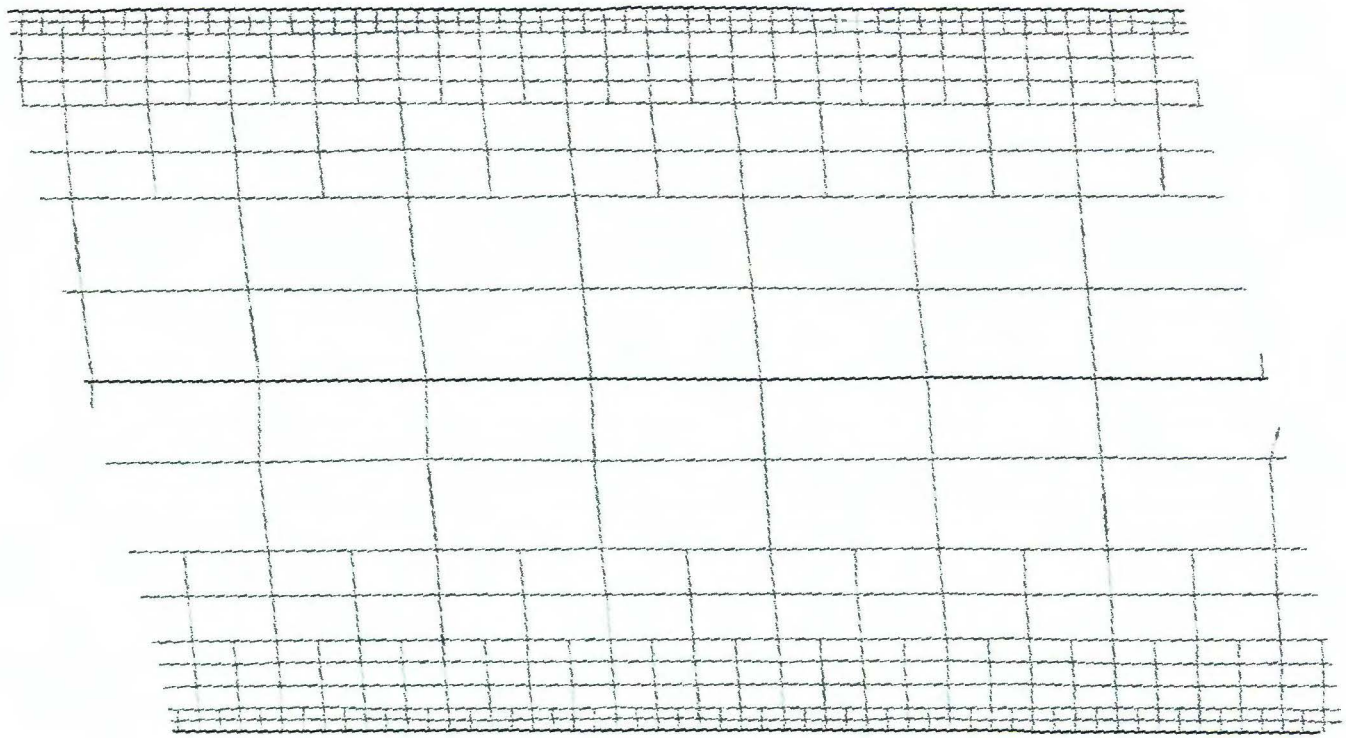

Figure 5-24. Close up of the wall-adapted mesh in the shear gap region used for simulation with the two layer zonal wall treatment.

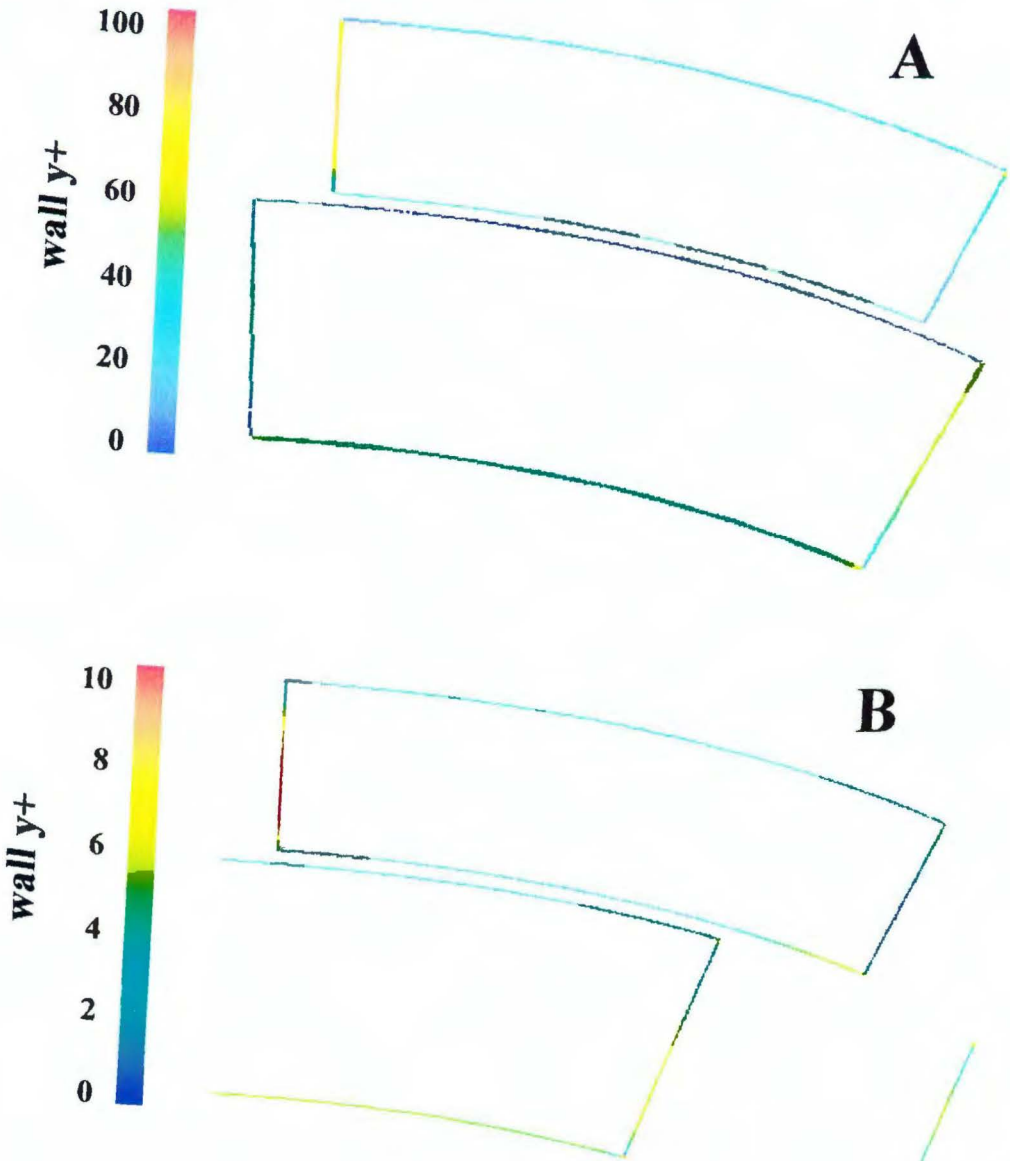

Figure 5-25. Wall y+ values at stator tooth 1 in the standard gap model. Simulation 5 at about time step 6,420 using standard wall functions (**A**), and the two layer zonal model (**B**).

extent the rotor side, of the gap have y+ values that are too low for proper application of wall functions. Thus, on this basis alone, not to mention the strong pressure gradients present at some places in the gap, the wall function approach may be a bad choice for simulating devices with very small gaps.

Generally, y+ values for the two-layer zonal model as applied in Fluent should be ≤ 1, but may be slightly larger (Fluent Inc., 1997). Figure 5-25b illustrates wall y+ values for the simulation using the two layer zonal model, and shows that the adapted mesh yields (barely) appropriate values of y+.

5.1.8 Slot Mass Flow Rates

Time dependent mass flow rates through the stator slots are shown in Fig. 5-22. For all slots, the maximum occurs at about 4 time steps (4.3°) after rotor-slot stator-slot alignment, which corresponds to a half-closed orientation (rotor position 4). This is the same position at which maximum slot mass outflow appears in the wide gap model (Fig. 4-14), however, there is a big difference between the mass outflow patterns in the two simulations. In the standard gap model, after attaining a maximum, mass outflow through all the slots very rapidly decreases to a minimum and remains approximately constant until a rotor tooth has completed its passage by the stator slot (time step 20 in Fig. 5-22). After this, the rotor and stator slots are just starting to become aligned (corresponding to Figs. 5-1 through 5-3), the jet in the gap region first enters the stator slot, and the mass flow rate through the slot begins to rapidly increase. One effect of decreasing the gap width from 4 to 0.5 mm appears to be that the slot mass outflows undergo extremely rapid changes, and when a rotor tooth is under a

stator slot, the flow is almost completely shut off (relative to the maximums). The rotor teeth in the standard gap simulation are more effective at acting like a fully opening-closing valve, controlling flow from the stator slots. The mass flow rates through each of the 12 stator slots in the standard gap simulation still correlate with their distance from the outlet (Figs. 5-22 and 5-26). However, the differences are more gradual and not as great as in the wide gap simulations: The mass outflows from slot to slot are much more evenly distributed. Clearly this is a result of the more pulsating nature of the slot mass flow rates, but a detailed physical explanation cannot be given at this time.

5.1.9 Mean Flow Patterns in The Stator Slots and Volute

The mean flow forms a vortex pattern in stator slot 1 at all times throughout the simulation. The size of the vortex in the standard gap model appears to change its size throughout a period of simulation. In Fig. 5-1, with the rotor slot just beginning to come into alignment with a stator slot, the vortex extends all the way from the left side of slot 1 to within about 0.5 mm of the right side. Later, when the rotor and stator slots are fully aligned, the right side of the slot vortex is shifted about 0.5 mm more to the left (Fig. 5-7). Even later, when the rotor and stator slots have moved back to half alignment, the right side of the vortex is further shifted so that it is at its smallest width, spanning only about one half of the stator slot (Fig. 5-10). This is in contrast to the vortex in the wide gap model where changes in its width were not as large. The difference is likely due to the fact that the gap mean velocities in the standard gap model undergo a much stronger shift from a tangential to radial direction throughout a

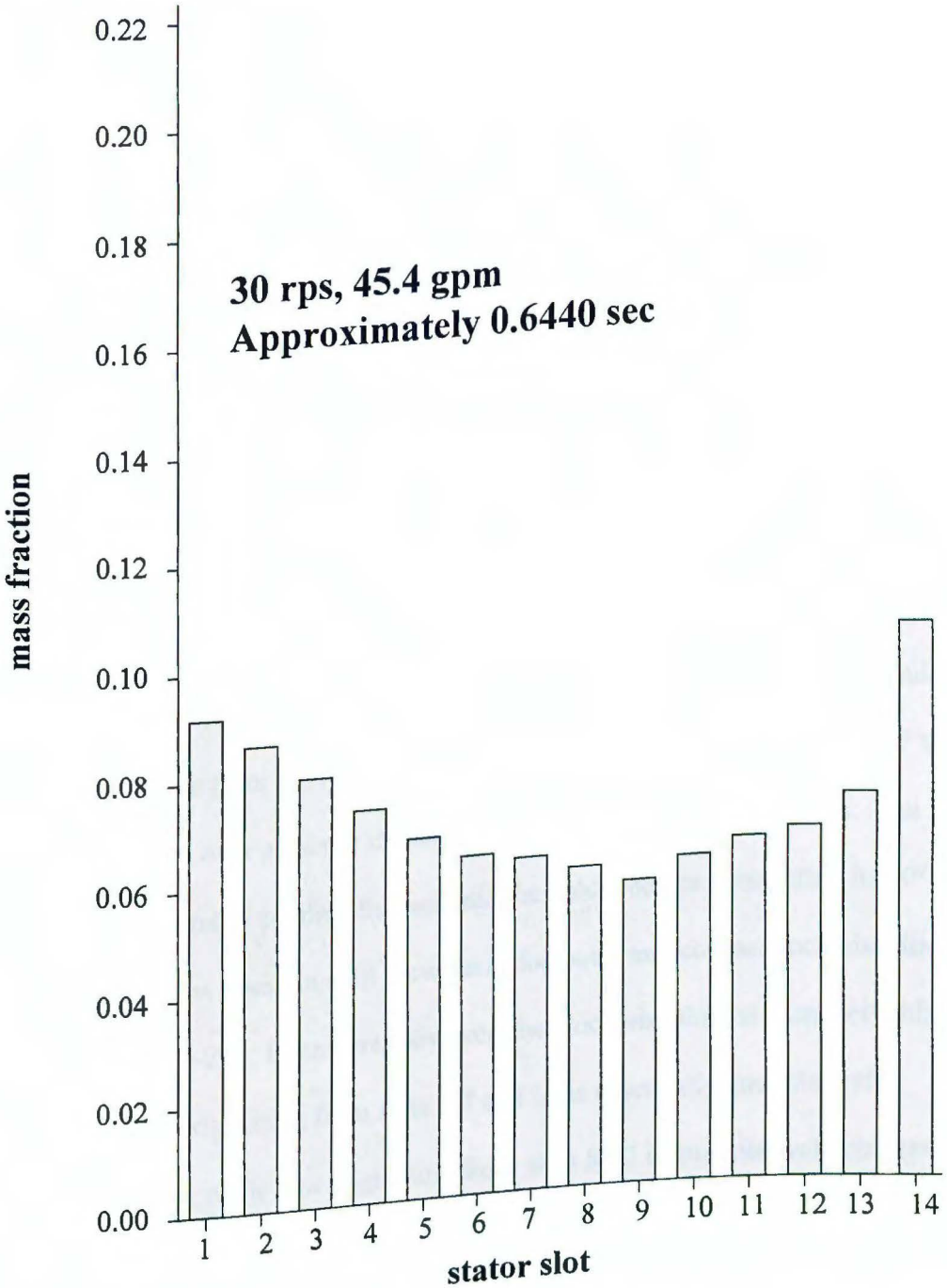

Figure 5-26. Fixed frame mass flow rates through stator slots in the standard gap model after about 6,420 time steps. Simulation 5

period of simulation than those in the wide gap models (compare Figs. 5-1 and 5-10 with 4-7 and 4-10). When the slots are half out of alignment in the standard gap simulations, the radial flow in the gap forces the vortex to reduce its width, whereas in the wide gap model the vortex always spans only about one half to two thirds of the slot width, since there is always a considerable amount of mass outflow from the slots.

In the volute, the mean flow directly at the top right of a stator slot changes in magnitude in a periodic fashion as the mass flow rate out the slot cycles. Superficially, the volute mean flow appears to be only weakly directionally periodic and so analysis of the fixed frame velocity field in this region is appropriate, as it was for the wide gap model. In the portion of the volute near stator slot 1 (Fig. 5-27), the fixed frame flow pattern is similar to that found in the wide gap simulation (Fig. 4-18) except it is not as stagnated and recirculatory close to stator teeth 1 and 14: Reversal of flow along the teeth from the volute back into the stator slots is not seen. Fluid entering the volute from the top right side of stator slot 1 appears to make a 90° turn towards the outlet over a shorter distance than in the wide gap simulations: The flow from the slot extends a smaller distance into the volute before completing its 90° turn).

Volute flow does not split between a clockwise and counterclockwise direction until slot 7 (Fig. 5-28). Even here, however, the clockwise flow is extremely minor so that volute flow originating from slots 1-7 and 14 is essentially quantitatively counterclockwise, while that originating from slots 8-12 is quantitatively clockwise. The volute flow field near slots 9 – 12 (Figs. 5-29 and 5-30) indicates that there may be some reentrainment of fluid back into the stator slots as was evident in the wide gap simulations. The volute flow patterns near slots 13 and 14 are qualitatively similar to

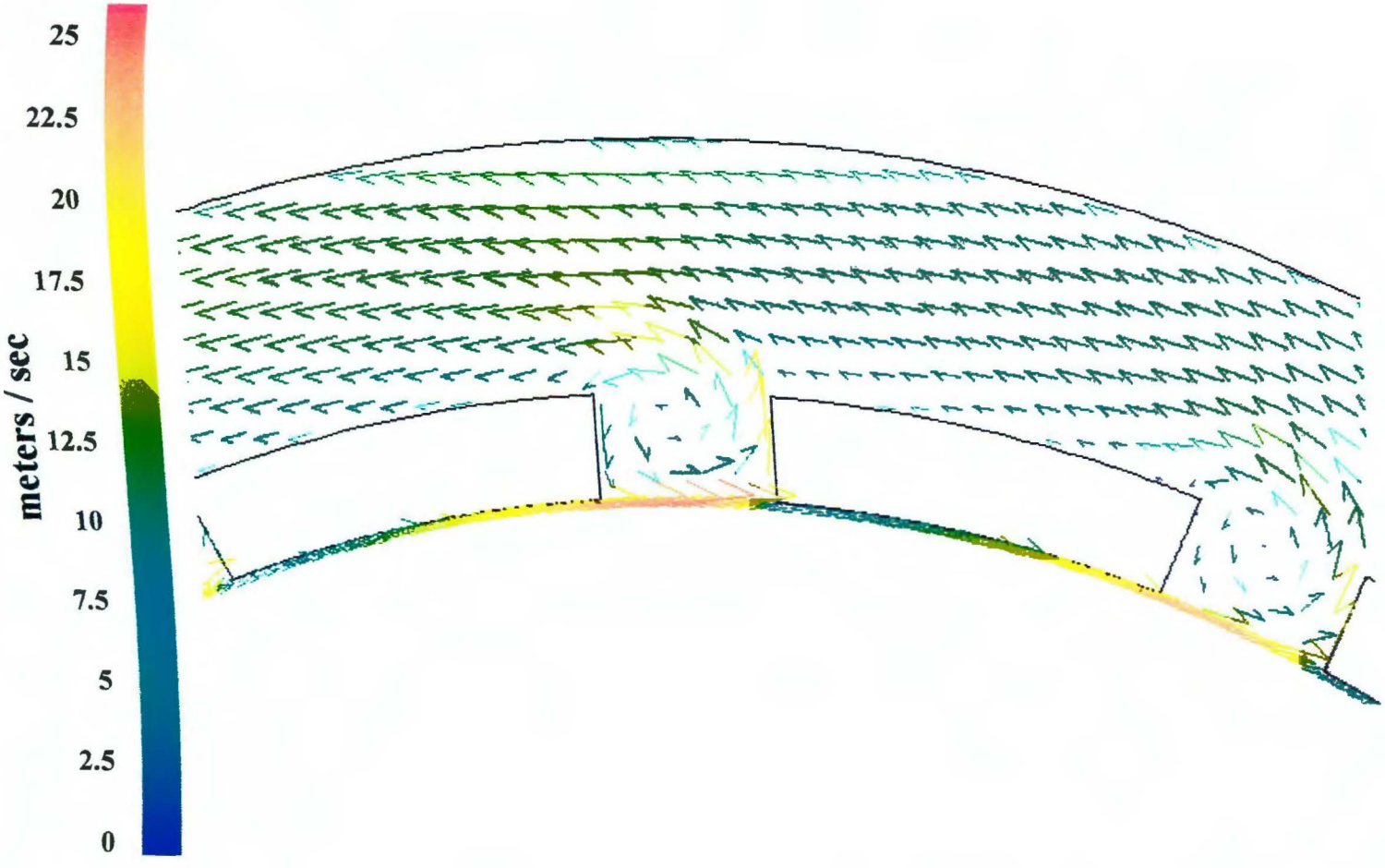

Figure 5-27. Fixed frame velocity vectors near slots 1 and 2 after 19 revolutions of simulation. Simulation 5

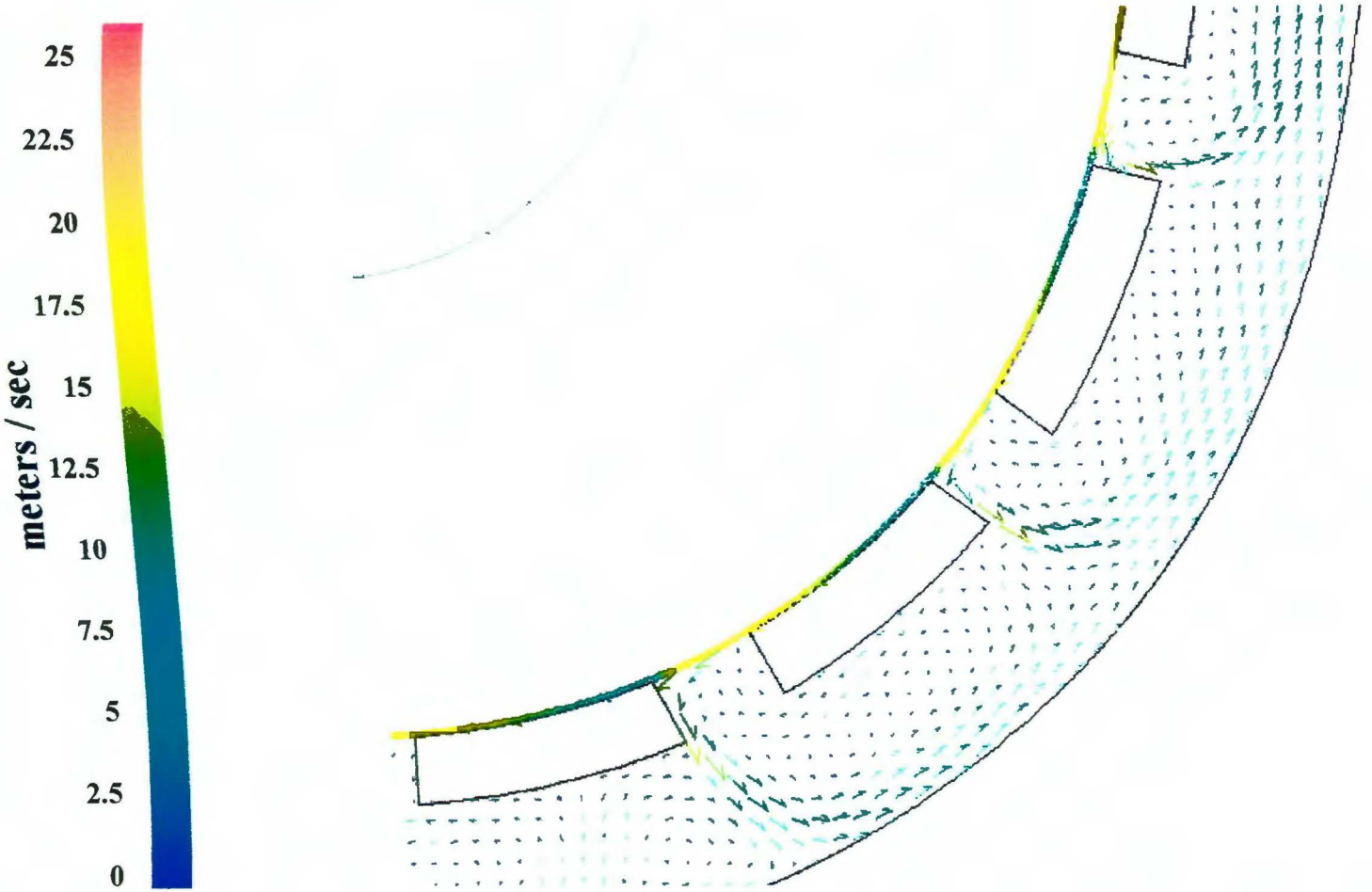

Figure 5-28. Fixed frame velocity vectors near slots 5 - 7 after 19 revolutions of simulation. Simulation 5

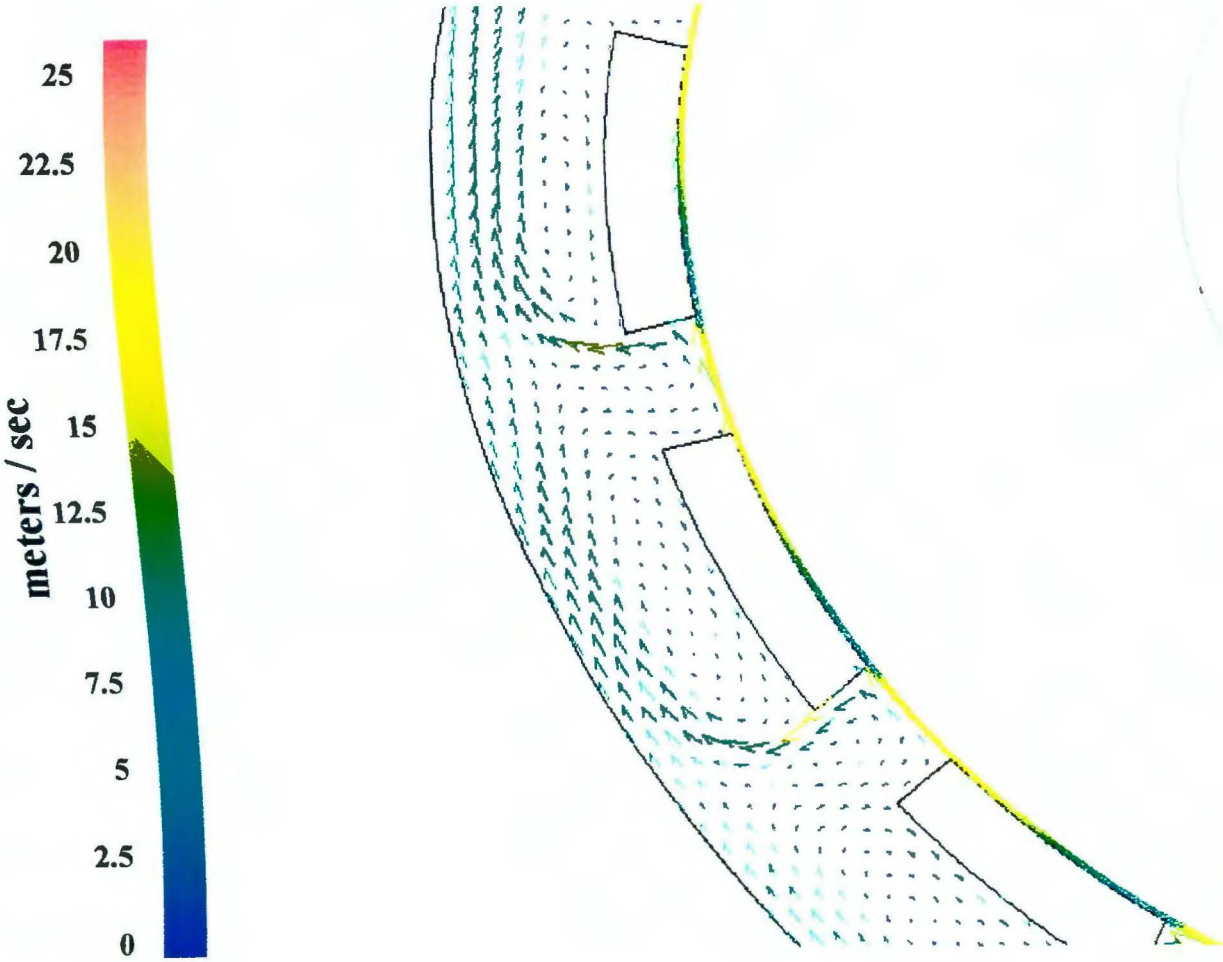

Figure 5-29. Fixed frame velocity vectors near slots 10 and 11 after 19 revolutions of simulation. Simulation 5

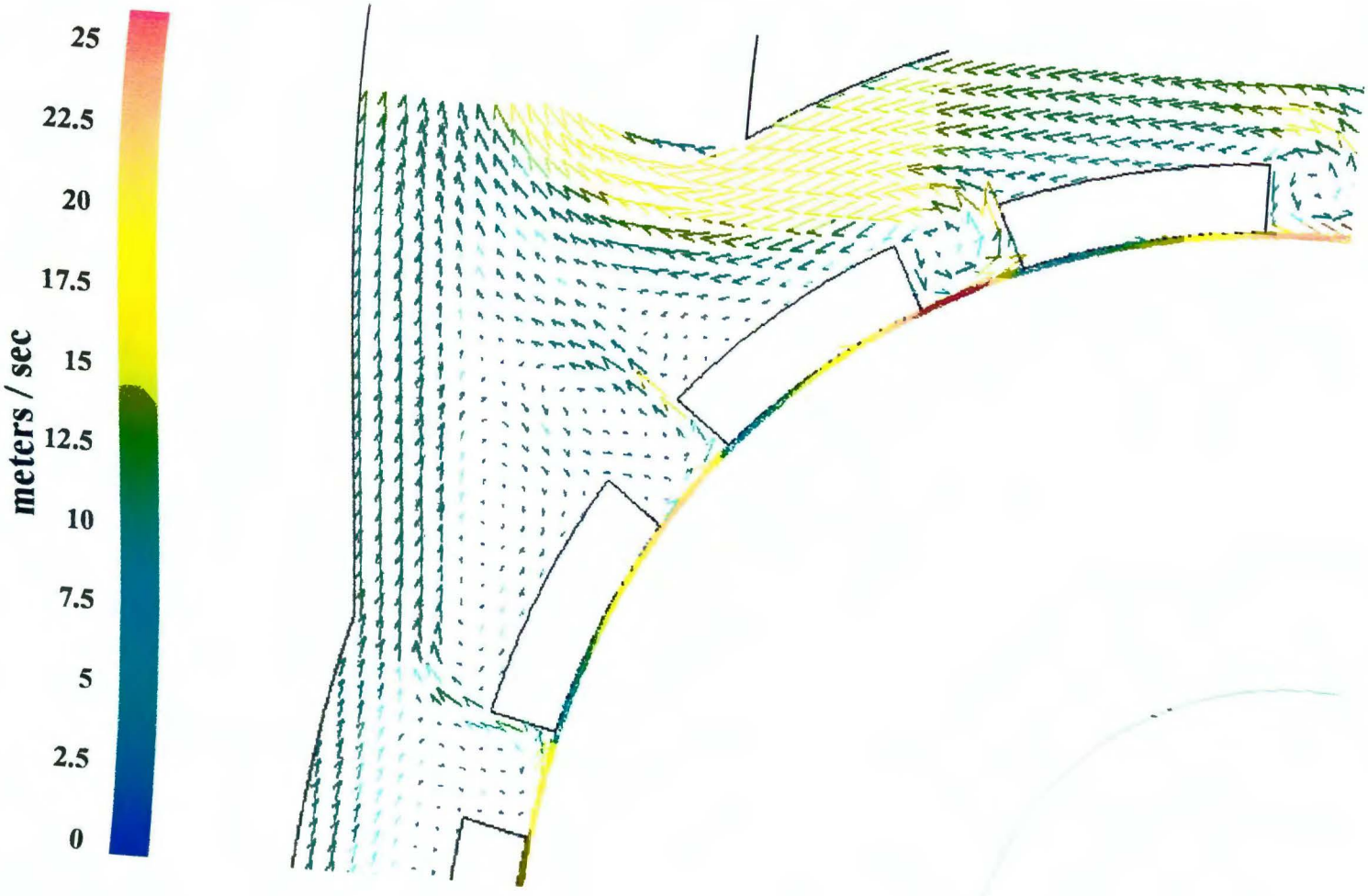

Figure 5-30. Fixed frame velocity vectors near slots 12-14 after 19 revolutions of simulation. Simulation 5

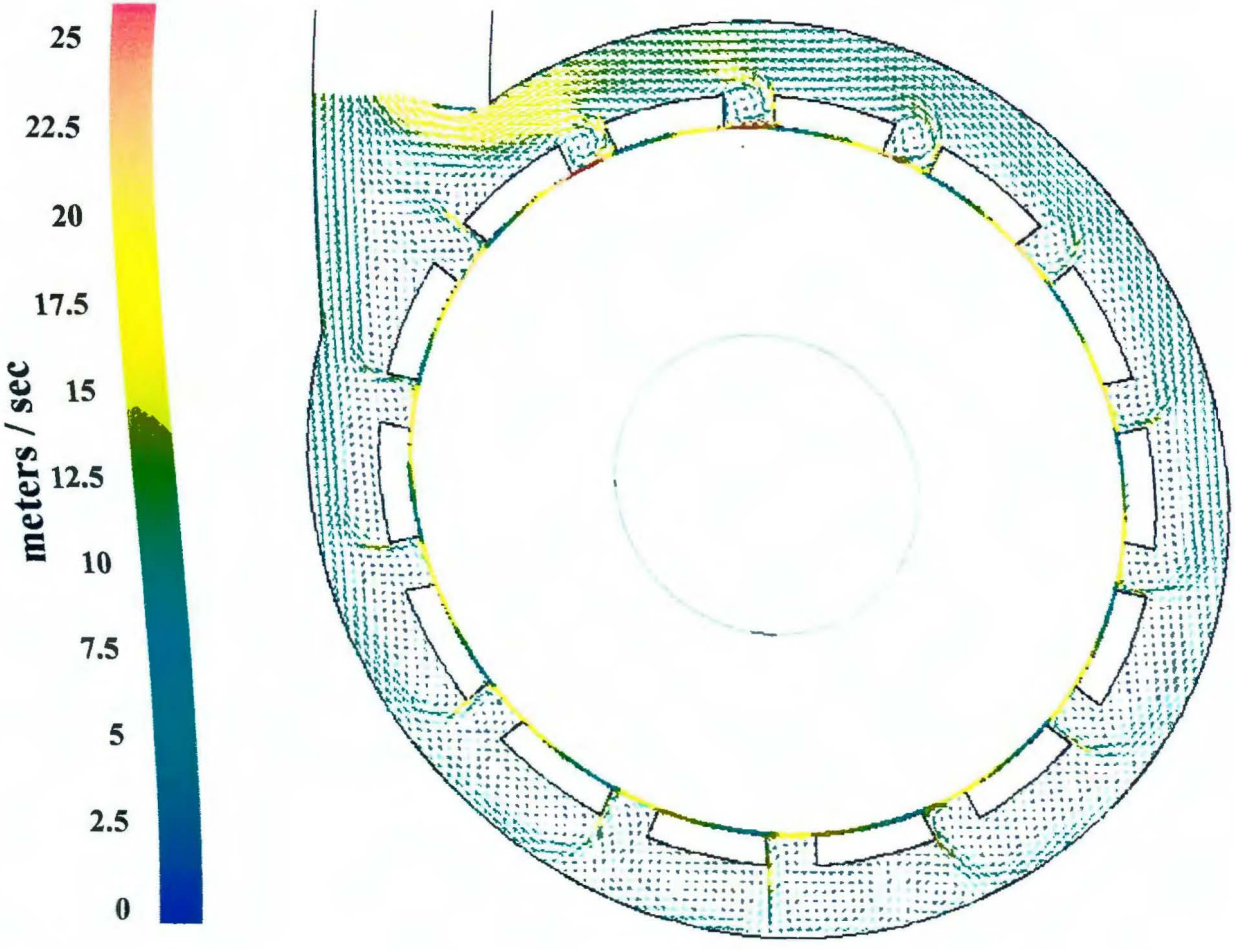

Figure 5-31. Fixed frame velocity vectors in the entire domain after 19 revolutions of simulation. Simulation 5

those found for the wide gap model (compare Figs. 4-21 and 5-30), however, note that the mean velocity magnitudes of the fluid exiting these slots are significantly smaller in the standard gap simulation. This is related to the fact that the slot mass outflows are more evenly distributed in the standard gap simulations.

Figures 5-32 and 5-33 show the pathlines, due to the fixed frame velocity field, followed by massless particles released from imaginary lines spanning all the way across the gap (compare to Figs. 4-23 and 4-24 for the wide gap simulations). In the standard gap model, the particles always exit the stator slot closest (in the downstream sense) to their point of release whereas, in the wide gap model, a substantial number of particles exit at the second or even third nearest stator slot. This difference is explained by the fact that in the wide gap model particles released near the rotor side of the gap must travel about 4 mm radially to exit the nearest slot. Since gap flow is for the most part only weakly radial in the wide gap simulations, a substantial number of particles do not exit the nearest stator slot. In the standard gap simulations, not only is the maximum radial distance that a particle must travel to span the gap 8 times smaller than in the wide gap model, but the gap velocities are at times more strongly radial (compare Figs. 4-10 and 5-10) which results in all particles exiting the slot nearest their release.

5.2 Mean Pressure Field

For reasons similar to those stated in section 4.7, full analysis of the simulated mean static pressure field in the standard gap simulations was not done. The (relative) invariance of the *simulated* static pressure near the inlet due to the numerical treatment

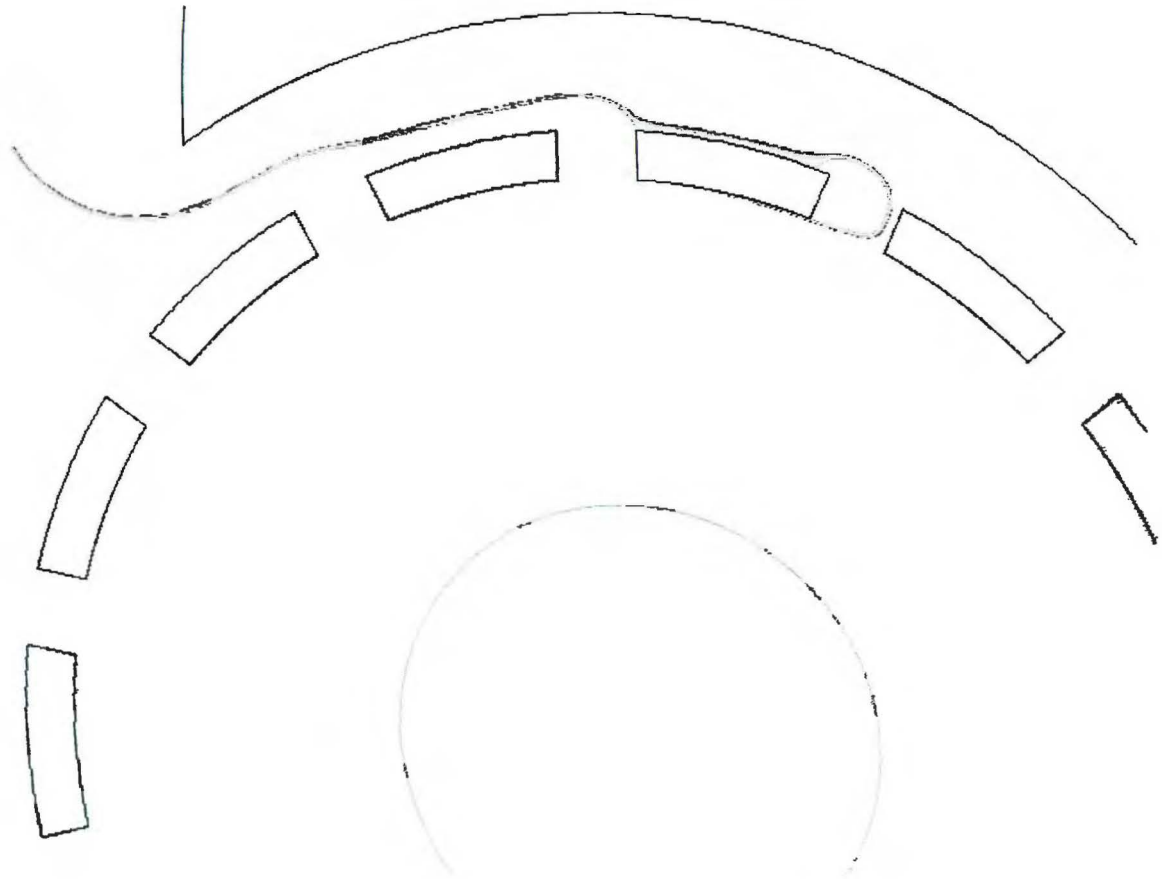

Figure 5-32. Pathlines near slot 2 due to the fixed frame velocity field after 19 revolutions of simulation. Simulation 5

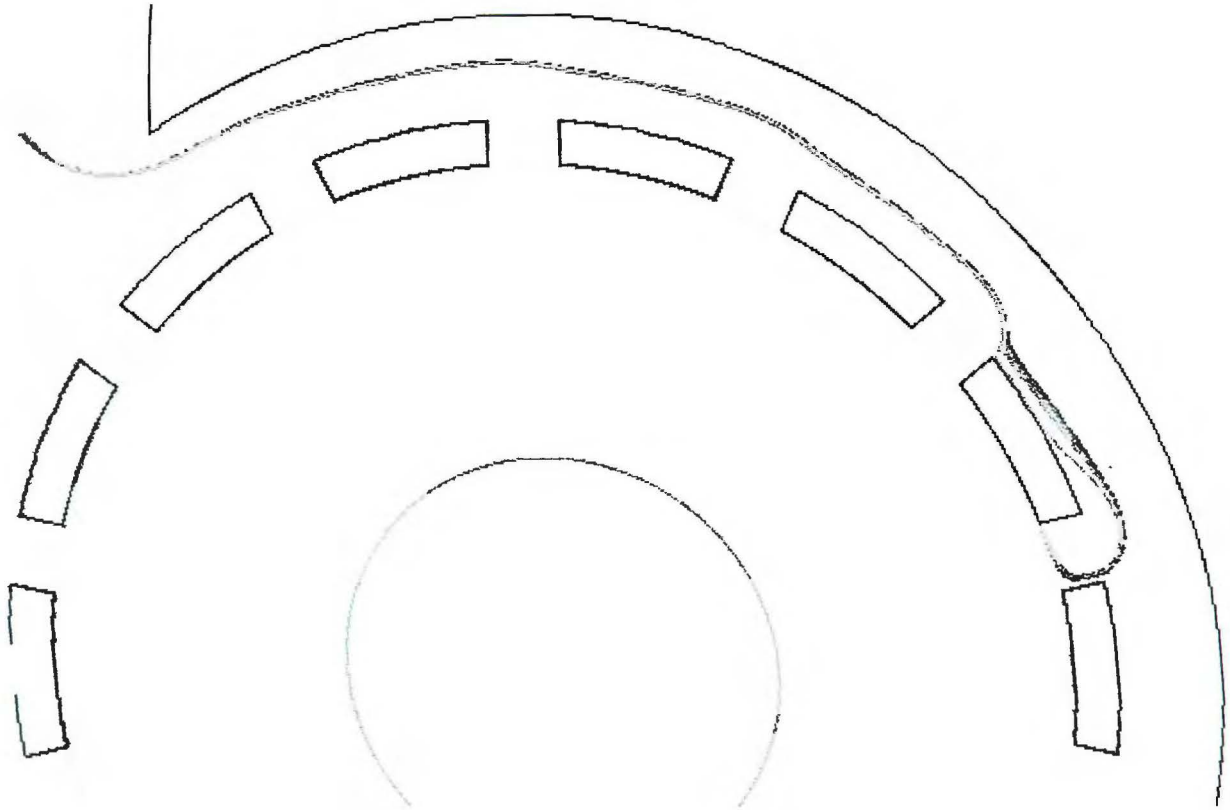

Figure 5-33. Pathlines near slot 4 due to the fixed frame velocity field after 19 revolutions of simulation. Simulation 5

used for the outflow boundary condition can be inferred from the sequence of Figs. 5-34 through 5-40, which show the time dependent mean static pressure near stator slot 1. Note that, near the bottom of these figures, the simulation resulted in a static pressure near zero at all times, although clearly there are small changes throughout the period there.

With the outflow boundary condition it is only possible to observe simulated mean pressure differences between regions that are insensitive to changes in the pressure field of the inlet region. Based on results from the wide gap simulations, it is hard to believe that this is fully true anywhere in the gap and stator slots. For instance, Figs. 4-32 and 4-33 clearly show that, when the mean pressure is very low or very high in the inlet region, then the mean pressures in the gap and slots are also (on average) high or low.

Nevertheless, it should still be possible to observe gross differences in static pressure in the gap, stator slots, and volute regions. Figures 5-34 through 5-40 are a sequence showing the simulated mean static pressure near stator slot 1 throughout a period. Immediately before a rotor slot and stator slot 1 become partially aligned (Fig. 5-34), the mean pressure in the stator slot is about –2 bar relative to the inlet. Four and eight time steps later, when the rotor and stator are in half (Fig. 5-35) or full (Fig. 5-36) alignment, the slot mean pressure first increases to about –1 bar relative and then decreases. The decrease in slot mean pressure continues as the rotor and stator slots move out of alignment (Figs. 5-37 and 5-38), the lowest slot mean pressure of about –7 bar being reached when the two slots first reach a fully closed orientation (Fig. 5-

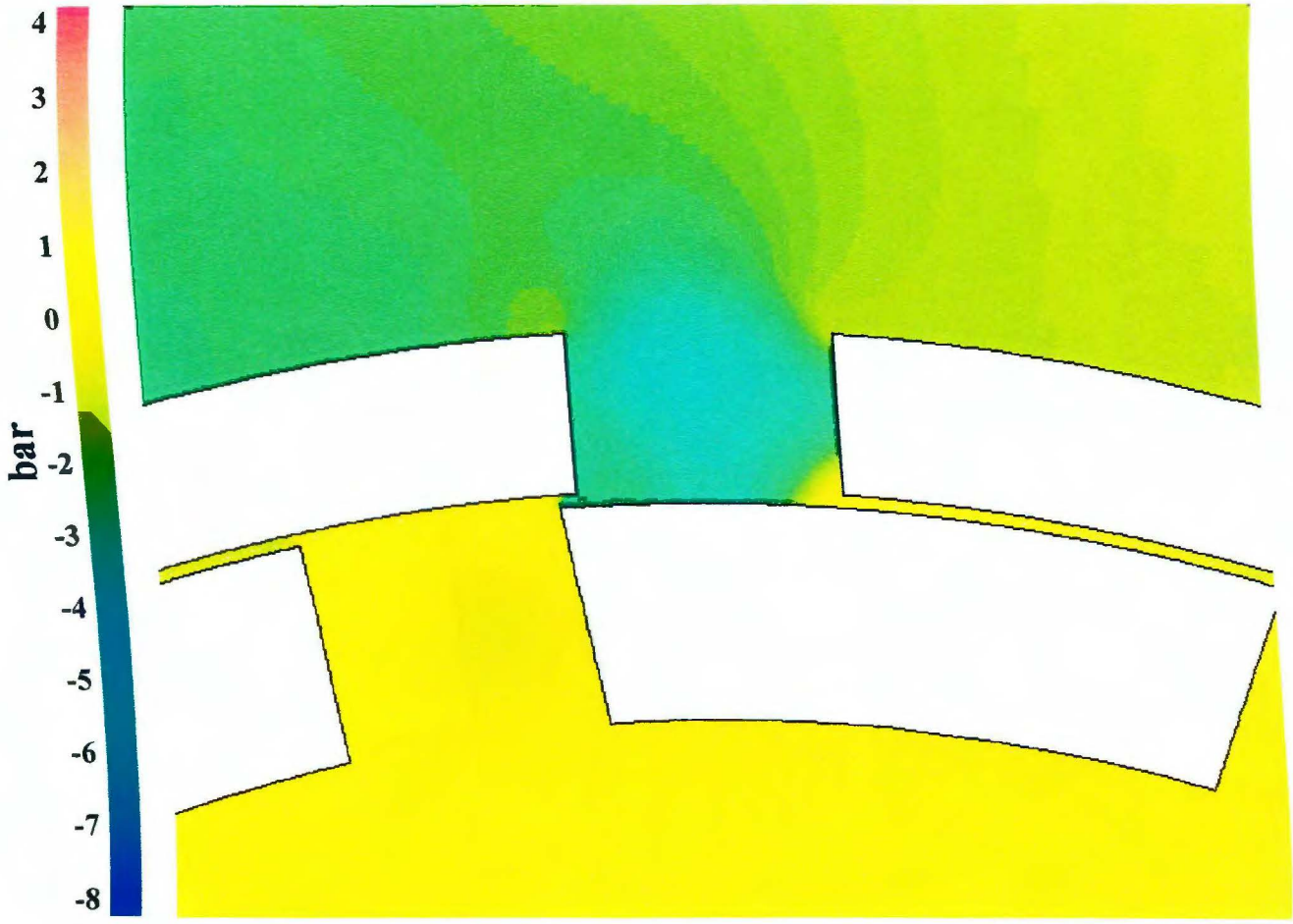

Figure 5-34. Angularly resolved mean static pressure near slot 1 at time step 6,412 (0.6432 seconds). Simulation 5.

Figure 5-35. Angularly resolved mean static pressure near slot 1 at time step 6,416 (0.6436 seconds). Simulation 5.

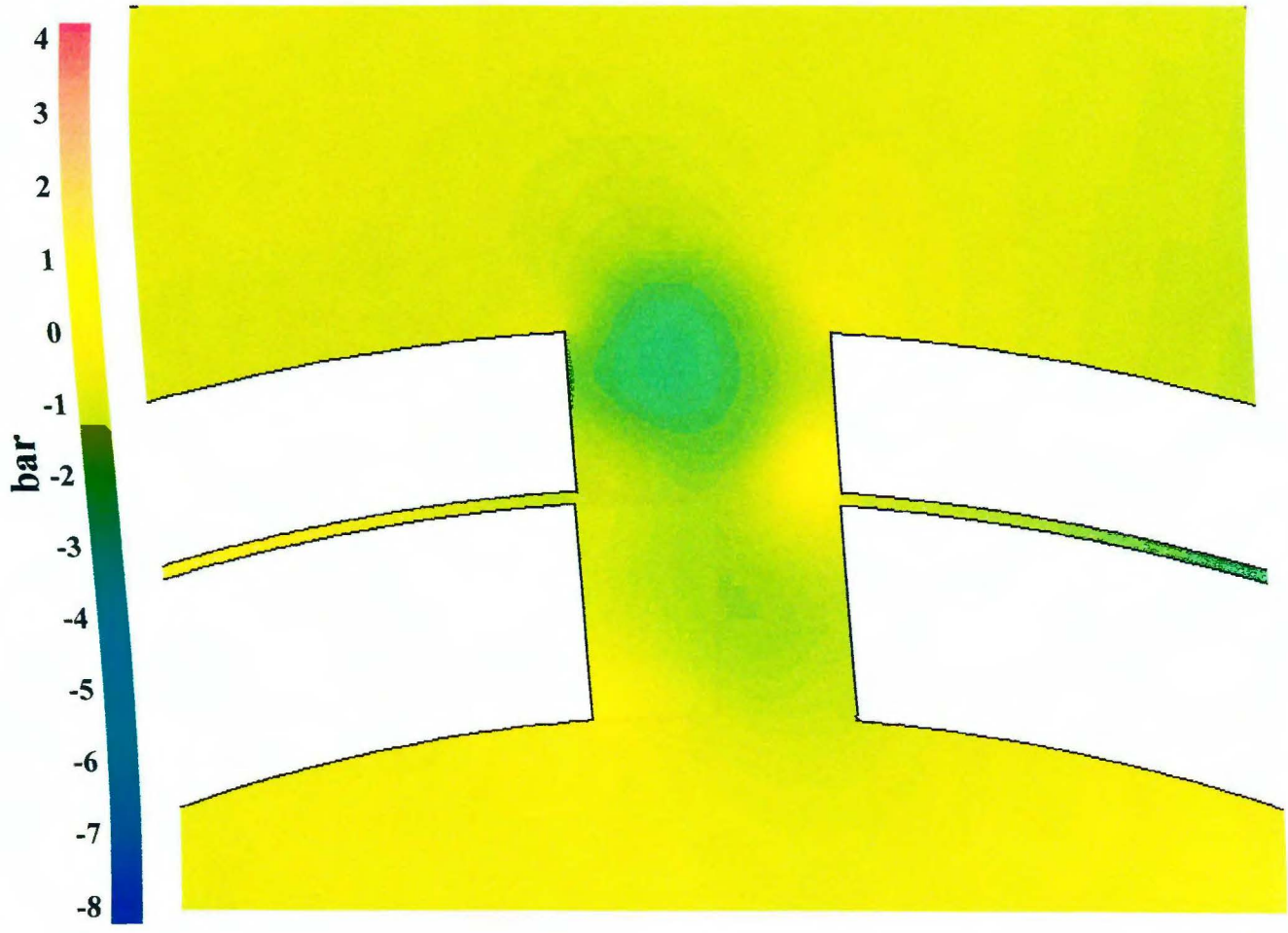

Figure 5-36. Angularly resolved mean static pressure near slot 1 at time step 6,420 (0.6440 seconds). Simulation 5.

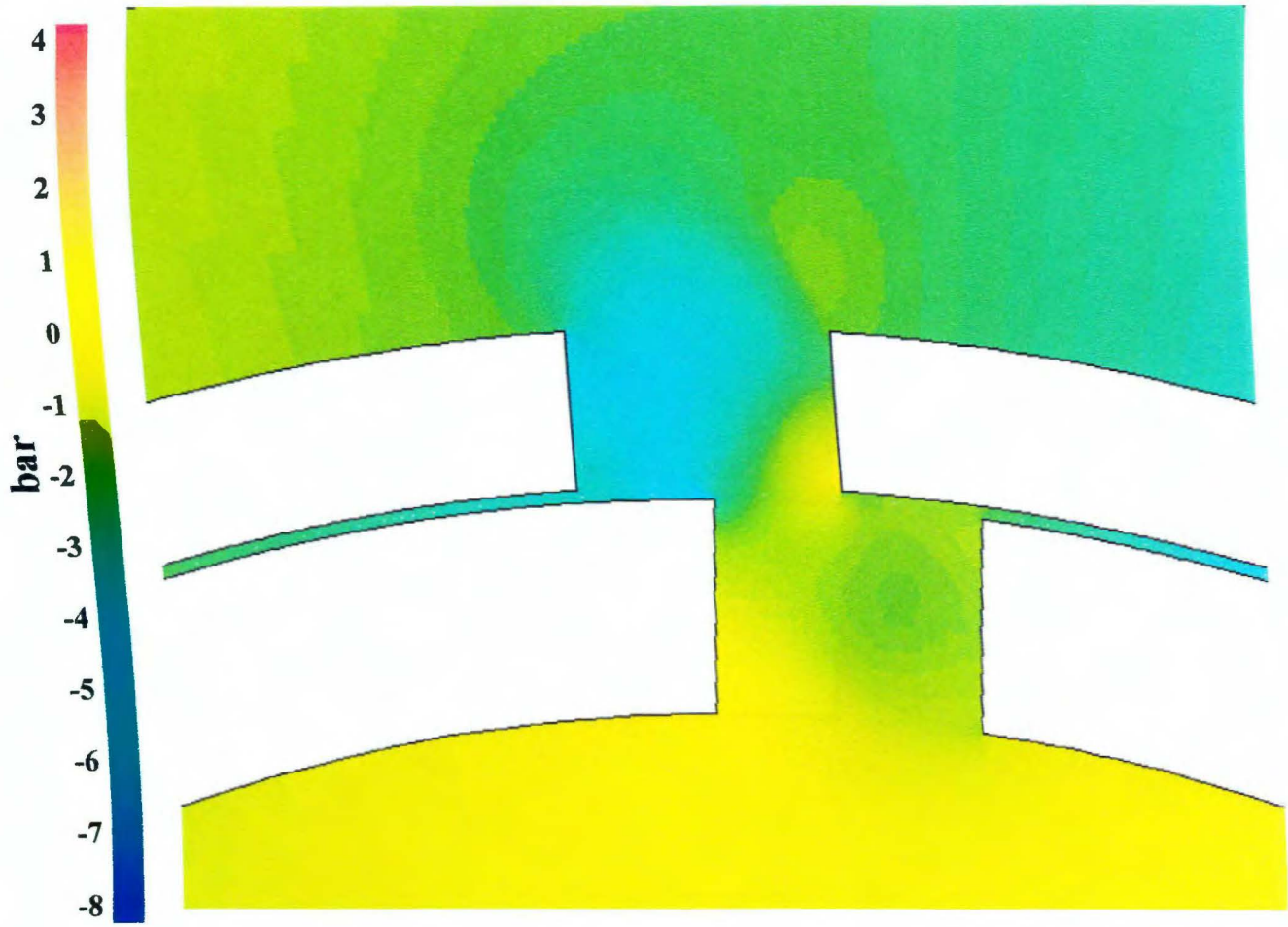

Figure 5-37. Angularly resolved mean static pressure near slot 1 at time step 6,424 (0.6444 seconds). Simulation 5.

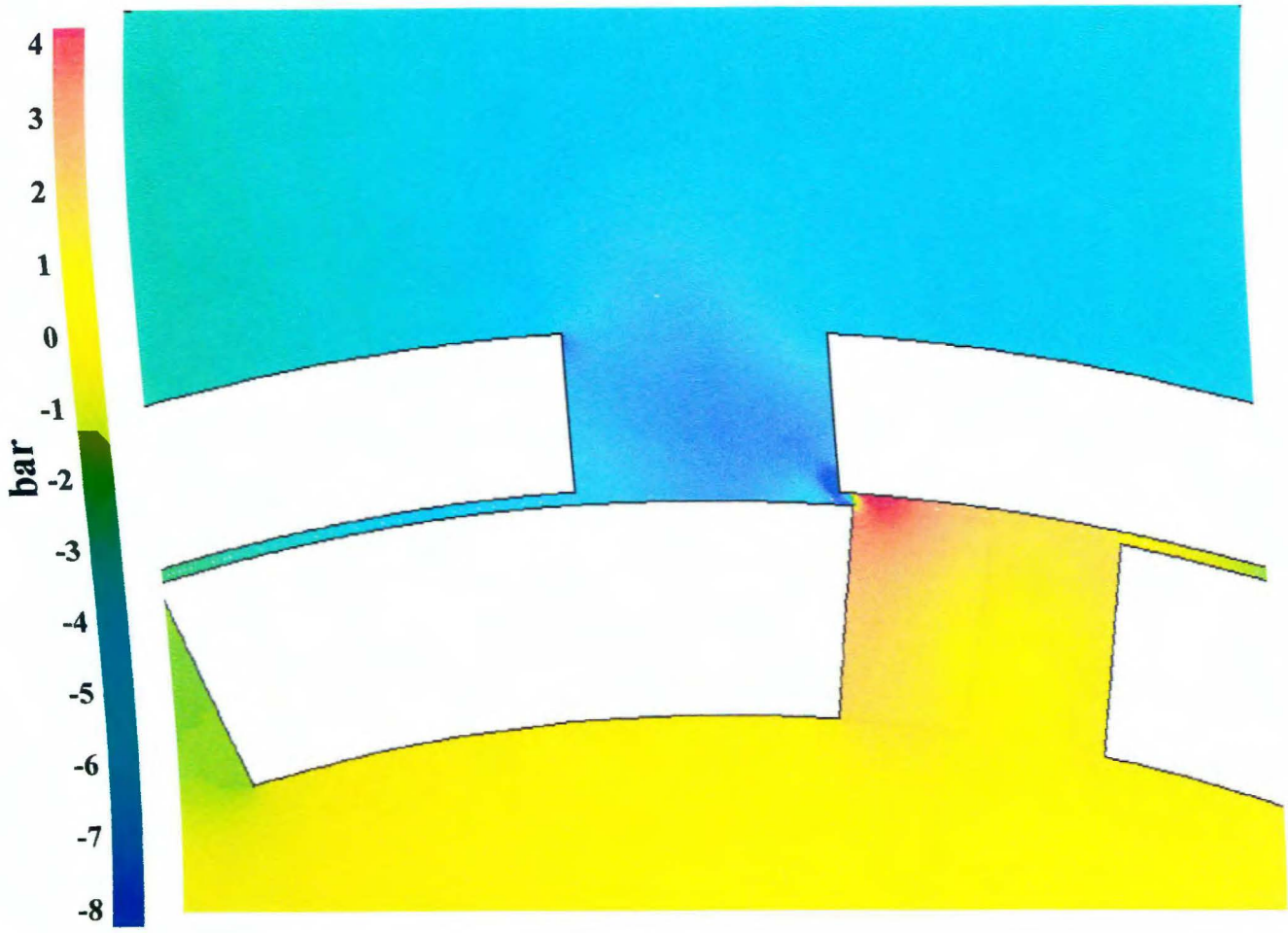

Figure 5-38. Angularly resolved mean static pressure near slot 1 at time step 6,428 (0.6448 seconds). Simulation 5.

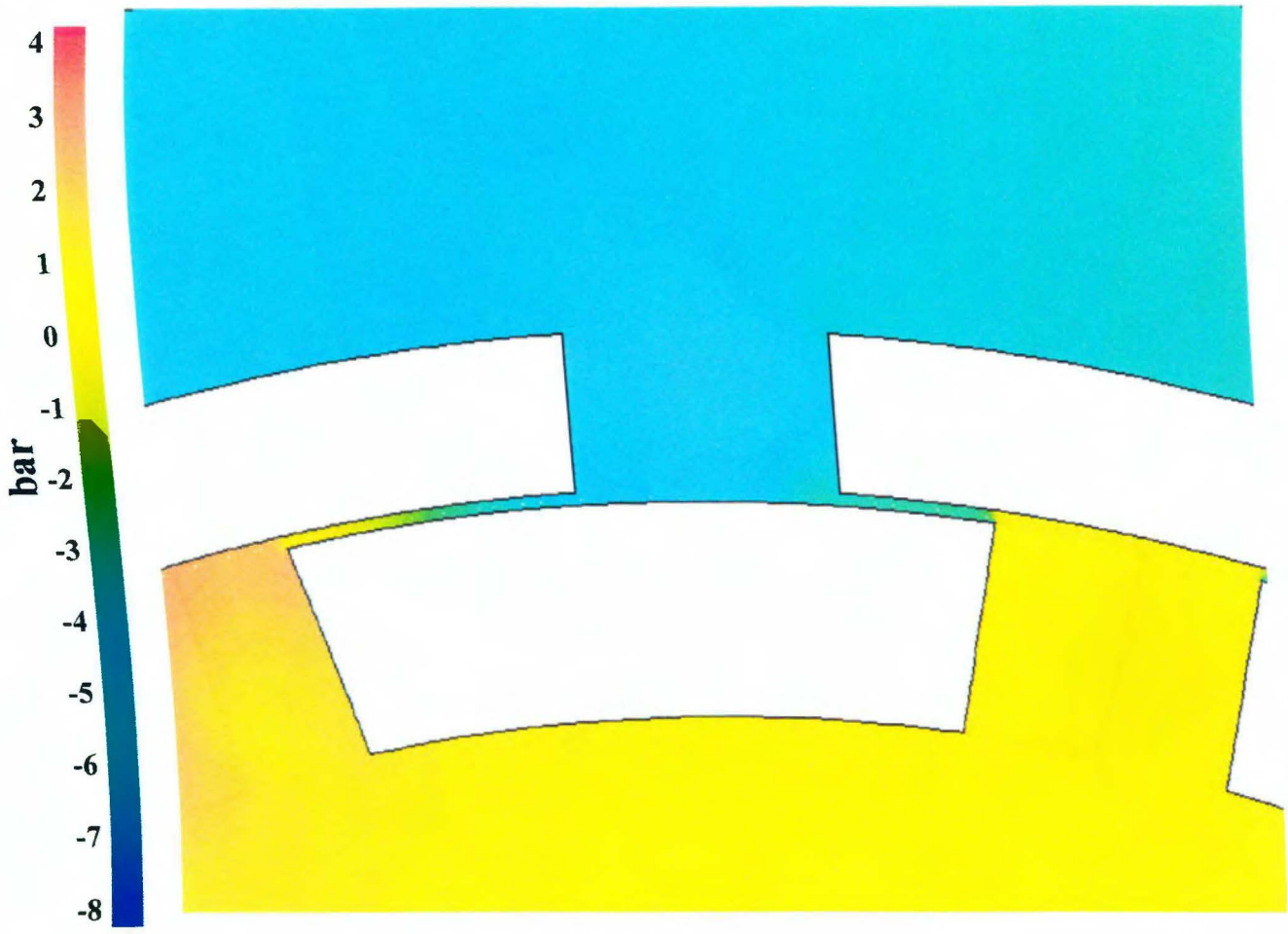

Figure 5-39. Angularly resolved mean static pressure near slot 1 at time step 6,432 (0.6452 seconds). Simulation 5.

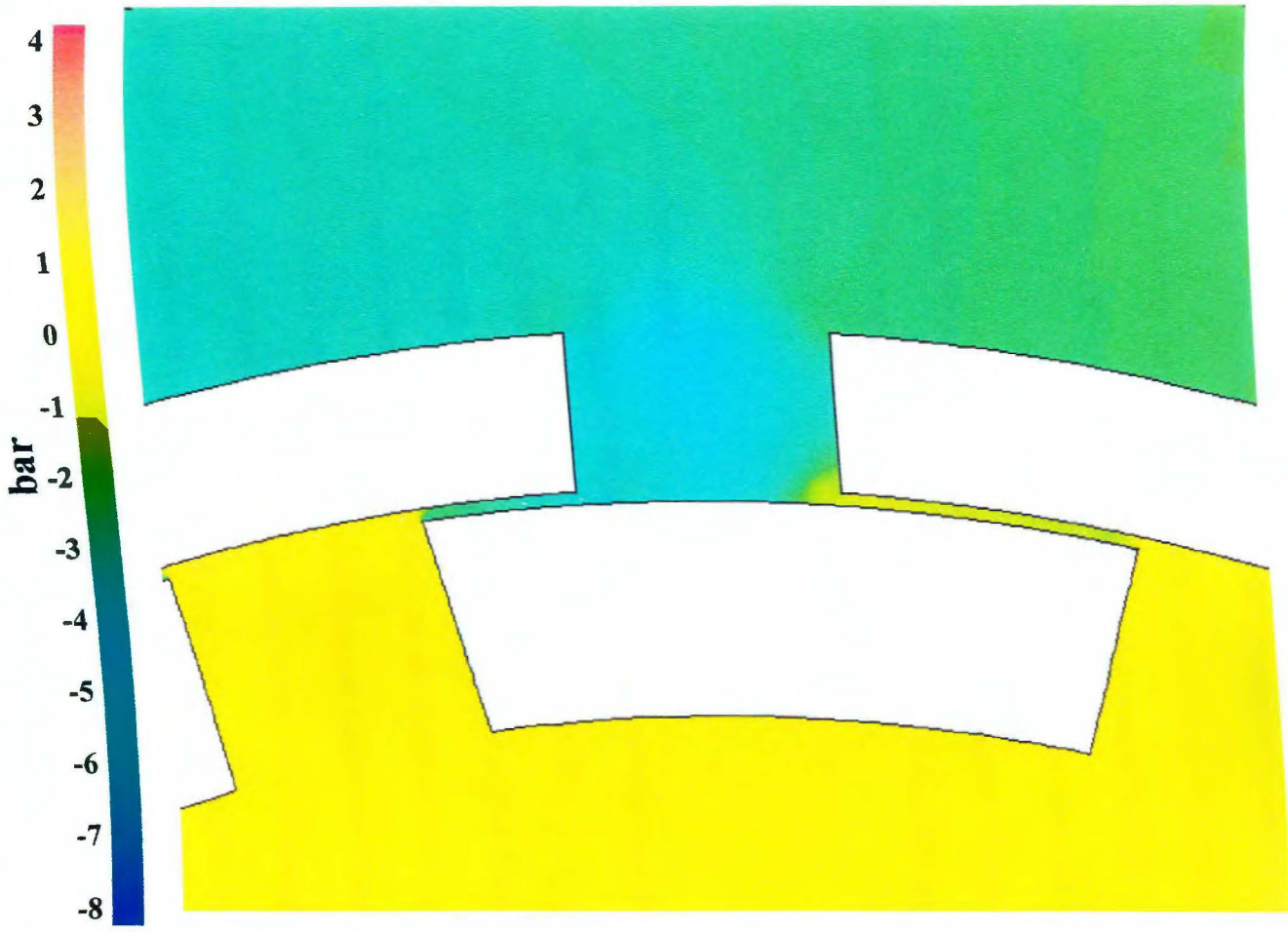

Figure 5-40. Angularly resolved mean static pressure near slot 1 at time step 6,436 (0.6456 seconds). Simulation 5.

38). Through the next 8.6° of rotation, the slot mean pressure increases to an average of about –2 bar relative (Figs. 5-39 and 5-40).

In the region near the right corner of slot 1, the mean pressure is relatively high even as the pressure goes low in the majority of slot 1 (Figs. 5-34 through 5-37). This corresponds to the high-pressure region seen on the same corner in the wide gap simulations. As soon as the two slots are fully closed (Fig. 5-38), the high-pressure region rounds the corner of stator tooth 1 and takes on its highest value of about 4 bar relative. The lowest slot mean pressure is also reached at this time, and occurs directly adjacent to the high-pressure region. These two adjacent regions of high and low pressure occur at the same position and rotor-stator orientation as that during gap flow reversal (Fig. 5-13).

5.3 Turbulence Field

Figures 5-41 through 5-47 illustrate the simulated turbulent kinetic energy near stator slot 1. Immediately before rotor-stator slot alignment (Fig. 5-41), there are two regions of relatively high turbulent kinetic energy. The first region occurs immediately above the top right corner of the rotor slot and is about 60 m^2/sec^2 in magnitude. The second region, which is of about equal magnitude, extends from the lower left corner of stator slot 1 to halfway across the slot. 4.3° of rotation later, when the rotor slot and stator slot 1 are half aligned (Fig. 5-42), both regions have decreased substantially so that their intensities are about 20 m^2 / sec^2. As the rotor slot moves past complete alignment with stator slot 1 and the opening between the slots decreases (Figs. 5-43 and 5-44), a region of high TKE is observed to form on the right lower

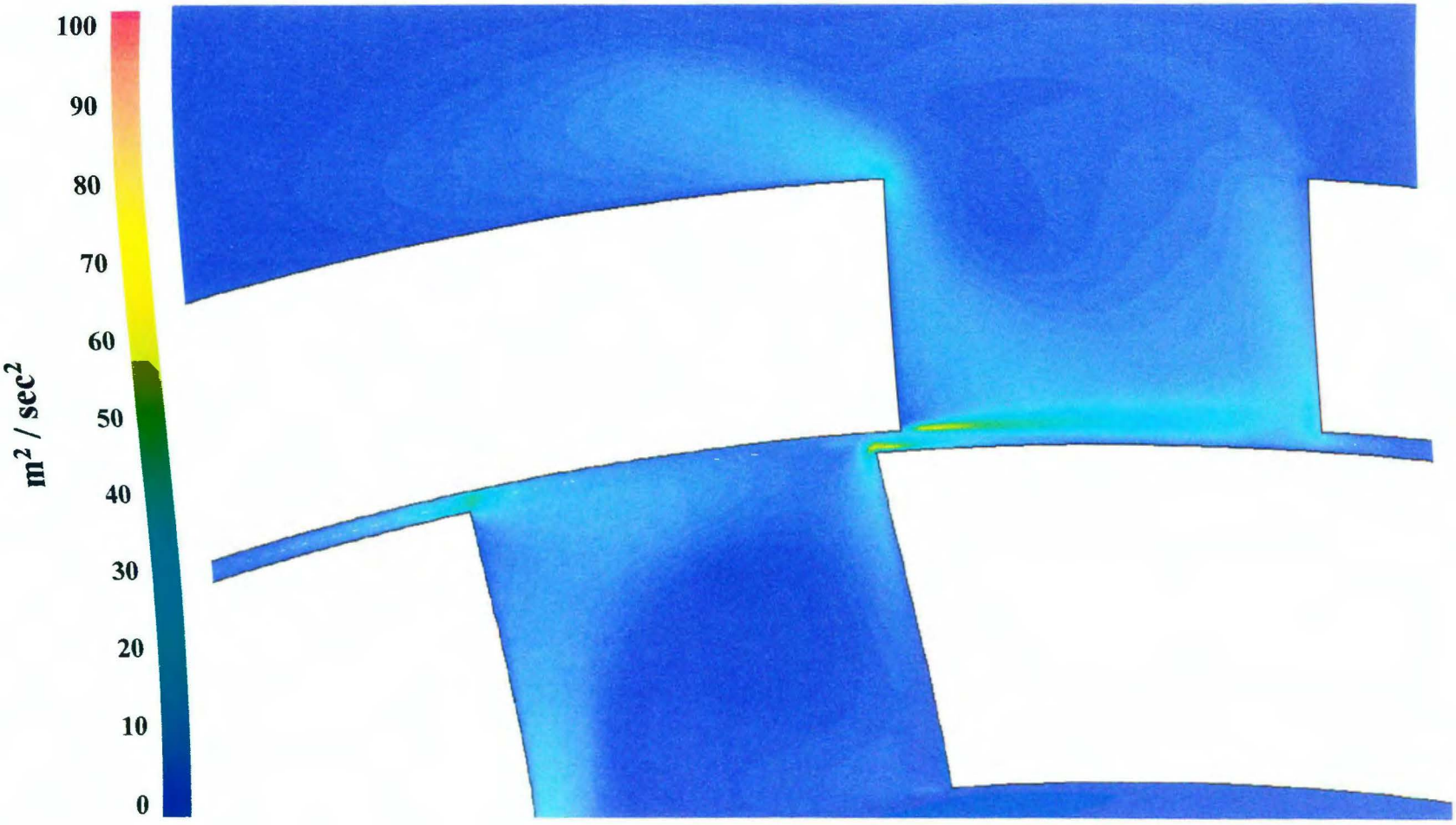

Figure 5-41. Angularly resolved turbulent kinetic energy near slot 1 at time step 6,412 (0.6432 seconds). Simulation 5.

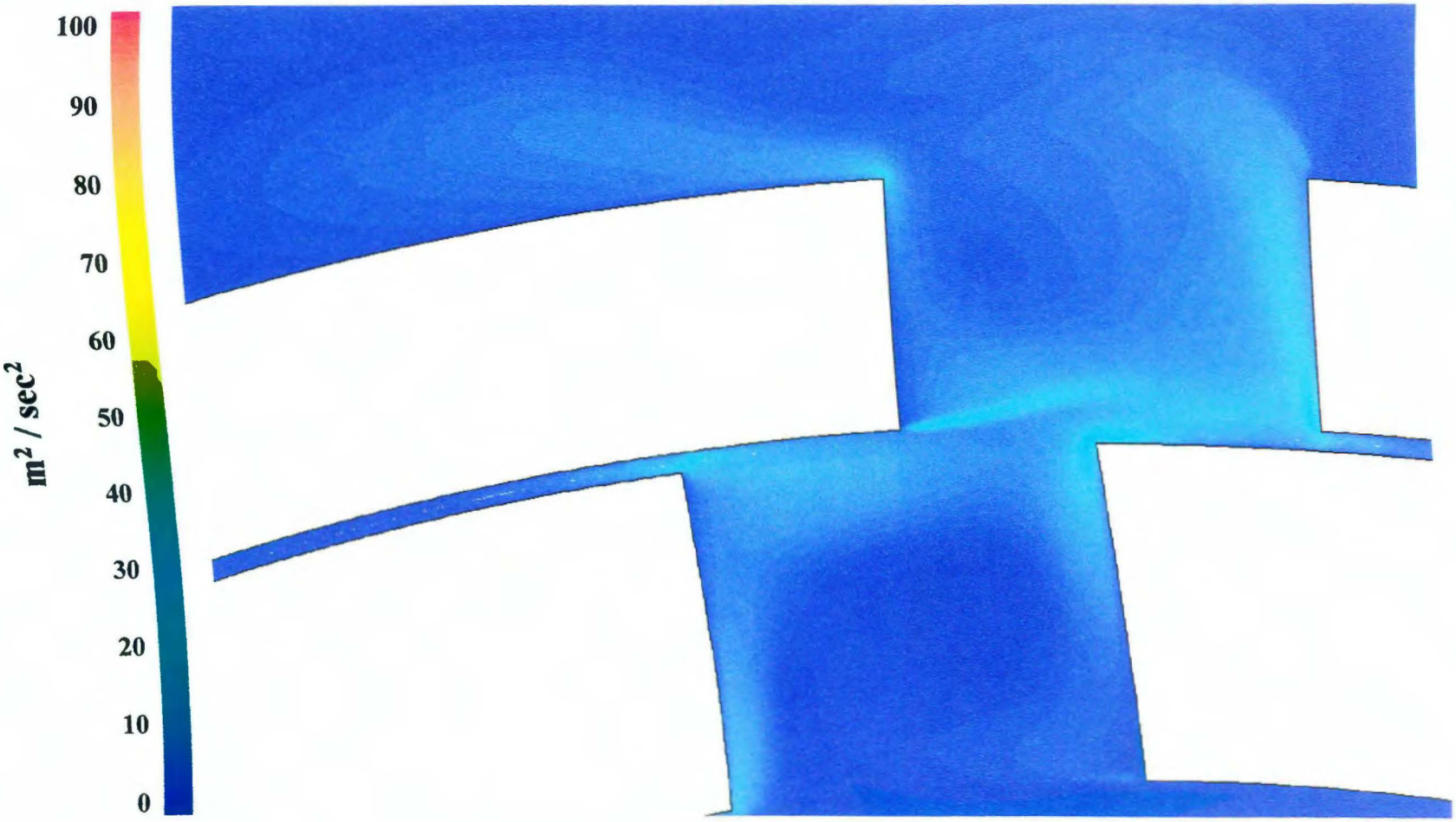

Figure 5-42. Angularly resolved turbulent kinetic energy near slot 1 at time step 6,416 (0.6436 seconds). Simulation 5.

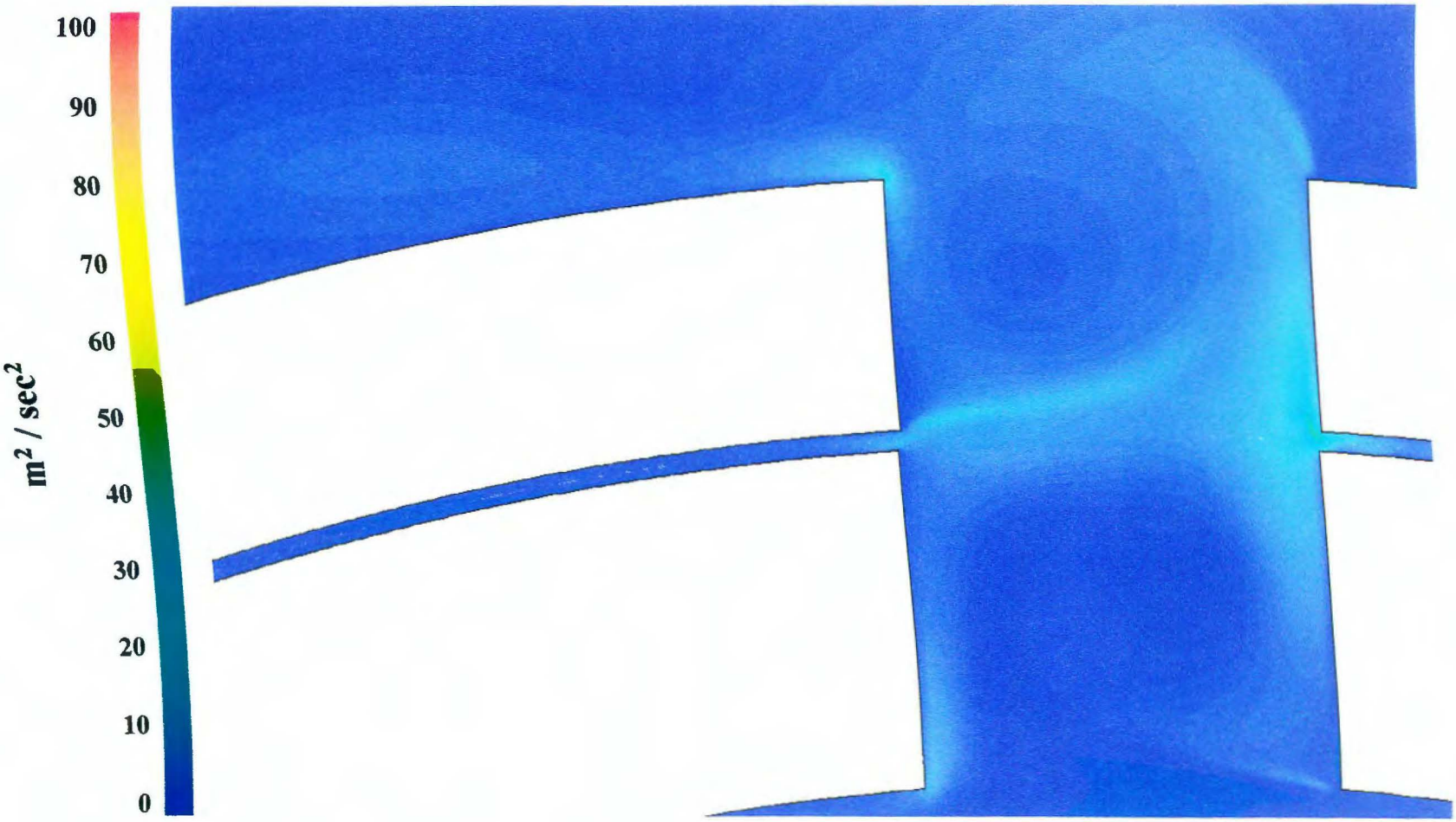

Figure 5-43. Angularly resolved turbulent kinetic energy near slot 1 at time step 6,420 (0.6440 seconds). Simulation 5.

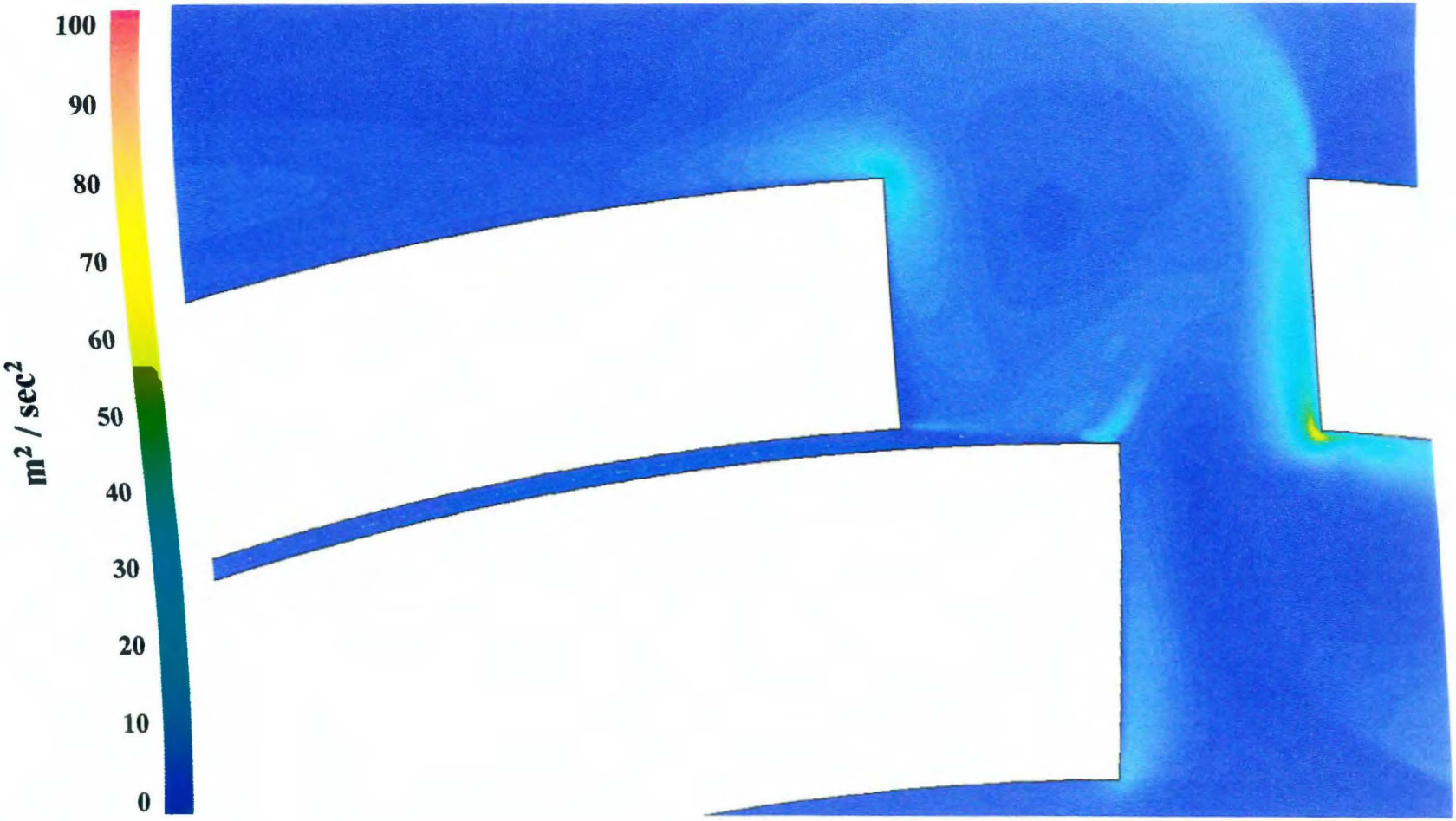

Figure 5-44. Angularly resolved turbulent kinetic energy near slot 1 at time step 6,424 (0.6444 seconds). Simulation 5.

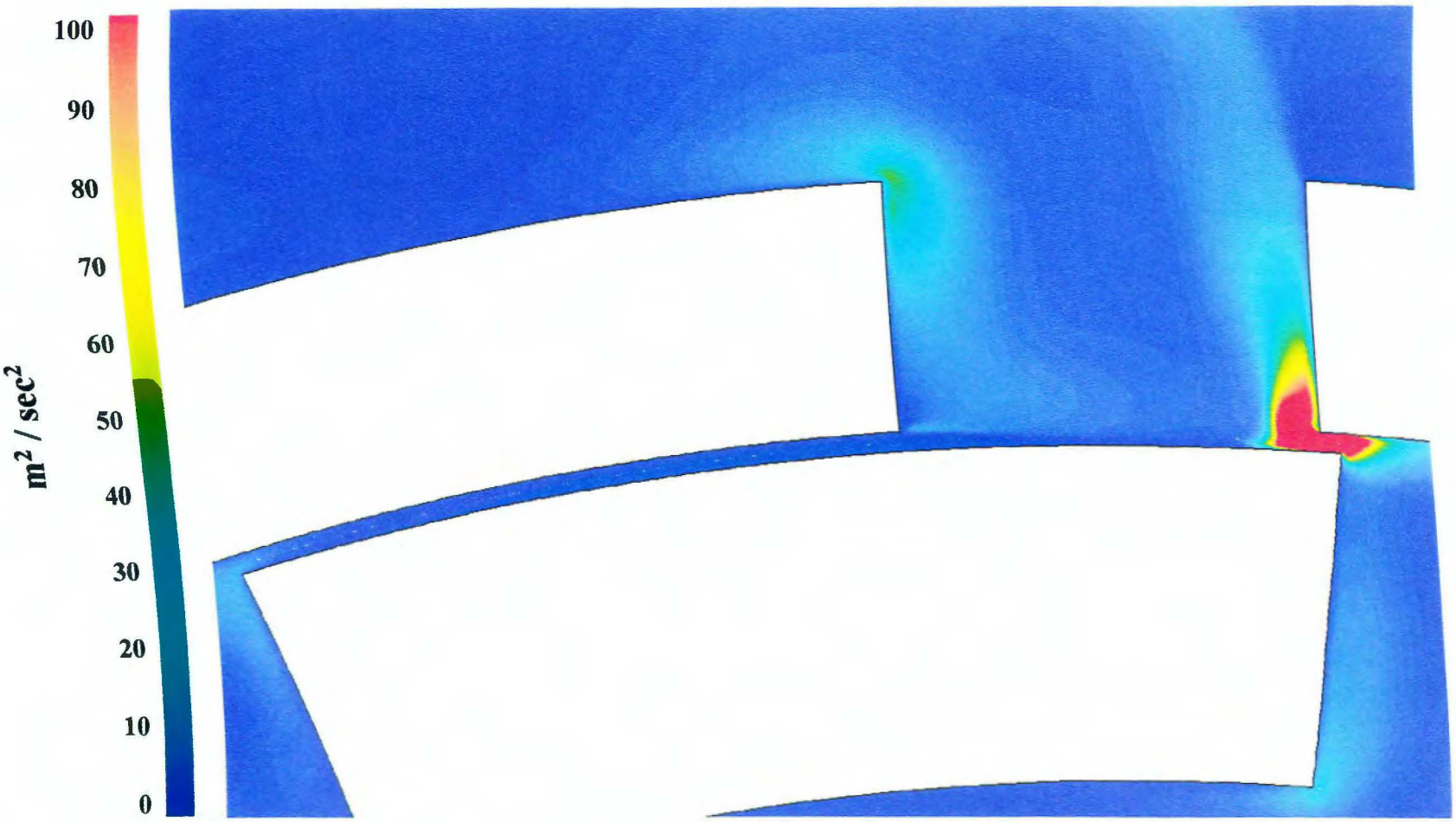

Figure 5-45. Angularly resolved turbulent kinetic energy near slot 1 at time step 6,428 (0.6448 seconds). Simulation 5.

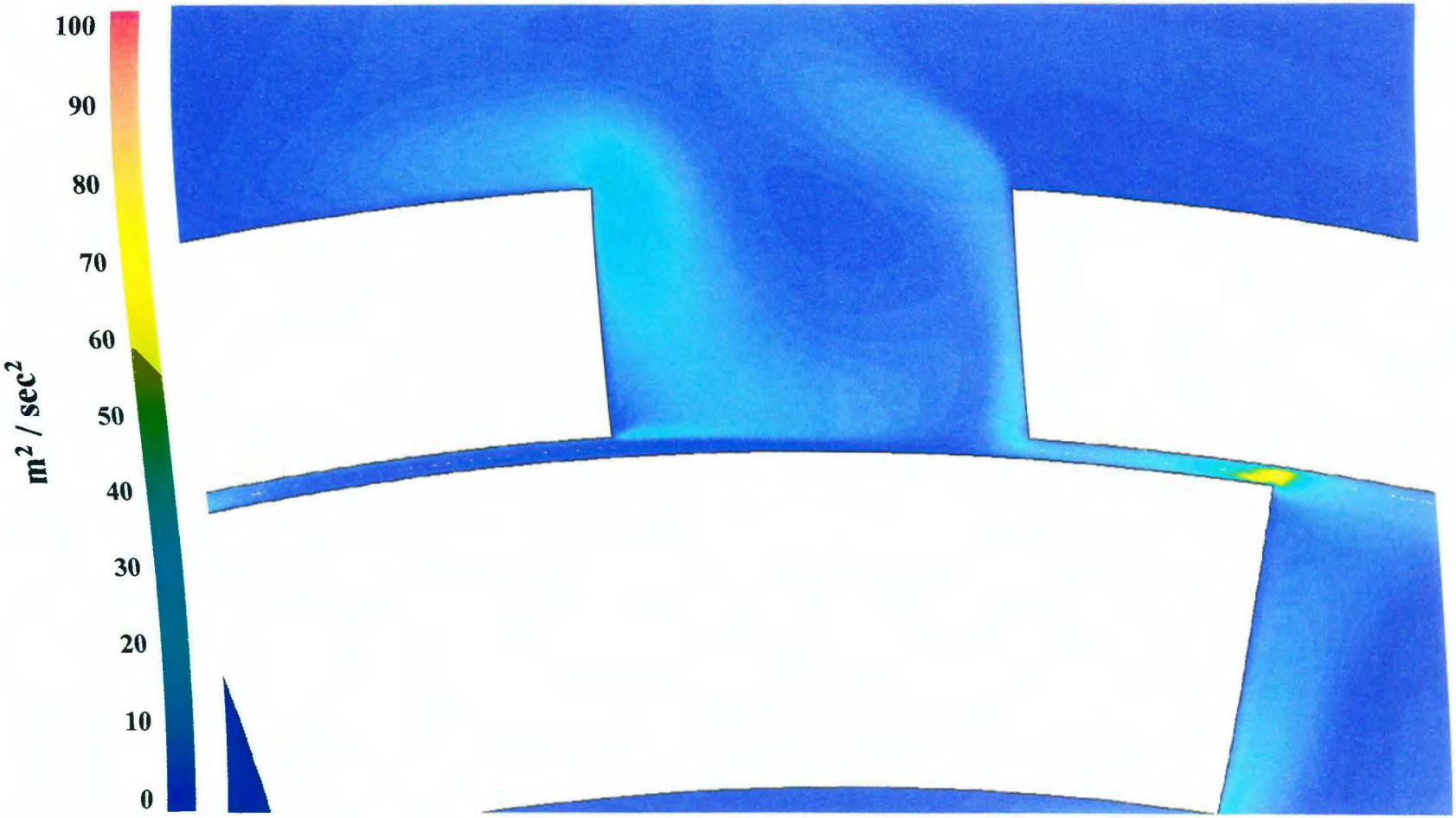

Figure 5-46. Angularly resolved turbulent kinetic energy near slot 1 at time step 6,432 (0.6452 seconds). Simulation 5.

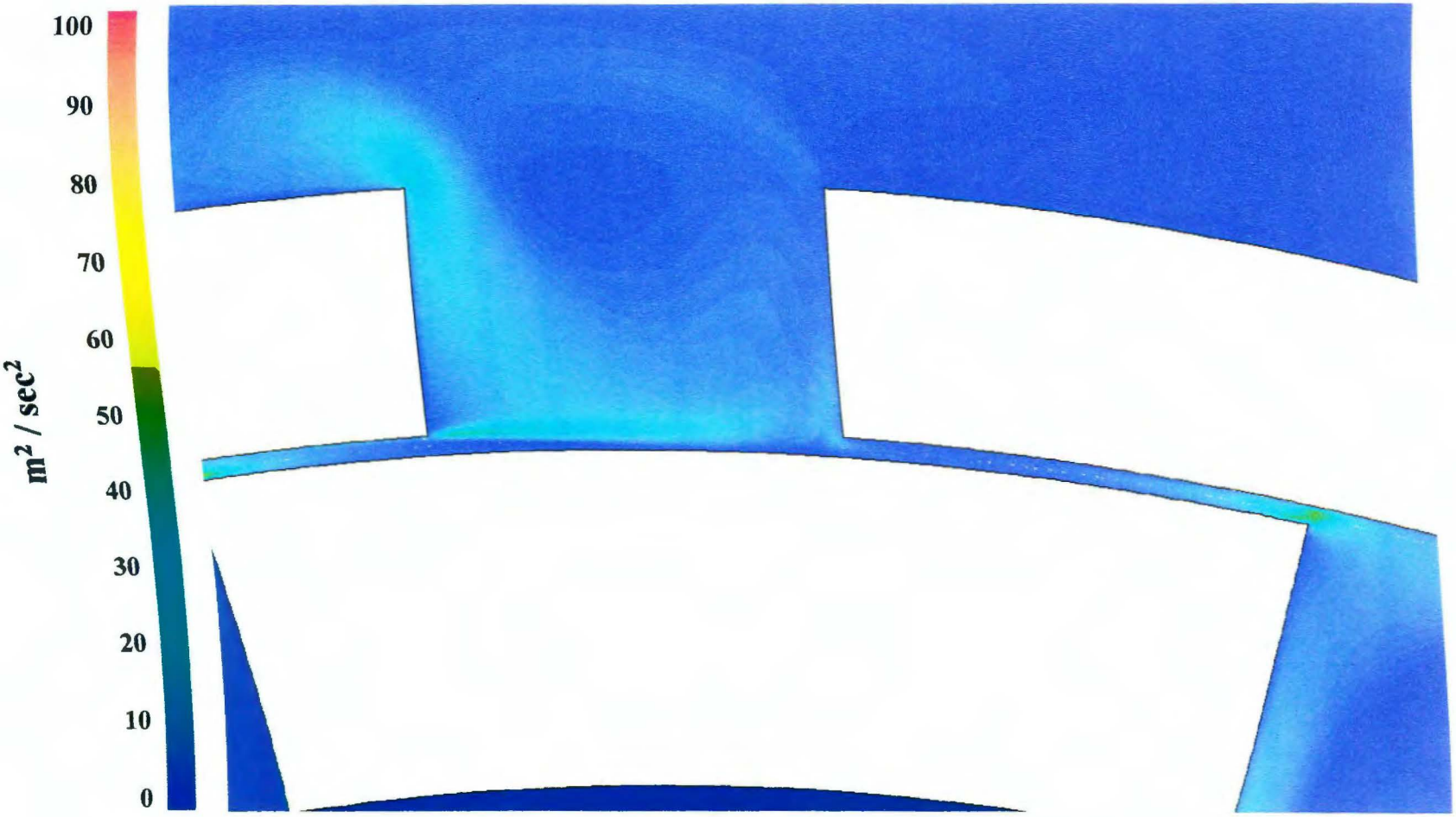

Figure 5-47. Angularly resolved turbulent kinetic energy near slot 1 at time step 6,436 (0.6456 seconds). Simulation 5.

corner of the stator slot. This region increases in size and magnitude as the distance between it and the corner of the approaching rotor tooth decreases. Simultaneously, the TKE intensity increases near the tip of the approaching rotor tooth. In Fig. 5-45, the corner of the rotor and stator teeth align, and the two regions combine. It is at this location and time that the TKE in slot 1 is at its highest value of about 200 m^2 / sec^2. As the rotor continues its motion, the region of high TKE near the corner of slot 1 moves into the gap, following the corner of the rotor tooth and decreasing in magnitude (Figs. 5-46 and 5-47).

Figures 5-48 through 5-54 show the simulated turbulent energy dissipation rate near stator slot 1. The patterns for the turbulent energy dissipation rate are identical to that for the TKE.

In comparison to the turbulence results obtained for the wide gap simulations there are both similarities and differences. The region of high turbulent kinetic energy above the leading edge of the rotor tooth that was apparent in the wide gap simulations (Figs. 4-34 and 4-35) is much less pronounced in the standard gap simulation (Figs. 5-41 and 5-42). Further, the region of high turbulence extending from the left lower corner of stator slot 1 in the standard gap simulation is much less pronounced in the wide gap simulation (compare Figs. 4-34 and 5-41). It appears that one of the primary effects of a decrease in gap width is that the high turbulence shifts from a 'moving vortex' in the wide gap simulations to a more stationary turbulent region extending from the left corner of the stator slot in the standard gap simulations.

While there is a region of high turbulent kinetic energy in the lower right region of stator slot 1 in both the wide and standard gap simulations, its magnitude in

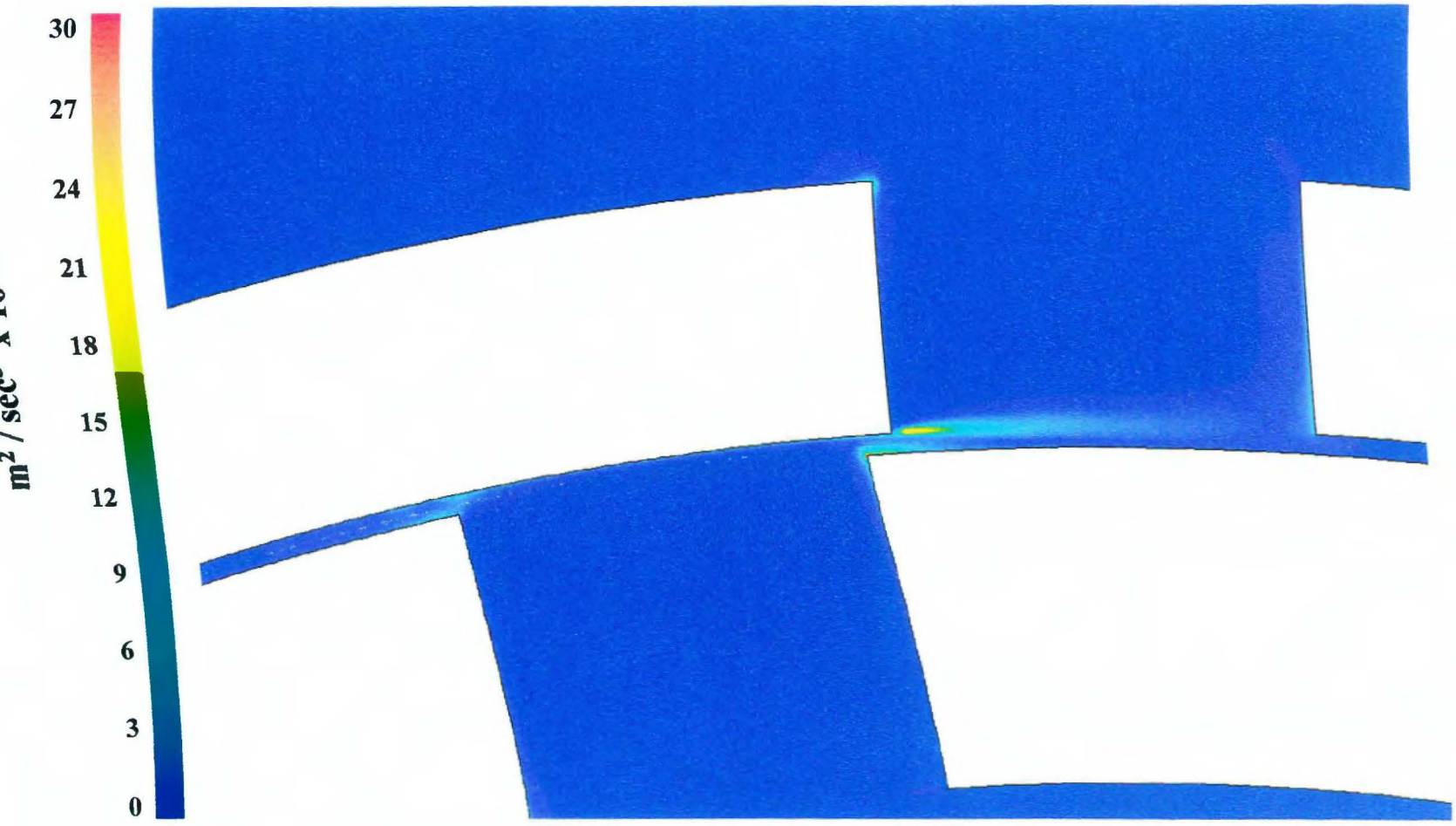

Figure 5-48. Angularly resolved turbulent kinetic energy dissipation rate near slot 1 at time step 6,412 (0.6432 seconds). Simulation 5.

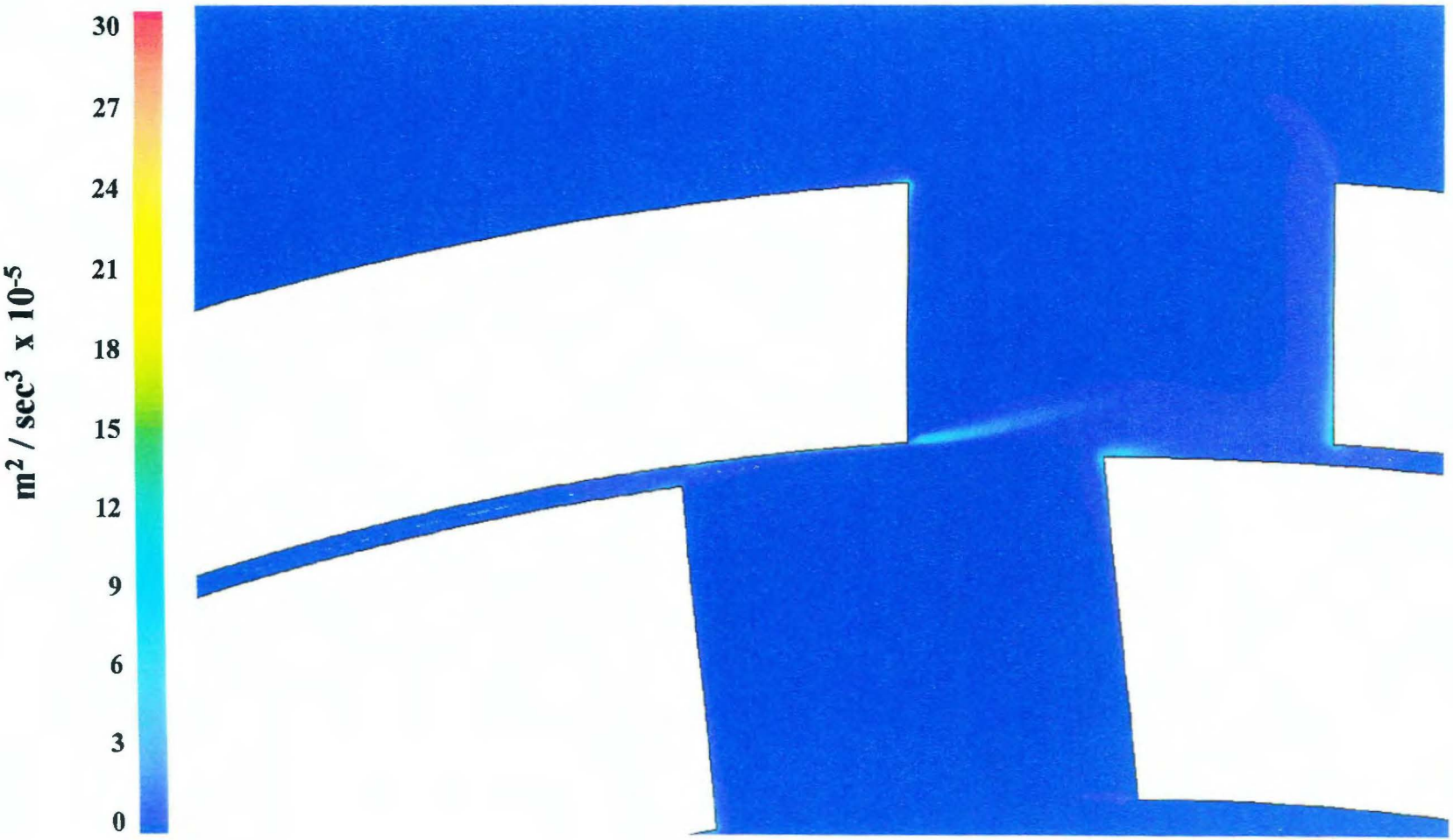

Figure 5-49. Angularly resolved turbulent kinetic energy dissipation rate near slot 1 at time step 6,416 (0.6436 seconds). Simulation 5.

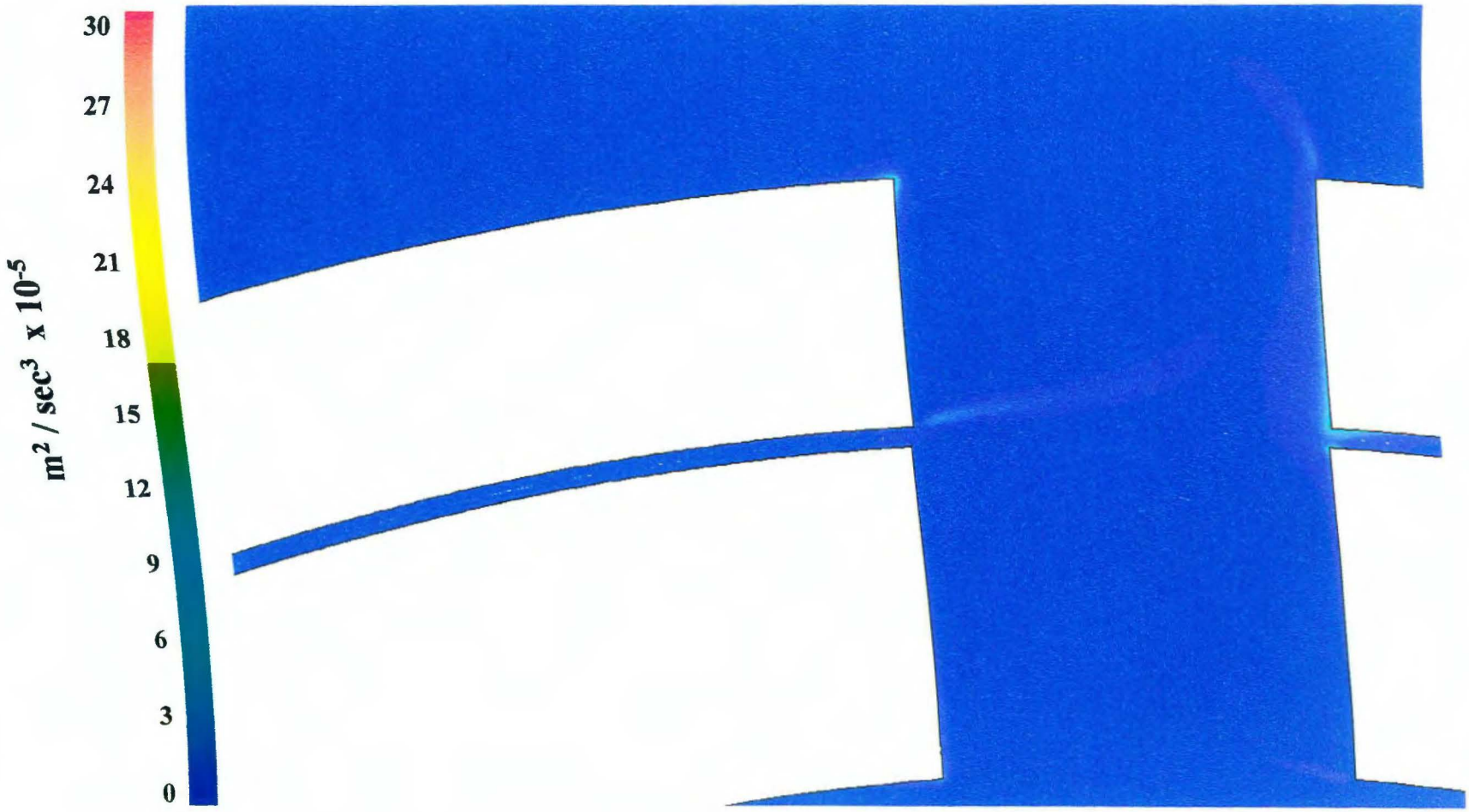

Figure 5-50. Angularly resolved turbulent kinetic energy dissipation rate near slot 1 at time step 6,420 (0.6440 seconds). Simulation 5.

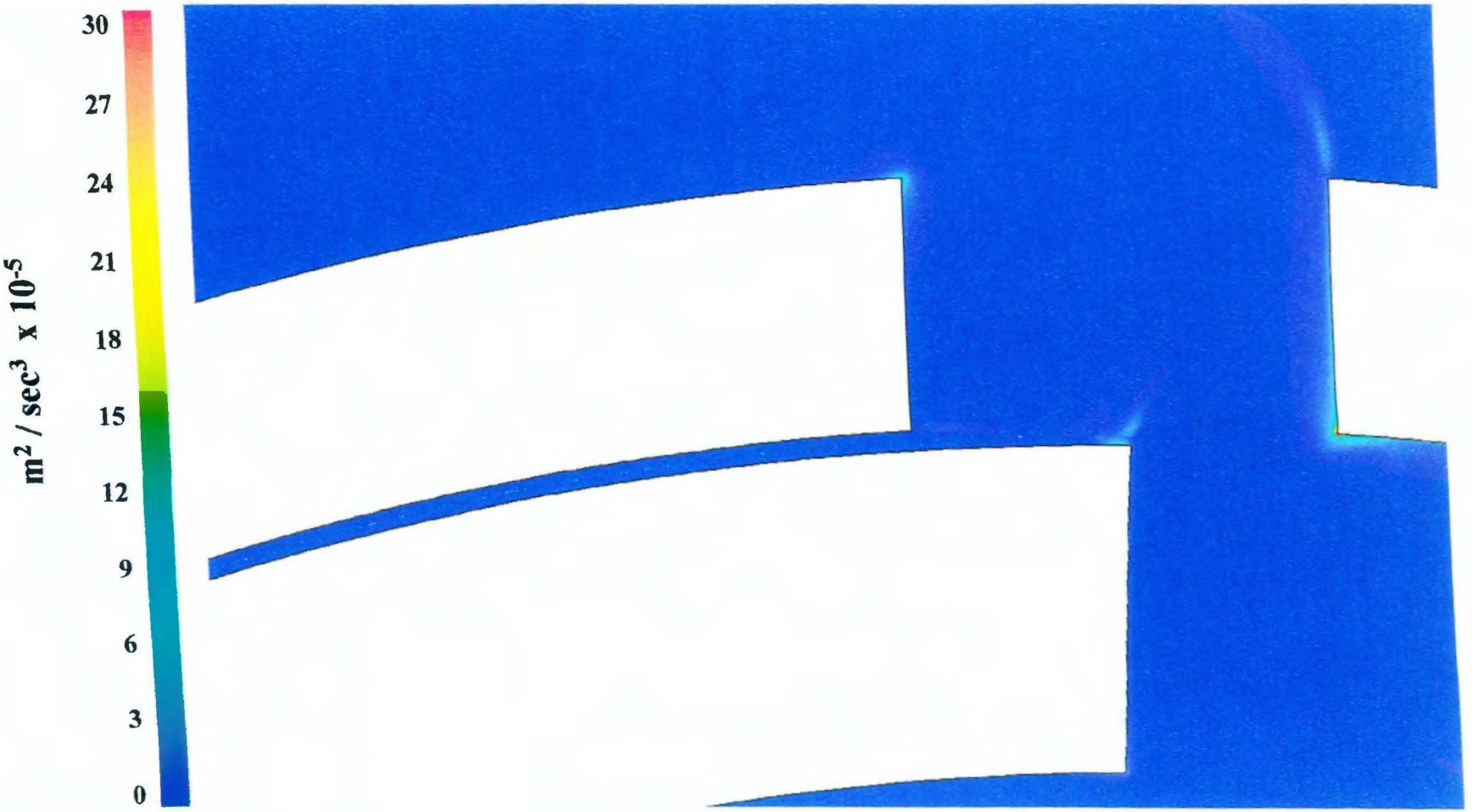

Figure 5-51. Angularly resolved turbulent kinetic energy dissipation rate near slot 1 at time step 6.424 (0.6444 seconds). Simulation 5.

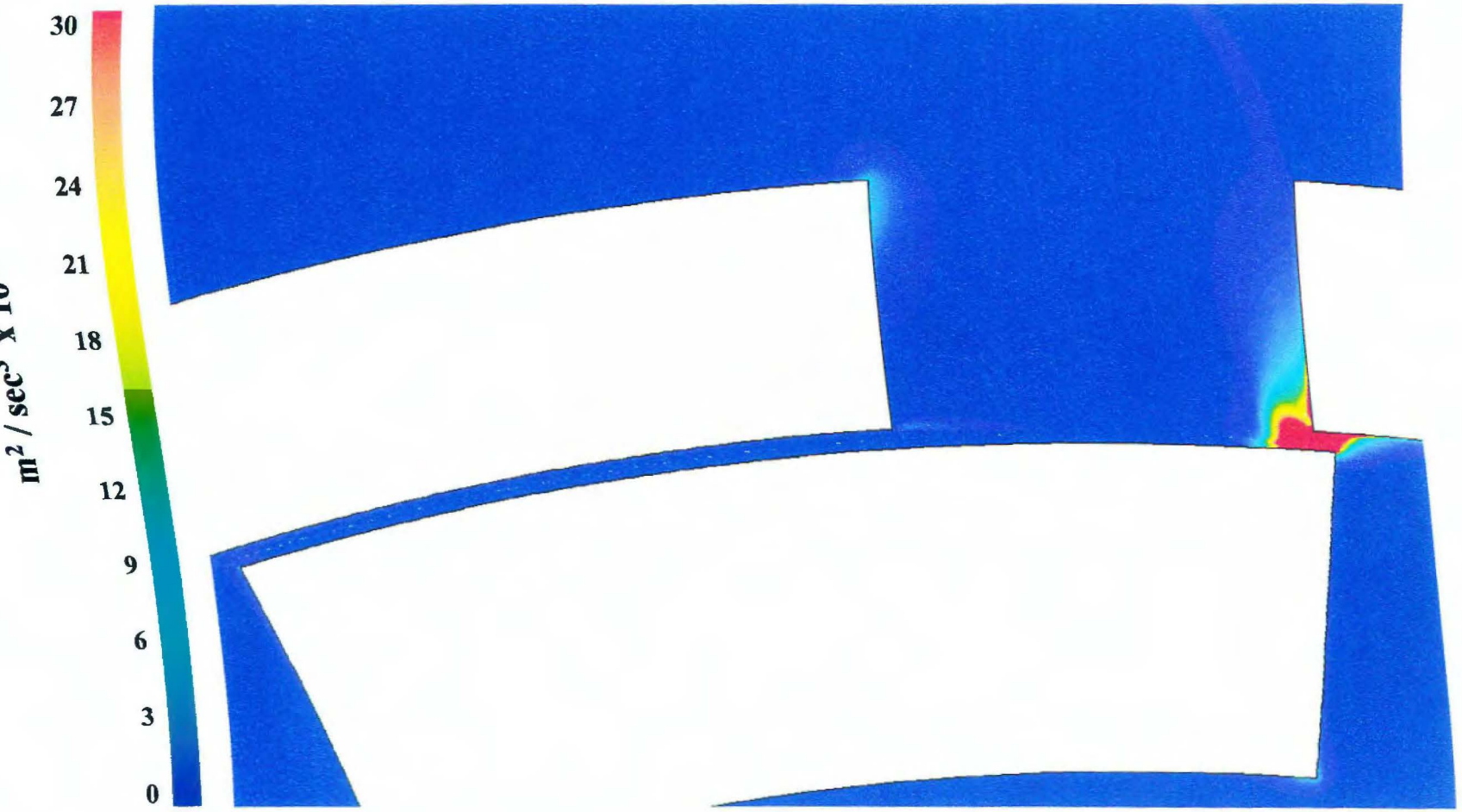

Figure 5-52. Angularly resolved turbulent kinetic energy dissipation rate near slot 1 at time step 6,428 (0.6448 seconds). Simulation 5.

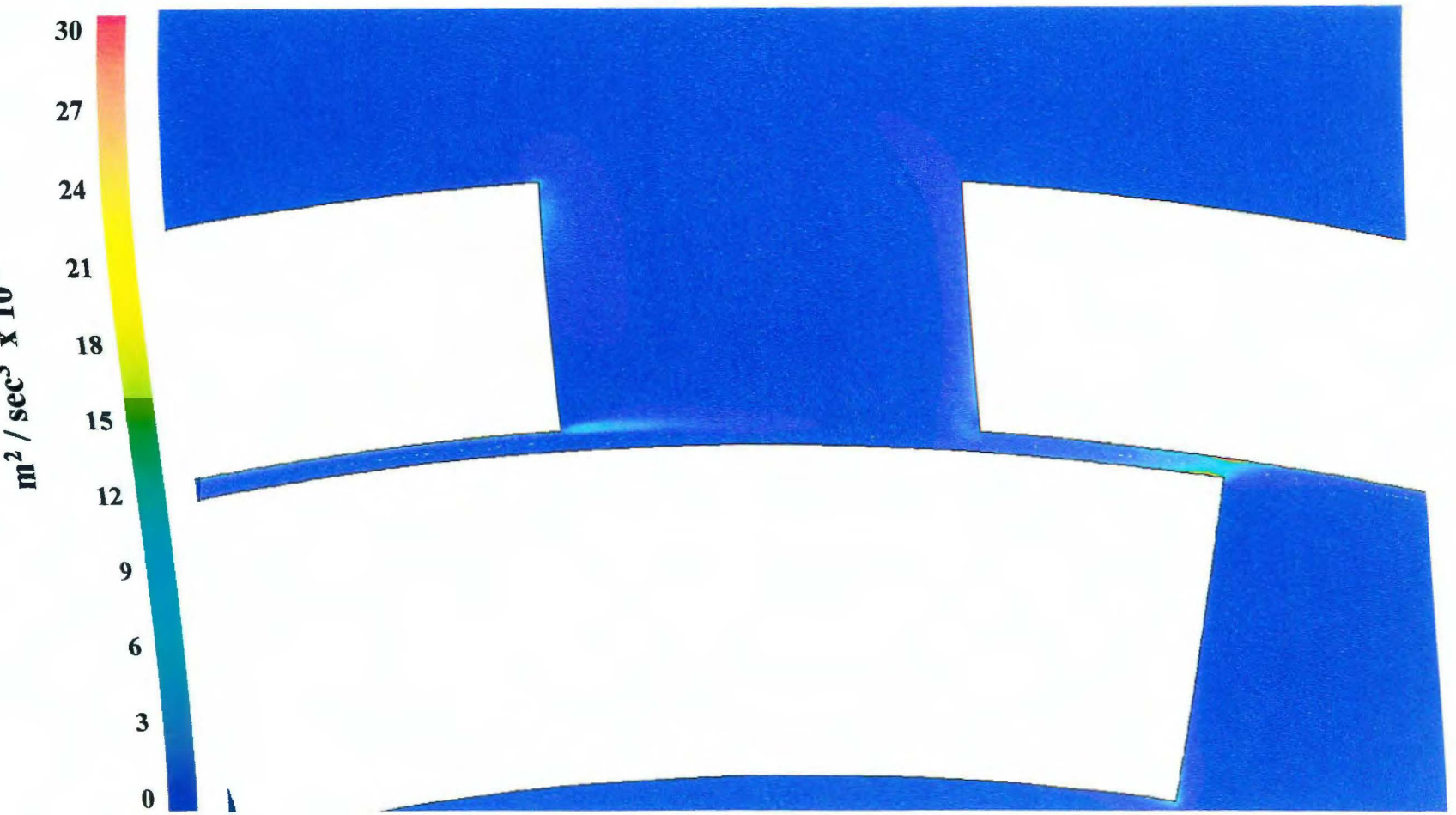

Figure 5-53. Angularly resolved turbulent kinetic energy dissipation rate near slot 1 at time step 6,432 (0.6452 seconds). Simulation 5.

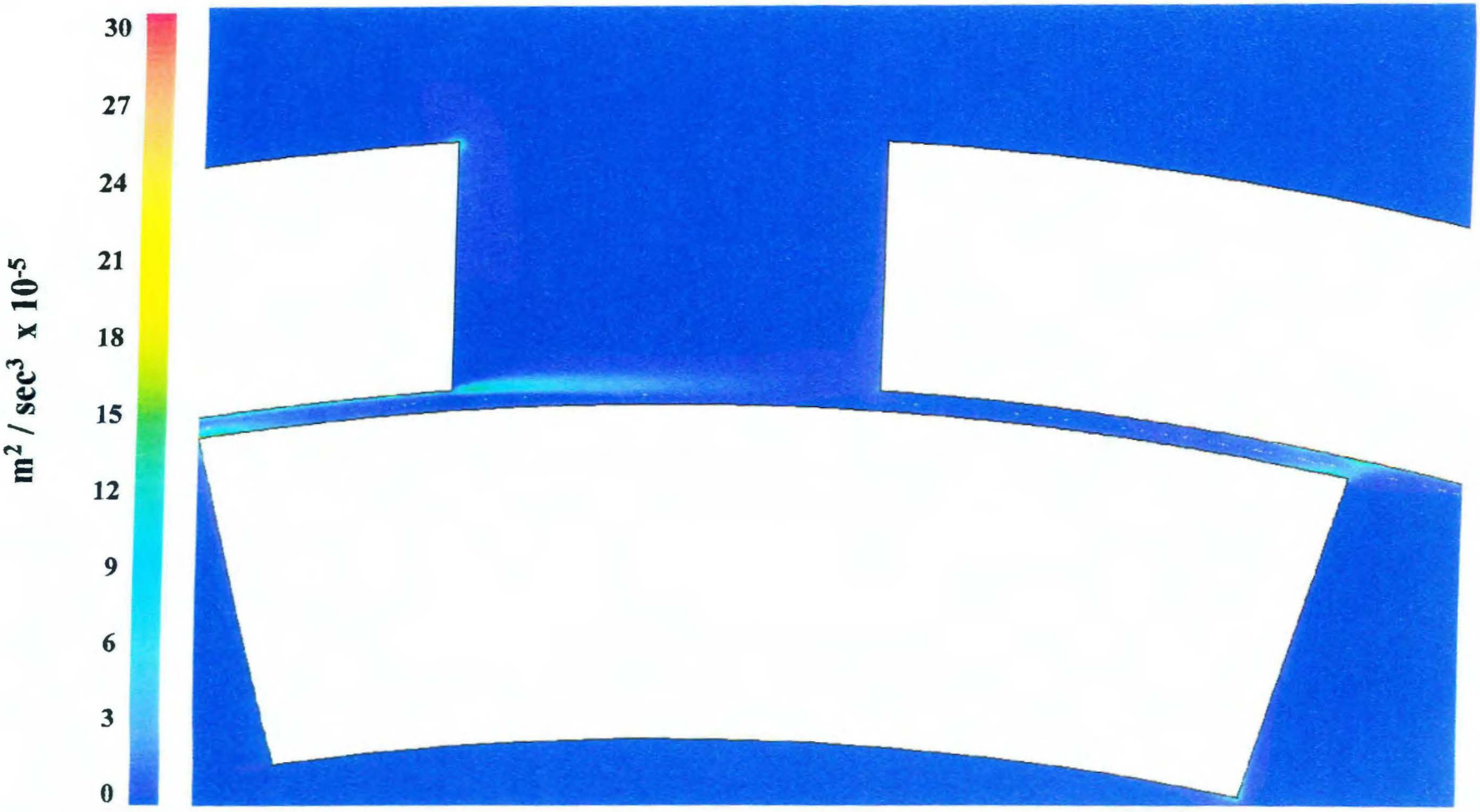

Figure 5-54. Angularly resolved turbulent kinetic energy dissipation rate near slot 1 at time step 6,436 (0.6456 seconds). Simulation 5.

the standard gap model is about 150 m^2/sec^2 whereas in the wide gap model it is only about 50 m^2/sec^2. Further, in the standard gap model, the absolutely highest value for the TKE is obtained slightly below this region, in the shear gap, and has a magnitude of about 250 m^2/sec^2 (This is difficult to see in Fig. 5-45 because the scale only goes to 100 m^2/sec^2, so any value greater than 100 m^2/sec^2 is red). In contrast, for the wide gap model there is not much difference between the magnitude of the TKE at the lower right corner of slot 1 and in the shear gap directly below (see Fig. 4-37). There is also a qualitative difference in the pattern of turbulence at the corner of slot 1 between the wide and standard gap models. In the wide gap simulation, the maximum TKE at the lower right corner occurs when the rotor and stator slots have passed full alignment and are only half open (Fig. 4-37). In the standard gap simulation, the maximum TKE occurs 4.3° later, when the slot is just closing (Fig. 5-45). Further, the turbulence on the right corner of stator tooth 1 appears to be more diffuse in the wide gap simulation and extends all the way up the side of the tooth into the volute. The standard gap model results in a more concentrated distribution of turbulence near the tooth corner.

Figures 5-55 and 5-56 show the time dependent behavior of the turbulent kinetic energy and turbulent energy dissipation rate spatially averaged over an imaginary line extending halfway across the gap from the corner of each stator tooth (see Fig. 4-1). The maximum turbulent kinetic energy in the gap is about 5 times larger in the standard model than in the wide gap model (compare Figs. 4-48 and 5-55). The turbulent energy dissipation rate is about 25 times greater in the standard gap model (compare Figs. 4-49 and 5-56). Also, as with the slot mass flow rates, the gap

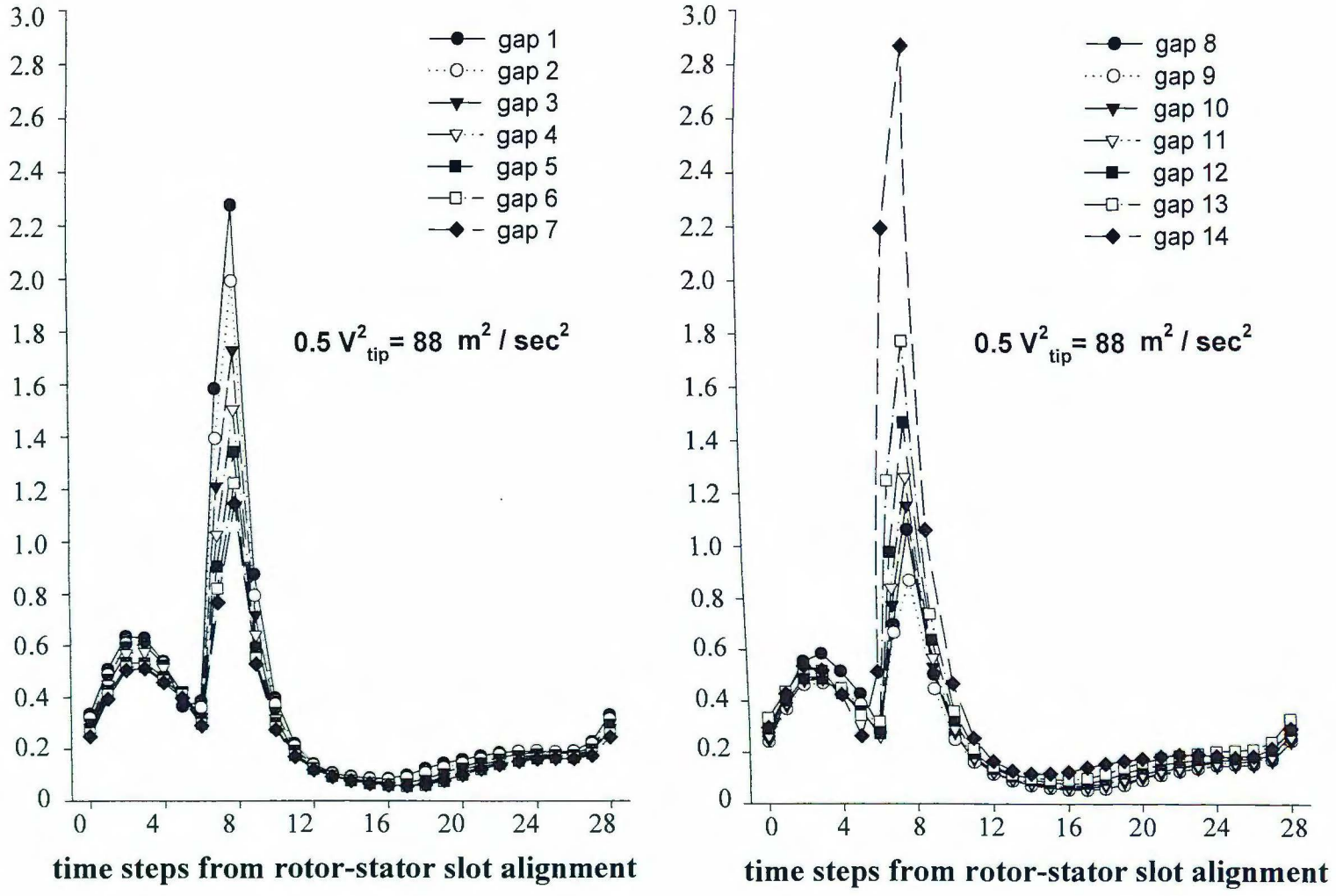

Figure 5-55. Time dependent turbulent kinetic energy (normalized to 0.5 V^2_{tip}) across lines spanning one-half the shear gap, as a function of slot alignment. Plots begin at approximately time step 6,412. Simulation 4.

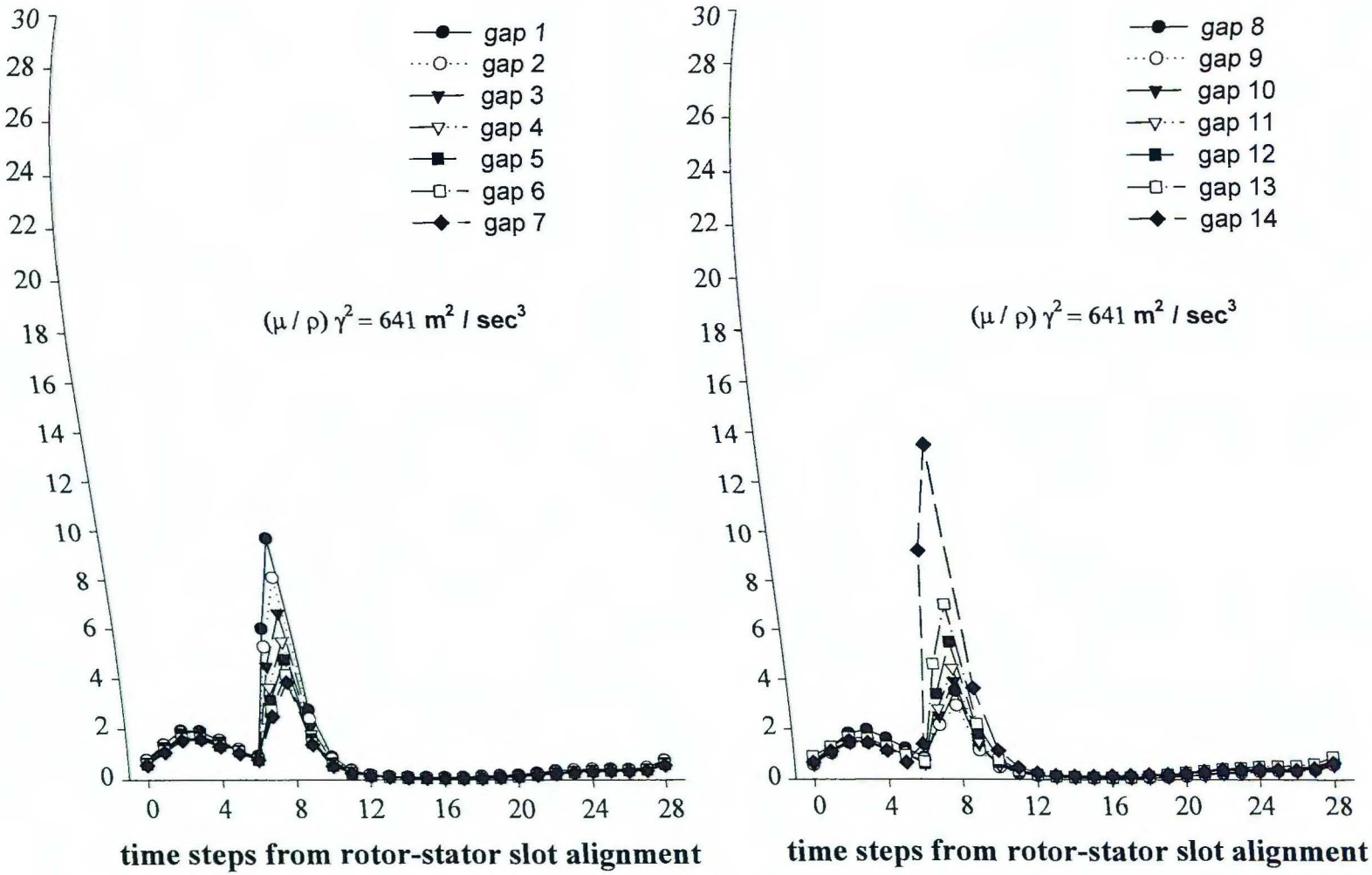

Figure 5-56. Time dependent turbulent energy dissipation rate (normalized to $(\mu/\rho)\,\gamma^2 / 10^3$) across lines spanning one-half the shear gap, as a function of slot alignment. Plots begin at approximately time step 6,412. Simulation 4.

turbulence values appear to be more nearly equal from slot to slot in the standard gap model.

Figures 5-55 and 5-56 also reveal a qualitative difference mentioned above for the TKE inside slot 1. In the wide gap model the peak turbulence values occur when the rotor slot is oriented about 5.3° past full alignment with the stator slot, with the exception of slot 14 (i.e. step 5 in Figs. 4-48 and 4-49). In the standard gap model, a local maximum in the turbulence occurs at the same rotor orientation, but a much stronger global maximum occurs immediately after a rotor slot passes a stator slot. This same pattern is also seen in the time dependent contour plots of the TKE and its dissipation.

5.4 Summary of Major Differences Between Standard and Wide Gap Models

Compared to the wide gap model, the mean velocity turbulent jet in the standard gap model is displaced further to the right, relative to the approaching rotor slot. Further, mean velocity magnitudes in the jet are up to 40% greater in the standard gap simulations.

During alignment of a rotor slot with a stator slot, the mean velocities in the lower portion of the stator slot take on an almost purely radial direction in the standard gap simulation. While this shift to a radial direction is also seen in the wide gap simulation, the extent of change is not nearly as great. The larger changes in the radial component of the mean flow seen in the standard gap device is probably also the reason that its slot vortex is seen to oscillate in its extent of span across the stator slot.

In the gap, near the downstream side of a given stator slot, the mean flow stagnates on the stator tooth corner, in both the wide and standard gap model, after a rotor tooth just blocks the corresponding slot. In the wide gap model, gap flow reversal is minor: Primarily, the flow is just stagnant (Fig. 4-12). In contrast, flow reversal is extreme in the standard gap model (Fig. 5-13). In fact, some of the largest mean velocities in the gap are seen to travel in a direction opposite to rotor motion.

In the volute, flow in both the wide and standard gap models is similar, but in the standard gap, slot outflow penetrates less deeply into the volute before turning toward the outlet. Both models predict reentrainment of flow from the volute into the stator slots.

Both models predict a correlation between slot proximity to the device outlet and extent of mass outflow from the slot. In the standard gap model, however, the difference in mass flow rate between slots is not nearly as exaggerated. Further, the standard gap model predicts that the rotor teeth act more efficiently at blocking outflow from stator slots, resulting in a more pulsating time dependent slot mass flow rate as compared to the wide gap model.

The turbulent kinetic energy in stator slot 1 of the standard gap model is about three times larger than that in the wide gap model. Further, in the gap itself, near the lower right corner of stator slot 1, the TKE is five times greater in the standard gap model. Qualitatively, the TKE in the slots of the wide gap model appears to be more diffuse than in the standard gap model.

In the wide gap model, the maximum gap TKE occurs near the bottom right corner of a stator slot when a rotor and stator slot are about 5.3° past full alignment.

In contrast, in the standard gap model the maximum TKE occurs when a rotor and stator slot are about 8.6° past full alignment. This implies that the maximum gap TKE in the wide gap model correlates with the maximum stator slot mass outflow, but in the standard gap model, it correlates with blockage of the slot.

Chapter 6 Experiment Versus Simulation

Laser Doppler anemometry (LDA) measurements of the flow field in the standard and wide gap IKA rotor-stator device were performed in both a fixed and angularly resolved reference frame by Dr. Ved P. Mishra using a two-component LDA supplied by Dantec Inc. Mean and root mean square (rms) turbulent velocity measurements were made in the r and θ directions. The raw LDA signals were processed using a Flow Velocity Analyzer (FVA), and all the figures in this chapter (except Fig. 6-12) were generated by Dr. Mishra. Like for the simulations, the current experimental facility did not allow measurement of the z-velocity component. Definition of the cylindrical coordinate system used for description of the rotor-stator device in this chapter is given in Fig. 6-1.

During experiments it was found that the volute cover did not fit tightly, leaving a clearance between its front face and the top of the stator teeth. This fact appears to result in fluid bypassing the shear gap and leaking over the rotor and stator teeth when a rotor tooth blocks a stator slot. Because of this, measurements for the standard gap model were performed using both the original volute cover (henceforth, volute cover 1) and a newer volute cover that fit more tightly with the stator teeth (henceforth, volute cover 2). All measurements for the wide gap device were made with volute cover 1. Volute cover 2 is shown in Fig. 6-2.

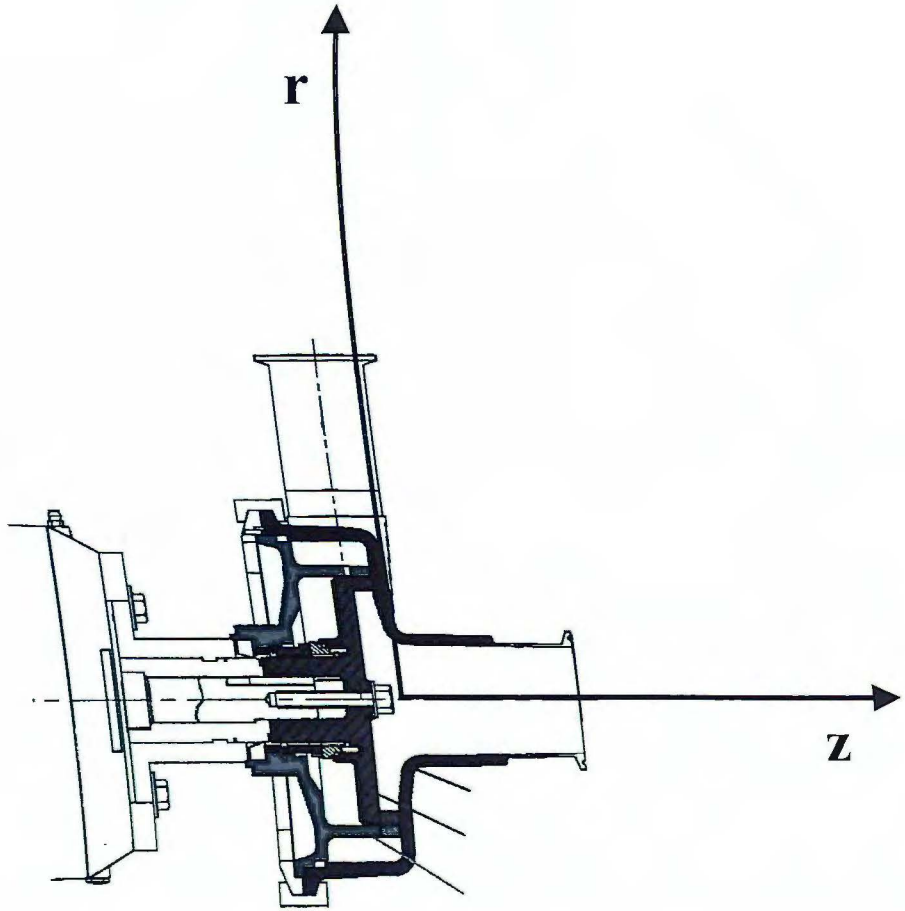

Figure 6-1. Radial cross section schematic of the IKA type inline rotor-stator mixer and coordinate system used to take the LDA data. Z = 0 corresponds to the position where the top of the stator teeth and volute cover (ideally) meet.

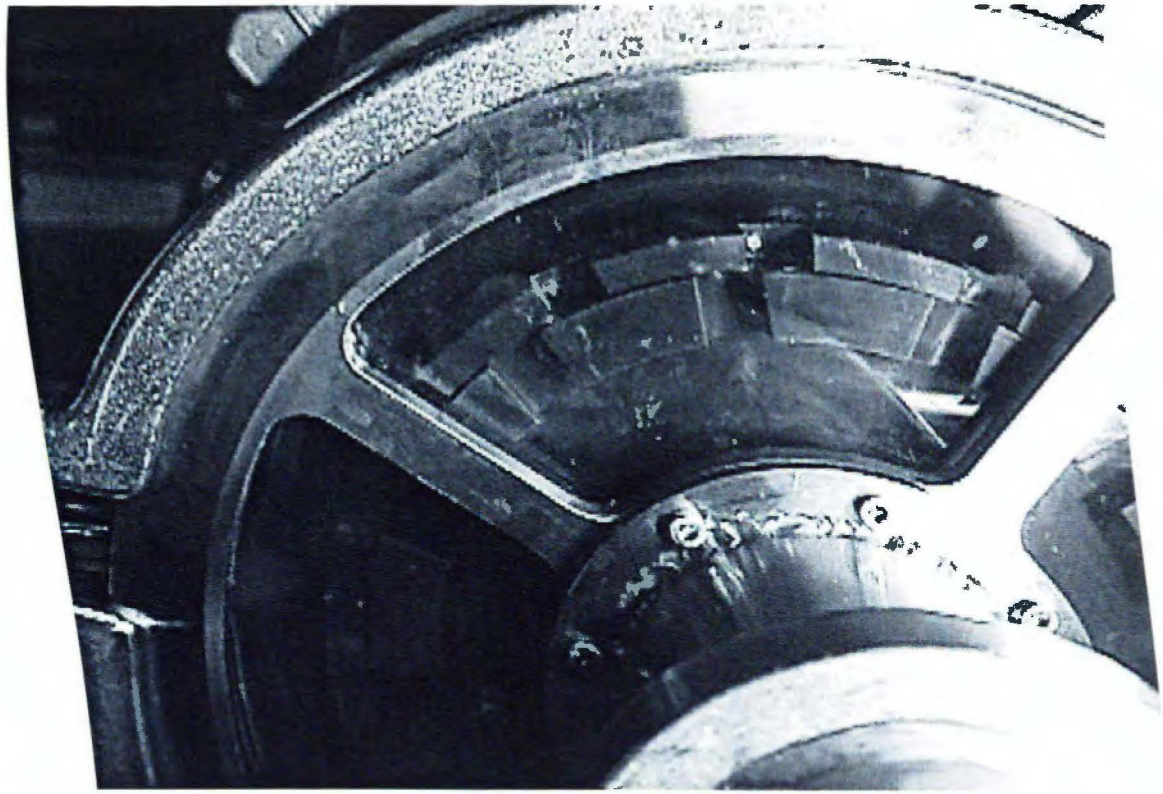

Figure 6-2. Volute cover 2

In both geometries, the clearance between the top of the rotor teeth and volute cover is between about 0.25 and 0.6 mm. When volute cover 1 is in place, the clearance between it and the stator teeth is about 0.5 mm. The clearance between the stator teeth and volute cover 2 is significantly less (about 0.1 mm), however it became apparent when LDA measurements were made that there was a slight asymmetry in the fit. Specifically, stator teeth 11, 12, and 13 appear to have been completely flush with volute cover 2 while the other stator teeth had a gap of ~0.1 mm. This fact was deduced by marks that teeth 11, 12, and 13 left on volute cover 2.

Volute cover 1 is partially made of transparent plexiglass for access of the LDA laser beams. However, it leaves stator slots 5, 12, and the volute, beyond a radius of about 80 mm, inaccessible for measurement. Volute cover 2 has a larger plexiglass window, allowing LDA access to all stator slots and nearly the entire volute. This is the reason why some of the figures in section 6.2 lack data for slots 5 and 12.

This chapter contains a comparison of CFD simulations 4 and 5 with LDA data taken primarily in the fixed frame of reference. Some LDA data for mass flow rates taken in the angularly resolved reference frame for the standard gap model with volute cover 1 are also included. The reader is reminded that both simulations 4 and 5 were performed for a rotor speed of 30 rps and 45.4 gpm. The LDA data were collected at two different operating conditions which are summarized in Table 6-1. The very slight differences between simulation and experiment is not expected to have a significant effect on validity of the comparison since there are already significant simplifications in the simulation models. Further, it is realistic to expect that the small

differences in operating conditions will not grossly effect the rotor-stator mixer flow field characteristics.

Table 6-1. Differences Between Simulation and Experimental Conditions

	Wide Gap		Standard Gap	
	Simulation 4	Experiment	Simulation 5	Experiment
Rotor speed (rps)	30	29.7	30	29.7
Rotor tip speed (m/sec)	12.63	12.50	13.29	13.16
Inlet flow rate (gpm)	45.4	45.6	45.4	40.4
Average inlet velocity (m/sec)	1.52	1.53	1.52	1.35
Working fluid	Water	Water	Water	Water
Temperature	25° C	25°- 35° C	25° C	25°- 35° C

While considerably more LDA data exists for both the wide and standard gap devices, it is not presented here. Further manipulation and analysis of the LDA data, beyond the scope of this work, is needed before a more meaningful comparison with simulation results can be made.

6.1 Fixed Frame Mean Velocity Field

The fixed frame velocity fields obtained by LDA measurements for the wide and standard gap devices are shown in Figs. 6-3 through 6-6 and Figs. 6-7 through 6-10 respectively. Both sets of figures come from data collected with volute cover 1 and correspond to r and θ velocities obtained on an axisymmetric plane topologically identical to that used for simulation (Fig. 1-3). The z-coordinate of the measurements is -6 mm, which is the axial depth at the physical centroid of a stator slot and the most logical place for comparison with two-dimensional simulations.

Comparison of Figs. 6-3 through 6-6 with Figs. 4-18 through 4-21 show that the simulated and experimental fields are qualitatively similar for the wide gap device. All exit flow from stator slots occurs on the downstream side (i.e. in stator slot 1 from the right-hand side). On the upstream side of each slot, flow is reentrained. The gap jet that was visible in the simulation fixed frame velocity field (Fig. 4-21) is not apparent in the LDA results as presented here. The slot vortices in the simulation results also appear to be exaggerated in comparison to the experimental measurements. Experimental flow patterns in the volute near the stator teeth is fairly complicated and, at least qualitatively, resembles the computed patterns. Recirculation near several of the stator teeth, for example stator tooth 1, is indicated by the LDA data. Recall that stator slot labels are shown in Fig. 4-1.

Examination of experimental measurements for the standard gap device show the fixed frame velocity field to be qualitatively similar to that obtained for the wide gap device (Figs. 6-7 through 6-10). The fixed frame velocity appears to be larger in the stator slots near the gap in the standard gap device: Compare, for instance, the

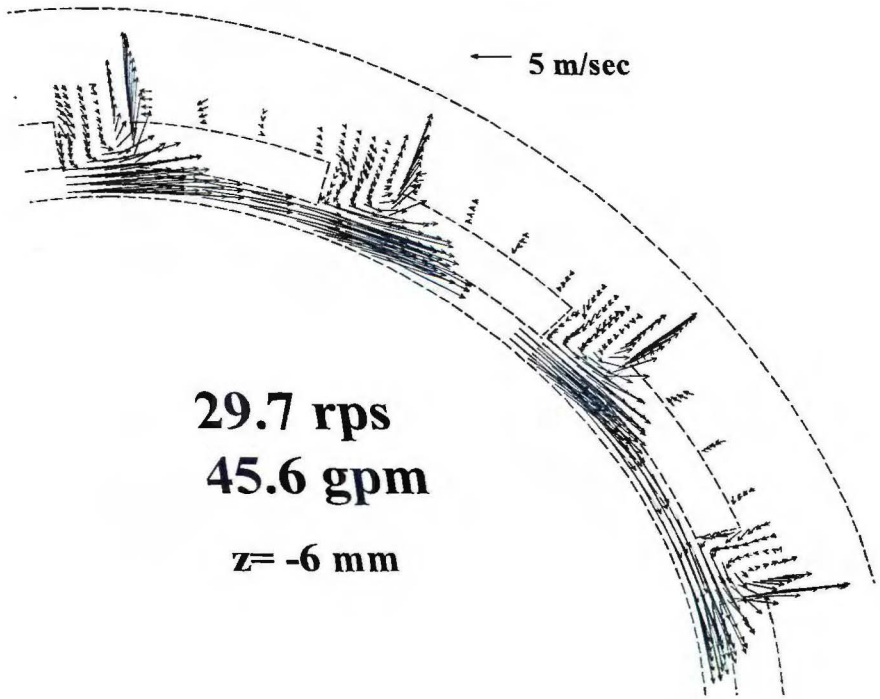

Figure 6-3. Fixed frame LDA velocity data near stator slots 1-4 in the wide gap device. Volute cover 1.

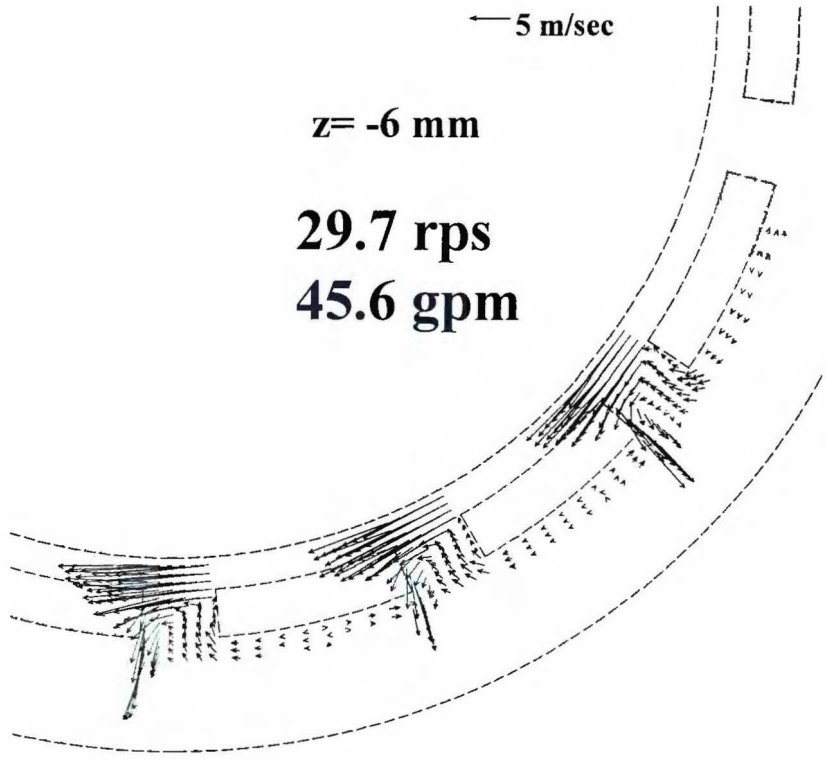

Figure 6-4. Fixed frame LDA velocity data near stator slots 6-8 in the wide gap device. Volute cover 1.

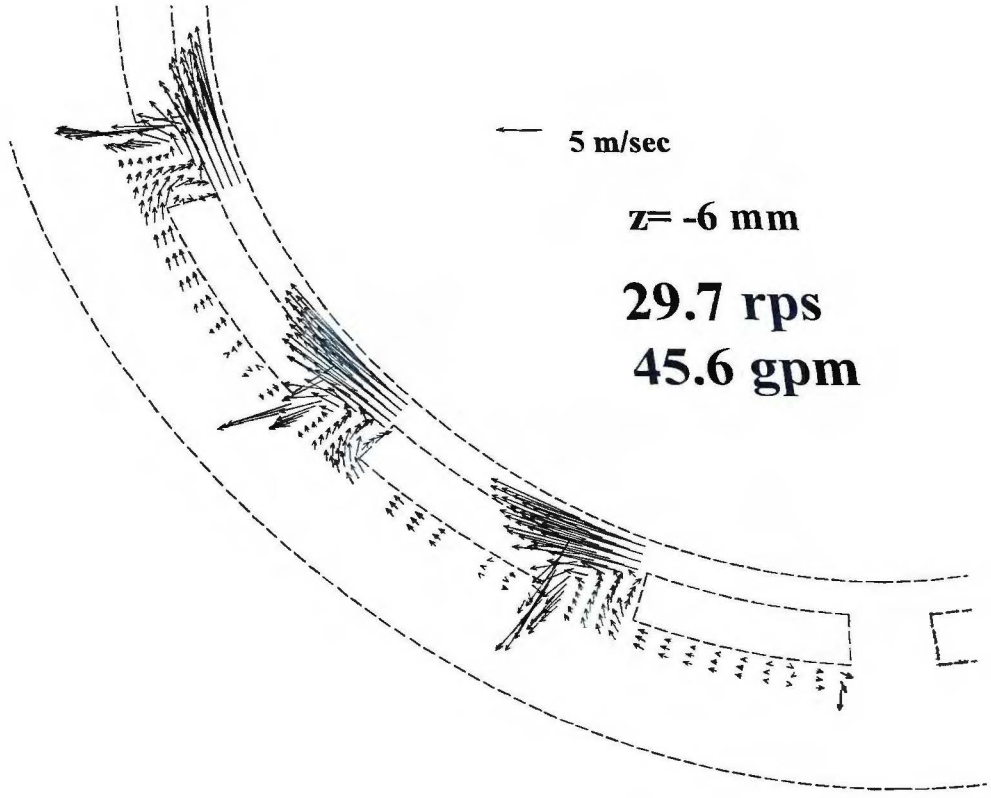

Figure 6-5. Fixed frame LDA velocity data near stator slots 9-11 in the wide gap device. Volute cover 1.

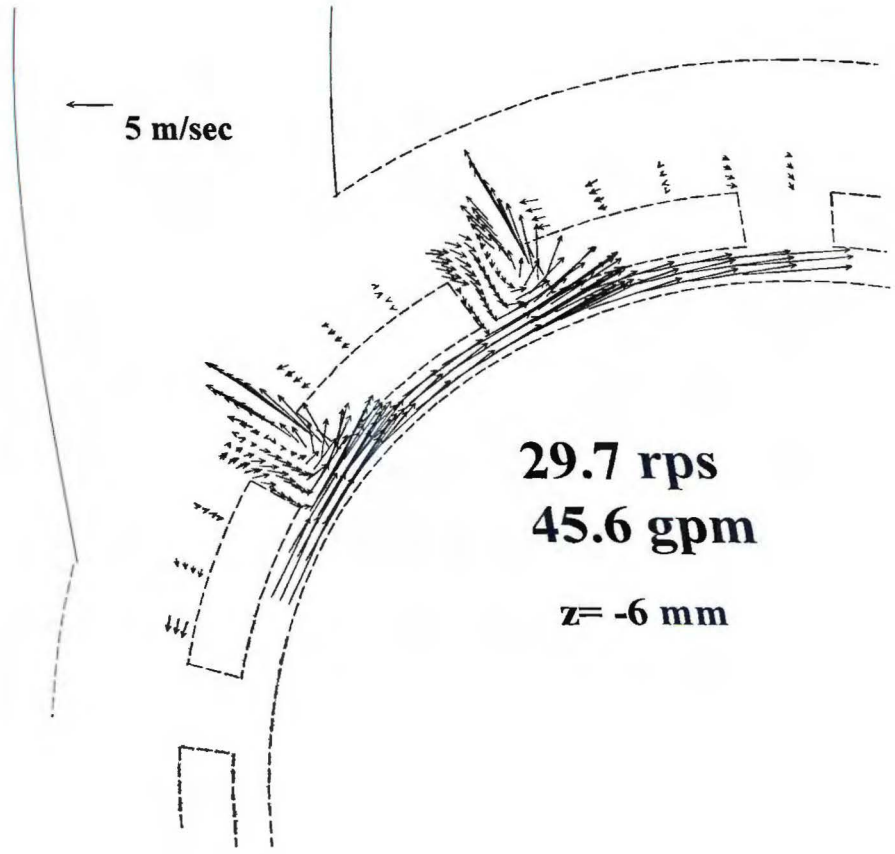

Figure 6-6. Fixed frame LDA velocity data near stator slots 13 and 14 in the wide gap device. Volute cover 1.

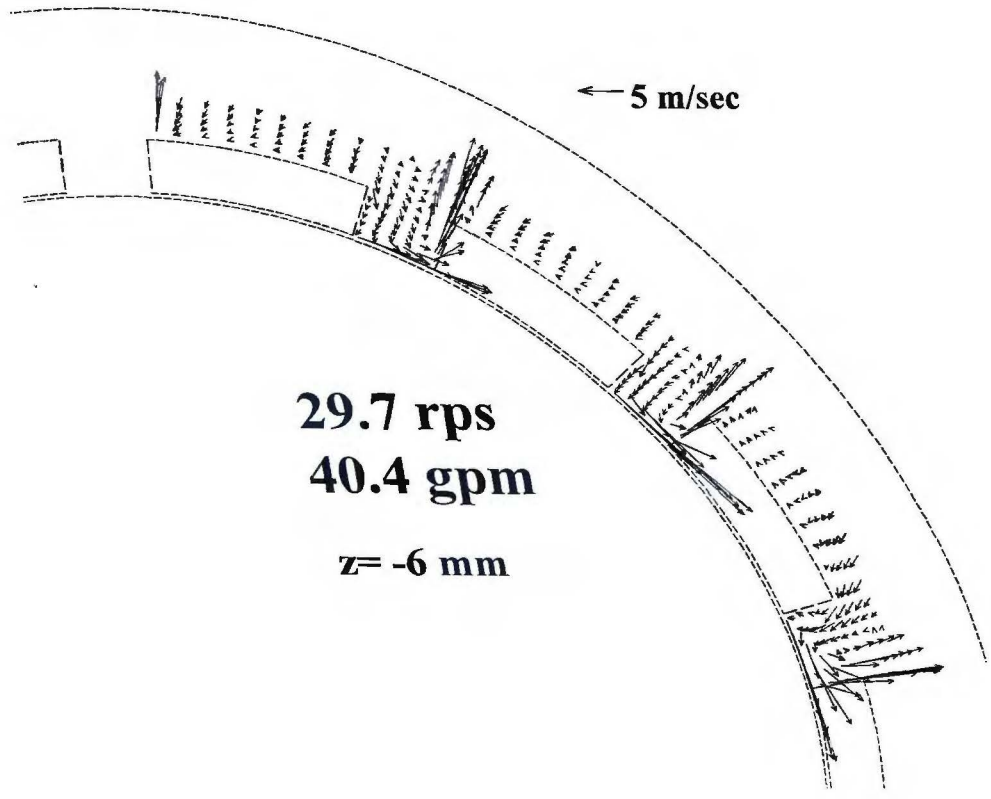

Figure 6-7. Fixed frame LDA velocity data near stator slots 2-4 in the standard gap device. Volute cover 1.

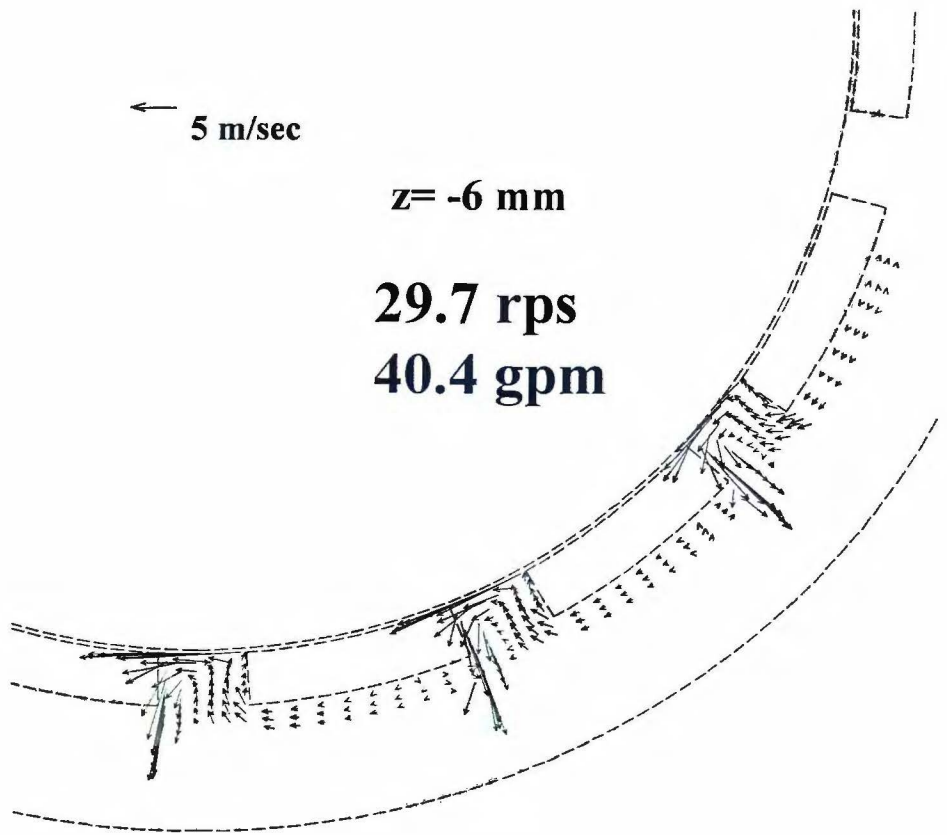

Figure 6-8. Fixed frame LDA velocity data near stator slots 6-8 in the standard gap device. Volute cover 1.

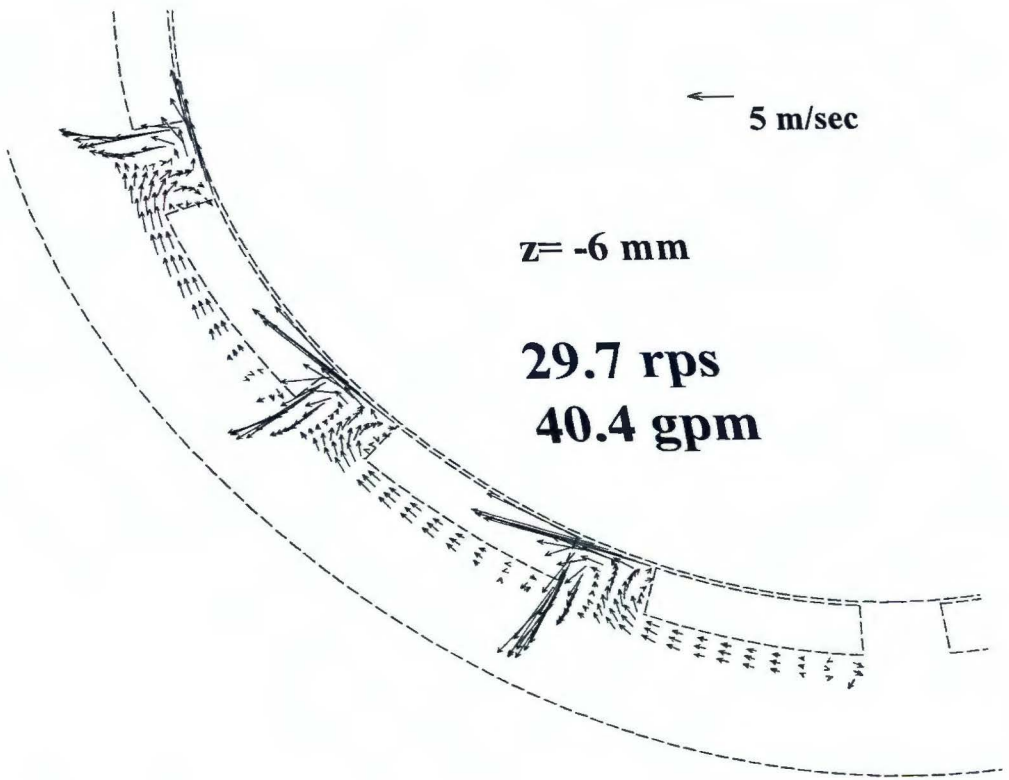

Figure 6-9. Fixed frame LDA velocity data near stator slots 9-11 in the standard gap device. Volute cover 1.

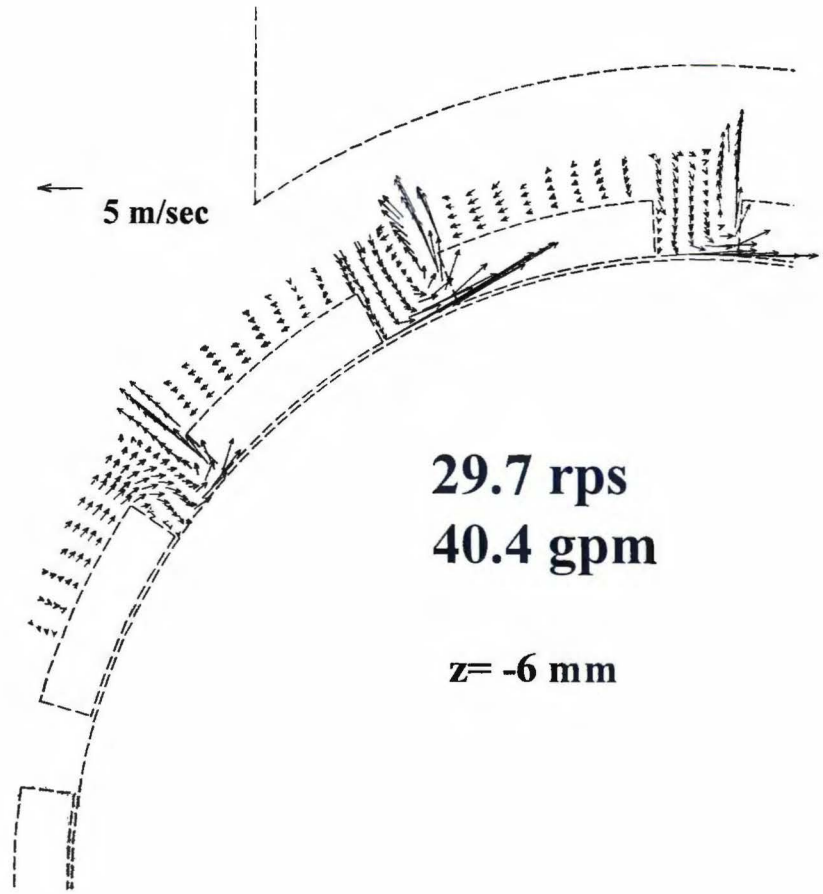

Figure 6-10. Fixed frame LDA velocity data near stator slots 13, 14, and 1 in the standard gap device. Volute cover 1.

fixed frame velocity vectors near the lower right corner of slot 14 in Fig. 6-10 with those in Fig. 6-6. Larger mean velocities near the downstream corners of the slots were also seen when the wide and standard gap simulations were compared: Recall that the mean jet velocities were 40% greater for the standard gap simulation.

In the simulations, there were significant qualitative differences in the mean velocities between the wide and standard gap models. For instance the location of the turbulent jet in the standard gap model was displaced to the right relative to the wide gap model. Also, the slot vortex in the standard gap model cycled in the extent of its span across the slot throughout a period of flow. With the current plots, it is not possible to see major qualitative differences in the LDA data for the wide and standard gap device mean flows. Future, more sophisticated analysis of angle correlated LDA data for the mean velocity field may help address this.

Figure 6-11 illustrates, for stator slot 1, an additional set of mean velocity measurements made for the standard gap rotor-stator device near the exit (r = 77 mm) of slot 1. At this location, the radial and tangential velocities were measured across the slot at several different axial depths. In measurements performed with volute cover 1 (Fig. 6-11a), reentrainment of the flow occurs at all depths. However, in measurements performed with volute cover 2 (Fig. 6-11b), there is no reentrainment very close to the volute cover (at z = -1 mm). Figure 6-12 illustrates the simulated fixed frame velocity at the exit of slot 1 in the standard gap model obtained by CFD. In the CFD simulation, reentrainment is clearly seen along the left one third at the slot exit. This is similar to the experimental results. Note that with volute cover 1,

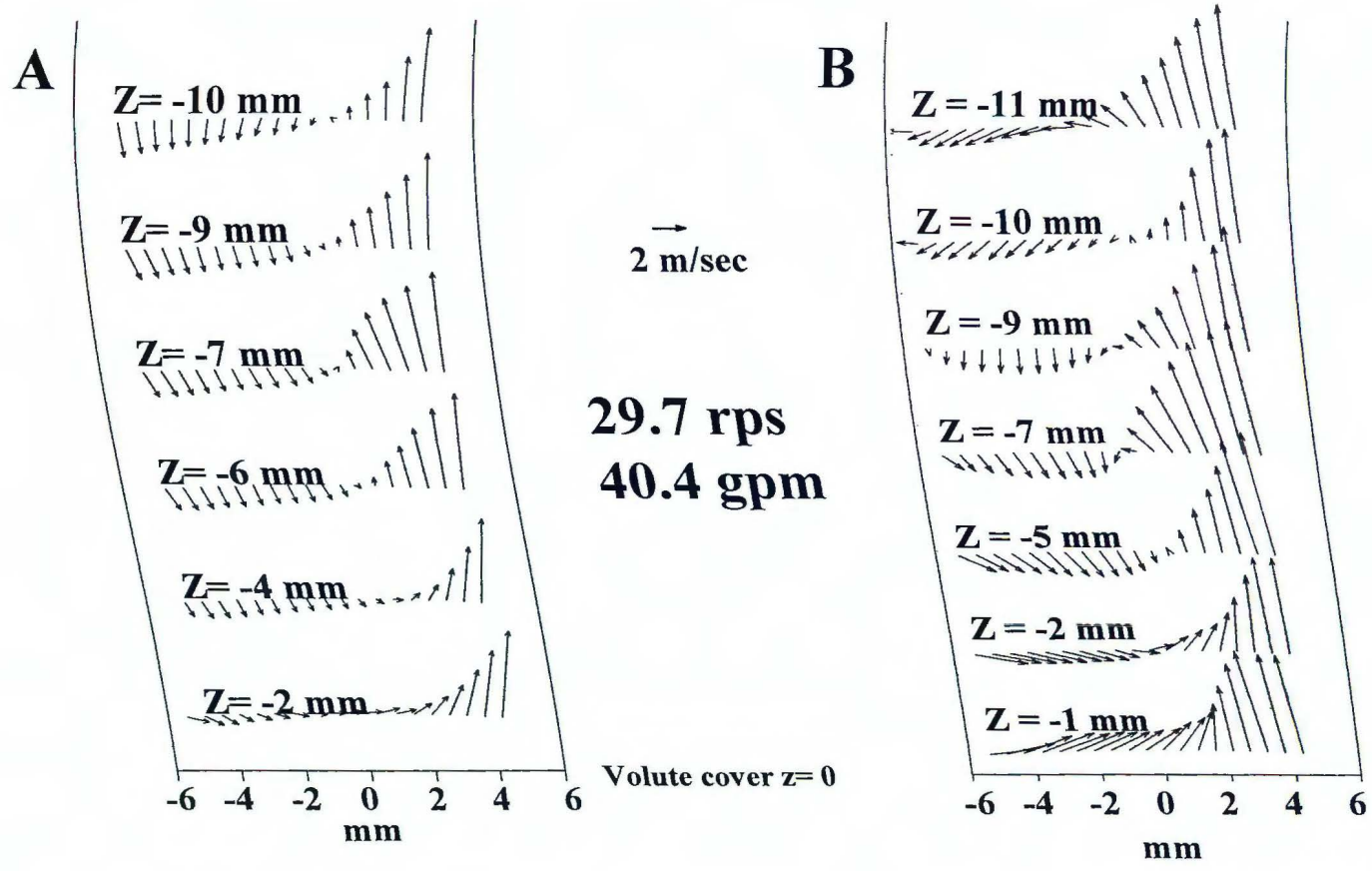

Figure 6-11. Fixed frame LDA velocity data at the exit to slot 7 (r = 77 mm) as a function of depth in the standard gap device. Volute cover 1 (**A**) and volute cover 2 (**B**).

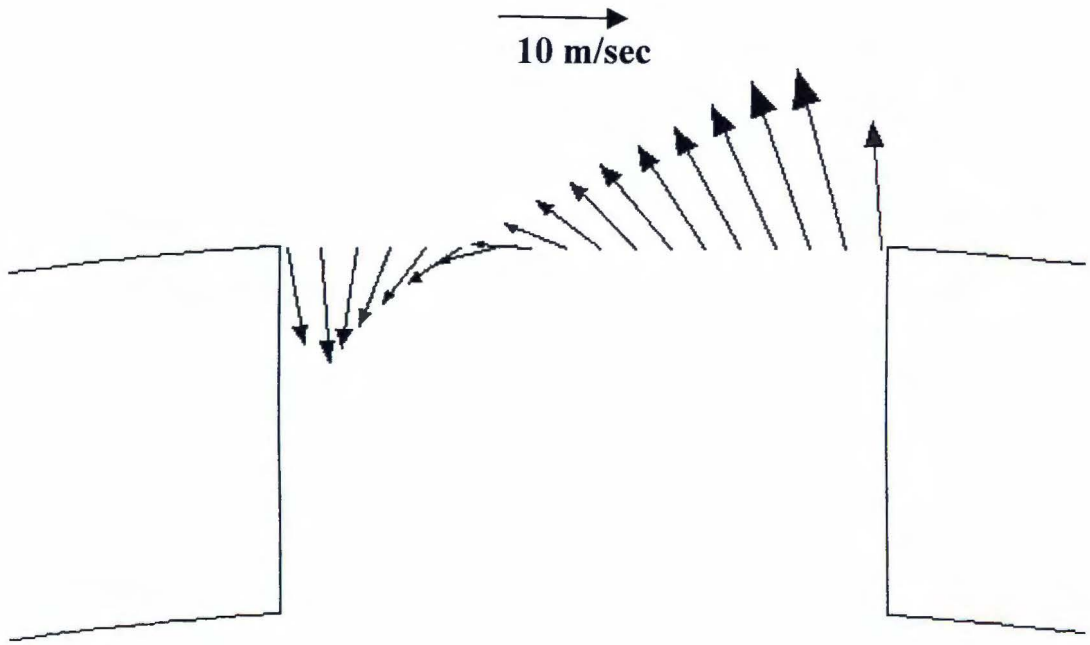

Figure 6-12. Fixed frame simulated velocity data at the exit to slot 1 (r = 77 mm) in the standard gap device. Simulation 5.

however, reentrained flow is seen along greater than one half the width of the slot, except at z = -2, where flow is reentrained for close to exactly one half the slot width.

The simulated flow pattern at the exit to slot 1 more closely resembles the experimental data obtained with volute cover 2: The velocity vectors on the right side of the slot exit point radially outward in a counterclockwise direction (toward the outlet) in both simulation and LDA measurements with volute cover 2. In contrast, LDA measurements of the flow with volute cover 1 show that the flow leaving the right side of stator slot 1 tends to have a smaller tangential component. The flow patterns near the exit of stator slot 1 vary greatly as a function of depth and are very complicated. Clearly a two dimensional model is an inadequate for simulating the full range of flows occurring in the stator slots.

6.2 Fixed Frame and Angularly Resolved Stator Slot Mass Flow Rates

Figures 6-13 and 6-14 are plots of the estimated fixed frame mass flow rates through stator slots in the wide and standard gap devices respectively, and are based on data collected at the midplane exit of the slots (z=-6 mm and r = 77mm) using volute cover 1. The estimated mass flow rates are based on the assumption that the flow field through the entire 12 mm depth of the stator slots is identical to that observed at the midplane. For both the wide and standard gap, the total mass fraction calculated in this way accounts for only about 60% of the total device throughput. This calculation does ignore slots 5 and 12 since no LDA data were collected there, but nonetheless, the value is clearly too low, indicating again that flow in the stator slots is highly dependent on depth

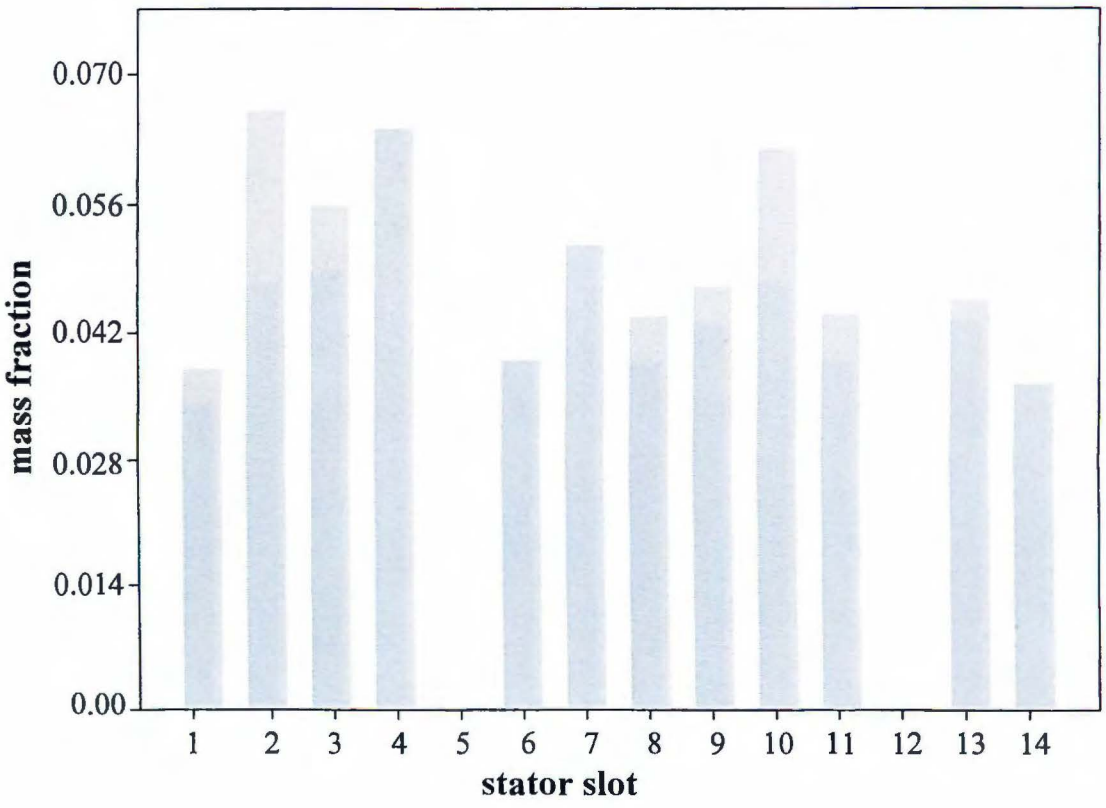

Figure 6-13. Fixed frame mass flow rates through stator slots in the wide gap device. Based on LDA data taken at z = -6 mm. Volute cover 1.

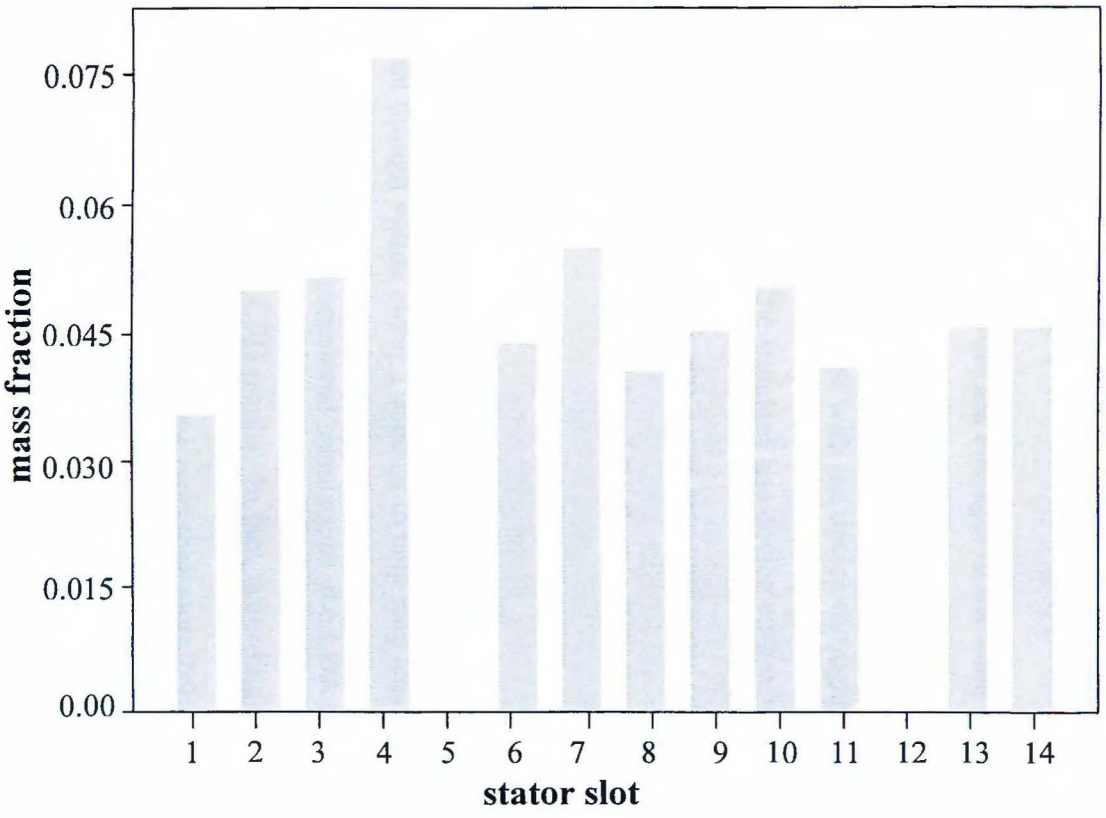

Figure 6-14. Fixed frame mass flow rates through stator slots in the standard gap device. Based on LDA data taken at z = -6 mm. Volute cover 1.

The region where mean velocity was collected for the standard gap device with volute cover 2 at the slot exits as a function of depth (Fig. 6-11 for stator slot 1) is defined by a two-dimensional array of points. Integration of the velocity data over this region results in a better estimate of the corresponding slot mass flow rate since a constant velocity throughout the slot depth is not assumed. Mass flow rates so calculated are illustrated by Fig. 6-15. The flow through slots 3 and 10 were estimated by assuming that their values were the averages of the mass flow rate through slots 2 and 4 or 9 and 11 respectively (data not available for slots 3 and 10). The resulting overall slot mass flow rate balances with the device throughput to 98%. Similar two-dimensional integration for the standard gap device with volute cover 1 and the wide gap device with volute covers 1 and 2 was also performed (data not shown). Comparison indicates that up to 29% of the flow in both the wide and standard gap device with volute cover 1 bypasses the stator slots, and instead leaks over the top of the stator teeth (Mishra, 2000).

Even though volute cover 2 appears to help stop leakage flow, which is clearly impossible to see in two-dimensional simulations, the LDA mass flow rate data still does not compare well with CFD results. In fact, according to Fig. 6-15, slots 1 and 14 have substantially smaller mass flow rates than slots 2-9 which is opposite to CFD prediction. Possibly this is due to the fact that volute cover 2 fits with the top of the stator teeth near the exit (teeth 12-14) better than with those opposed to the exit (teeth 4,5,6) as stated earlier.

The only angularly resolved LDA data presented here (Figs. 6-16 through 6-18) illustrate the periodically time dependent mass flow rates through stator slots 13,

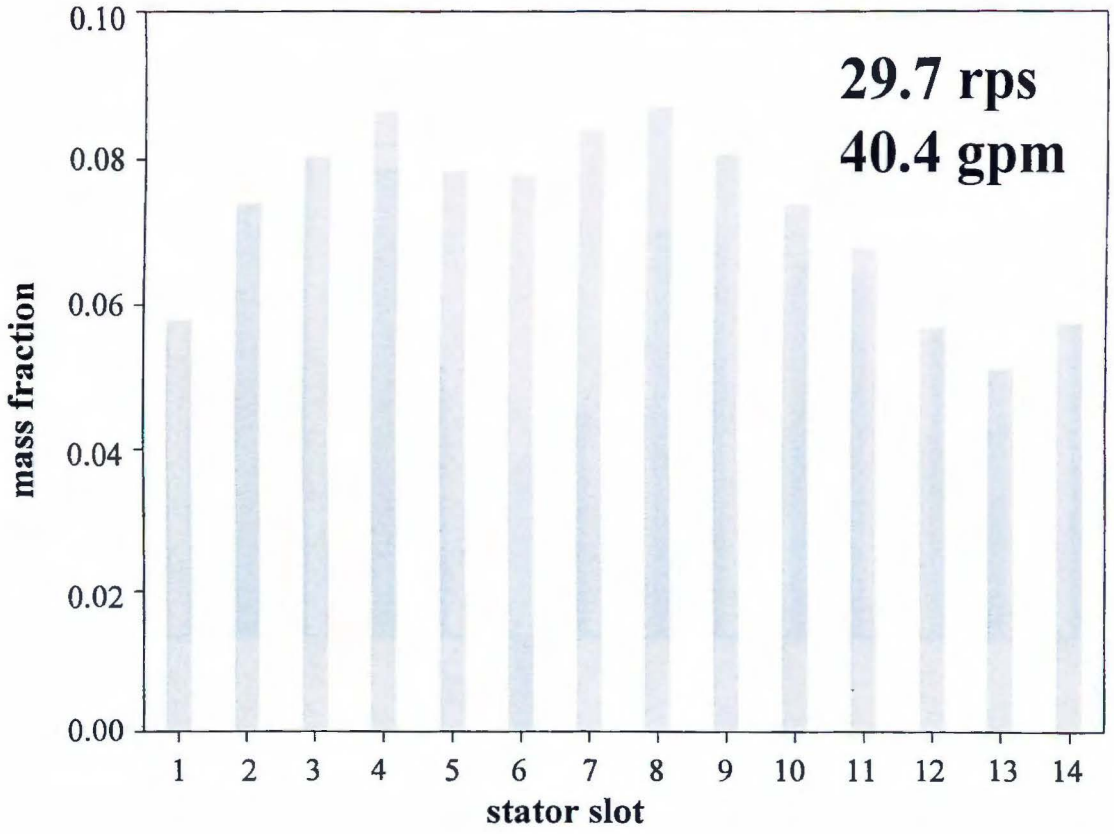

Figure 6-15. Fixed frame mass flow rates through stator slots in the standard gap device. Based on LDA data taken in the entire θ-z plane bounding the slot exits at r = 77 mm. Volute cover 2.

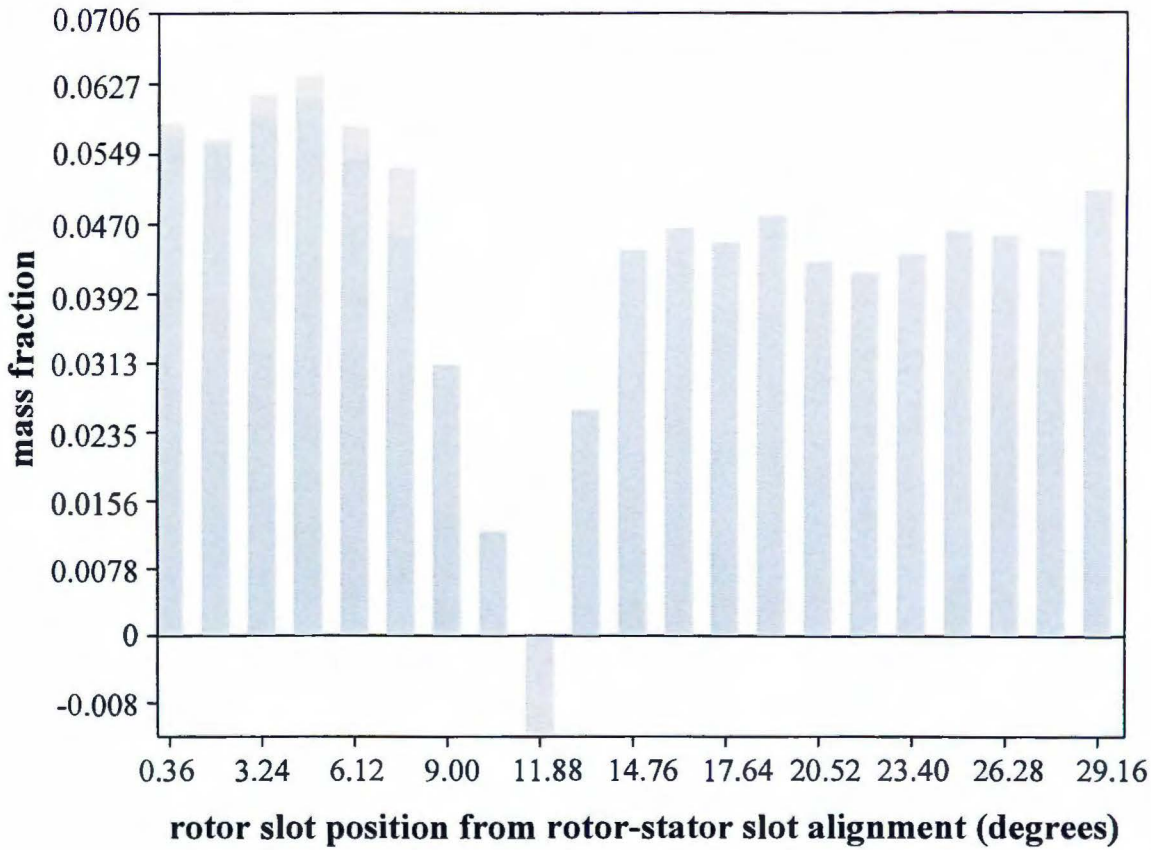

Figure 6-16. Time dependent mass flow rate through stator slot 13 in the standard gap device over one period. Based on LDA data at z = -6 mm. Volute cover 1.

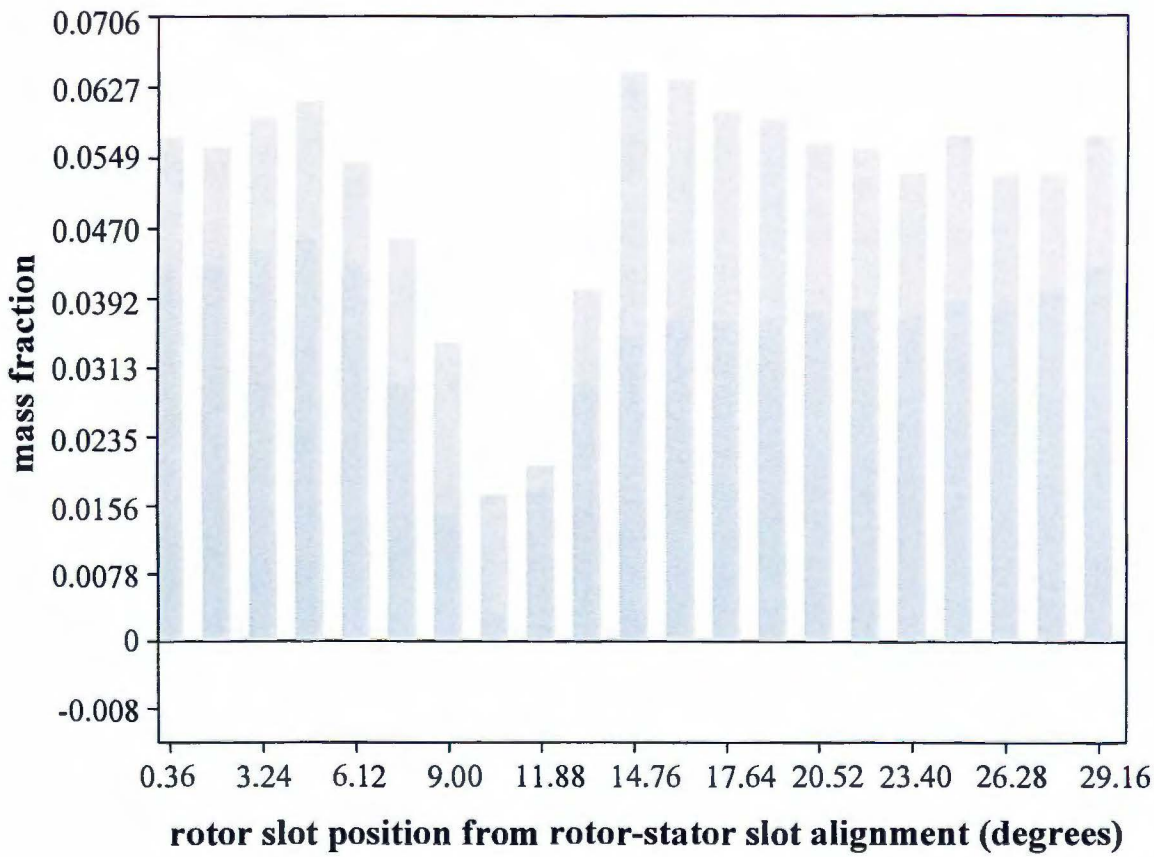

Figure 6-17. Time dependent mass flow rate through stator slot 14 in the standard gap device over one period. Based on LDA data at z = -6 mm. Volute cover 1.

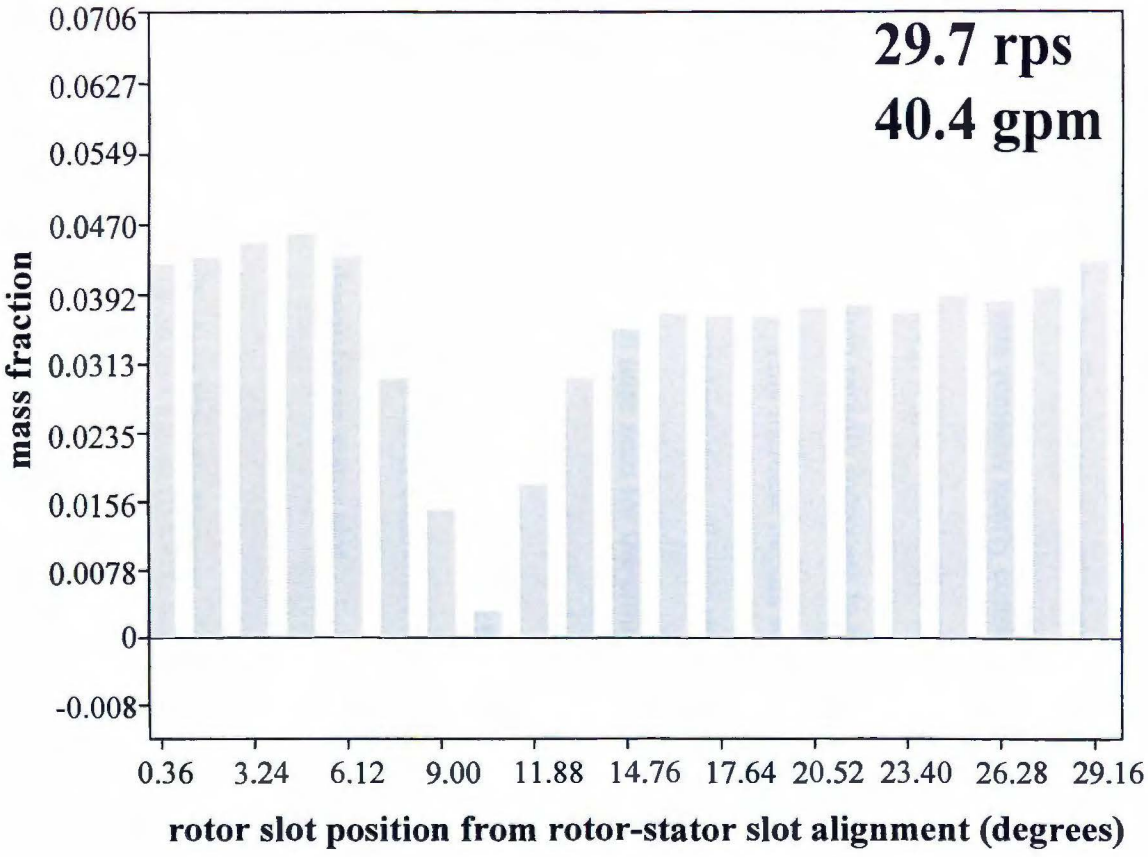

Figure 6-18. Time dependent mass flow rate through stator slot 1 in the standard gap device over one period. Based on LDA data at z = -6 mm. Volute cover 1.

14, and 1, respectively, for the standard gap rotor-stator device with volute cover 1. The calculation of these mass flow rates is based on measurement in only the z = -6 plane of the device and therefore are not completely accurate, but nevertheless may be useful for comparison to simulation. In these figures, 0.36° indicates a rotor slot orientation in perfect alignment with the corresponding stator slot (see, for instance, Fig. 5-7). In all three slots, the flow is near a maximum when the stator slot is completely open. The flow rate remains nearly constant until a rotor slot has completely passed a stator slot (~9°), at which time the flow rapidly decreases to its minimum value. The flow then rapidly increases to nearly the same level that it was when the slot was fully open. This increase occurs well before the stator slot has begun to reopen, which is counterintuitive. Recall that CFD simulation predicted that the slot mass flow rates remain near zero for the entire time that a rotor tooth blocks the slot (Fig. 5-22). This indicates that, in the physical device, when a stator slot is blocked by a rotor tooth, the path of least resistance to flow for fluid in the gap is between the stator teeth and volute cover clearance, rather than tangentially through the gap to the next open downstream stator slot.

6.3 Fixed Frame Turbulent Kinetic Energy

The turbulent kinetic energy based on fixed frame LDA measurements of the r and θ velocity fluctuations in the z = -6 mm plane for the wide gap model are shown in the vicinity of slots 14, 1, and 2 in Figs. 6-19 through 6-21. Unfortunately, fixed frame turbulence measurements include a psudoturbulence due to the periodicity of the rotor and, therefore, direct comparison to CFD results is ambiguous. Nevertheless,

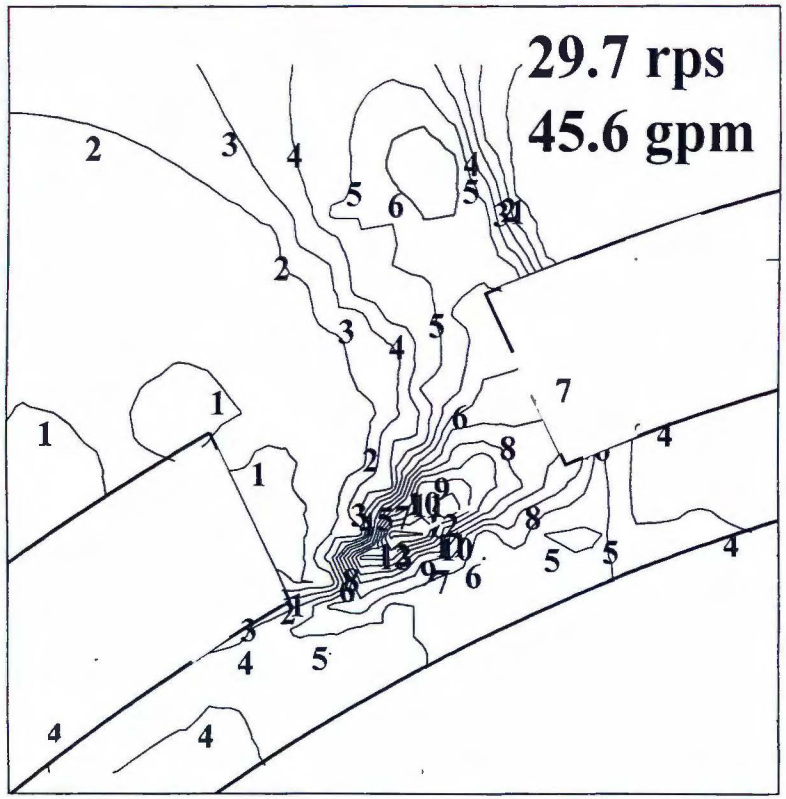

Figure 6-19. Fixed frame LDA turbulent kinetic energy data (m^2/sec^2) in the z = -6 mm plane near stator slot 14 of the wide gap device. Volute cover 1.

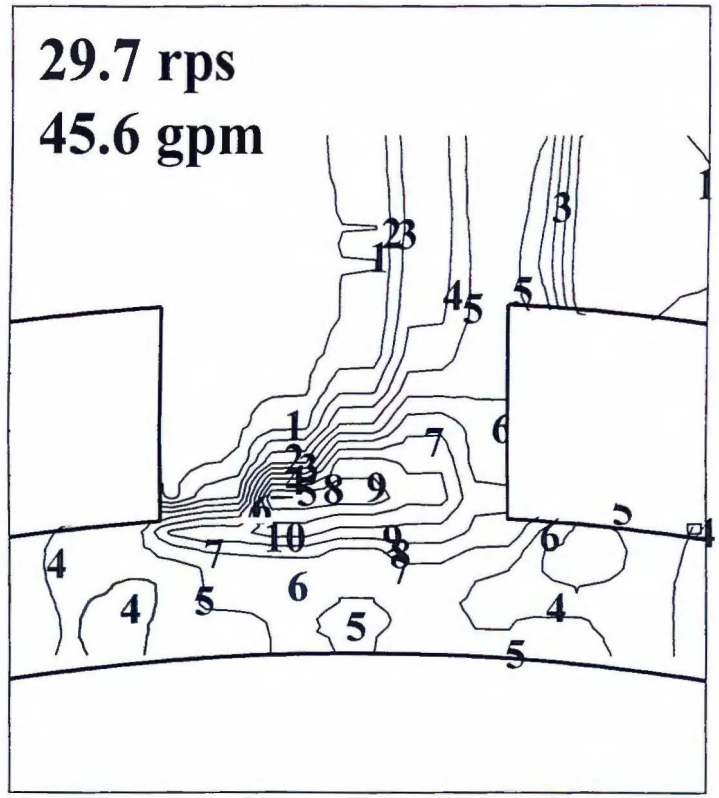

Figure 6-20. Fixed frame LDA turbulent kinetic energy data (m^2/sec^2) in the z = -6 mm plane near stator slot 1 of the wide gap device. Volute cover 1.

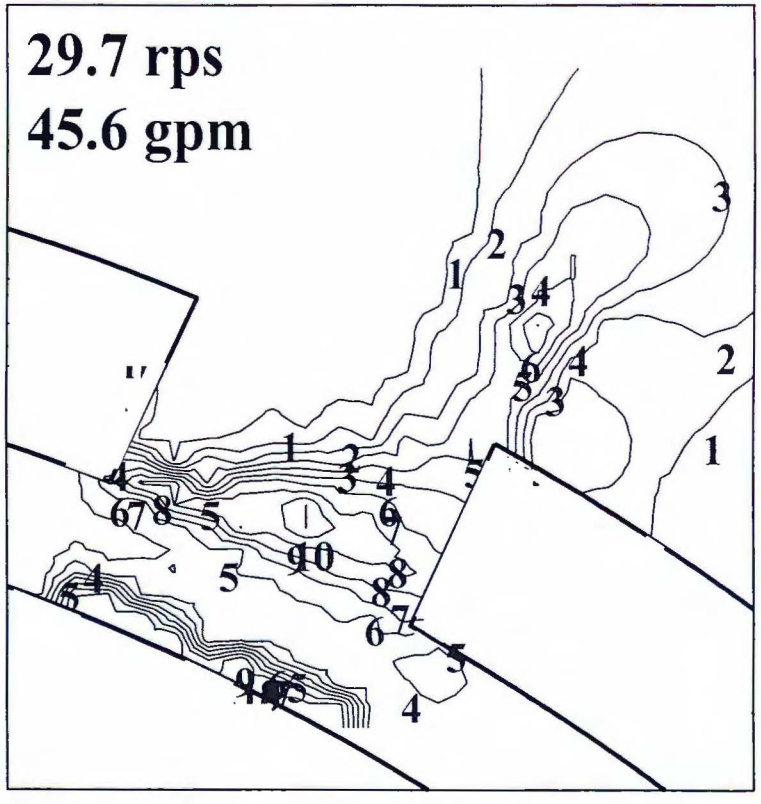

Figure 6-21. Fixed frame LDA turbulent kinetic energy data (m^2/sec^2) in the z = -6 mm plane near stator slot 2 of the wide gap device. Volute cover 1.

the LDA data indicate that in all 3 slots the highest turbulence occurs near the left lower corner of the stator slot. The volute regions near the slots have relatively low turbulence values. Of the three regions depicted, only the gap near slot 2 has significantly high turbulence values (up to 9 m^2/sec^2 or $0.05V^2_{tip}$)

The measured fixed frame turbulent kinetic energies for the standard gap device in the z = -6 mm plane (Figs. 6-22 through 6-24) show that the highest turbulence occurs all the way across each stator slot very near the boundary with the gap. The maximum TKE in the standard gap model is also on the order of $0.05V^2_{tip}$. In comparison to the wide gap device, the stator slot TKE in the standard gap device appears to be concentrated more towards the shear gap. Measurements in the gap itself were not possible for the standard gap device.

Very roughly, the differences in the localization of high turbulence between the standard and wide gap devices found experimentally coincide with the differences predicted by CFD. In the standard gap CFD simulation, a region of high turbulent kinetic energy was found to extend from the left lower corner of a stator slot much further across the slot width than in the wide gap simulations (compare Figs. 4-34 and 5-48). Further, similarly to the fixed frame LDA data, CFD simulations predicted that the slot turbulence in the standard gap device is concentrated into a smaller region near the shear gap than in the wide gap device. CFD predicted maximum angularly resolved TKE values in the right corner of stator slot 1 to be about 50 m^2/sec^2 ($0.30V^2_{tip}$) for the wide gap device and 150 m^2/sec^2 ($0.90V^2_{tip}$) for the standard gap device (section 5.3) which seems to be an overestimate. However, it should be kept in

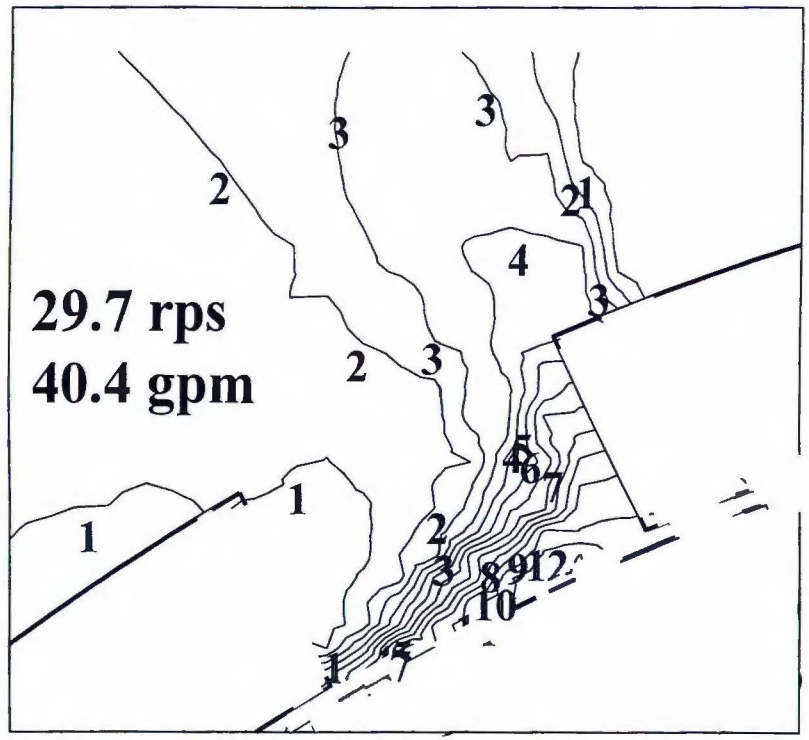

Figure 6-22. Fixed frame LDA turbulent kinetic energy data (m^2/sec^2) in the z = -6 mm plane near stator slot 14 of the standard gap device. Volute cover 1.

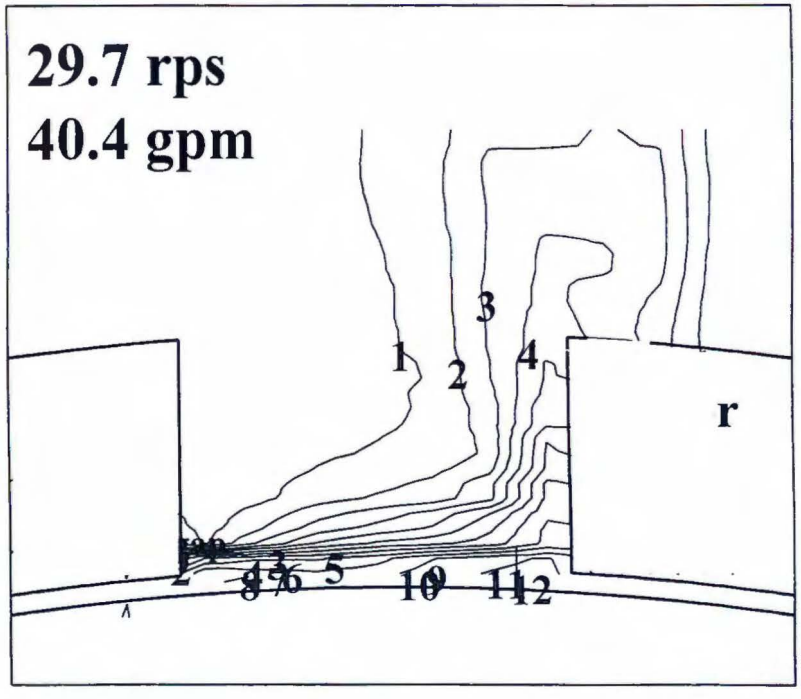

Figure 6-23. Fixed frame LDA turbulent kinetic energy data (m^2/sec^2) in the z = -6 mm plane near stator slot 1 of the standard gap device. Volute cover 1.

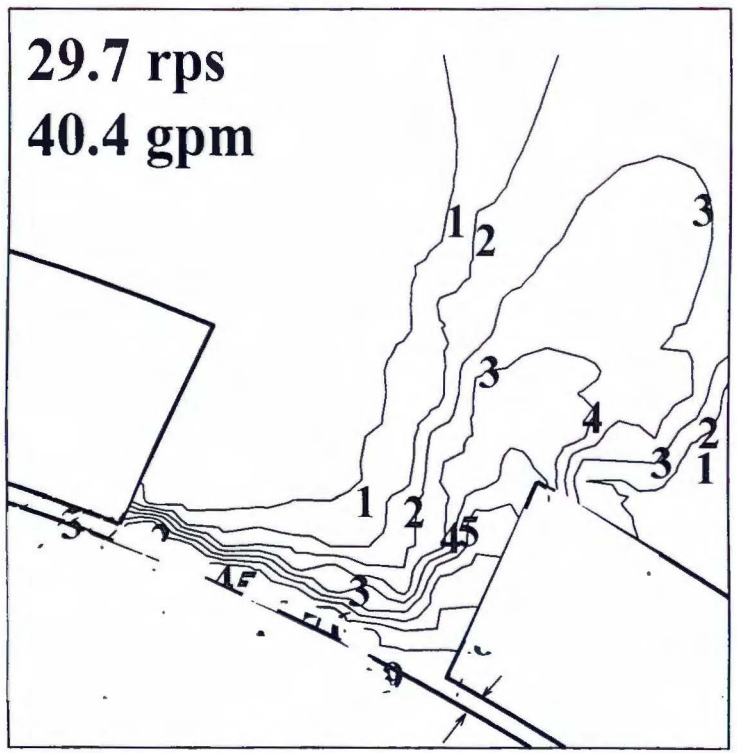

Figure 6-24. Fixed frame LDA turbulent kinetic energy data (m^2/sec^2) in the z = -6 mm plane near stator slot 2 of the standard gap device. Volute cover 1.

mind that LDA cannot measure close to walls, where the CFD predicted the highest values due to stagnation of the gap jet with the wall.

6.4 Summary

Qualitatively, CFD simulation compares well with fixed frame LDA data of the mean velocity field in stator slots for both the wide and standard gap devices. Both simulation and experiment predict vortices in the slots, with reentrainment of flow from the volute. Further, both simulation and LDA show that velocities near the portion of the slots closer to the gap are higher in the standard gap device, Measurements in the shear gap of the standard gap device cannot be compared with simulation due to limitations of LDA. Future comparisons of gap mean velocity data with simulation need to be performed for further validation of the wide gap model.

The CFD simulations, obviously, do not do a good job in predicting the strong dependence of stator slot flow patterns on axial depth. When volute cover 2, which reduces leakage flow over the stator teeth, is used for experiment, the flow patterns at the slot exit more closely resemble those obtained with simulation.

Further, due at least in part to leakage flow between the volute cover and the top of stator teeth when a stator slot is blocked by a rotor slot, CFD does not predict the fixed frame distribution of flow rates between the slots correctly. In the angularly resolved reference frame, both CFD and LDA data do show that, in the standard gap device, individual slot flow rates undergo a rapid decrease as soon as a rotor tooth completely blocks a stator slot. However, experimentally, the slot flow rate rapidly increases back to a maximum long before the rotor tooth completes its passage. CFD

simulation, on the other hand, predicts that the slot mass flow rate remains very low for the entire passage of a rotor tooth. This discrepancy is also likely due to leakage flow.

Patterns of the fixed frame turbulent kinetic energy in the stator slots are crudely predicted by CFD: The TKE is more focused near the interface of a stator slot and the shear gap in the standard gap model. Nevertheless, the simulations appear to overpredict the magnitude of TKE significantly. Because of pseudoturbulence, a more meaningful comparison of the device turbulence field predicted by simulation and observed with experiment cannot be done until the angularly resolved LDA data is fully analyzed.

Chapter 7 Conclusions and Recommendations

The simulations presented in this work have shown that CFD may indeed provide insight into the fundamental physics of flows occurring in rotor-stator mixers. Significant differences in the simulated flow occurring in the wide and standard gap models were found, and indicate that parametric studies may be the best approach to the use of CFD for rotor-stator mixers. The simulations show several interesting phenomenon that are not necessarily intuitive. These include the finding that, according to simulation, shear in the gap is much smaller than what might have been expected in both the standard and wide gap models. Thus, high shear in rotor-stator mixers may play only a very small role in dispersion processes. Further, flow reversal in the gap region, according to simulation, is more likely as the gap width decreases, and the maximum gap mean velocities actually occur in a direction opposite that of the rotor motion.

While many of the simulation results are interesting, and have significant potential to be an aid in the design of rotor-stator mixers, there are many issues to be addressed before CFD simulations of these devices can be utilized with confidence. First among these is continued, in-depth, comparison of simulation with angle correlated LDA data. The preliminary comparison done here has shown that the two-dimensional approximation appears to correctly predict, on a qualitative level, the mean velocity field, in the mid-plane of the device, in the stator slots and volute.

However, it is still not known whether the CFD simulations captured the qualitative nature of flow in the shear gap region for the wide gap device.

It is clear, however, that a quantitative prediction of the mean velocity field is not obtained with the present simulations: The maximum fixed frame velocities are overpredicted by CFD. It appears that leakage flow between the tops of stator teeth and the volute cover is a very significant feature of the flow. It is therefore essential that future CFD simulations address this three-dimensional nature of the flow.

Further, the simulations appear to over predict the turbulent kinetic energy. This is opposite to most turbulent simulations in stirred tanks (Robinson, 2001), and the reason for this is not clear at present, but it may also be due to leakage flow. It is also likely that the k-ε turbulence model and the wall function treatment are not sophisticated enough for the complex flows occurring in the gap, and it is recommended that other models, such as RSM or large eddy simulation (LES) be employed without wall functions in the future.

The difficulty with using more sophisticated turbulence models in conjunction with fully three-dimensional simulations is the very long compute times required. In the short time since CFD work began for the rotor-stator mixer under consideration here, computing power has increased at a rapid pace. With the present ability to run CFD simulations on parallel processor systems, it is possible to routinely run three-dimensional sliding mesh simulations with upwards of 1.5 million cells. Clearly, however, the fact that it takes upwards of 9 rotor revolutions before a periodic steady state is reached makes simulations of rotor-stator mixers, as performed here, very time consuming and not feasible for routine use. For instance, for simulation 5 (~350,000

computational cells) , on a two-processor machine, each time step required approximately 100 outer iterations (about 20 minutes of CPU time) as described in chapter 3. This corresponds to roughly 31 days of CPU time for a single simulation. This is not to say that it is essential to carry out computations until a truly periodic solution is reached: In many cases an approximately periodic solution will suffice. However, if future simulations are to be three-dimensional and incorporate turbulence models like LES, then the grids are going to have to be extremely fine. One solution, of course, is to use brute force and carry out simulation on massively parallel machines.

Alternatively, there are several properties of the rotor-stator simulation solutions that suggest changes to the computational methods employed, at least for RANS models. It is recommended that highly specialized and optimized codes and / or subroutines be written specifically for the simulation of rotor-stator mixers.

For instance, the fact that the pressure reaches periodicity much faster than other flow variables raises the possibility that, rather than using the previous pressure field as a first guess for the pressure field at a new time step, the periodic nature of the (fast developing) pressure can be exploited to provide a better initial guess. This may result in convergence at each time step in fewer iterations. Clearly this could not be done during initial startup of simulation, but could be implemented after a few periods have been completed.

Besides algorithm optimization, there are some simple steps that can be taken to decrease the amount of computational time required in future simulations. For instance, it may be possible to speed the solution process by initially running quasi-

steady state simulations as a first approximation. Time dependence could then be turned on after flow in regions of stagnation has had a chance to develop. Rotor-stator mixer simulations could be started with 'moving' rotor walls but a non-moving mesh to yield a steady state approximation to the problem at a given rotor position. In this type of simulation, rotor adjacent cells would be treated computationally as if the rotor were moving, but the overall discretization of the problem would be steady state. While physically unrealistic, this hybrid RRF type of treatment is conceptually simple to implement and similar in spirit to simulations of stirred tank reactors performed by Harvey, Lee, and Rogers (1995).

REFERENCES

Abid, M., Xuereb, C., and Bertrand, J., "Modeling of the 3D Hydrodynamics of 2-Blade Impellers in Stirred Tanks Filled with a Highly Viscous Fluid", *Can J Chem. Eng*, **72**, 184-193, (1994).

Bakker, A., LaRoche, R. D., Wang, M.H., and Calabrese, R. V., "Sliding Mesh Simulation of Laminar Flow in Stirred Reactors", *Trans. IChemE.*, **75**, 42-44, (1997).

Bird, R. B., Stewart, W. E., and Lightfoot, E. N., *Transport Phenomena*, New York: John Wiely & Sons, (1960).

Bourne, J. R. and Garcia-Rosas, J., "Rotor-Stator Mixers for Rapid Micromixing," *Chem. Eng. Res. Des.*, **64**, 11-17, (1986).

Carpenter, K. J., "Fluid Processing in Agitated Vessels", *Chem. Eng. Res. Des.*, **64**, 3-9, (1986).

Derksen, J. and Van den Akker, H. E. A., "Large Eddy Simulations on the Flow Driven by a Rushton Turbine", *AIChEJ.*, **45**, 209-221, (1999).

Epee-Bounya, S., "Sliding Mesh Simulation of a Rotor-Stator Device", M.S. Thesis, University of Maryland, College Park, MD, (1998).

Ferziger, J. H. and Peric, M., *Computational Methods for Fluid Dynamics*, 2 ed. Berlin: Springer, (1966).

FLUENT Version 4.4 User Guide, vols. 1-4 2nd Ed., New Hampshire: Fluent Inc., (1997).

Geankopolis, C. J., *Transport Processes and Unit Operations*, Englewood Cliffs: Prentice Hall, (1993).

Harvey, P. S. and Greaves, M., "Turbulent Flow in an Agitated Vessel Part I: A Predictive Model," *Trans IChemE*, **60**, 195-200, (1982).

Harvey, P. S. and Greaves, M., "Turbulent Flow in an Agitated Vessel Part II: Numerical Solutions and Model Predictions," *Trans IChemE*, **60**, 201-210, (1982).

Harvey, A. D. III, Lee C. K., and Rogers, S. E., " Steady-State Modeling and Experimental Measurement of a Baffled Impeller Stirred Tank," *AIChEJ*, **41**, 2177-2186 (1995)

Hinze, J. O., *Turbulence*, New York: MaGraw-Hill, (1950).

Hiraoka, S. I., Yamada, T. I., Aragaki, H., Nishiki, A, Sata, and Takagi, "Numerical Analysis of Flow Behavior of Highly Viscous non-Newtonian Fluid in Agitated Vessel with Paddle Impeller," *J. Chem. Eng. Japan*, **12**, 56-62 (1979).

Kresta, S. and Wood, P. E., "Prediction of the Three-Dimensional Turbulent Flow in Stirred Tanks," *AIChEJ*, **37**, 448-460 (1991).

Kuriyama, M., Inomata, H., Arai, K, and Saito, S., "Numerical Solution for Flow of Highly Viscous Fluid in Agitated Vessel with Anchor Impeller," *AIChEJ*, **28**, 385-391, (1982).

Le Clair, M., L., "Optimize Rotor-Stator Performance Using Computational Fluid Dynamics." *PCI*, **11**, 46-48, (1995).

Luo, J. Y., Gosman, A. D., Issa, R. I., Middleton, J. C., and Fitzgerald, M. K., "Full Flow Field Computaition of Mixing in Baffeled Stirred Vessels," *Trans IchemE*, **71** Part A, 342-44 (1993).

Mishra, V. P., *Personal communication.*, (2000).

Middleton, J. C., Pierce, F., and Lynch, P. M., " Computations of Flow Fields and Complex Reaction Yeild in Turbulent Stirred Reactors, and Comparision with Experimental Data," *Chem. Eng. Res. Res.*, **64**, 18-22, (1986).

Mohammadi, B. and Pironneau, O., *Analysis of the K-Epsilon Turbulence Model*, New York: John Wiley & Sons, (1994).

Ng, K., Fentiman, N. J., Lee, K. C., and Yianneskis, M., "Assessment of Sliding Mesh CFD Predictions and LDA Measurements of the Flow in a Tank Stirred by a Rushton Impeller," *Trans IChemE*, **76**, 737-747. (1998).

Ranade, V. V. and Joshi, J. B., "Flow Generated by Pitched Blade Turbines II: Simulation Using k-ε Model", *Chem. Eng. Comm.*, **81**, 225-245 (1989).

Ranade, V. V. and Joshi, J. B., "Flow Generated by a Disc Turbine: Part II Mathematical Modeling and Comparision with Experimental Data", *Trans IChemE*, **68 Part A**, 34-50 (1990).

Sheng, J., Meng, H., and Fox, R.O., "Validation of CFD Simulations od a Stirred Tank Using Particle Image Velocimetry Data," *Can. J. Chem Eng.*, **76**, 611-625, (1998).

Stoots, C. M., "The Velocity Field Relative to a Rushton Turbine Blade", Ph.D. Dissertation, University of Maryland, College Park, MD, (1989).

Sturesson, C. and Rasmuson, A, "Numerical simulation of turbulent flow of agitated liquid with pitched blade impeller," *Chem. Eng. Comm.*, **138**, 1-23, (1995).